

**UNIVERSITA' DEGLI STUDI DI PADOVA**

**Scuola di Dottorato in Scienza e Ingegneria dei Materiali**

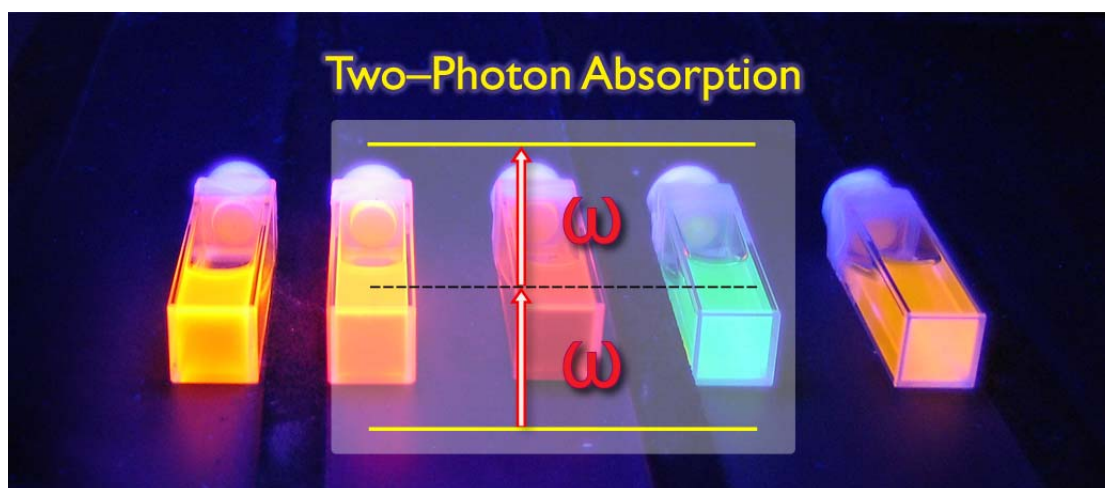
**Ciclo XX**

**Dipartimento di Scienze Chimiche  
Sede Amministrativa: Università di Padova**



**Tesi di Dottorato:**

**INVESTIGATIONS OF MULTIPHOTON ABSORPTION  
PROCESSES IN MOLECULAR SYSTEMS  
IN SOLUTION AND IN SOL-GEL MATRICES  
FOR NONLINEAR OPTICAL APPLICATIONS**



**COORDINATORE: Prof. Gaetano Granozzi**

**SUPERVISORE: Prof. Renato Bozio**

**DOTTORANDA: Ilaria Fortunati**

**31 Dicembre 2007**



*1 - Esci dalla confusione, trova semplicità.*

*2 - Dalla discordia, trova armonia.*

*3 - Nel pieno delle difficoltà risiede l'occasione favorevole.*

*Albert Einstein (Tre regole di lavoro)*



---

# CONTENTS

- <b>ABSTRACT (<i>English</i>)</b>	pag. 1
- <b>ABSTRACT (<i>Italiano</i>)</b>	pag. 5
- <b>INTRODUCTION</b>	pag.11
- <b>CHAPTER 1: Interaction between electromagnetic field and matter</b>	pag. 15
1.1 Linear optical response of a material system	pag. 16
1.2 Nonlinear optical properties	pag. 17
1.3 Parametric versus nonparametric processes: examples of second and third-order processes	pag. 20
1.4 Determination of nonlinear optical susceptibility	pag. 21
1.4.1 Schrödinger equation calculation of the nonlinear susceptibility	pag. 22
1.4.2 Density matrix formalism for the determination of the optical susceptibility	pag. 25
- Derivation of the linear susceptibility	pag. 27
- Derivation of nonlinear susceptibilities	pag. 28
1.5 Two-photon absorption (TPA)	pag. 30
1.6 Saturable absorption (SA) and Reverse Saturable absorption (RSA)	pag. 31
1.7 Sequential Multiphoton absorption processes	pag. 34
- <b>CHAPTER 2: Materials for two-photon absorption</b>	pag. 41
2.1 Dipolar D-A organic chromophores	pag. 41
2.2 Quadrupolar organic chromophores	pag. 45
2.3 Octupolar molecules	pag. 48
2.4 Porphyrins and squaraine systems	pag. 50
2.5 Semiconductor quantum dots	pag. 51
- <b>CHAPTER 3: The Sol-Gel process: a useful tool for the preparation of solid-state devices</b>	pag. 55
3.1 Principles of sol-gel process	pag. 56
3.1.1 First step: Hydrolysis	pag. 58
3.1.2 Second step: Condensation	pag. 59
3.1.3 Third step: Gelification	pag. 60
3.1.4 Fourth step: Drying	pag. 61
3.1.5 Fifth step: Dehydration and densification	pag. 63
3.2 Organic-inorganic hybrid sol-gel precursors	pag. 63
3.3 Reactivity of hybrid precursor	pag. 65

---

3.4 Two examples of network modifiers: 3-Glycidoxypropyl-trimethoxysilane (GPTMS) and 3-methacryloxypropyl-trimethoxysilane (MPTMS)	pag. 66
3.5 Applications of hybrid organic-inorganic materials	pag. 68
<b>- CHAPTER 4: Experimental techniques for the characterization of samples</b>	pag. 73
4.1 Z-scan and Non Linear Transmittance (NLT) techniques	pag. 74
4.1.1 Open aperture z-scan technique: theory	pag. 75
4.1.2 Open aperture z-scan technique: experimental set-up	pag. 76
4.1.3 Non-linear transmission measurements	pag. 78
4.2 Pump&Probe method	pag. 78
4.3 Two-photon Induced Fluorescence technique	pag. 78
4.3.1 Analysis of the physical background of TPIF	pag. 78
4.3.2 Second-order temporal dependence	pag. 80
4.3.3 Spatial dependence	pag. 81
4.3.4 Fluorescence collection efficiency	pag. 82
4.3.5 Fluorescence quantum yield (FQY) measurements	pag. 82
4.3.6 Experimental TPIF method	pag. 85
4.3.7 Deviation from quadratic-intensity law	pag. 85
4.3.8 Experimental set-up and tests	pag. 87
4.3.9 Two-photon fluorescence spectra	pag. 93
4.4 Confocal microscopy: a powerful tool for the investigation on the morphology of micro- and nano-structures	pag. 94
<b>- CHAPTER 5: Requirements for the realization of an Optical Power Limiter</b>	pag. 101
5.1 Requirements for the Optical limiter	pag. 102
5.2 Optical limiter based on nonlinear phenomena	pag. 103
5.3 Fulleropyrrolidine as RSA material: a convenient replacement for C <sub>60</sub>	pag. 104
5.4 Optical limiter in a "Tandem" configuration	pag. 106
5.5 Heterocyclic quadrupolar push-pull TPA dye	pag. 107
<b>- CHAPTER 6: Characterization of new materials showing TPA properties</b>	pag. 113
6.1 Non linear optical characterization of TPA dyes in solution	pag. 114
6.2 TPIF characterization of push-pull systems	pag. 114
- Dipolar molecules	pag. 114
- Dimeric structures of PEP and MePEP	pag. 118
- Quadrupolar and octupolar structures	pag. 120
6.3 TPIF characterization of squaraines	pag. 124
6.4 TPIF characterization of semiconductor Quantum Dots	pag. 126
6.5 Z-scan characterization using ns pulses	pag. 129
- Characterization of push-pull systems	pag. 129
- Characterization of squaraines and porphyrins	pag. 131

---

- Characterization of helicenes	pag. 134
- Characterization of semiconductor quantum dots	pag. 134
6.6 Conclusions of the nonlinear optical characterization of TPA absorbers in solution	pag. 136
<b>- CHAPTER 7: Synthesis and characterization of new sol-gel matrices for Optical Limiting</b>	pag. 139
7.1 Synthesis of the hybrid matrices	pag. 140
7.2 Non linear optical characterization: a measurement of the optical damage threshold	pag. 142
7.3 Experimental analyses	pag. 144
IR analyses	pag. 145
Thermal analyses	pag. 147
UV-Visible spectra	pag. 148
Mechanical characterization	pag. 148
Laser damage measurements	pag. 149
Optical analyses	pag. 150
7.4 Embedding of core-shell nanoparticles in a sol-gel matrix	pag. 153
7.5 Concluding remarks	pag. 154
<b>- CHAPTER 8: Up-converted lasing</b>	pag. 157
8.1 Two-photon pumping of organic push-pull dyes in solution	pag. 157
8.2 Measurements of ASE emission under two-photon pumping of a dipolar and a quadrupolar push-pull molecule in solution	pag. 159
8.3 Using CdSe-CdS-ZnS Quantum Dots as highly efficient material for amplified spontaneous emission	pag. 161
8.4 Measurements of the gain of zirconia doped films	pag. 163
8.5 Conclusions	pag. 168
<b>- CHAPTER 9: One- and Two-photon induced Photopolymerization</b>	pag. 173
9.1 State of the art of photopolymerization technique	pag. 174
9.2 Non linear optical characterization of photoinitiators	pag. 176
9.3 Materials used as prepolymer blend for further photopolymerization process	pag. 177
9.4 Thermal polymerization: a preliminary study before the photopolymerization	pag. 179
9.5 One-photon polymerization	pag. 182
9.6 Two-photon polymerization	pag. 186
9.6.1 TPIP on SAN-Mon films	pag. 187
9.6.2 TPIP on MZrMAMon and MZrMA films	pag. 188
9.7 Conclusions	pag. 192
<b>- FINAL REMARKS</b>	pag. 195



## ABSTRACT

The investigation of non linear optical properties of organic and inorganic materials has been obtained great attention during last decades for a large number of applications.

One important property is the multiphoton absorption; it is based on the coherent absorption of two or more photons (instantaneous two- or three-photon absorption) or the sequential absorption (for example, the excited state absorption or the reverse saturable absorption processes).

The two-photon absorption (TPA) process is characterized by important properties, such as the instantaneity, useful in applications where low response times are required, or the quadratically dependence with the intensity of the incident laser radiation, allowing high 3D resolution. Another important aspect is the fact that common organic molecules, such as those present in biological tissues, are linearly transparent in the wavelength domain where TPA occurs (near-infrared), providing increasing penetration. Biosensoristic or photodynamic therapy applications take advantage of this important feature. In addition, the Rayleigh scattering is lower if IR wavelengths are employed.

Thanks to these properties, the TPA process is largely exploited in many applications, such as the optical limiting; the photodynamic therapy, for the local treatment of tumours; the realization of three-dimensional optical memories; the micro- and nano-fabrication; the design of compact laser devices based on the two-photon induced up-converted lasing.

It is important to note that often the realization of such devices, based on the TPA process, requires the fulfilment of other photophysical properties.

Anyway, in order to avoid the damage of the material, the intensity required for the activation of the process must be as low as possible. One strategy can be the design of a TPA material with high TPA properties. The TPA efficiency of a system is described by the TPA cross-section ( $\sigma_{\text{TPA}}$ ), which is associated to the third-order nonlinear optical response of a single molecule. In the first step, it is therefore necessary to characterize the TPA chromophores in solution. Successively, the systems, which meet the requirements for the specific application, might be included in a solid material toward the realization of an all-solid state device.

Large part of this work has been devoted to the nonlinear optical characterization of many classes of materials. Different methods and excitation sources are employed in order to fully characterize the dyes in a large wavelengths range and in different temporal regimes (ns and fs). In particular, the set-up for a new technique is realized in our laboratories, allowing the determination of the TPA cross-section through the measurement of the emission induced by two-photon absorption (TPIF). The excitation source is an ultrafast mode-locked Ti:Sapphire laser in the range 720-930 nm. The systems characterized with this method are: dipolar, quadrupolar, octupolar push-pull compounds, dimeric systems of push-pull molecules, squaraines, core-shell semiconductor quantum dots with different radii.

This optical characterization is useful to identify the more promising materials for the three studied applications: 1) optical limiting; 2) up-converted lasing; 3) microfabrication.

### **Optical limiting**

The first application regards the realization of an optical power limiter. The prototype of the final device, called "Tandem optical limiter", consists of two sol-gel disks doped with a TPA absorber and a fullerene derivative showing reverse saturable absorption (RSA). The RSA process is activated by long pulses (ns or ps). Previous studies have shown that our fullerene derivative has the best efficiency at 690 nm under ns laser pulses irradiation. At the same wavelength, the previously studied TPA compound is not so efficient to increase the optical limiting properties of the final device.

In this work we will report the results on the characterization of new TPA dyes which can be used as counterpart material of the fullerene system. Push-pull dipolar, quadrupolar and octupolar systems, porphyrins, squaraines, and semiconductor quantum dots are

analysed with "z-scan" and "nonlinear transmittance" methods. The ns laser system produces pulses with duration of about 12 ns in the 670-850 nm wavelengths region. The TPA cross-section, measured in long-pulses regime, becomes an effective value and it is denoted as  $\sigma_{\text{TPA}}^{\text{eff}}$ . From the comparison between the  $\sigma_{\text{TPA}}^{\text{eff}}$  data at 690 nm of all the TPA chromophores, we can observe one of the analysed porphyrins can be a promising material for optical limiting application. Its hydroxyl-functionalized derivative is under preparation for the further embedding a solid matrix.

Moreover, we have synthesized and characterized some sol-gel hybrid organic-inorganic matrices as host for active material in high energy application. We have changed the precursors, the catalysts and the synthesis protocol, in order to induce a modification in the microstructural properties of the final materials. The obtained matrices are mechanically, thermally and optically characterized. In particular, in this context we are interested in the investigation of the correlation between the laser damage resistance, measured at 690 nm with a ns laser source, and the microstructural properties. One of the main results is the direct correlation between the elasticity properties of the materials and their resistance to the laser irradiation. These hybrid matrices can be used as powerful host for NLO-active systems.

### **Up-Converted Lasing**

The up-converted lasing is an alternative method to produce laser sources in the visible range. When a system is excited by a light source, spontaneous emission can occur and it is in general incoherent and randomly emitted in all directions. However if the pump pulse is polarized, the emission will have a preferred direction perpendicular to the pump's polarization. Thus, spontaneous emission will create coherent stimulated emission along its direction of propagation, the Amplified Spontaneous Emission (ASE). When the two-photon pumping mechanism is involved, the NLO system is excited through the simultaneous absorption of two photons in the near-IR range. One of the main characteristics of the ASE peak is its strong spectral narrowing.

We have studied the up-conversion lasing process both in push-pull organic dyes in solution and in semiconductor core-shell CdSe-ZnS quantum dots embedded in zirconia films. The excitation source is an amplified Ti:Sapphire laser at 800 nm. For the organic compounds, the ASE emission is measured only in solution.

On the contrary, for the quantum dots it is possible to detect the ASE peak only if the nanocrystals are embedded in a zirconia matrix. The matrix plays an important role in the

reduction of the non-radiative pathways. We have determined the gain values of the ASE process for films doped with nanocrystals having diameters varying from 2.1 and 3.2 nm. We have demonstrated that the dimension of the quantum dots influence the ASE threshold and the stability data.

### **Microfabrication**

For microfabrication applications, the photo-induced polymerization offers multiple advantages, including spatial and temporal controls, fast curing speed at room temperature, large efficiency and great versatility on the initial prepolymer blend.

In this work we have studied the photopolymerization process induced both by one-photon and two-photon absorption of a properly synthesised photoinitiator. The prepolymer blends contain photopolymerizable (meth)acrylic groups. We exploit the novel possibility to use organic-inorganic hybrid precursors, with acrylic and methacrylic functionalities, as components for the polymerizable mixture, instead of the common all-polymeric blends.

The photopolymerization have been performed with different laser sources, a CW Ar laser and a femto-second laser, using many excitation energies, for different times, in air and inert atmosphere. After irradiation the samples are developed by the suitable solvent and the remaining structures are morphologically characterized through atomic force, scanning electron and confocal microscopies.

One of the main factors influencing the efficiency in one-photon polymerization is the presence of molecular oxygen. Instead, this issue becomes less important when two-photon excitation is employed. Our results regarding the two-photon polymerization process on hybrid organic-inorganic materials are preliminary but they open the way for the realization of prominent micro- and nano-structures based on these new materials.

## ABSTRACT (*Italiano*)

Lo studio delle proprietà ottiche non lineari di materiali organici e inorganici ha rivestito un ruolo sempre più importante nella comunità scientifica, sia dal punto di vista teorico che applicativo. Tra le proprietà ottiche non lineari spicca l'assorbimento multifotonico previsto da Marie Goppert Mayer, già nel 1931, e mostrato sperimentalmente solo a partire dagli anni '60, grazie allo sviluppo delle sorgenti laser.

L'assorbimento multifotonico si basa sulla capacità del materiale di assorbire due o più fotoni in modo coerente (assorbimento puro a due-, tre-, n-fotoni) o sequenziale (per esempio, assorbimento da stato eccitato o assorbimento saturabile inverso). Tale processo è legato alla suscettività ottica non lineare di ordine superiore a uno. Poiché all'aumentare dell'ordine coinvolto il valore della suscettività diminuisce in modo sostanziale ( $\chi^{(1)}$  [adimensionale] :  $\chi^{(2)}$  [ $\text{m V}^{-1}$ ] :  $\chi^{(3)}$  [ $\text{m}^2 \text{V}^{-2}$ ] = 1 :  $10^{-12}$  :  $10^{-23}$ ), sono necessarie alte intensità incidenti, raggiungibili attraverso sorgenti laser focalizzate, che permettono di innescare il processo ottico non lineare.

Concentriamoci per semplicità sul processo di assorbimento a due fotoni (chiamato TPA). Le caratteristiche che lo contraddistinguono sono l'istantaneità (proprietà importante per le applicazioni dove è richiesta una risposta rapida) e l'elevata risoluzione tridimensionale dell'eccitazione, che può avvenire solo in corrispondenza del volume focale. A queste si aggiunge la possibilità di sfruttare l'emissione del cromoforo, a seguito di eccitazione per

TPA (Two-photon excited emission – TPE): essa cade circa a metà della lunghezza d'onda della radiazione incidente. L'utilizzo di sorgenti laser nel vicino IR, per eccitare le molecole TPA, permette inoltre l'applicazione nel campo della biosensoristica o della terapia fotodinamica, essendo i tessuti biologici trasparenti in questa finestra. Infine l'uso di lunghezze d'onda nell'infrarosso riduce l'effetto di scattering Rayleigh sui materiali stessi.

Le applicazioni del processo TPA sono molteplici, quali la limitazione ottica, per la protezione di sensori o dell'occhio umano; la terapia fotodinamica, per il trattamento localizzato di tumori; la realizzazione di memorie ottiche tridimensionali, che aumentano la capacità di memoria estendendola all'intera struttura 3D del materiale, grazie all'elevato confinamento spaziale della regione eccitata; la micro- e nano-fabbricazione, la progettazione di dispositivi laser compatti, basati sull'emissione laser indotta dall'assorbimento a due fotoni (up-converted lasing).

Da questa semplice carrellata dei possibili campi di utilizzo del processo di assorbimento a due fotoni, si può intuire che spesso la realizzazione di un dispositivo o di una tecnologia basata sul processo di TPA richiede la compresenza di varie proprietà. Quando un meccanismo, anche complesso, è innescato in una prima fase da un processo TPA, spesso il requisito di base per il materiale usato è avere una bassa soglia di attivazione dell'assorbimento non lineare; in questo modo è possibile utilizzare sorgenti eccitatrici meno intense e quindi meno dannose per il materiale stesso. Questo requisito viene soddisfatto utilizzando sistemi con un'alta sezione d'urto per l'assorbimento a due fotoni ( $\sigma_{\text{TPA}}$ ), sezione che definisce il parametro molecolare del coefficiente di assorbimento non lineare. In una prima fase è dunque importante caratterizzare le proprietà ottiche non lineari dei sistemi in soluzione; successivamente si trasferiscono i sistemi che soddisfano alle caratteristiche volute nel materiale ospitante, in precedenza scelto per la realizzazione del dispositivo. A seconda dell'applicazione finale, lo stesso materiale TPA dovrà essere in grado di apportare ulteriori funzionalità. Ad esempio, per la microscopia a fluorescenza o per l'up-converted lasing, esso dovrà avere una buona resa quantica di fluorescenza, oppure, per la terapia fotodinamica, dovrà trasferire efficientemente popolazione allo stato di tripletto per la generazione di ossigeno di singoletto.

Nell'ambito di questo progetto di dottorato una buona parte del lavoro è stata dedicata alla caratterizzazione ottica non lineare di molti sistemi organici, metallorganici e inorganici, usando diverse tecniche d'indagine e varie sorgenti laser, caratterizzate da impulsi di durata variabile tra i nanosecondi e i femtosecondi. In particolare è stato allestito nel

nostro laboratorio un set-up che permette di misurare la sezione d'urto di assorbimento a due fotoni, mediante la rivelazione dell'emissione indotta dall'assorbimento a due fotoni (TPIF). Il sistema di eccitazione usato è una sorgente laser al Titanio-Zaffiro, con impulsi di durata temporale di circa 130 fs e una frequenza di ripetizione di 76 MHz, in un intervallo di lunghezze d'onda compreso tra 720 e 930 nm. Tale tecnica permette di stimare la sezione d'urto di assorbimento a due fotoni istantanea ( $\sigma_{\text{TPA}}$ ). Molteplici sono le classi di molecole studiate in soluzione: composti push-pull dipolari, quadrupolari e ottupolari, sistemi dimerici di strutture push-pull, porfirine e squaraine, quantum dots con struttura core-shell aventi diversi diametri.

La caratterizzazione ottica non lineare è importante al fine di individuare i composti più promettenti per le tre diverse applicazioni studiate durante il progetto di dottorato:

1. limitazione ottica
2. up-converted lasing
3. microfabbricazione

### **Limitazione Ottica**

La prima applicazione si basa sulla realizzazione di un **limitatore ottico**. Il prototipo di tale dispositivo consiste nella cosiddetta "*configurazione Tandem*": due dischetti, ottenuti mediante la tecnica *sol-gel*, sono drogati rispettivamente con un derivato fullerenico, caratterizzato da assorbimento saturabile inverso RSA (Reverse Saturable Absorption) e con un assorbitore a due fotoni. Il primo sistema, già ampiamente studiato nel nostro gruppo, necessita di un pompaggio con impulsi lunghi e mostra la massima efficienza a 690 nm. Pertanto, anche il dispositivo finale deve essere testato con impulsi lunghi e alla medesima lunghezza d'onda. Diverse tipologie di molecole TPA sono state caratterizzate mediante le tecniche "z-scan" e "trasmissione non lineare" con un sistema laser con impulsi di 12 ns nell'intervallo di lunghezze d'onda compreso tra 670 e 850 nm. Mediante questi metodi è possibile stimare la sezione d'urto di assorbimento a due fotoni efficace del composto. In questo caso si parla di un valore efficace, in quanto, essendo la durata dell'impulso maggiore o paragonabile al tempo di vita degli stati eccitati molecolari, nell'espressione di  $\sigma_{\text{TPA}}$  non sono trascurabili i contributi dovuti all'assorbimento multifotonico sequenziale. Tra i vari cromofori studiati, i più promettenti sembrano essere dei sistemi porfirinici simmetrici. E' in fase di sintesi un derivato porfirinico, funzionalizzato con gruppi ossidrilici, in modo da aumentarne la solubilità nelle soluzioni sol-gel.

Parallelamente sono state studiate delle matrici ibride organico-inorganico ottenute mediante la tecnica *sol-gel*, che rappresenta un ottimo metodo per la preparazione di materiali utilizzati nel campo dell'ottica. Tra i molteplici vantaggi di questa tecnica ricordiamo l'alta versatilità, la grande varietà di precursori disponibili in commercio, le basse temperature di lavoro, il basso costo, la facile processabilità del sol. La scelta dei precursori e delle condizioni di sintesi permettono di modulare le proprietà del materiale finale, riuscendo a volte a correlare le proprietà macroscopiche con quelle microscopiche che si determinano in fase di sintesi.

Sono state sintetizzate diverse matrici ottenute mediante l'uso di vari precursori ibridi e inorganici e sono stati cambiati i parametri di sintesi al fine di variare la microstruttura del materiale finale. Per tutte le matrici è stata misurata la soglia di danneggiamento al laser, stimata mediante misure di trasmittanza non lineare a 690 nm con il sistema laser a ns. Le quattro matrici che hanno mostrato una maggiore resistenza al danneggiamento sono state più accuratamente caratterizzate dal punto di vista meccanico, termico e microstrutturale. In tal modo è stato possibile ricavare una correlazione tra le soglie al danneggiamento e i valori di modulo elastico.

### **Up-Converted Lasing**

L'up converted lasing è un metodo alternativo per produrre sorgenti laser nel visibile. Un sistema fluorescente può essere eccitato verso uno stato permesso per TPA in seguito a pompaggio nella regione dell'IR. Il sistema può quindi diseccitarsi emettendo radiazione di fluorescenza che è centrata a lunghezze d'onda inferiori a quella di pompa. Se l'intensità incidente è sufficientemente alta e la dinamica del sistema lo permette, è possibile l'inversione di popolazione tra lo stato fondamentale e lo stato eccitato. Si origina così un processo di emissione stimolata (*ASE, Amplified Spontaneous Emission*), la quale è caratterizzata da una banda molto stretta rispetto alla banda di emissione spontanea non amplificata. Se il sistema è posto in un'opportuna cavità ottica, si può indurre emissione laser la cui lunghezza d'onda può essere modulata, all'interno dello spettro di emissione, variando la cavità usata.

Nei nostri laboratori è stato studiato il processo di up-conversion sia per molecole push-pull organiche sia per nanoparticelle core-shell di CdSe-ZnS (quantum dots – QDs), in seguito a pompaggio con un laser a fs amplificato a 806 nm. Nel primo caso è stato possibile misurare emissione ASE solo in soluzione.

Nel secondo caso, invece, è stato possibile eseguire delle misure di lasing e di gain di QDs core-shell di CdSe-ZnS, stabilizzati con gruppi amminici, inglobati in un film di zirconia. La scelta della matrice è importante al fine di ridurre i processi di diseccitazione non radiativa. Lo studio è stato esteso a nanoparticelle di raggio variabile tra 2.1 e 3.2 nm. Tali QDs di semiconduttori generano un regime di confinamento quantico forte, dovuto alle loro dimensioni che sono inferiori al raggio di Bohr dell'eccitone. L'emissione di fluorescenza che ne deriva è centrata ad una lunghezza d'onda che è fortemente influenzata dalla dimensione dei QDs. La dimensione della nanoparticella influenza sia la soglia di attivazione dell'emissione ASE sia la sua stabilità temporale.

### **Microfabbricazione**

Nella microfabbricazione viene sfruttato il processo TPA per l'eccitazione di un fotocatalizzatore, che in seguito all'irraggiamento si rompe generando due radicali. Tali prodotti radicalici possono innescare il processo di polimerizzazione di gruppi (met)acrilici o epossidici. Si parla in questo caso di fotopolimerizzazione indotta dall'assorbimento a due fotoni. Il fotoiniziatore usato è stato sintetizzato dal gruppo della prof. C. Andraud dell'università di Lione. Le matrici sintetizzate, contenenti gruppi acrilici e metacrilici, sono tre: una di natura completamente organica e due di natura ibrida organico-inorganica ottenuta mediante la tecnica sol-gel.

Sono state poi usate due sorgenti laser per indurre una fotopolimerizzazione per assorbimento a uno o a due fotoni. Nel primo caso si è usata un laser in continuo a 488 nm, mentre nel secondo un laser a fs a 850 nm. Variando l'energia incidente, il tempo d'irraggiamento e l'ambiente esterno al campione, è stato possibile creare delle microstrutture nei campioni. Dopo lavaggio con un opportuno solvente, le strutture rimaste nel substrato possono essere microstrutturalmente caratterizzate mediante microscopia a forza atomica (AFM), elettronica a scansione (SEM) e microscopia confocale.

Nell'ambito di questo progetto di dottorato è stato quindi possibile studiare il comportamento ottico non lineare di molteplici tipologie di sistemi. In particolare si è concentrata l'attenzione sui cromofori che mostrano un processo di assorbimento a due fotoni. L'efficienza del processo è un parametro importante per le applicazioni pratiche del sistema studiato, in quanto un'alta efficienza abbassa l'energia di attivazione richiesta, a parità di concentrazione. Il nostro lavoro si è concentrato sulla caratterizzazione ottica e

sulla scelta dei cromofori TPA aventi le caratteristiche più vicine a quelle richieste per le tre diverse applicazioni studiate: limitazione ottica, up-conversion lasing e microfabbricazione. Per tutte le applicazioni, è stato possibile testare anche le prestazioni dei materiali solidi contenenti alcune tra le molecole attive in precedenza caratterizzate in soluzione.

## INTRODUCTION

During the last years there has been an increase in the study of the interaction between intense light sources and matter. Many mechanisms can be activated and exploited in different areas of academic studies and industrial applications. Nowadays the interest in nanoscience, or more specifically in nanophotonics, is the natural consequence of the need to investigate new phenomena emerging from the interaction between matter and electromagnetic radiation on a nanometer scale.

In nanophotonics one way to induce an interaction between light and nanometer sized matter is to confine light to scale dimensions that are much smaller than the wavelength of light. Alternatively, it is possible to use nanomaterials where the interaction is physically limited to the nanoscopic dimensions. Moreover, the nanoscale confinement of a photoprocess, where photochemistry or a light-induced phase change are induced, can provide innovative methods for nanofabrication of photonic structures.

In this context, we have studied the two-photon absorption (TPA), or more generally the multiphoton absorption, as an excitation mechanism for inducing photophysical or photochemical modifications in the active material. The TPA process is quadratically dependent on the light intensity. Moreover, the photo-induced changes in the material are spatially localized near the high intensity region of the focal point of the focusing system

employed. This property becomes important for such applications where the confinement is required.

Chromophores with enhanced TPA are useful in a variety of potential applications including diverse fields such as optical limiting, micro- and nanofabrication, photodynamic therapy, realization of 3D optical memories and compact lasers and so on. This work is aimed at investigating the non linear optical (NLO) properties of many classes of systems both in solution and in solid matrices. The optical characterization is useful to identify the materials which best meet the requirements for the applications studied: optical limiting, up-conversion lasing and two-photon polymerization.

The first chapter offers a synthetic theoretical background to understand the basic characteristics of non linear optical processes, generated from the interaction between a material and an intense laser source. The second one is an overview of many classes of materials already studied for their TPA properties: simple theoretical models will be exposed to emphasize a possible way to increase the non linear optical response of such systems. Further, in the third chapter, the sol-gel technique will be introduced as a powerful method for the synthesis of solid matrices, useful as host material for NLO systems in photonics applications.

The fourth chapter will describe the different techniques employed for the non linear optical characterization of TPA systems and the determination of the TPA cross-section, the most important parameter to define the TPA efficiency. The z-scan, the non linear transmittance and the two-photon induced fluorescence (TPIF) methods and their experimental set-ups will be described in that chapter. Detailed attention is devoted to an in depth explanation of the principles of TPIF, a technique newly implemented in our laboratory during this work.

Chapters 5, 6 and 7 will describe the trials for the realization of an optical power limiter. Firstly, the requirements for this device will be explained and the limits of the previously studied materials will be evidenced. In our group a new configuration has been proposed in order to increase the performances of the device. This configuration, called "Tandem", consists in two sol-gel disks doped, respectively, with a two-photon and a reverse saturable absorbers.

Chapter 6 will show the results of the non linear optical characterization of a great variety of TPA chromophores in solution, using both femtosecond and nanosecond pulses at different wavelengths. This preliminary characterization is important to find the material with the highest TPA cross section at the same wavelength where the RSA system shows

the best performance (about 690 nm). Moreover, chapter 7 will present the results of the synthesis and the characterization of different sol-gel matrices prepared in order to find a host material showing the highest laser damage resistance.

In chapter 8, the up-conversion lasing is studied as the second application of TPA processes. A zirconia film, doped with semiconductor quantum dots, is used for generating amplified radiation in the visible region when irradiate with an IR pumping beam.

Finally, the TPA mechanism is exploited for the excitation of a properly synthesized photoinitiators. Upon excitation the initiator acts as generator of radicals useful for the activation of the photopolymerization of (meth)acrylic units. The multiphoton absorption processes is a promising technique for the fabrication of 3D microstructures. Our tests will be reported in chapter 9.



## CHAPTER 1

# Interaction between electromagnetic field and matter

Aim of this chapter is the analysis of the most important physical quantities and processes involved in optical interactions between an electromagnetic field and materials.

After an initial introduction on the general principles of linear and nonlinear optics, involving the different approaches used for the theoretical study, most attention will be devoted to the illustration of nonlinear absorption. In fact the understanding and the analysis of the properties related to this phenomenon are necessary for the applications examined in this work.

Moreover, a section will be devoted to the description of the properties of two particular nonlinear optical processes, Two Photon Absorption (TPA) and Reverse Saturable Absorption (RSA), which are characteristic of various classes of materials. These processes will be described by using a phenomenological approach. Regarding the TPA process, the next chapter will present some theoretical models for the description of the nonlinear absorption properties of different classes of materials.

In the last paragraph of this chapter, some comments about the effect of the pulse duration on the measured NLO response are reported.

## 1.1 Linear optical response of a material system

The effect of an electromagnetic field on a material is the induction of a macroscopic polarization  $P$  which can be expressed, for weakly interacting particles, as:

$$P = N \langle \mu \rangle \quad 1.1$$

where  $N$  is the number of atoms or molecules per unit volume of the medium and  $\mu$  is the average atomic or molecular dipole moment.

The polarization is dependent on the applied electric field and generally it can be expressed as a power series in the field strength  $\bar{E}(t)$ :

$$\bar{P}(t) = \chi^{(1)} \bar{E}(t) + \chi^{(2)} \bar{E}^2(t) + \chi^{(3)} \bar{E}^3(t) + \dots = P_{Lin} + \sum_i \tilde{P}_{NonLin}^{(i)}(t) \quad 1.2$$

$\chi^{(1)}$  is the *linear susceptibility* and  $\chi^{(n)}$ , known as *nonlinear susceptibilities*, are material coefficient represented by  $(n+1)$ -rank tensors.

When light sources with low intensity are employed, it is possible to exclude all terms of higher order because  $\chi^{(3)} \ll \chi^{(2)} \ll \chi^{(1)}$ . In this case, only the first-order component determines the linear relationship between the polarization and the applied electric field. On the contrary, the nonlinear components are non negligible when intense sources, such as laser pulses, are used.

The propagation of an electromagnetic wave in a medium is determined by the Maxwell equation:

$$\nabla^2 \bar{E} = \frac{1}{c^2} \frac{\partial^2 \bar{E}}{\partial t^2} + \frac{1}{c^2 \epsilon_0} \frac{\partial^2 \bar{P}}{\partial t^2} \quad 1.3$$

When  $\bar{P} \cong \bar{P}^{(1)} = \epsilon_0 \chi^{(1)} \bar{E}(t)$ , the expression 1.3 can be rewritten in:

$$\nabla^2 \bar{E} = \frac{1}{c^2} (1 + \chi_e) \frac{\partial^2 \bar{E}}{\partial t^2} \quad 1.4$$

The solution is a plane wave:  $\bar{E}(\bar{r}, t) = \bar{E}_0 \exp[i(\bar{K} \cdot \bar{r}) - \omega t]$  1.5

$\bar{K}$  is the wavevector and its modulus is equal to:

$$K = |\bar{K}| = \frac{\omega}{c} (1 + \chi_e)^{1/2} \quad 1.6$$

If the medium is transparent:  $(1 + \chi_e)^{1/2} = n(\omega)$  1.7

where  $n(\omega)$  is the refractive index. On the contrary, if absorption is not negligible, the refractive index is written as a complex quantity:

$$\hat{n}(\omega) = n(\omega) + ik(\omega) = (1 + \hat{\chi}_e)^{1/2} = \sqrt{\varepsilon} \quad 1.8$$

Here,  $n$  considers the dispersive processes, while  $k$  is called the extinction coefficient and indicates the amount of absorption of the incident wave.  $\varepsilon$  is the dielectric constant. Processes, such as refraction or reflection of an input beam, are linked to the complex refractive index  $\hat{n}(\omega)$ . The Kramers-Krönig relations link together the real and the imaginary part of  $\hat{n}(\omega)$ .

Considering Eqs. 1.7 and 1.6, Eq. 1.5 can be rewritten, in a one dimension ( $x$ ) propagation, as:

$$\bar{E}(x,t) = \bar{E}_0 \exp\left(-\frac{\omega}{c}kx\right) \exp\left[i\left(\frac{\omega n}{c} - \omega t\right)\right] \quad 1.9$$

Equation 1.9 is relative to the propagation of a plane wave with frequency  $\omega$ , phase velocity ( $c/n$ ) and amplitude exponentially decreasing with  $k$ .

The irradiance of a beam depends on  $|E|^2$  and its decrease through the material, along the  $x$ -direction, is given by the Lambert-Beer law:

$$I(x) = I(0) \exp(-\alpha x) \quad 1.10$$

$I(0)$  and  $\alpha$  are the incident irradiance of the beam and the absorption coefficient respectively.  $\alpha$  is correlated to the extinction coefficient by the relation:

$$\alpha = \frac{2\omega k}{c} \quad 1.11$$

Common experimental techniques measure the absorbance after the sample, which is defined by the formula:

$$A(\omega) = -\text{Log}T(\omega) = -\text{Log}\left[\frac{I(\omega,d)}{I(\omega,0)}\right] = \alpha(\omega)d \text{Log}(e) = \varepsilon d C \quad 1.12$$

where  $d$  is the sample thickness,  $\varepsilon$  is the molar extinction coefficient (expressed in  $\text{M}^{-1} \text{cm}^{-1}$ ) and  $C$  is the concentration of the absorbing species (in M).

## 1.2 Nonlinear optical properties

The formal relation 1.2 is the simplest way to express the relationship between the polarization and the applied electromagnetic field.

Two major approaches have been employed in nonlinear optics.<sup>1,2</sup> The first consists in a semi-classical theory considering molecules or atoms as quantum mechanical objects and

light is described by the classical Maxwell equations. The second one is a more rigorous theoretical approach, evaluating the probability of an interaction between the photon field and the medium, both expressed as eigenfunctions. This approach can describe quantitatively the effects and the phenomena related to this interaction, showing the paths involved in the transition of the molecular system from the initial energy state to the final state. In quantum-mechanics, two are the main theories studied. The first one is based on a quantum-mechanical perturbation theory of the atomic or molecular wavefunction. The final expressions are quantitative predictions of nonresonant responses of the molecular systems. Indeed, when the frequencies involved in the interaction are near resonance, it is necessary to introduce the relaxation process terms in the formalism. The second approach, using the density matrix formalism, is capable to efficiently describe the physical resonance processes.

In this chapter, the general formulas for the nonlinear susceptibilities and their properties will be firstly introduced. Successively, some details about the description of the two theories will be presented.

The radiation electric field can be written as sum of components at different frequencies  $\omega_n$ :

$$\bar{E}(\vec{r}, t) = \sum_{n>0} \bar{E}_n(\vec{r}, t) = \sum_{n>0} E_n e^{-i\omega_n t} + c.c. = \sum_{n>0} A_n e^{i(\vec{k}_n \cdot \vec{r} - \omega_n t)} + c.c. \quad 1.13$$

The running index ( $n > 0$ ) means that the summation must be taken over positive frequencies only.

Because the electric field  $\bar{E}$  is a real quantity, the frequency components in 1.13 must satisfy the condition:

$$E_n^* \equiv E(\omega_n)^* = E(-\omega_n) \quad A_n^* \equiv A(\omega_n)^* = A(-\omega_n) \quad 1.14$$

The expression for the electric field can be rewritten as sum over all frequencies, both positive and negative:

$$\bar{E}(\vec{r}, t) = \sum_n E(\omega_n) e^{-i\omega_n t} = \sum_n A(\omega_n) e^{i(\vec{k}_n \cdot \vec{r} - \omega_n t)} \quad 1.15$$

A similar notation can be used also for the polarization:

$$\bar{P}(\vec{r}, t) = \sum_n P(\omega_n) e^{-i\omega_n t} \quad 1.16$$

The component  $i$  of the polarization can be decomposed in different order terms:

$$P_i(\omega_n) = P_i^{(1)}(\omega_n) + P_i^{(2)}(\omega_n) + P_i^{(3)}(\omega_n) \quad 1.17$$

$$P_i^{(1)}(\omega_n) = \varepsilon_0 \sum_j \chi_{ij}^{(1)}(\omega_n) E_j(\omega_n) \quad 1.17a$$

$$P_i^{(2)}(\omega_n = \omega_p + \omega_q) = \varepsilon_0 \sum_{j,k} \sum_{p,q} \chi_{ijk}^{(2)}(\omega_n = \omega_p + \omega_q) E_j(\omega_p) E_k(\omega_q) \quad 1.17b$$

$$P_i^{(3)}(\omega_n = \omega_p + \omega_q + \omega_r) = \varepsilon_0 \sum_{j,k,l} \sum_{p,q,r} \chi_{ijkl}^{(3)}(\omega_n = \omega_p + \omega_q + \omega_r) E_j(\omega_p) E_k(\omega_q) E_l(\omega_r) \quad 1.17c$$

Here the indices  $j,k,l$  refer to the cartesian coordinates of the fields involved in the interaction and the summation over  $p,q,r$  is related to the degeneracy properties of  $\omega_p, \omega_q, \omega_r$ . In fact, for a process, the sum  $(\omega_p + \omega_q + \omega_r)$  is to be fixed, although the individual terms of the sum can be varied.

The optical susceptibilities are characteristic of the material, so some symmetry properties of the medium allow a simplification of the expression of  $\chi$ , which is normally constituted by numerous terms, when the interaction needs high nonlinear order description.

For the second-order susceptibility, for example, the symmetry properties are as follows.

1- *Reality of the fields*. Since the fields are physically measurable quantities, hence are real, it is correct to consider:

$$\begin{aligned} P(-\omega_p - \omega_q) &= P(\omega_p + \omega_q)^* \\ \chi_{ijk}^{(2)}(-\omega_p - \omega_q; -\omega_p, -\omega_q) &= \chi_{ijk}^{(2)}(\omega_p + \omega_q; \omega_p, \omega_q)^* \end{aligned} \quad 1.18$$

2- *Intrinsic permutation symmetry*. Susceptibilities obtained by exchanging the order of both the incoming fields and their Cartesian indexes are equivalent:

$$\chi_{ijk}^{(2)}(\omega_p + \omega_q; \omega_p, \omega_q) = \chi_{ikj}^{(2)}(\omega_q + \omega_p; \omega_q, \omega_p) \quad 1.19$$

3- *Symmetries for lossless media*. The transparent media have a real susceptibility:

$$\chi_{ijk}^{(2)}(\omega_p + \omega_q; \omega_p, \omega_q) = \chi_{ikj}^{(2)}(-\omega_p - \omega_q; -\omega_p, -\omega_q)^* \quad 1.20$$

4- *Full permutation symmetry*. When the medium is lossless and its interaction with the fields does not involve frequencies near the resonance frequencies of the systems, all the frequencies of the nonlinear susceptibility, including those of the incoming fields and of the nonlinear polarization, can be interchanged if also the Cartesian indexes are interchanged simultaneously.

$$\chi_{ijk}^{(2)}(\omega_n = \omega_p + \omega_q) = \chi_{jki}^{(2)}(\omega_p = -\omega_q + \omega_n) = \chi_{kij}^{(2)}(\omega_q = \omega_n - \omega_p) \quad 1.21$$

5- *Kleinman's symmetry*. Under the condition that the field frequencies are lower than the resonance frequencies of the material system, the nonlinear susceptibility is independent

of frequency. This is equivalent to change the indices of  $\chi$  without changing the frequencies:

$$\chi_{ijk}^{(2)}(\omega_p + \omega_q; \omega_p, \omega_q) = \chi_{jki}^{(2)}(\omega_p + \omega_q; \omega_p, \omega_q) = \dots \quad 1.22$$

This property is often satisfied in the second-order process.

6- *Spatial symmetry*. Some spatial symmetries of the material are useful to reduce the number of independent non-zero tensor components of the susceptibility. One of these is the inversion symmetry causing the vanishing of all the components of even-order susceptibilities. So, to have a measurable even-order process, it is necessary to avoid the inversion symmetry of the system.

### 1.3 Parametric versus nonparametric processes: examples of second and third-order processes

The optical processes can be distinguished in parametric, or passive, and non-parametric, or active. The non-parametric ones are characterized by a transfer of population from the ground level of the system to an excited one: they are described by a complex susceptibility. Viceversa, in the parametric processes only virtual states are involved in the interaction. In these cases the interaction is described by a real susceptibility. Another characteristic is that the active processes are expressed by susceptibilities  $\chi^{(n)}$ , where  $n$  is an odd number. Therefore, the linear absorption will be described by the imaginary part of  $\chi^{(1)}$  and, for nonlinear absorption, the  $m$ -photon absorption will be expressed by the imaginary component of  $\chi^{(2m-1)}$ .

In this work, we are mainly interested in the study of non-parametric processes where the nonlinear optical system absorbs the incident photons. Here, only a few examples of second-order processes are reported and most attention will be focused on the description of two different third-order processes.

When the incident optical field is composed of two distinct frequencies, expressed by the relation:

$$\bar{E}(t) = E_1(t)e^{-i\omega_1 t} + E_2(t)e^{-i\omega_2 t} + c.c. \quad 1.23$$

The induced polarization can be written as:

$$\bar{P}^{(2)}(t) = \chi^{(2)} \bar{E}(t)^2 = \sum_n P(\omega_n) e^{-i\omega_n t} \quad 1.24$$

where different processes are described:

- a)  $P(2\omega_i)=\chi_i^{(2)}E_i^2 \quad i = 1,2$  **Second-Harmonic Generation (SHG)**
- b)  $P(\omega_1 + \omega_2)=2\chi^{(2)}E_1E_2$  **Sum-Frequency Generation (SFG)**
- c)  $P(\omega_1 - \omega_2)=2\chi^{(2)}E_1E_2^*$  **Difference-Frequency Generation (DFG)**
- d)  $P(0)=2\chi^{(2)}(E_1E_1^* + E_2E_2^*)$  **Optical Rectification (OR)**

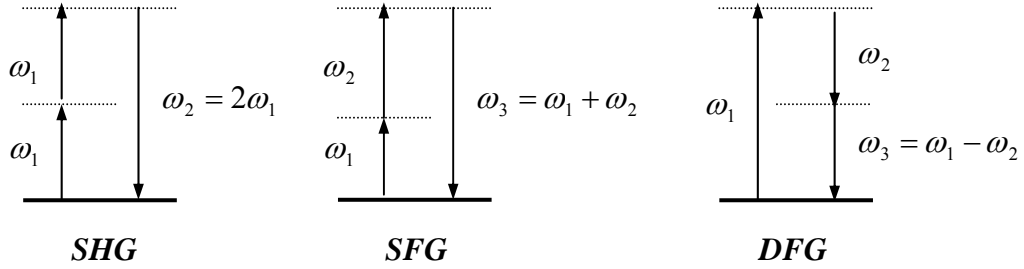


**Fig. 1.1:** Energy diagrams for Second Harmonic Generation (SHG), Sum Frequency Generation (SFG) and Difference Frequency Generation (DFG)

Four different frequency components in  $P^{(2)}$  are nonzero. However, only if the *phase-matching* condition<sup>2</sup> for one of these is satisfied, it is possible to experimentally observe the corresponding output signal.

Other parametric phenomena described by the third-order susceptibility are the *Third Harmonic Generation (THG)* and the *Optical Kerr effect*. The first one, analogously to SHG, is the generation of a frequency that is the triple of one of the frequencies of the incident fields. The Optical Kerr effect is an important process exploited in optoelectronics when it is necessary to change the refractive index of the medium. In fact, when an intense light source crosses an optical medium, its refractive index is given by:

$$n = n_0 + n_2 I \quad 1.25$$

$n_0$  is the linear refractive index,  $n_2$  is the nonlinear index and  $I$  is the intensity of the incident beam. The nonlinear coefficient is given by:

$$n_2 = \frac{12\pi^2}{n_0^2 c} \chi^{(3)} \quad 1.26$$

This coefficient can be positive (*self-focusing process*) or negative (*defocusing process*).

#### 1.4 Determination of nonlinear optical susceptibility

In this paragraph, will be presented some details on the calculation of the expressions for nonlinear optical susceptibility, using the quantum-mechanical laws. These expressions

are important because they show how the nonlinear coefficients are dependent on the material parameters, such as the transition dipole moments and the energy levels of the systems. In the first part, the results obtained by the solution of the Schrödinger's equation, applied to the atomic wavefunctions, are described. In the second one, the density matrix formalism will be introduced.

### 1.4.1 Schrödinger equation calculation of the nonlinear susceptibility

In the assumption that the properties of the atomic system are described through the time-dependent Schrödinger's equation

$$i\hbar \frac{\partial \psi}{\partial t} = \hat{H} \psi \quad 1.27$$

whose solution is the time dependent wavefunction  $\psi(\vec{r}, t)$ .

The Hamiltonian can be expressed as the sum of the Hamiltonian of the free atom/molecule and a term expressing the interaction between the system and the external electric field, valid for electric dipole interaction:

$$\hat{H} = \hat{H}_0 + \hat{V}(t) = \hat{H}_0 - \hat{\mu} \cdot \vec{E}(t) = \hat{H}_0 + e\hat{r}(t) \cdot \vec{E}(t) \quad 1.28$$

Using perturbation theory, it is possible to get an approximate solution of the Schrödinger's equation. In this assumption,  $\hat{H}$  and  $\psi(\vec{r}, t)$  are written as:

$$\hat{H} = \hat{H}_0 + \lambda \hat{V}(t) \quad 1.29$$

$$\psi(\vec{r}, t) = \psi^{(0)}(\vec{r}, t) + \lambda \psi^{(1)}(\vec{r}, t) + \lambda^2 \psi^{(2)}(\vec{r}, t) + \dots \quad 1.30$$

where  $\lambda$  is the expansion parameter. Its value,  $\lambda < 1$ , characterizes the strength of the interaction and makes the successive terms in Eqs. 1.29 and 1.30 of decreasing importance.

By substitution of the Eq. 1.30 in 1.27, it is possible to separate N different equations. Every expression is obtained by the equality of terms related to the same order of  $\lambda^N$ . The set of equations are:

$$i\hbar \frac{\partial \psi^{(0)}}{\partial t} = \hat{H}_0 \psi^{(0)} \quad 1.31$$

$$i\hbar \frac{\partial \psi^{(N)}}{\partial t} = \hat{H}_0 \psi^{(N)} + \hat{V} \psi^{(N-1)} \quad N = 1, 2, 3, \dots \quad 1.32$$

The solution for the Nth-order equation is written as a linear combination of the wavefunctions of the free molecule which are a complete set of basis function:

$$\psi^{(N)}(\vec{r}, t) = \sum_l a_l^{(N)}(t) u_l(\vec{r}) e^{-i\omega_l t} \quad 1.33$$

$a_l^{(N)}(t)$  is the probability amplitude that the atom is in the energy eigenstate  $l$  at time  $t$ , in the N-th order step.

It is important to know the expressions for the wavefunctions of the system, because they allow the calculation of the polarization that is the expectation value of the electric dipole moment:

$$\langle \bar{p} \rangle = \langle \psi | \bar{\mu} | \psi \rangle \quad 1.34$$

The polarization per molecule, which is the induced dipole moment, at the first-order is given by:

$$\langle \bar{p}^{(1)} \rangle = \langle \psi^{(0)} | \bar{\mu} | \psi^{(1)} \rangle + \langle \psi^{(1)} | \bar{\mu} | \psi^{(0)} \rangle \quad 1.35$$

The linear polarization for N atoms is:

$$\bar{P}^{(1)} = N \langle \bar{p}^{(1)} \rangle = \sum_p \bar{P}^{(1)}(\omega_p) e^{-i\omega_p t} \quad P_i^{(1)}(\omega_p) = \sum_j \chi_{ij}^{(1)} E_j(\omega_p) \quad 1.36$$

Using this relation, it is possible to determine the form of the linear optical susceptibility:

$$\chi_{ij}^{(1)}(\omega_p) = \frac{N}{\hbar} \sum_m \left( \frac{\mu_{gm}^i \mu_{mg}^j}{\omega_{mg} - \omega_p} + \frac{\mu_{gm}^j \mu_{mg}^i}{\omega_{mg}^* + \omega_p} \right) \quad 1.37$$

$\mu_{mg}$  represents the matrix element of the dipole moment operator evaluated between the  $m$  and  $g$  states and is denoted as transition dipole moment:

$$\mu_{mg} = \langle u_m | \bar{\mu} | u_g \rangle \quad 1.38$$

The transition frequency  $\omega_{mg}$  is expressed as a complex quantity:

$$\omega_{mg} = \omega_{mg}^{(0)} - i\gamma_m \quad 1.39$$

In this case,  $\omega_{mg}^{(0)}$  is the real frequency identifying the energy difference between the two states and  $\gamma_m$  is the population decay rate from the upper level  $m$ . In this way, the damping effects are introduced even if this choice can not explain correctly all the dephasing processes: these effects will be described by the density matrix theory.

The first and the second terms of equation 1.37 are respectively the *resonant* and the *nonresonant* contributions to the linear susceptibility. State  $g$  is generally identified as the

ground state of the system and  $m$  is a *virtual* state that represents one of the energy eigenstates of the system.

When the incident field has a frequency  $\omega_p \approx \omega_m - \omega_g = \omega_{mg}$ , this frequency can be absorbed by the system (see Fig. 1.2-a). In this case, the first term, and consequentially the first-order optical response, increases.

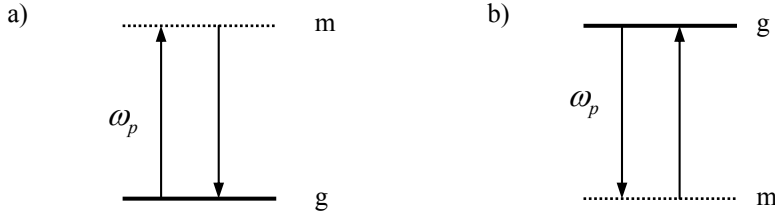


**Fig. 1.2:** Energy diagrams for resonant (a) and nonresonant (b) contributions to linear susceptibility

In the second term the frequency  $\omega_p$  is emitted by the system and has a positive sign in Eq. 1.37.

Analogously, it is possible to calculate the second and the third-order susceptibility. We will concentrate on the treatment of the third-order expression.

The induced dipole moment per molecule, using the results of the third-order perturbation theory, can be expressed, analogously to Eq. 1.35, as:

$$\langle \bar{p}^{(3)} \rangle = \langle \psi^{(0)} | \bar{\mu} | \psi^{(3)} \rangle + \langle \psi^{(1)} | \bar{\mu} | \psi^{(2)} \rangle + \langle \psi^{(2)} | \bar{\mu} | \psi^{(1)} \rangle + \langle \psi^{(3)} | \bar{\mu} | \psi^{(0)} \rangle \quad 1.40$$

The expression for the third-order optical susceptibility contains 24 terms, but it can be written in a more compact form using the intrinsic permutation operator  $\wp_I$ . This operator allows the generation of the other terms from Eq. 1.41, through the permutation of the frequencies, and the Cartesian indexes, of the incident electric fields.

$$\chi_{ijkl}^{(3)}(\omega_\sigma, \omega_r, \omega_q, \omega_p) = \frac{N}{\hbar^3} \wp_I \sum_{mnv} \left( \begin{array}{l} \frac{\mu_{gv}^k \mu_{vn}^j \mu_{nm}^i \mu_{mg}^h}{(\omega_{vg} - \omega_r - \omega_q - \omega_p)(\omega_{ng} - \omega_q - \omega_p)(\omega_{mg} - \omega_p)} + \\ \frac{\mu_{gv}^j \mu_{vn}^k \mu_{nm}^i \mu_{mg}^h}{(\omega_{vg}^* + \omega_r)(\omega_{ng} - \omega_q - \omega_p)(\omega_{mg} - \omega_p)} + \\ \frac{\mu_{gv}^j \mu_{vn}^i \mu_{nm}^k \mu_{mg}^h}{(\omega_{vg}^* + \omega_r)(\omega_{ng}^* + \omega_r + \omega_q)(\omega_{mg} - \omega_p)} + \\ \frac{\mu_{gv}^j \mu_{vn}^i \mu_{nm}^h \mu_{mg}^k}{(\omega_{vg}^* + \omega_r)(\omega_{ng}^* + \omega_r + \omega_q)(\omega_{mg}^* + \omega_r + \omega_q + \omega_p)} \end{array} \right) \quad 1.41$$

Figure 1.3 identifies the resonances for the four terms Eq. 1.41.

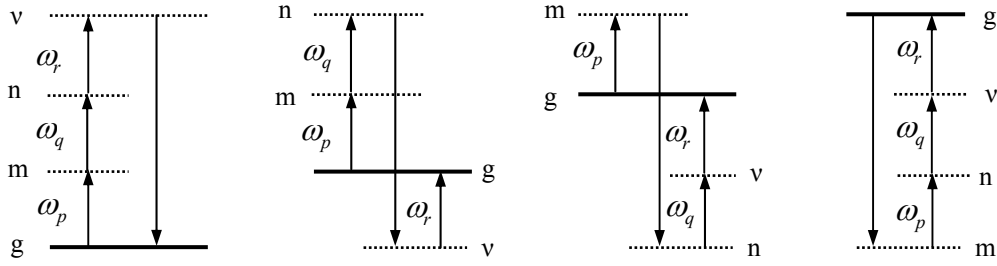


**Fig. 1.3:** Location of the resonances of the terms in the expression 1.41.

For highly nonresonant excitation (the resonance frequencies can be taken to be real quantities) the expression 1.41 can be rewritten as:

$$\chi_{kjih}^{(3)}(\omega_\sigma; \omega_r, \omega_q, \omega_p) = \frac{N}{\hbar^3} \wp_F \sum_{mnv} \left( \frac{\mu_{gv}^k \mu_{vn}^j \mu_{nm}^i \mu_{mg}^h}{(\omega_{vg} - \omega_\sigma)(\omega_{ng} - \omega_q - \omega_p)(\omega_{mg} - \omega_p)} \right) \quad 1.42$$

with  $\omega_\sigma = \omega_p + \omega_q + \omega_r$ .

$\wp_F$  is the full permutation operator and permits, in the expression that follows it, the permutation of all the input ( $\omega_r, \omega_q, \omega_p$ ) and output ( $\omega_\sigma$ ) frequencies.

### 1.4.2 Density matrix formalism for the determination of the optical susceptibility

The elements of the density matrix can be expressed as:

$$\rho_{mn} = \sum_s p(s) C_m^s(t) * C_n^s(t) \quad 1.43a$$

$$\psi_s(\vec{r}, t) = \sum_n C_n^s(t) u_n(\vec{r}) \quad 1.43b$$

$$\hat{H}_0 u_n(\vec{r}) = E_n u_n(\vec{r}) \quad 1.43c$$

In these expressions,  $p(s)$  is the statistical probability that the system is in the state  $s$  and  $C_n^s(t)$  is the probability amplitude that the molecule, which is in the time dependent state  $s$ , is in energy eigenstate  $n$  at time  $t$ .  $C_m^s * (t)$  represents the conjugate transpose of  $C_m^s(t)$ . The functions  $u_n(\vec{r})$  are the stationary eigenstates of the time-independent Schrödinger's equation, using the Hamiltonian for a free molecule, they are orthonormal. The sum in 1.43a runs over all the  $s$  states.

The diagonal elements ( $\rho_{nn}$ ) give the probability that the system is an energy eigenstate  $n$ . The other components ( $\rho_{nm}$ ) represent the “coherence” effects between  $n$  and  $m$  and they are nonzero only in the case of coherent overlapping of the two energy eigenstates.

The advantage of using this formalism is in the calculation of the average of any observable quantity. The expectation value of one observable  $A$  in the quantum mechanical state  $s$  is given by:

$$\langle A \rangle = \sum_{mn} C_m^s * C_n^s \langle u_m | \hat{A} | u_n \rangle = \sum_{mn} C_m^s * C_n^s A_{mn} \quad 1.44$$

The statistical average of this quantity over all the possible quantum mechanical states of the system is:

$$\overline{\langle A \rangle} = \sum_s p(s) \sum_{nm} C_m^s * C_n^s A_{mn} = \sum_{nm} \rho_{nm} A_{mn} = \text{tr}(\hat{\rho} \hat{A}) \quad 1.45$$

The time evolution of the density matrix, and of its elements, is governed by the Liouville equation:

$$\frac{\partial \rho}{\partial t} = \frac{-i}{\hbar} [\hat{H}, \hat{\rho}] \quad \frac{\partial \rho_{nm}}{\partial t} = \frac{-i}{\hbar} [\hat{H}, \hat{\rho}]_{nm} \quad 1.46$$

All the interactions, included in the Hamiltonian form, are described by this equation. In some cases, some interactions, such as all the relaxation or collision processes, are not efficiently included in the Hamiltonian. A phenomenological damping term is also included in Eq. 1.46 in order to describe these processes.

$$\frac{\partial \rho_{nm}}{\partial t} = \frac{-i}{\hbar} [\hat{H}, \hat{\rho}]_{nm} - \gamma_{nm} (\rho_{nm} - \rho_{nm}^{eq}) \quad 1.47$$

In this relation,  $\gamma_{nm}$  is the damping term and it is the relaxation rate coefficient for the decay of  $\rho_{nm}$  to the equilibrium condition  $\rho_{nm}^{eq}$ . The relaxation coefficients for the off-diagonal elements can be written as:

$$\gamma_{nm} = \frac{1}{2} (\Gamma_n + \Gamma_m) + \gamma_{nm}^{col} \quad 1.48$$

$\Gamma_n$  and  $\Gamma_m$  represent the total decay rates of population from levels  $n$  and  $m$  respectively. The term  $\gamma_{nm}^{col}$  is the pure dephasing rate for the processes that do not involve transfer of population.

To solve Eq. 1.47, it is necessary to resort to a perturbative approach. We assume, as done in previous section, that the form of the hamiltonian is:

$$\hat{H} = \hat{H}_0 + \hat{V}(t) = \hat{H}_0 - \hat{\mu} \cdot \bar{E}(t) = \hat{H}_0 + e\hat{r} \cdot \bar{E}(t) \quad 1.49$$

If we calculate the commutator applied on  $\hat{H}_0$  and  $\rho$ , we can obtain:

$$\left[\hat{H}_0, \hat{\rho}\right]_{nm} = \hbar\omega_{nm}\rho_{nm} \quad \omega_{nm} = \frac{E_n - E_m}{\hbar} \quad 1.50$$

$\omega_{nm}$  is the transition frequency .

Using Eqs. 1.49 and 1.50, Eq. 1.47 becomes:

$$\frac{\partial\rho_{nm}}{\partial t} = -i\omega_{nm}\rho_{nm} - \frac{i}{\hbar} \sum_v (V_{nv}\rho_{vm} - \rho_{nv}V_{vm}) - \gamma_{nm}(\rho_{nm} - \rho_{nm}^{eq}) \quad 1.51$$

This expression cannot be solved analytically, but can be solved by using a perturbative expansion of  $\rho_{nm}$  :

$$\rho_{nm} = \rho_{nm}^{(0)} + \lambda\rho_{nm}^{(1)} + \lambda^2\rho_{nm}^{(2)} + \dots \quad 1.52$$

The parameter  $\lambda$  has the same meaning as in Eq. 1.30. For every power of  $\lambda$ , the coefficients must satisfy the relation 1.51:

$$\frac{\partial\rho_{nm}^{(0)}}{\partial t} = -i\omega_{nm}\rho_{nm}^{(0)} - \gamma_{nm}(\rho_{nm}^{(0)} - \rho_{nm}^{eq}) \quad 1.53a$$

$$\frac{\partial\rho_{nm}^{(1)}}{\partial t} = -i(\omega_{nm} + \gamma_{nm})\rho_{nm}^{(1)} - \frac{i}{\hbar} \left[\hat{V}, \hat{\rho}^{(0)}\right]_{nm} \quad 1.53b$$

$$\frac{\partial\rho_{nm}^{(n)}}{\partial t} = -i(\omega_{nm} + \gamma_{nm})\rho_{nm}^{(n)} - \frac{i}{\hbar} \left[\hat{V}, \hat{\rho}^{(n-1)}\right]_{nm} \quad 1.53c$$

These equations can be integrated in order to obtain the expression of the elements of the density matrix used to calculate the expectation value of any observable quantity, such as the induced dipole moment and the correlated optical susceptibility. We remark that every order equation is dependent on the result of the previous one.

Equation 1.53a describes the recovery of statistical equilibrium in the absence of any external field. The steady-state solution is:  $\rho_{nm}^{(0)} = \rho_{nm}^{eq}$ . Using this expression, the first-order solution is:

$$\rho_{nm}^{(1)}(t) = \int_{-\infty}^t \frac{-i}{\hbar} \left[\hat{V}(t'), \hat{\rho}^{(0)}\right]_{nm} e^{(i\omega_{nm} + \gamma_{nm})(t'-t)} dt' \quad 1.54$$

### - Derivation of the linear susceptibility

We assume that the applied electric field is expressed in the form reported in Eq. 1.15 and the interaction Hamiltonian  $\hat{V}(t')$  is given by:  $\hat{V}(t') = -\hat{\mu} \cdot \bar{E}(t')$ . By calculating the integral in Eq. 1.54, the first-order density matrix element can be written as:

$$\rho_{nm}^{(1)}(t) = \hbar^{-1}(\rho_{nm}^{(0)} - \rho_{nn}^{(0)}) \sum_p \frac{\bar{\mu}_{nm} \cdot \bar{E}(\omega_p) e^{-i\omega_p t}}{(\omega_{nm} - \omega_p) - i\gamma_{nm}} \quad 1.55$$

The polarization, induced in the system by the electric field, is given by:

$$\bar{P}(\omega_p) = N \langle \bar{\mu}(\omega_p) \rangle = \bar{\chi}^{(1)}(\omega_p) \cdot \bar{E}(\omega_p) \quad 1.56$$

The expectation value of the induced dipole moment is:

$$\langle \bar{\mu}(t) \rangle = \text{tr}(\hat{\rho}^{(1)} \hat{\mu}) = \sum_{mn} \frac{1}{\hbar} (\rho_{mn}^{(0)} - \rho_{nm}^{(0)}) \sum_p \frac{\bar{\mu}_{mn} [\bar{\mu}_{nm} \cdot \bar{E}(\omega_p)] e^{-i\omega_p t}}{(\omega_{nm} - \omega_p) - i\gamma_{nm}} \equiv \sum_p \langle \bar{\mu}(\omega_p) \rangle e^{-i\omega_p t} \quad 1.57$$

The last equivalence is due to the decomposition into frequency components.

Using the Eqs. 1.56 and 1.57, it is possible to calculate the expression for the susceptibility in cartesian coordinates:

$$\chi_{ij}^{(1)}(\omega_p) = \frac{N}{\hbar} \sum_{nm} (\rho_{mn}^{(0)} - \rho_{nm}^{(0)}) \frac{\mu_{mn}^i \mu_{nm}^j}{(\omega_{nm} - \omega_p) - i\gamma_{nm}} \quad 1.58$$

In this relation,  $\mu_{mn}^i$  and  $\mu_{nm}^j$  are the dipole moment components for the transition between  $m$  and  $n$ ;  $i$  and  $j$  are the Cartesian components of the electric fields.  $\omega_{nm}$  is the characteristic transition frequencies from  $n$  to  $m$  states and  $\gamma_{nm}$  is the element of the relaxation matrix.

It is important to observe that the transition between two states with the same population ( $\rho_{mn}^{(0)} \approx \rho_{nm}^{(0)}$ ) does not contribute to the summation in  $\chi^{(1)}$ .

### - Derivation of nonlinear susceptibilities

The second-order susceptibility is obtained by the perturbation expansion of Eq. 1.54:

$$\rho_{nm}^{(2)} = e^{-(i\omega_{nm} + \gamma_{nm})t} \int_{-\infty}^t \frac{-i}{\hbar} [\hat{V}, \hat{\rho}^{(1)}]_{nm} e^{(i\omega_{nm} + \gamma_{nm})t'} dt' \quad 1.59$$

$$[\hat{V}, \hat{\rho}^{(1)}]_{nm} = - \sum_v (\bar{\mu}_{nv} \rho_{vm}^{(1)} - \rho_{nv}^{(1)} \bar{\mu}_{vm}) \cdot \bar{E}(t) \quad 1.60$$

Using a procedure analogous to that used in the derivation of the linear susceptibility, it is possible to derive the formula for  $\chi^{(2)}$ . In this case it is necessary to evaluate every frequency component of  $\chi^{(2)}$ . For example, the term containing the sum frequency ( $\omega_p + \omega_q$ ) can be expressed by:

$$\chi_{ijk}^{(2)}(\omega_p + \omega_q, \omega_q, \omega_p) = \frac{N}{2\hbar^2} \sum_{lmn} (\rho_{ll}^{(0)} - \rho_{mm}^{(0)}) \left\{ \begin{array}{l} \frac{\mu_{ln}^i \mu_{mn}^j \mu_{ml}^k}{(\omega_{nl} - \omega_p - \omega_q - i\gamma_{nl})(\omega_{ml} - \omega_p - i\gamma_{ml})} + \\ \frac{\mu_{ln}^i \mu_{nm}^k \mu_{ml}^j}{(\omega_{nl} - \omega_p - \omega_q - i\gamma_{nl})(\omega_{ml} - \omega_q - i\gamma_{ml})} + \\ \frac{\mu_{ln}^j \mu_{nm}^i \mu_{ml}^k}{(\omega_{nm} + \omega_p + \omega_q + i\gamma_{ni})(\omega_{ml} - \omega_p - i\gamma_{ml})} + \\ \frac{\mu_{ln}^k \mu_{nm}^k \mu_{ml}^j}{(\omega_{nm} + \omega_p + \omega_q + i\gamma_{nm})(\omega_{ml} - \omega_p - i\gamma_{ml})} \end{array} \right\} \quad 1.61$$

In Eq. 1.61,  $\mu_{ln}^i$  is the dipole moment related to the transition from the state  $n$  to the state  $l$  and the labels  $i, j, k$  indicate the Cartesian coordinates of the electric fields at frequency  $\omega_p + \omega_q$ ,  $\omega_p$  or  $\omega_q$ .

Analogously, the third-order susceptibility can also be obtained. The total expression consists of 48 terms that are obtained from the permutation of the input frequencies  $\omega_p$ ,  $\omega_q$  and  $\omega_r$  in the Eq. 1.62.

$$\chi_{ijih}^{(3)}(\omega_p + \omega_q + \omega_r, \omega_r, \omega_q, \omega_p) = \frac{N}{\hbar^3} \delta_{I} \sum_{nmvl} \rho_{ll}^{(0)} \times \left\{ \begin{array}{l} \frac{\mu_{mn}^k \mu_{nv}^j \mu_{vl}^i \mu_{lm}^h}{[(\omega_{vl} - \omega_p - \omega_q - \omega_r) - i\gamma_{vl}][(\omega_{nl} - \omega_p - \omega_q) - i\gamma_{nl}][(\omega_{ml} - \omega_p) - i\gamma_{ml}]} + \\ \frac{\mu_{lv}^h \mu_{vn}^k \mu_{nm}^j \mu_{ml}^i}{[(\omega_{nv} - \omega_p - \omega_q - \omega_r) - i\gamma_{nv}][(\omega_{mv} - \omega_p - \omega_q) - i\gamma_{mv}][(\omega_{vl} + \omega_p) + i\gamma_{vl}]} + \\ \frac{\mu_{lv}^i \mu_{vn}^k \mu_{nm}^i \mu_{ml}^h}{[(\omega_{nv} - \omega_p - \omega_q - \omega_r) - i\gamma_{nv}][(\omega_{vm} + \omega_p + \omega_q) + i\gamma_{vm}][(\omega_{ml} - \omega_p) - i\gamma_{ml}]} + \\ \frac{\mu_{lv}^h \mu_{vn}^i \mu_{nm}^k \mu_{ml}^j}{[(\omega_{mv} - \omega_p - \omega_q - \omega_r) - i\gamma_{mv}][(\omega_{nl} + \omega_p + \omega_q) + i\gamma_{nl}][(\omega_{vl} + \omega_p) + i\gamma_{vl}]} + \\ \frac{\mu_{lv}^j \mu_{vn}^k \mu_{nm}^i \mu_{ml}^h}{[(\omega_{vn} + \omega_p + \omega_q + \omega_r) + i\gamma_{vn}][(\omega_{nl} - \omega_p - \omega_q) - i\gamma_{nl}][(\omega_{ml} - \omega_p) - i\gamma_{ml}]} + \\ \frac{\mu_{lv}^h \mu_{vn}^j \mu_{nm}^k \mu_{ml}^i}{[(\omega_{nm} + \omega_p + \omega_q + \omega_r) + i\gamma_{nm}][(\omega_{mv} - \omega_p - \omega_q) - i\gamma_{mv}][(\omega_{vl} + \omega_p) + i\gamma_{vl}]} + \\ \frac{\mu_{lv}^i \mu_{vn}^j \mu_{nm}^k \mu_{ml}^h}{[(\omega_{nm} + \omega_p + \omega_q + \omega_r) + i\gamma_{nm}][(\omega_{vm} + \omega_p + \omega_q) + i\gamma_{vm}][(\omega_{ml} - \omega_p) - i\gamma_{ml}]} + \\ \frac{\mu_{lv}^h \mu_{vn}^i \mu_{nm}^j \mu_{ml}^k}{[(\omega_{ml} + \omega_p + \omega_q + \omega_r) + i\gamma_{ml}][(\omega_{nl} + \omega_p + \omega_q) + i\gamma_{nl}][(\omega_{vl} + \omega_p) + i\gamma_{vl}]} \end{array} \right\} \quad 1.62$$

In the case of non resonance excitation, Eq. 1.62 reduces to Eq. 1.41 through the neglect of the terms ( $i\omega_{\alpha\beta}$ ) in the denominators.

It is clear that the solution of this expression is very complicated because the summation is done over all the states of the system and involves the knowledge of a lot of physical quantities related to the excited states.

### 1.5 Two-photon absorption (TPA)

In this section we will describe the two-photon absorption process, characterized by the simultaneous absorption of two photons from a light source. In the first part, only a phenomenological approach will be presented to better explain the properties of this process. In the next chapter, an excursus of the most important classes of systems showing TPA properties will be reported.

As it is represented in Fig. 1.4, after the interaction with the first photon the system enters a state of polarization that can be described as a coherent overlap of the initial state with the virtual states of the molecule. Before the coherent state decays, a second photon is employed to excite the system to a real excited state. When the input intensity increases, a multi-photon absorption process can occur in the system and it is characterized by the simultaneous absorption of three or more photons (see Fig. 1.4-b).

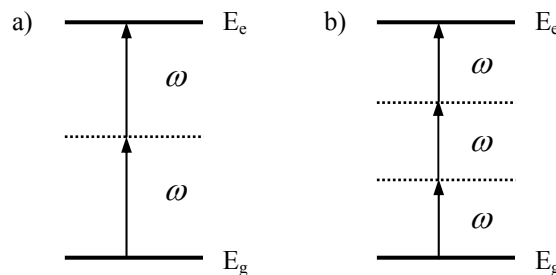


**Fig. 1.4:** Two-photon absorption (a) and three-photon absorption (b)

In all cases, the system is transparent to the frequency  $\omega$  at low input energies. The probability to have absorption of two or more photons increases at high incident energies. In particular, the variation of the incident intensity with the optical path is given by:

$$\frac{\partial I}{\partial z} = -\alpha I - \beta I^2 - \gamma I^3 \quad 1.63$$

The coefficients  $\alpha$ ,  $\beta$  and  $\gamma$  are respectively the one-, two- and three- photon absorption coefficients. At low energies, only the first term becomes important and the others can be neglected because of the relation  $\alpha \ll \beta \ll \gamma$ .

$\beta$  depends on the third-order susceptibility as expressed in the Eq. 1.64.

$$\beta = \frac{3\pi}{\varepsilon_0 c n^2 \lambda} \text{Im}[\chi^{(3)}(-\omega; \omega, -\omega, \omega)] \quad [\beta] = \text{cm} / W \quad 1.64$$

Analogously, the three-photon coefficient depends on the imaginary part of  $\chi^{(5)}$ :

$$\gamma = \frac{3\pi}{\varepsilon_0^{(2)} c^2 n^2 \lambda} \text{Im}[\chi^{(5)}(-\omega; \omega, -\omega, \omega, -\omega, \omega)] \quad 1.65$$

For TPA process, at a molecular scale, it is possible to define the TPA cross-section ( $\sigma^{(2)}$ ) as a microscopic quantity:

$$\sigma^{(2)} = \frac{\hbar \omega \beta}{N} \quad [\sigma^{(2)}] = \text{cm}^4 \text{s} / (\text{mol} \cdot \text{fotoni}) \quad 1.66$$

In this relation  $N$  is the number of absorbing species per unit volume and  $\sigma^{(2)}$  is the third-order nonlinear optical response of a single molecule.

The common unit for the  $\sigma^{(2)}$  is the Göppert Mayer (from the first researcher that predicted the possibility to have a TPA event<sup>3</sup>) defined as:

$$1 \text{ GM} = 10^{-50} \text{ cm}^4 \text{ s} / (\text{mol} \cdot \text{photons}) \quad 1.67$$

The values of  $\sigma^{(2)}$  for organic chromophores are only few units or tens, but this value can be improved through a suitable design of the molecular structure.

The techniques most used for the characterization of TP absorbers are based on the determination of the transmittance variation. The expression for this quantity can be derived from Eq. 1.63.<sup>1</sup>

When the linear absorption at the wavelength used is small and only the TPA process is important, the transmittance through the thickness  $z$  is given by:

$$T = \frac{I(z)}{I_0} = \frac{1}{1 + z\beta I_0} \quad 1.68$$

This expression is obtained in a steady-state condition, with an input laser beam possessing an homogenous rectangular transverse intensity distribution. If the laser beam has a nearly gaussian transverse distribution, the transmittance is expressed by:<sup>4</sup>

$$T = \frac{I(z)}{I_0} = \frac{\ln(1 + z\beta I_0)}{z\beta I_0} \quad 1.69$$

## 1.6 Saturable absorption (SA) and Reverse Saturable absorption (RSA)

The Saturable absorption (SA) and the Reverse Saturable Absorption (RSA) are nonparametric nonlinear processes, both of interest for application in nonlinear optical devices. In SA, the absorption coefficient of the material decreases at high incident

intensities and the material becomes more transparent. The second one is characterized by the increase of the absorption coefficient. The RSA is a two-step sequential two-photon absorption, each step consisting of a one-photon absorption process, as depicted in Fig. 1.5.

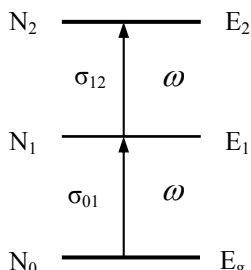


**Fig. 1.5:** Nonlinear absorption mechanism for Reverse Saturable Absorption

State 1 represents a one-photon allowed excited state resonant with the incident light, that can be populated by photoexcitation from the ground state. For some materials, it is possible to make a further transition from the initially excited state 1 to an upper excited state 2. The probability of this process is proportional to the number of molecules in state 1 and to the intensity of the incident beam.  $N_1$  depends to the incident intensity and the number of molecules  $N_0$  through the coefficient  $\sigma_{01}$ , which is the one-photon absorption cross-section for the transition from state 0 to state 1.

$$\begin{aligned} N_2 &\propto N_1 I \\ N_1 &\propto \sigma_{01} N_0 I \end{aligned} \quad 1.70$$

By increasing the incident intensity,  $N_1$  and  $N_2$  increase. Materials possessing a  $\sigma_{12}$  higher than  $\sigma_{01}$  show RSA. The change of the populations of the states is determined by the appropriate kinetics equations discussed below.<sup>5,6</sup>

There are different classes of materials showing RSA and studied for application in optical limiting devices, such as the organic dyes solutions or doped solids<sup>7</sup>, fullerene solutions or solids<sup>8-14</sup> and organometallic systems.<sup>15-18</sup>

Fullerene solutions and doped solid samples have been among the most studied materials for optical limiting. In particular, in order to better include the fullerene in solid hosts, a lot of fullerene-derivatives, such as methanofullerenes or fulleropyrrolidine derivatives, have been synthesized and characterized.<sup>19-26</sup>

In this context we focus attention on the photophysical properties of fullerene, but analogous consideration can be done for the fullerene-derivatives. The energy diagram of  $C_{60}$  is reported in Fig. 1.6.

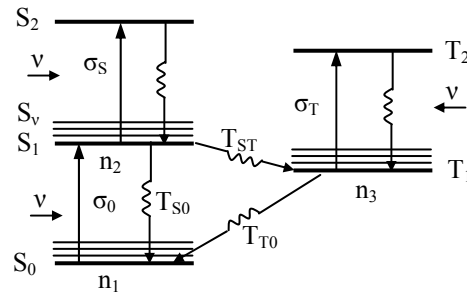


**Fig. 1.6:** Representation of energetic diagram of fullerene C<sub>60</sub>

The incident radiation excites the system from the singlet ground level (S<sub>0</sub>) to a vibrational level S<sub>ν</sub> of the first excited state S<sub>1</sub>. This process is only weakly allowed in the visible range and σ<sub>0</sub> is therefore small. These excited molecules rapidly decay to the lowest zero-vibration state of S<sub>1</sub> in a temporal scale of hundreds fs or less. The excited molecule can relax radiatively or non radiatively to the S<sub>0</sub> state or can undergo Intersystem Crossing (ISC) to the lowest triplet-state T<sub>1</sub>. This second path occurs in some ns, with nearly unit quantum efficiency for C<sub>60</sub>. Molecules in S<sub>1</sub> and in T<sub>1</sub> can be promoted to the higher level S<sub>n</sub> and T<sub>n</sub>, respectively, with cross-sections considerably larger than that for transition from the ground state to the first excited state S<sub>1</sub>. At high incoming light fluences, the global absorption is therefore larger than at low fluence, where only the ground state is populated. Because the state T<sub>1</sub> is metastable with lifetime of hundreds of μs, long-laser pulses (ns-μs) undergo one-photon absorption from T<sub>1</sub> to T<sub>n</sub>, before the T<sub>1</sub> state, populated by ISC from S<sub>1</sub>, decays.

Because of the two-step nature of the RSA, this process is also classified as an excited state absorption (ESA) event.

The final states S<sub>n</sub> and T<sub>n</sub> have very short lifetimes (less than ps) and it is possible to neglect their population. The same consideration holds for the vibronic level S<sub>ν</sub>. The system of kinetics equations for the populations of three levels S<sub>0</sub>, S<sub>1</sub> and T<sub>1</sub> is:

$$\begin{aligned} \frac{dn_1}{dt} &= -\frac{\sigma_0 I n_1}{h\nu} + \frac{n_2}{\tau_{S0}} + \frac{n_3}{\tau_{T0}} \\ \frac{dn_2}{dt} &= \frac{\sigma_0 I n_1}{h\nu} - \frac{\sigma_s I n_2}{h\nu} - \frac{n_2}{\tau_{S0}} - \frac{n_2}{\tau_{ST}} \\ \frac{dn_3}{dt} &= -\frac{\sigma_T I n_3}{h\nu} + \frac{n_2}{\tau_{ST}} - \frac{n_3}{\tau_{T0}} \end{aligned} \quad 1.71$$

$\tau_{S0}$  and  $\tau_{T0}$  are the relaxation times for the singlet S<sub>0</sub> and the triplet T<sub>1</sub>.

The intensity change along the propagation direction  $z$  is given by:

$$\frac{dI}{dz} = -\alpha I = -I(\alpha_0 + \alpha_S + \alpha_T) = -I(\sigma_0 n_1 + \sigma_S n_2 + \sigma_T n_3) \quad 1.72$$

Using this equation, it is possible to fit the typical transmittance curve ( $T$  vs  $E_{inc}$ ) measured for the RSA system in order to fully characterize the nonlinear absorption and the photophysical quantities. The calculated curves are generally in good agreement with the experimental data for moderate intensity ( $1 \text{ J/cm}^2$ ). At higher energies, a deviation of the experimental data can be caused by different non linear effects, like thermal lensing or non linear scattering.<sup>27,5</sup>

### 1.7 Sequential Multiphoton absorption processes

The nonlinear optical response of a material, in particular the two-photon absorption, depends on the pulse duration of the used laser beam.

By using pulses with different  $\tau_L$  it is possible to discriminate between three main possible contributions to the observed TPA cross section (see figure 1.7): (I) pure coherent TPA, with a negligible population of excited states, (II) TPA giving rise to a population of the excited state (either the final state of the two-photon transition or a different one reached after internal conversion or intersystem crossing), followed by a sequential absorption of a third photon, (III) incoherent two-step TPA.<sup>28</sup>

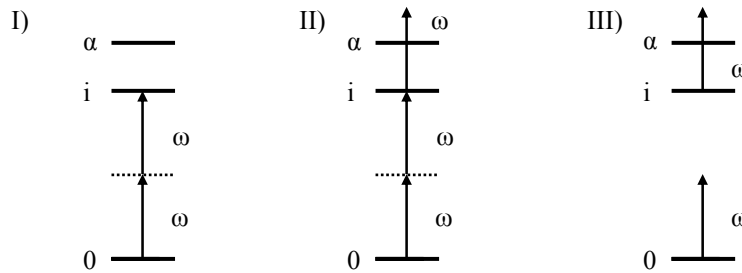


**Fig. 1.7:** Energy-level diagram: I) coherent one-step TPA; II) two-step three-photon absorption; III) incoherent two-step TPA

The second process is due to incoherent excited state absorption followed by the absorption of a third photon: this process is described by fifth-order susceptibility and depends on the fluence of the laser pulse as the build-up of excited state population implies time integration within the pulse duration. The third process is a third-order effect permitting the population of the excited state through a pre-resonant one-photon absorption. This process depends on the laser fluence as well.

The last two effects are mainly involved when ns-laser pulses are employed. In this regime the TPA cross-section is called " $\sigma_{\text{eff}}^{(2)}$ " and is generally higher than that measured in the fs-laser regime by one order of magnitude or more.

An effective multiphoton absorption cross section can be defined as:

$$\sigma_{TPA}^{\text{eff}} = \sigma_1^{(2)} + \sigma_2^{(2)} + \sigma^{(3)}I \quad 1.73$$

Here,  $\sigma_1^{(2)}$  is the pure coherent TPA cross section (denoted as mechanism I),  $\sigma_2^{(2)}$  is the incoherent two-step (sequential) TPA (mechanism III),  $\sigma^{(3)}I$  is the contribution coming from a coherent TPA followed by absorption of a third photon (mechanism II).

The formula for one-step TPA cross-section ( $\sigma_1^{(2)}$ ), omitting the averaging over the molecular orientations, is expressed by:

$$\sigma_1^{(2)} = \frac{\omega}{c^2 \epsilon_0^2 \hbar^3} \left[ \frac{\Gamma_{i0}}{(2\omega - \omega_{i0})^2 + \Gamma_{i0}^2} \right] \sum_{\alpha} \frac{\mu_{i\alpha}^2 \mu_{\alpha 0}^2}{(\omega - \omega_{\alpha 0})^2} \quad 1.74$$

Here,  $\omega_{mn}$ ,  $\mu_{mn}$ ,  $\Gamma_{mn}$  are the transition frequency, the dipole moment and the dephasing rate of the transition  $m \leftarrow n$ .

If we focus on quadrupolar donor-acceptor structures, they can be modeled including a minimum of three electronic states:<sup>29</sup> the ground state (0 subscript), a two-photon allowed state ( $i$  subscript), corresponding to a symmetric intramolecular charge transfer state, and an asymmetric charge transfer state ( $\alpha$  subscript), that lies at intermediate energy between the ground and the two-photon allowed state. We consider a rectangular pulse, with duration  $\tau_p$ , having intensity equals to I and 0 for  $0 \leq t \leq \tau_p$  and  $t < 0$ ,  $t > \tau_p$  respectively.

The two-step TPA cross-section (mechanism III) can be expressed as:<sup>28</sup>

$$\sigma_2^{(2)} = \frac{k}{c \epsilon_0^2 \hbar^3} \left[ \varpi_i \left\langle \frac{v_{i0}}{\Gamma_{ii}} \left( \sum_{\alpha} v_{\alpha i}^- - v_{i0}^- \right) \right\rangle - \sum_{\alpha} \varpi_{\alpha} \left\langle \frac{v_{\alpha 0}^+}{\Gamma_{\alpha\alpha}} (v_{\alpha i}^- + v_{\alpha 0}^-) \right\rangle \right] \quad 1.75$$

The pulse factor is:

$$\varpi_j = 1 - \exp(-\Gamma_{jj} \tau_p) \approx \begin{cases} 1 & \text{long pulse} \\ \Gamma_{jj} \tau_p & \text{short pulse} \end{cases} \quad 1.76$$

$$v_{ij}^{\pm} \text{ is given by: } \quad v_{ij}^{\pm} = \mu_{ij}^2 \Gamma_{ij} \left( \frac{1}{(\omega - \omega_{ij})^2} \pm \frac{1}{(\omega + \omega_{ij})^2} \right) \quad 1.77$$

Equation 1.75 shows that the two-step two-photon absorption (and analogously the three-photon absorption) depends on the pulse duration. In fact, the population increases linearly with the pulse duration ( $\approx \Gamma_{jj} \tau_p$ ) and reaches its maximum for a long pulse

( $\Gamma_{ij}\tau_p \gg 1$ ). In our case, the first and the second terms in Eq. 1.75 can be neglected both in the steady-state limit (the laser pulse duration  $\tau_p$  is much longer than the decay time of the intermediate state,  $(1/\Gamma_\alpha)$ ) and in the short pulse limit (because  $\mu_{i0}$  vanishes for quadrupolar structures).

The effective TPA cross section for the two-step process can be written in the form:

$$\sigma_2^{(2)} \approx \frac{\omega\tau_{2-step}}{c\epsilon_0^2\hbar^3}\sigma_{\alpha 0}(-\Delta)[\sigma_{i\alpha}(\Delta)-\sigma_{\alpha 0}(-\Delta)] \quad 1.78$$

where  $\sigma_{\alpha 0}(-\Delta)$  and  $\sigma_{i\alpha}(\Delta)$  are the one-photon absorption cross sections for the transitions  $\alpha \leftarrow 0$  and  $i \leftarrow \alpha$ , respectively, at a laser frequency  $\omega$  detuned on opposite sides of the center frequency of those transitions by an amount  $\Delta = |\omega_{\alpha 0} - \omega| = |\omega - \omega_{i\alpha}|$ .

In the long pulse (steady-state) limit, the characteristic time  $\tau_{2-step}$  equals the lifetime of the intermediate state  $\tau_\alpha$  whereas in the short pulse limit it equals the pulse duration  $\tau_p$ .

Comparing the cross-section for the one-step coherent TPA,  $\sigma_1^{(2)}$  in Eq. 1.74, with that for the two-step sequential TPA,  $\sigma_2^{(2)}$  in Eq. 1.78, is not easy without resorting to numerical simulations. However, we can work out a sort of rule of thumb by manipulating these two equations to get:

$$\frac{\sigma_2^{(2)}}{\sigma_1^{(2)}} \approx \Gamma_{\alpha 0}\tau_{2-step} \left[ \frac{\Gamma_{i0}\Gamma_{i\alpha}}{\Delta^2} - \frac{\Gamma_{i0}\Gamma_{\alpha 0}}{\Delta^2} \left( \frac{\mu_{\alpha 0}}{\mu_{i\alpha}} \right)^2 \right] \quad 1.79$$

For the specific case we are considering, i.e. a quadrupolar dye with inversion symmetry and a one-photon allowed state lying below the two-photon state, Eq. 1.79 shows that the two-step TPA mechanism adds or subtracts to the coherent one-step process depending mainly on the ratio  $(\mu_{\alpha 0}/\mu_{i\alpha})$ . In most cases, this ratio is smaller than one, since dipole moments for transitions starting from an excited state are greater than those starting from the ground state; hence, we expect the quantity in square brackets to be positive.

In the long-pulse limit,  $\Gamma_{\alpha 0}\tau_{2-step} = \Gamma_{\alpha 0}\tau_\alpha \gg 1$ , since the dephasing time for a room temperature dye is much faster than the decay rate of the lowest excited state.

Hence, if the detuning from one-photon resonance is not much greater (two orders of magnitude or more) than the width of the lowest absorption band, the two-step sequential

TPA will prevail over the coherent one-step TPA when using long pulses ( $\tau_p/\tau_\alpha \gg 1$ ).

Indeed, for the two-step process to become negligible one would need to satisfy the condition  $\Gamma_{\alpha 0}\tau_p \ll 1$ , which is a very stringent requirement since the dephasing time in room temperature solutions can be of the order of a few tens of femtoseconds.

For the description of the sequential process in which coherent TPA is followed by the absorption of a third photon (mechanism II) we need to go beyond the essential three-state model and to consider other states at energies higher than the two-photon state  $i$ . Let us denote one of these states as  $\beta$  and assume that the orientational averaging implied in the NL response of the system at fifth-order of perturbation (needed to describe a three-photon absorption process) can be decoupled into separate ones for the TPA and for the subsequent one-photon absorption. Then, in the long pulse (steady-state) limit, we get:

$$\sigma^{(3)} \approx \frac{\tau_i}{2} \sigma_1^{(2)} \sigma_{\beta i}(\Delta') \quad 1.80$$

where  $\sigma_{\beta i}(\Delta')$  is the one-photon absorption cross section for the  $\beta \leftarrow i$  transition at a detuning  $\Delta'$  of  $\omega$  from exact resonance. In the short pulse limit the expression for  $\sigma^{(3)}$  would scale down by a factor  $\tau_p/\tau_i \ll 1$  with respect to Eq. 1.80. The contribution of sequential three-photon absorption to the measured  $\sigma_{TPA}^{eff}$  (see Eq. 1.73) introduces a linear dependence on the pulse irradiance, but it is much smaller in the short than in the long pulse limit. It is worth mentioning that when using long pulses the absorption of the third photon may start from a state different from the two-photon state  $i$ , which is reached through non radiative processes like internal conversion or intersystem crossing. Of course, the characteristic time of the non radiative process would enter into the picture and the expression for  $\sigma^{(3)}$  would turn into one more complicated than Eq. 1.80.



## REFERENCES:

- <sup>1</sup> G.S. He and S.H.Liu, *Physics of nonlinear optics*, World Scientific Ed., 1999
- <sup>2</sup> Boyd, R. W. *Nonlinear optics*, Academic Press, 1992
- <sup>3</sup> Mayer, G. *Ann. Phys.*, 1931, 9, 273-295
- <sup>4</sup> He, G. S. et al. *Opt. Lett.*, 1995, 20, 435-437
- <sup>5</sup> Li, C. et al. *J. Opt. Soc. Am. B*, 1994, 11, 1356-1360
- <sup>6</sup> Hennary, B. et al. *Chem. Phys. Lett.*, 1992, 199, 144-148
- <sup>7</sup> Shuang, Z. et al. *Synth. Metals*, 2001, 121, 1471-1472
- <sup>8</sup> Kamanina, N.V. et al. *Opt. Comm.*, 1998, 152, 280-282
- <sup>9</sup> Bindhu, C.V. et al. *Appl. Phys. B*, 2000, 70, 429-434
- <sup>10</sup> Kojima, Y. et al. *J. of Mater. Science Lett.*, 1997, 2029-2031
- <sup>11</sup> Kamanina, N.V. *Synth. Metals*, 2002, 127, 121-128
- <sup>12</sup> Chollet, P.A. and Kajzar, F. *J. of Sol-gel Science and Techn.*, 2001, 22, 255-265
- <sup>13</sup> Kamanina, N.V. et al. *Opt. Comm.*, 2001, 194, 367-372
- <sup>14</sup> Bin, Ma et al. *J. Phys. Chem. B*, 1998, 102, 5999-6009
- <sup>15</sup> Qureshi, F.M. et al. *Chem. Phys.*, 1998, 231, 87-94
- <sup>16</sup> Santhi, A. et al. *J. Of Appl. Phys.*, 2006, 100, 053109-
- <sup>17</sup> De Boni, L. et al. *Chem. Phys. Lett.*, 2006, 419, 417-420
- <sup>18</sup> Sun, Z. et al. *Chem. Phys. Lett.*, 2001, 342, 323-327
- <sup>19</sup> Brusatin, G. and Innocenzi, P. *J. of Sol-gel Science and Techn.*, 2001, 22, 189-194
- <sup>20</sup> Rio, Y. and Felder, D. *J. of Sol-gel Science and Techn.*, 2003, 26, 625-628
- <sup>21</sup> Kopitkovas, G. et al. *Opt. Material*, 2004, 27, 285-291
- <sup>22</sup> Schell, J. et al. *J. of Sol-gel Science and Techn.*, 2001, 22, 225-236
- <sup>23</sup> Dou, K. et al. *J. of Luminescence*, 1999, 83-84, 241-246
- <sup>24</sup> Rio, Y. et al. *New J. Chem.*, 2002, 26, 1146-1154
- <sup>25</sup> Ouyang, J. et al. *Chem. Phys. Lett.*, 2002, 366, 224-230
- <sup>26</sup> Prato, M. et al. *Synth. Metals*, 1996, 77, 89-91
- <sup>27</sup> Signorini, R. et al. *Carbon*, 2000, 38, 1653-1662
- <sup>28</sup> Gel'mukhanov, F. et al. *J. Opt. Soc. Am. B*, 2002, 19 (5), 937-945
- <sup>29</sup> Signorini, R. et al., *J. Phys. Chem. A*, 2007, submitted



## CHAPTER 2

# Materials for two-photon absorption

The study of new materials possessing high two-photon efficiency plays an important role for their practical use in technological applications.

In this chapter, an excursus of the most important classes of nonlinear optical chromophores, already studied in the literature, will be presented. Some theoretical models describing simple molecular structures will be exposed in order to emphasize a possible way for incrementing the nonlinear optical response of materials. More attention will be reserved to systems which are prototypes for the molecules characterized and studied in our laboratory.

### 2.1 Dipolar D-A organic chromophores

In this section we will analyze some basic concepts used for the study of the TPA properties of *push-pull* molecules.<sup>1-5</sup> These compounds are characterized by an electron donor group (D) and an electron acceptor one (A), connected by a  $\pi$  conjugation path:

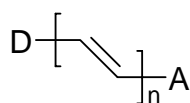


**Fig. 2.1:** Schematic representation of molecular structure of polyenic D-A system

Push-pull molecules are characterized by a low-lying high-intensity absorption band, related to the intramolecular charge transfer (ICT) between the D and A groups. This transition is associated to a large dipole change allowing a large static quadratic hyperpolarizability  $\beta$ . The two-state expression for  $\beta$  is:<sup>1</sup>

$$\beta \propto \mu_{eg}^2 \Delta\mu / E_{eg}^2 \quad 2.1$$

Here  $\Delta\mu$  is the difference between the permanent dipole moment of the ICT state and that of the ground state,  $\mu_{eg}$  is the transition dipole moment and  $E_{eg}$  is the transition energy.

Because of the asymmetric structure of molecule, like the one reported in Fig. 2.1, the low-lying absorption band related to ICT phenomenon is allowed both by one-photon absorption (OPA) and two-photon absorption (TPA).<sup>6</sup>

In order to obtain Eq. 2.1, and analogously the other nonlinear optical quantities, in the Sum Over States (SOS) calculation only two states (the ground and the ICT state) contribute to the nonlinear optical response. The ground state structure is a combination of the neutral and the zwitterionic (with charge-separation) forms. For a polyenic D-A structure, the limiting-resonance forms are reported in Fig. 2.2.

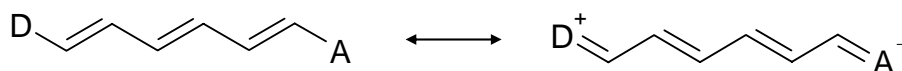


**Fig. 2.2:** Two limiting-resonance forms of polyenic D-A structure

When the D and A groups are weak, the ground state is dominated by the neutral form and the structure is characterized by a high degree of Bond Length Alternation (BLA; i.e. alternation of single and double bonds). On the contrary, when the D and A substituents are strong, the contribution of the limiting-resonance forms in the ground state is large and consequently the BLA decreases. In this case, the polarity of the solvent has an important role in the determination of the importance of the charge-separated forms in the description of the states. In particular, by increasing the polarity of the solvent, the charge separation is favored and the nonlinear polarizabilities increase. This effect of the solvent on NLO properties is in accord with the experimental evidences in linear solvatochromic optical responses for organic chromophores.<sup>7</sup>

Considering a two-state model, the molecular Hamiltonian has the form:

$$H = \begin{vmatrix} E_N & -t \\ -t & E_Z \end{vmatrix} \quad 2.2$$

Here,  $E_N$  and  $E_Z$  are the energies of the neutral and the zwitterionic forms respectively.  $t$  is the interaction non-diagonal matrix element between the two resonance forms.

The normalized wavefunction of the ground and the excited state are combinations of the neutral and the zwitterionic forms:<sup>1</sup>

$$\begin{aligned} |\psi_g\rangle &= \cos\frac{\theta}{2}|\psi_N\rangle + \text{sen}\frac{\theta}{2}|\psi_Z\rangle \\ |\psi_e\rangle &= -\text{sen}\frac{\theta}{2}|\psi_N\rangle + \cos\frac{\theta}{2}|\psi_Z\rangle \end{aligned} \quad 2.3$$

In the range  $0 \leq \theta \leq \pi/2$ , the ground state is dominated by the neutral form and, viceversa, in the range  $\pi/2 \leq \theta \leq \pi$ , the zwitterionic form is the most important.

In this model, two parameters are introduced in order to have a simple description of the nonlinear optical response. The first is the parameter  $t$  defined by:

$$-t = \langle \psi_Z | H | \psi_N \rangle \quad 2.4$$

The parameter  $t$  is always positive: it diminishes with the length of the conjugation path or with deviations from planarity of the  $\pi$  bridge.

The second factor is the energy difference between the zwitterionic and the neutral forms:

$$V = \langle \psi_Z | H | \psi_Z \rangle - \langle \psi_N | H | \psi_N \rangle \quad 2.5$$

Using the last equations, the value of  $\theta$  is given by:

$$\text{tg}\theta = \frac{2t}{V} \quad 2.6$$

It is possible to derive the expressions for the ground state ( $\mu_g$ ) and the excited state ( $\mu_e$ ) dipoles, the transition dipole ( $\mu_{eg}$ ) and the energy gap ( $E_{eg}$ ) in the assumption that the mutual transition dipole is negligible ( $\langle \psi_N | \mu | \psi_Z \rangle = 0$ ):

$$\begin{aligned} \mu_g &= \langle \psi_g | H | \psi_g \rangle = \frac{\mu_N + \mu_Z - \mu_{CS} \cos\theta}{2} \\ \mu_e &= \langle \psi_e | H | \psi_e \rangle = \frac{\mu_N + \mu_Z + \mu_{CS} \cos\theta}{2} \\ \mu_{eg} &= \langle \psi_e | H | \psi_g \rangle = \frac{\mu_{CS} \text{sen}\theta}{2} \\ E_{eg} &= \frac{2t}{\text{sen}\theta} \end{aligned} \quad 2.7$$

In these expressions,  $\mu_{CS}$  is the difference between  $\mu_Z$  and  $\mu_N$ , where  $\mu_Z$  and  $\mu_N$  are the dipoles of the zwitterionic and the neutral forms respectively. All expressions in Eq. 2.7 depend on the angle  $\theta$ . It is useful to define another quantity (MIX), expressed by:<sup>1,8</sup>

$$MIX = -\cos\theta = -\frac{V}{\sqrt{V^2 + 4t^2}} \quad 2.8$$

If the neutral form is more energetically stable than the zwitterionic one ( $V > 0$ ), the ground and the first excited states are dominated by the neutral and the zwitterionic forms respectively and  $-1 < MIX < 0$ .

From the two-state model, the dipolar term of the third-order susceptibility is useful to determine the expression for the TPA cross-section. Near to the two-photon resonance condition ( $E_{eg} \sim 2\hbar\omega$ ) and if  $\hbar\omega \gg i\gamma_{eg}$ ,  $\chi^{(3)}$  is given by:

$$\chi^{(3)}(-\omega; \omega, -\omega, \omega) = \left[ \frac{\mu_{eg}^2 \Delta\mu_{eg}^2}{E_{eg}^2 (-i\hbar\gamma_{eg})} \right] = i \frac{\mu_{eg}^2 \Delta\mu_{eg}^2}{E_{eg}^2 \hbar\gamma_{eg}} \quad 2.9$$

The expression of  $\sigma^{(2)}$ , introduced in paragraph 1.5, for dipolar molecules can be written as:

$$\sigma_D^{(2)} = \frac{3\pi\hbar\omega}{\varepsilon_0 c n^2 \lambda N} \text{Im}[\chi^{(3)}(-\omega; \omega, -\omega, \omega)] = \frac{3\pi\hbar\omega}{\varepsilon_0 c n^2 \lambda N} \frac{\mu_{eg}^2 \Delta\mu_{eg}^2}{E_{eg}^2 \hbar\gamma_{eg}} \quad 2.10$$

where  $\gamma_{eg}$  is the excited-state linewidth. The quantities in Eq. 2.10 are the same as those reported in Eq. 2.7 and can be further written as function of the MIX parameter. Substituting the new relations, Eq. 2.10 can be rewritten in:

$$\sigma_D^{(2)}(\omega^*) \propto \frac{\mu_{CS}^4 (1 - MIX^2)^2 MIX^2}{\gamma_{eg} t^2} \quad 2.11$$

The variation of  $\sigma_D^{(2)}$  as a function of the parameter MIX is reported in Fig. 2.3.

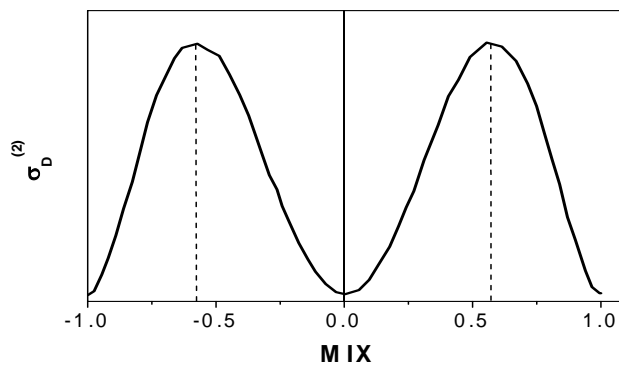


**Fig. 2.3:** Variation of  $\sigma_D^{(2)}$  versus MIX

The TPA cross-section for dipolar D-A molecules has a minimum at  $MIX=0$ . The maximum value is at  $\pm 1/\sqrt{3}$  ( $V = \mp\sqrt{2}t$ ), corresponding to an intermediate structure between the neutral and the zwitterionic forms. The maximum values of  $\sigma_D^{(2)}$  can be

obtained by choosing the nature of the end-groups which permit the tunability of the energy gap  $V$ , in order to reach the optimal  $MIX = \pm 1/\sqrt{3}$  values.  $\sigma_D^{(2)}$  can also be enhanced by lengthening the distance between the donor and the acceptor end groups in order to increase  $\mu_{CS}^4/t^2$ .

## 2.2 Quadrupolar organic chromophores

A strategy to enhance the efficiency of a two-photon absorber is the use of quadrupolar molecular structure, where two D-A pairs are grafted symmetrically on the  $\pi$ -bridge.<sup>9,10,11</sup> Push-pull quadrupolar D-A-A-D molecules show symmetric CT transitions from the ends towards the middle of the conjugation path and viceversa for A-D-D-A systems.

Semiempirical calculations demonstrate that it is necessary to use a three-states model for the determination of the optical properties of these systems: the ground ( $g$ ) and two excited states ( $a$  and  $e$ ). Contrary to the dipolar case, the quadrupolar system has a symmetric structure. This imposes that the states which are involved in the one-photon transition are not the same for two-photon transition. The OPA transition is allowed between  $g$  and  $a$  states, having opposite symmetry. Instead, the TPA process involves the  $g$  and  $e$  states. State  $a$  lies at intermediate energy between the ground and the TPA allowed state.

The three-state model is analogous to the two-state model, so we will report only the main results for quadrupolar dyes. The neutral and the zwitterionic forms for a D-AA-D molecule are depicted in Fig. 2.4.

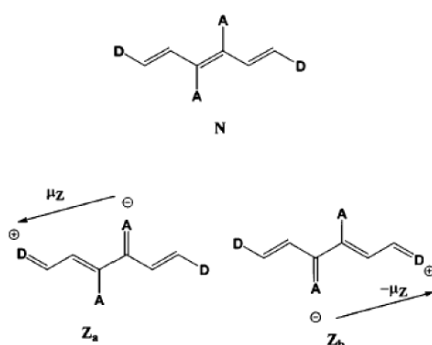


**Fig. 2.4:** Neutral and zwitterionic forms of a push-pull D-AA-D quadrupolar system

The hamiltonian matrix in the  $\{|N\rangle, |Z_a\rangle, |Z_b\rangle\}$  basis set is given by:

$$H = \begin{pmatrix} E_N & -t & -t \\ -t & E_Z & 0 \\ -t & 0 & E_Z \end{pmatrix} \quad 2.12$$

The zwitterionic forms are degenerate ( $E_Z = \langle Z_a | H | Z_a \rangle = \langle Z_b | H | Z_b \rangle$ ) on account of the symmetry of the molecule. The meaning of the parameter  $t$  is analogous to that defined for dipolar structures in Eq. 2.4.

The wavefunctions of the molecular states  $|g\rangle, |a\rangle, |e\rangle$  are linear combinations of the three states. It is more convenient to define three new wavefunctions as basis set:

$$\left\{ |N\rangle, |Z^+\rangle = \frac{|Z_a\rangle + |Z_b\rangle}{\sqrt{2}}, |Z^-\rangle = \frac{|Z_a\rangle - |Z_b\rangle}{\sqrt{2}} \right\} \quad 2.13$$

Using these functions, the derived expressions for the three molecular wavefunctions  $|g\rangle, |a\rangle, |e\rangle$  are:

$$\begin{aligned} |g\rangle &= \cos^2 \frac{\theta}{2} |N\rangle + \sin^2 \frac{\theta}{2} |Z^+\rangle \\ |a\rangle &= |Z^-\rangle \\ |e\rangle &= -\sin^2 \frac{\theta}{2} |N\rangle + \cos^2 \frac{\theta}{2} |Z^+\rangle \end{aligned} \quad \cos \theta = \frac{V}{\sqrt{V^2 + 8t^2}} \quad 2.14$$

The ground and the excited state energies can also be calculated by diagonalizing the molecular hamiltonian:

$$\begin{aligned} E_{ag} &= \sqrt{2}t \sqrt{\frac{1 - MIX}{1 + MIX}} \\ E_{eg} &= \frac{2\sqrt{2}t}{\sqrt{1 - MIX^2}} \end{aligned} \quad MIX = -\cos \theta \quad 2.15$$

Also the transition dipoles can be written as function of the parameter  $MIX$ . The transition dipole  $\mu_{eg}$  is zero because of this transition is forbidden by OPA. The other dipoles  $\mu_{ag}$  and  $\mu_{ea}$  are both parallel to  $\mu_Z$ , the zwitterionic dipole moment. Their expressions are written below:

$$\begin{aligned} \mu_{ag} &= \mu_Z \sqrt{\frac{1 + MIX}{2}} \\ \mu_{ea} &= \mu_Z \sqrt{\frac{1 - MIX}{2}} \end{aligned} \quad 2.16$$

From the sum-over-states using three states, the third-order susceptibility is given by:

$$\chi^{(3)}(-\omega; \omega, -\omega, \omega) = 6 \frac{\mu_{ag}^2 \mu_{ea}^2}{(E_{ag} - \hbar\omega - i\hbar\gamma_{ag})^2 (E_{eg} - 2\hbar\omega - i\hbar\gamma_{eg})} \quad 2.17$$

In this expression,  $\hbar\gamma_{eg}$  and  $\hbar\gamma_{ag}$  correspond to the two-photon and one-photon excited-state line-widths.

Near two-photon resonance, the TPA cross-section for quadrupolar systems is:

$$\sigma_Q^{(2)}(\omega) \propto \frac{24\mu_{ag}^2 \mu_{eg}^2}{\hbar\gamma_{eg} (2E_{ag} - E_{eg})^2} = \frac{1}{\hbar\gamma_{eg}} \frac{3\mu_Z^4 (1 - MIX^2)^2}{4t^2 MIX^2} \quad 2.18$$

Also the  $\sigma_Q^{(2)}(\omega)$ , analogously to  $\sigma_D^{(2)}(\omega)$ , varies with  $\mu_Z^2/t^4$ . The dependence of  $\sigma_Q^{(2)}(\omega)$  with the parameter  $MIX$  is reported in Fig. 2.5.

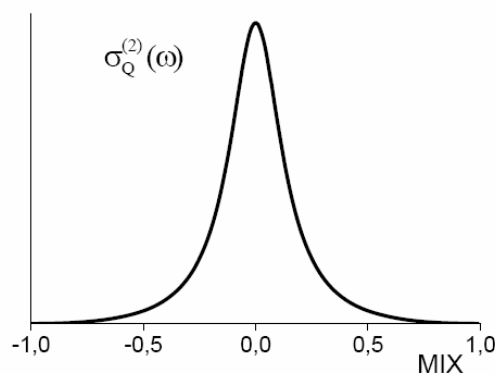


**Fig. 2.5:** Plot of the resonant TPA cross-section as function of  $MIX$  parameter for quadrupolar molecules

The optimal  $MIX$  value, in order to reach the maximum  $\sigma_Q^{(2)}(\omega)$  value, corresponds to  $MIX=0$ : this is, on the contrary, the value that cancels the TPA cross-section for dipolar push-pull molecules. So, the strategy used for the design of dipolar structures can be inadequate for quadrupolar molecules. Anyway, one strategy consists on choosing the best donor-acceptor groups in order to modify the value of the energy gap  $V$  and, by this way, to tune the  $MIX$  toward the optimal value. Another technique is the lengthening of the conjugation path. If for dipolar molecules there is only one way for lengthening of the CP, for quadrupolar systems there are several strategies. Besides lengthening of the CP along the D-D axis or the A-A axis, it is possible to move from 1D structures to two-dimensional systems, towards branched structures.

Using Eqs. 2.11 and 2.18, for the same value of  $MIX$ , the quadrupolar structures are characterized by values of TPA cross-sections that are one order-of-magnitude higher than one optimized push-pull dipolar chromophore.

## 2.3 Octupolar molecules

The multipolar and/or multibranching strategies can be a way for the improvement in NLO response with respect to dipolar and quadrupolar molecules.<sup>12-16</sup>

In Ref. 13, three structures, reported in Fig. 2.6, are theoretically and experimentally analyzed.

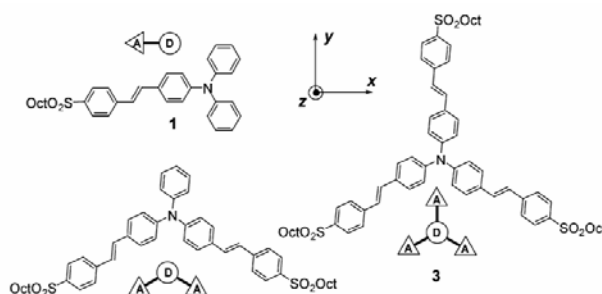


**Fig. 2.6:** Molecular structures of the series of dipolar (1), V-shaped (2) and octupolar (3) molecules (Ref. 13)

Using the Frenkel exciton model, we assume an electrostatic interaction between monomers  $V$  that is smaller than the transition energy. For the monomer 1, the lowest excited state is the one responsible of OPA and TPA spectra. For the branched structures 2 and 3, the lowest excitonic manifold is derived by the hamiltonian:

$$H = \hbar\omega_{eg} \sum_i^{2or3} B_i^+ B_i + V \sum_{i,j \neq i}^{2or3} B_j^+ B_i \quad 2.19$$

Here  $B_i^+$  ( $B_i$ ) is the excitonic creation (annihilation) operator on branch  $i$ . The energy diagrams of the three compounds are depicted below:

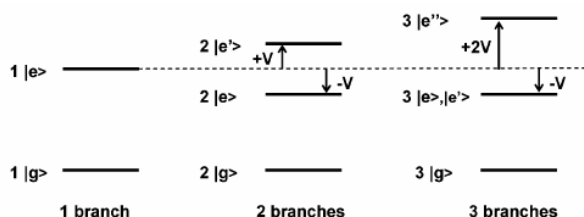


**Fig. 2.7:** Representation of the energy diagrams for one-, two- and three branches molecules

In particular, the three branches system possesses a  $C_3$  symmetry. This generates twofold degenerated excited state ( $|e\rangle$  and  $|e'\rangle$ ) which is both one- and two-photon allowed. The

second excited state  $|e''\rangle$  is allowed only by two-photon absorption. It is possible to use these ground and excited states in the SOS expression to obtain the formula of  $\sigma^{(2)}$ .

Calculations reveal that pronounced intramolecular charge transfer occurs within the chromophores after excitation. For symmetry reason, the octupolar specie undergoes a two-dimensional ICT from the trigonal core towards the branches.

From experimental data, the authors show an enhancement of the TPA response going from the monomer to the three branched structure. In particular, they underline the necessity of normalization of the  $\sigma^{(2)}$  peak values in order to directly confront the TPA response. Two normalization procedures are proposed, one is based on the molecular weight and the second on the number of branches. With the first method, the chromophores 2 and 3 show larger normalized TPA values than dipolar system in the whole spectral range. Analogous results are obtained within the second method. In this case the enhancement in respect to dipolar system is wavelength dependent, as depicted in Fig. 2.8.

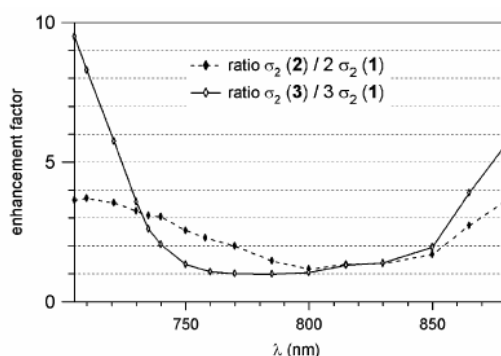


**Fig. 2.8:** Wavelength dependence of branching effect on TPA response

The  $\sigma^{(2)}$  for the octupolar compound is found to be 10 times larger than  $\sigma^{(2)}$  of dipolar system at the peak, revealing a cooperative enhancement. This is more pronounced towards the visible region (700 nm), where absorption of the monomer is low, and it is not true for the red-shifted absorption band of the octupolar compound.

This study shows that assembling the dipolar chromophores in a trigonal structure can be an efficient route for the enhancement of TPA.

In another paper<sup>17</sup>, the authors use the valence-bond three-charge-transfer (VB-3CT) model to describe the NLO properties of octupolar molecules. They demonstrate that the TPA cross-section increases as the donor or acceptor strength increases and is linearly proportional to the first hyperpolarizability. They do not show any direct comparison with

the dipolar structure in order to verify some enhancement effect from dipolar to octupolar structures.

Another class of octupolar molecules, recently studied, is the octupolar metal complexes.<sup>18-24</sup> Some examples of metal-organic octupolar complexes are reported below.

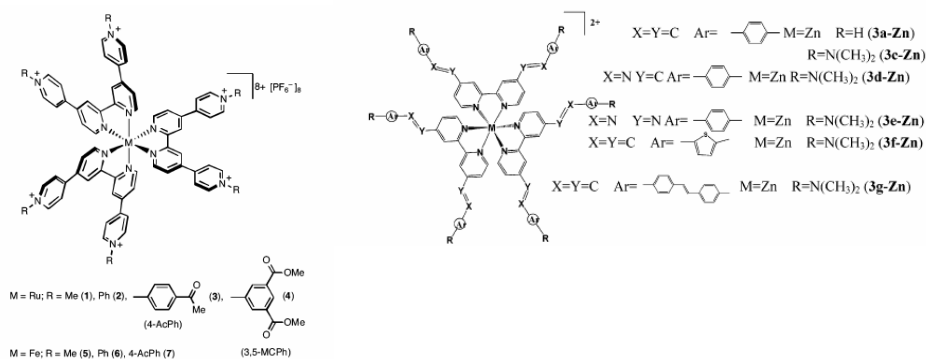


**Fig. 2.9:** Examples of metal octupolar structures

Metal ions can assemble organic ligands in a variety of multipolar structures showing interesting electronic and optical properties. In particular, the possibility of changing the central metal ion (from Zn(II), to Ru(II), Fe(II) and Ni(II)) and the nature of ligands permit the tuning of their properties. The metal has also the important property to act as a Lewis acid that induces a strong Intra-Ligand Charge-Transfer (ILCT) determining the absorption band in the visible region.

The coordination with some metals, such as Ru(II) and Fe(II), induces a second absorption band due to Metal-to-ligand Charge-Transfer (MLCT) process. It is not so clear which is the contribution of the MLCT to the NLO properties. Anyway, coordination chemistry can be a promising tool for the synthesis of efficient TPA structures.

## 2.4 Porphyrins and squaraine systems

Porphyrins<sup>25-29</sup> and squaraines are very likely candidates for TPA materials because of their highly conjugated and large  $\pi$ -system. They have potential for applications on the technological front, including optical limiting, optical switching, optical data processing and optoelectronic device fabrication.

However, the metal-free porphyrins have shown small  $\sigma^{(2)}$  for femtosecond excitation, one of the key design of TPA efficient porphyrins is to modify the porphyrin ring by

changing the metal in the center or by adding different D or A groups in the ring: this is generally possible without compromising the excellent chemical and thermal stability of the porphyrin ring. Another strategy can be the synthesis of aggregates or oligomers.<sup>30,31</sup>

The linear spectrum of the porphyrins is generally characterized by a low energy band (*Soret band*) and a band at higher energies that is called *B band*. It is shown<sup>25</sup> that the  $\sigma^{(2)}$  values near the *Soret band* ( $10\text{-}10^2$  GM) are larger than near *Q band* ( $<10$  GM). The TPA cross section increases monotonically towards higher frequencies than the *B band*. This enhancement is described assuming that, in the 710-810 nm excitation region, the TPA is nearly resonant with the first pure electronic Q(0-0) one-photon transition. The TPA becomes a sequential process which involves three states: the initial, the final and the intermediate levels. If the energy of the intermediate level is closer to the photon energy, the resonance enhancement is stronger.<sup>32,33</sup>

Recently, some asymmetrically substituted porphyrins have been studied: these molecules show a very strong TPA response in the range 810-830 nm ( $\sigma^{(2)} \sim 10^3$  GM).<sup>34</sup>

Besides, the NLO response of some squaraines has been studied.<sup>35-37</sup> These molecules are characterized by a large, but spectrally narrow, electronic oscillator strength in the Visible-NIR region. They are cyanine-like molecules, but, instead of being linear systems, they possess a more two-dimensional character in part due to the presence of the conjugated ring along the chain. From theoretical calculations, it is found that the squaraine molecules are best described by three-states model. This is in agreement with experimental data, which shows very large  $\sigma^{(2)}$  ( $\sim 8600$  GM<sup>37</sup>) for a squaraine with an acceptor group in the conjugated chain due to the significant resonance enhancement for both the intermediate and the final states just below the linear absorption edge.

## 2.5 Semiconductor quantum dots

In last years inorganic semiconductor quantum dots (CdSe, CdS, etc.) have received great attention for their important properties in optics. These systems are characterized by 3D-nanoscale dimensions ( $R < 10$  nm), corresponding to a strong confinement effect well defined when their dimensions are comparable or below the exciton Bohr radius. As the QD size decreases, the energy gap between the conduction and the valence bands increases, leading in particular in a blue-shift of the emission band.<sup>38</sup> In particular, the great possibility to tune the wavelength emission, together with their high fluorescence

quantum efficiency, can be largely exploited in photonic and optoelectronic technological applications.

In this context, some considerations only about their NLO properties are presented even if a complete understanding of the NLO processes is not already achieved. Other important properties will be introduced in chapter 8.

The third-order nonlinearity of various semiconductor QDs has been investigated and it has been found that the surface quality plays an important role in determining their optical properties. In particular, it has been demonstrated that an efficient surface capping, especially through the growth of wider band-gap inorganic shell in a core/shell structure, can largely improve the nonlinear optical absorption.<sup>39,40</sup> Going from bulk materials to quantum confinement dimensions in QDs, the nonlinear absorption becomes more intense. The enhancement of the third-order nonlinearity characterizing the QDs can be attributed to the concentration of exciton oscillator strength. In fact, as the particle size decreases, the series of transitions at slightly different energies in the bulk are compressed by quantum confinement effect into a single and intense transition in a quantum dot. Therefore, the oscillator strength of the QD is concentrated into few transitions. The two-photon absorption coefficient is by this way enhanced when the size is less than the bulk Bohr diameter.<sup>41,42</sup> For ZnS the TPA cross-section of nm-scale QDs is five times higher than the bulk sample.<sup>43</sup>

It is experimentally and theoretically demonstrated that, for CdSe and CdTe QDs with dimensions near the exciton size, the TPA cross-section values decrease with a reduction in the QD size even when they are normalized by the volume.<sup>44,45</sup>

This new class of materials is very promising for their high TPA efficiency in respect of the organic media.<sup>46</sup>

## REFERENCES

- <sup>1</sup> Barzoukas, M. et al. *Chem. Phys. Lett.*, 1996, 257, 531-537
- <sup>2</sup> Meyers, F. et al. *J. Am. Chem. Soc.*, 1994, 116, 110703-10714
- <sup>3</sup> Marder, S. et al. *Science*, 1994, 265, 632-635
- <sup>4</sup> Kogej, K. et al. *Chem. Phys. Lett.*, 1998, 298, 1-6
- <sup>5</sup> Gorman, C.B. and Marder, S. *Proc. Natl. Acad. Sci. U.S.A.*, 1993, 90, 11297-11301
- <sup>6</sup> Bonin, K.D. and McIlrath, T.J. *J. Opt. Soc. Am. B*, 1984, 1, 52-55
- <sup>7</sup> Sharma, N. et al. *Spect. Chim. Acta A*, 2007, 66, 171-176
- <sup>8</sup> Thompson, W. H. *J. Phys. Chem. A*, 1998, 102, 7712-7722
- <sup>9</sup> Barzoukas, M. and Blanchard-Desce, M. *J. Chem. Phys.*, 2000, 113, 3951-3959
- <sup>10</sup> Ventelon, L. et al. *Synth. Metals*, 2002, 127, 17-21
- <sup>11</sup> Hahn, S. et al. *J. Phys. Chem. B*, 1999, 103, 8221-8229
- <sup>12</sup> Lee, W-H et al. *J. Am. Chem. Soc.*, 2001, 123, 10658-10667
- <sup>13</sup> Katan, C. et al. *J. Phys. Chem. A*, 2005, 109, 3024-3037
- <sup>14</sup> Ray, P. C. et al. *J. Phys. Chem. A*, 2005, 109, 6689-6696
- <sup>15</sup> Blanchard-Desce, M. et al. *Opt. Mater.*, 1999, 12, 333-338
- <sup>16</sup> Brunel, J. et al. *Chem. Mater.*, 2003, 15, 4139-4148
- <sup>17</sup> Lee, W-H et al. *J. Am. Chem. Soc.*, 2001, 123, 10658-10667
- <sup>18</sup> Maury, O and Le Bozec, H. *Acc. of Chem. Res.*, 2005, 38, 691-704
- <sup>19</sup> Mazzucato, S. et al. *Phys. Chem. Chem. Phys.*, 2007, 9, 2999-3005
- <sup>20</sup> Liu, X.-J. et al. *J. of Chem. Phys.*, 2004, 120, 11493-11499
- <sup>21</sup> Le Bozec, H. et al. *Synth. Met.*, 2001, 124, 185-189
- <sup>22</sup> Maury, O. et al. *Chem. Eur.*, 2004, 10, 4454-4466
- <sup>23</sup> Zhang, B.-X. et al. *J. Phys. Chem. A*, 2007, 111, 1328-1338
- <sup>24</sup> Coe, B.J. et al. *J. Phys. Chem. A*, 2007, 111, 472-478
- <sup>25</sup> Drobizhev, M. et al. *Chem. Phys. Lett.*, 2002, 355, 175-182
- <sup>26</sup> Kruk, M. et al. *J. of Lumin.*, 2003, 105, 45-55
- <sup>27</sup> Narayana Rao, D. *Opt. Mater.*, 2002, 21, 45-49
- <sup>28</sup> Drobizhev, M. et al. *J. Phys. Chem.*, 2006, 110, 9802-9814
- <sup>29</sup> Rebane, A. et al. *Proc. SPIE, Linear and nonlinear Optics of organic materials VII*, 2007, 6653, 665307
- <sup>30</sup> Kim, D. Y. et al. *J. Phys. Chem. A*, 2005, 109, 2996-2999
- <sup>31</sup> Collini, E. et al. *J. Phys. Chem. B*, 2005, 109, 2-5
- <sup>32</sup> Rebane, A. et al. *Proc. of SPIE*, 2007, 6653, 665307-1-8
- <sup>33</sup> Rao, S. V. et al. *Opt. Comm.*, 2000, 182, 255-264
- <sup>34</sup> Drobizhev, M. et al. *J. Phys. Chem. B*, 2006, 110, 9802-9814
- <sup>35</sup> Schrerer, D. et al. *Chem. Phys.*, 2002, 279, 179-207
- <sup>36</sup> Andrews, H.J. et al. *Proc. of SPIE*, 1998, 3473, 68-78
- <sup>37</sup> Fu, J. et al. *J. Opt. Soc. Am. B*, 2007, 24, 67-76
- <sup>38</sup> *Semiconductor and Metal nanocrystals*, 2004, Ed. Klimov V. I., Marcel Dekker Inc.
- <sup>39</sup> Lad, A.D. et al. *Appl. Phys. Lett.*, 2007, 90, 133113-1-3
- <sup>40</sup> Wang, X. et al. *J. Phys. Chem. B*, 2006, 110, 1566-1570
- <sup>41</sup> Gondar, J.L. et al. *Braz. J. of Physics*, 2006, 36, 960-963
- <sup>42</sup> He, J. et al. *J. of Appl. Phys.*, 2004, 95, 6381-6386
- <sup>43</sup> Nikesh, V.V. *Appl. Phys. Lett.*, 2004, 84, 4602-4604
- <sup>44</sup> Padhila, L.A. et al. *Opt. Exp.*, 2005, 13, 6460-6467
- <sup>45</sup> Padhila, L.A. et al. *Phys. Rev. B.*, 2007, 75, 075325-1-8
- <sup>46</sup> Larson, D. et al. *Science*, 2003, 300, 1433-1436



## CHAPTER 3

# The Sol-Gel process: a useful tool for the preparation of solid-state devices

In many cases of practical use of nonlinear optical active materials, the preparation of solid-state devices is one of the major requirements. Therefore, the maintenance of the optical properties of the dyes, in going from solution to solid materials, is indispensable. The synthesis and the characterization of the optimal guest-host system play an important role in the design of a material possessing the functional properties required by the device they are made for. In this context, the *sol-gel* chemistry is an important technique for the synthesis of solid-state materials usable in optics and photonics applications. This synthesis combines the great flexibility of choice in the experimental parameters (precursors, synthetic routes, catalysts,...) to the possibility of obtaining samples with different shapes (films or bulks, with various thicknesses, or powders). Besides, relative low temperatures, employed in sol-gel synthesis, prevent the damaging of the chromophores (often organic species) embedded in the material.

The sol-gel process was born as a method for the synthesis of pure inorganic powders of Ti-, Si-, Al-, Zr-oxides. One of the first studies was done by Stober et al.<sup>1</sup> which showed that, using ammonia as a catalyst for the Tetraethoxysilane hydrolysis reaction, it was possible to control both the morphology and the size of the final silica powders. Successively, this technique has been largely exploited for the realization of films for a great variety of applications and functionalities: in microelectronics<sup>2,3,4</sup>, electrochromic

films for smart windows and displays<sup>5-8</sup>, semiconductor or superconductor films, materials for catalysis<sup>9</sup> and so on. Nowadays, the intense research of new precursors makes the sol-gel process an important technique in several kinds of applications where the soft-chemistry is required.

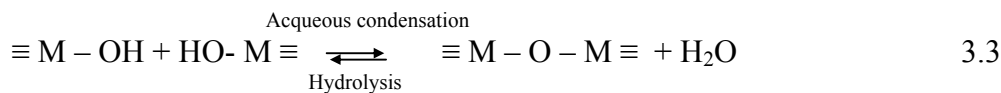
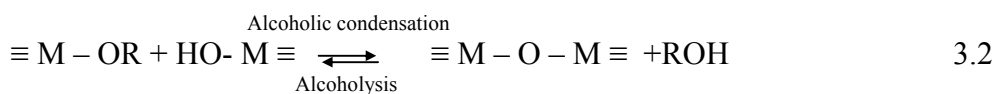
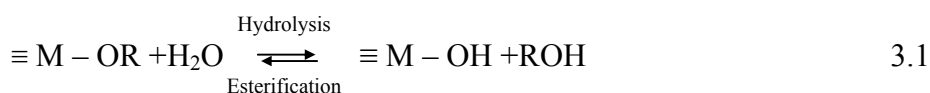
The importance of these materials consists on the great opportunity to have a synergic effect due to the close coexistence of an organic network and an inorganic one, which are mixed at a nanometric scale. The advantages of the organically modified materials, with respect to those obtained with the classic inorganic sol-gel recipes, are the higher mechanical and optical performance, with low porosity, no sensitivity to the humidity and suitability for obtaining thick films without cracking.

In the first part of this chapter some details about the steps characterizing the sol-gel method will be presented, in order to emphasize the key features that influence the sol-gel process.

Successively, more attention will be dedicated to the use of hybrid organic-inorganic precursors for the preparation of optical materials. Some details about their reactivity will be described and, in the last part, some applications will be analyzed.

### 3.1 Principles of sol-gel process

The main reactions that regulate a sol-gel process are:<sup>10,11</sup>



In these expressions, R is generally an alkyl group ( $\text{C}_x\text{H}_{2x-1}$ ). The main difference is between the alkoxy silane precursors (where M is the silicon metal) and the transition (Zr-, Ti-, V-,...) and semimetal (B-, Al-,...) ones.

One, and the most used, of the silicon alkoxides is the tetraethoxysilane (TEOS) where the substituent is an ethoxy group:

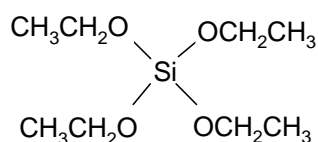


**Fig. 3.1:** Molecular structure of TEOS

Changing the length of the chain in -OR can induce some differences in the reactivity of the silane, as it will be described later.

The second class of precursors can be generally distinguished from the silicates by the greater chemical reactivity resulting from the lower electronegativity of the transition metal.<sup>12,13</sup> These metals exhibit several coordination states, allowing a spontaneous coordination expansion upon reaction with water or other nucleophilic reagents.

In the hydrolysis and condensation reactions reported above, the  $\text{HO}^{\delta-}$  acts as nucleophilic group, which attacks the positive charged metal. Hence, the reactivity towards the hydrolysis increases when the electronegativity decreases or, alternatively, when the partial charge increases. This effect is enlightened by the data reported in table 3.I.

Alkoxide	Electronegativity $\chi$	Part. positive charge $\delta_M$	Ionic Radius R(Å)	Coordination number N
Si(OPr) <sub>4</sub>	1.74	+0.37	0.40	4
Ti(OPr) <sub>4</sub>	1.32	+0.60	0.64	6
Zr(OPr) <sub>4</sub>	1.29	+0.64	0.87	7
Ce(OPr) <sub>4</sub>	1.17	+0.75	1.02	8

**Table 3.I:** Electronegativity, partial positive charge on the metal, ionic radius and coordination number data of the metals in some alkoxydes precursors

These data explain the low reactivity of Si-alkoxydes with respect to the transition metal precursors. In the first case it is often necessary to use some catalysts to increase the reaction rate and, on the contrary, some chelating agents are indispensable to stabilize the transition metal precursors. Common complexing agents are the acetic acid<sup>14,15</sup> or diketones, which exhibit keto-enol tautomerization, such as acetylacetone and acetoacetate.<sup>16,17</sup> These bidentate molecules reduce some of the active functionalities of the tetrafunctional precursors.

### 3.1.1 First step: Hydrolysis

In these sections, we will examine only the features of the reactions for silicate precursors.

During the first step of the process, the nucleophilic oxygen, contained in water, attacks the silicon atom and the alkoxides groups (OR) are replaced by hydroxyl groups (OH) through an  $S_N2$  mechanism. Hydrolysis is facilitated in the presence of homogenizing agent, generally an alcohol, which permits the miscibility of alkoxide and water. It should be emphasized that the addition of solvents may promote esterification and depolymerization reactions, avoiding the incoming sol-gel reactions.

The hydrolysis is most rapid in the presence of catalysts, especially if the alkoxide groups are long. Many factors influence the hydrolysis kinetics, such as the nature and the concentration of the catalyst (acid, base), the nature of the solvent, the type of alkoxide and the temperature.

The most used catalysts are inorganic acids (HCl, HNO<sub>3</sub>, H<sub>2</sub>SO<sub>4</sub>), basic species (NH<sub>4</sub>OH, NaOH) or Lewis basis (n-Bu<sub>4</sub>NF, NaF). In acidic conditions, H<sup>+</sup> attacks the alkoxy group and, besides, the metal is more positive and can be attacked by water:

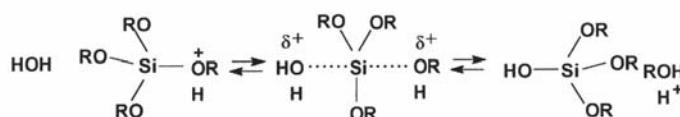


Fig. 3.2: Hydrolysis mechanism in acidic condition

The hydrolysis rate constant in this case increases when the lateral substituents reduce the steric (spatial) hindrance and when they stabilize the partial positive charge on the central metal. The basicity scale for the substituents is: (SiO<sup>-</sup>) < (HO<sup>-</sup>) < (RO<sup>-</sup>) < (R<sup>-</sup>). Hence, the presence of an alkoxide RO<sup>-</sup> group increases the electronic density on the Si more than a SiO<sup>-</sup> group, which is formed by condensation reactions. The hydrolysis rate diminishes after the first stages in acid-catalyzed sol, but the contrary occurs in basic conditions.

In basic conditions, the OH<sup>-</sup> groups attack the Si atom and they can replace the alkoxy groups in a second step. The more negative substituents stabilize the partially charged intermediate species, favouring the hydrolysis. The presence of the SiO<sup>-</sup>, which is a good electron acceptor, speeds up the hydrolysis after the first steps. The mechanism of the hydrolysis in basic conditions is depicted as:

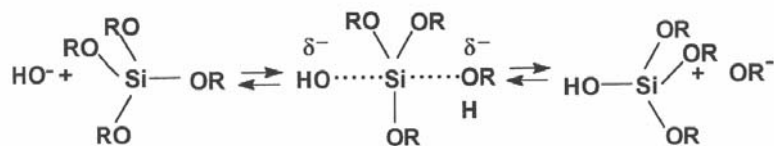


Fig. 3.3: Hydrolysis mechanism in basic condition

### 3.1.2 Second step: Condensation

The second step of the process is based on the condensation reaction towards the formation of water or alcohol molecules. Also this reaction is largely influenced by the type of catalyst used.

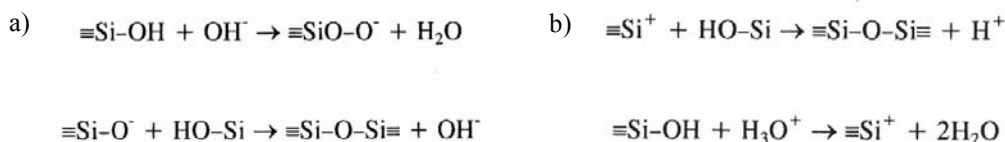


Fig. 3.4: Condensation mechanism in basic condition (a) and in acidic condition (b)

In basic condition, the condensation rate increases with the pH of the solution. The condensation occurs between a deprotonated silanol (more condensed and acid) and a neutral and less condensed specie, as shown in Fig. 3.4-a. The presence of SiO<sup>-</sup> groups, which stabilize partially negative-charged intermediate specie, promotes a rapid condensation process. This imposes that the condensation reactions rapidly occur and the gelation time decreases. In acidic conditions, on the contrary, the substituents, that stabilize a positive intermediate, promote a rapid condensation reaction.

It is possible to investigate the evolution of the *sol*, which is a dispersion of colloidal particles with diameters of 1-100 nm, towards the formation of a *gel*, which is an interconnected and rigid network with pores of submicrometric dimensions and polymeric chains whose average length is greater than a  $\mu\text{m}$ . The evolution can be monitored by X-ray small-angle scattering, neutron scattering and light scattering.<sup>11</sup>

These analyses show a different microstructure of the particles generated in acidic and in basic conditions. In the first case, the chains are mostly linear and less condensed while, in the second case, the chains become more branched, with a high degree of cross-linking. This is due to the fast mechanism of basic condensation that already starts in the first stages of the sol-gel process.

Sol-gel particle growth has been modelled by using fractal concepts.<sup>10,11,12</sup> The nature of fractals requires that they are invariant with scale and their density decreases with size. Fractal objects are quantified by their fractal dimension,  $d_f$ , which is related to the mass,  $M$ , and their radius,  $R$ , by the expression:

$$M \propto R^{d_f} \quad 3.4$$

Fig. 3.5 shows objects with increasing fractal dimension. For linear-like structures:  $1 < d_f < 2$  (as shown in Fig. 3.5-A,B). Fractally rough structures have a mass fractal dimension  $2 < d_f < 3$  (as shown in Fig. 3.5-C). Finally, uniform nonfractal objects have a fractal dimension  $d_f = 3$  (Fig. 3.5-D).

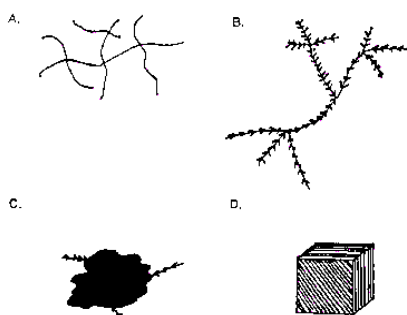


**Fig. 3.5:** Fractal objects: (A,B) linear structures,  $1 < d_f < 2$ ; (C) fractally rough structures,  $2 < d_f < 3$ ; (D) solid structure,  $d_f = 3$ . (Ref. 11)

### 3.1.3 Third step: Gelification

As the sol particles grow and collide, condensation occurs and macroparticles form. The sol becomes a gel when it forms a tridimensional network which can support a stress elastically. This is typically defined as the gelation point or gelation time,  $t_{gel}$ . There is no activation energy that can be measured and the point where the sol changes from a viscous fluid to an elastic gel can not be precisely defined. The change is gradual as more and more particles become interconnected.

One of the most precise methods to measure  $t_{gel}$  consists of the measurement of the viscoelastic response of the gel as a function of shear rate. The shear modulus is a complex quantity expressed by the relation:

$$G = G'(\omega) + i G''(\omega) \quad 3.5$$

Where  $G'$  is the storage modulus arising from the elastic component of the sol-gel and  $G''$  is the loss modulus coming from the viscous component.

The rapid increase in the storage modulus near  $t_{gel}$  is consistent with the concept that the interconnection of the particles becomes sufficient to support a load elastically.

There is at least one indication that the gelation time is not only an intrinsic property of the sol, but depends on many factors, such as the effects of the alkoxy groups and the solvent, the type and the concentration of the catalyst, the temperature, the quantity of water, the size of the container. It is often difficult to model the global effect of these factors on the determination of the gelation time. The considerations generally derive from experimental evidences. For example, it has been seen that long molecules of solvent and large substituent groups increase the gelation time. Besides, the amount of water for hydrolysis has a dramatic influence on gelation time, as shown in Fig. 3.6.

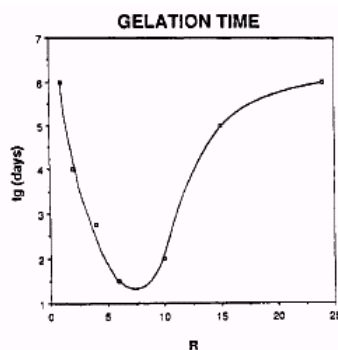


**Fig. 3.6:** Effect of the ratio  $R=H_2O/Si(OR)_4$  on the gelation time (expressed in days)

For low water contents, generally an increase of the amount of hydrolysis water decreases the gelation time, although there is a dilution effect. For higher water contents, the gelation time increases with the quantity of water. The location of the minimum in the curve  $t_{gel}$  vs  $R$  depends on the experimental conditions, such as the nature of the chemicals, the catalyst, and the temperature.

### 3.1.4 Fourth step: Drying

The gel is a tridimensional network of oxide where the liquid fills the pores. This liquid can be extracted above the critical temperature ( $T_c$ ) and critical pressure ( $P_c$ ) of the liquid. Under these conditions, there is no longer any distinction between the liquid and vapor phases and, by this way, there is no liquid-vapor interface and no capillary pressure. This process, called "supercritical drying", prevents the material from cracking during the shrinkage.<sup>18</sup> The final sample is called *aerogel*.

More commonly, the liquid evaporates upon thermal treatment, towards a formation of a *xerogel* when the pores become empty. The specific surface area of the gel is large ( $> 400 \text{ m}^2/\text{g}$ ) and the dimensions of the pores are small ( $< 10\text{nm}$ ).

In the first phase of drying, the decrease in volume of the gel is equal to the volume of the liquid lost by evaporation. The network modifies towards the formation of pores with a superficial meniscus characterized by a radius  $r$ . The difference between the pressures generates a capillary force that is defined by:  $P = -2\gamma_{L-V}/r$ , where  $\gamma_{L-V}$  is the difference in the liquid-vapor interfacial energies.

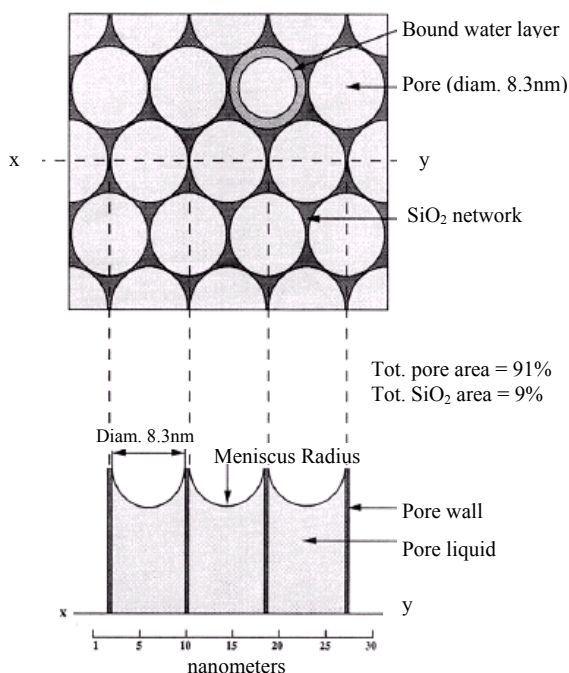


**Fig. 3.7:** Representation of the gel surface during the 'constant rate period' (Ref. 11)

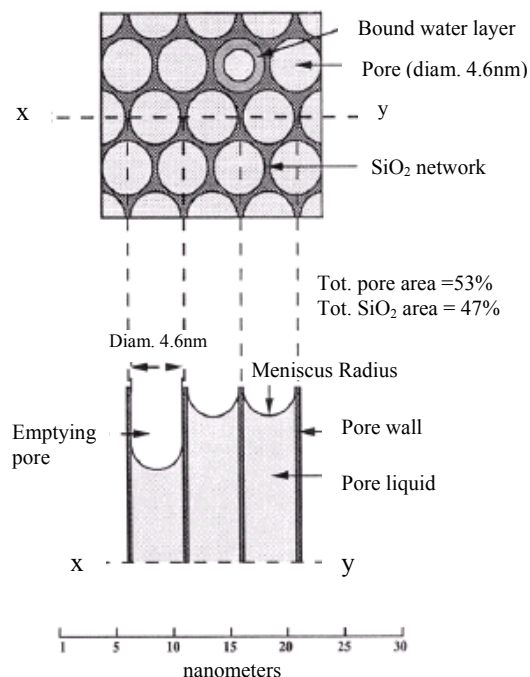


**Fig. 3.8:** Representation of the gel surface at the critical point (Ref. 11)

The capillary forces increase when the meniscus radius decreases. The first stage of drying is called "the constant rate period" because the rate of evaporation per unit area of the drying surface is independent of time.

This process continues until the critical point (see Fig. 3.8): at this point the matrix becomes rigid and resists toward a successive shrinkage. The meniscus radius becomes equal to the pore radius and is able to penetrate the bulk. In the "falling rate period" the liquid evaporates, firstly, through partially empty pores, and after, by diffusion of its vapour to the surface.

This is a critical step for the process because the material can undergo fracture. A distribution of pore sizes exists in these materials, and some pores can empty before others, generating a pressure gradient between adjacent pores with different diameters. The modulus of the gel is very high and the compressive stress is in the order of 100 MPa. The pores that empty first (at the larger end of the distribution) stop shrinking and can

only passively shrink under the influence of nearby saturated pores. The possibility of cracking at this point is great, due to the high stresses and low strain tolerance of the material.

There are three main possibilities of avoiding the cracking of the sol-gel material. One consists on the use of supercritical drying process, as mentioned before. The second is the use of surfactants or DCCA (*drying control chemical additives*)<sup>19-23</sup> which, added to the solution, reduce the interfacial energy and thereby decrease the capillary stress. The last one involves the use of hybrid organic-inorganic precursors which will be described later.

### 3.1.5 Fifth step: Dehydration and densification

An important step in the sol-gel synthesis is the densification of the material, involving the removal of surface silanol (Si-OH) bonds from the pore network. Porous materials, made by sol-gel method, are optically transparent with interconnected porosity and possessing sufficient strength to be used as unique optical components. This is possible only if the material is thermally and chemically stabilized: the pores become unable to rehydrate. The free water within the ultraporous gel structure (i.e., physisorbed water) can be removed with a thermal treatment at about 170°C. The dehydration is completely reversible, up to about 400 °C. Only at higher temperatures, the dehydration process is irreversible as a result of the shrinkage and sintering across pores. The densification is complete between 850 and 1000°C where also the single hydroxyl groups condensate.

## 3.2 Organic-inorganic hybrid sol-gel precursors

The synthesis of organic-inorganic hybrid materials, called also ORMOCERS or ORMOSIL, is an innovative and more attractive method useful in many industrial and technological applications.

The nature of the interface between the organic component and the inorganic counterpart divides these materials into two distinct classes. In *class I*, organic and inorganic components are embedded and connected only by weak bonds (hydrogen bonds, Van der Waals or ionic bonds). In *class II*, the two phases are linked together through strong chemical bonds (covalent or ionic-covalent bonds).

The most prominent examples representing class I are organic dyes or biomolecules incorporated in porous sol-gel matrices.<sup>24</sup> The guest molecules are physically dissolved

together with the precursors of the inorganic host (e.g., TEOS or TMOS) or introduced to the sol state. They become entrapped in the gel or xerogel, resulting from condensation and drying of the mixture. In these cases, sol-gel based low temperature processing is a good way to combine the unique optical or catalytic properties of organic constituents with the inertness and transparency of a widely inorganic environment. Sol-gel biosensors<sup>25,26</sup> and active laser devices<sup>27,28,29</sup> have been developed by this approach.

The most studied strategy to construct *class II* hybrid materials consists of using compounds where the organic and the inorganic parts are already linked together by strong bonds. **Organically modified metal alkoxides** are hybrid molecular precursors used for this purpose. The general formula of these systems is given by  $R'_nSi(OR)_{4-n}$  with  $n=1,2,3$ , and R can be alkyl, methyl, etc.

In most sol-gel conditions, the Si-C bond remains stable towards hydrolysis and R' group introduces new properties to the inorganic network, such as flexibility, hydrophobicity, refractive index modification, optical response, etc.

R' can be an organofunctional group. If it is a simple nonhydrolyzable organic group (methyl, alkyl, phenyl,...), it will have a **network modifying effect**. If R' can react with itself (R' contains a vinyl, a methacryl or an epoxy group or additional polymerizable monomers), it acts as a **network former**.<sup>30,31</sup>

Some examples of organo-alkoxy-silanes and metal-alkoxides acting as network formers or network modifiers are reported below.

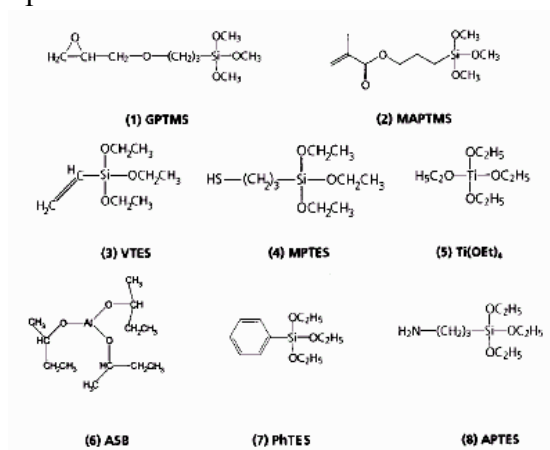


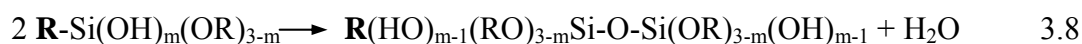
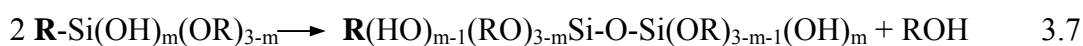
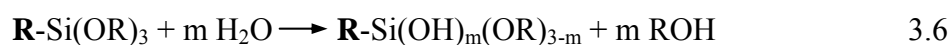
**Fig. 3.8:** Organo-alkoxy-silanes and metal alkoxides serving as precursors for sol-gel-derived (hybrid) materials. (Ref. 31)

If R' is a network modifier, it also decrease the inorganic crosslinking due to the partial reduction of reactivity around the silicon atom. This allows obtaining sample with high

densification degree at low temperatures, much lower than the densification temperatures of the inorganic counterpart. In this case, the organic chains fill the pores between the inorganic oxide chains, avoiding formation of cracks during the drying stage.<sup>32,33</sup> The hybrid materials allow also the preparation of monolith samples.

### 3.3 Reactivity of hybrid precursors

The reactions of the sol-gel process based on organically modified precursors are the same already indicated for the inorganic sol-gel synthesis. They are reported below.



Reaction 3.6 is relative to the hydrolysis which involves only the alkoxides substituents, while the R group is hydrolytically stable. The other reactions are relative to the inorganic condensation towards the formation of clusters with different dimensions depending on the condensation degree. The organic group remains inert to these reactions, but, acting as network modifier, it will undergo parallel reactions related to its type of reactivity.

Generally, trifunctional alkoxy-silanes and metal alkoxides are efficient crosslinkers conferring to the materials a high Young's Modulus ( $E > 10$  GPa) values and high, or not measurable, transition temperature  $T_g$ . Difunctional precursors generate linear and cyclic oligomers behaving as hybrid elastomers with low Young's Modulus and low  $T_g$ . Meanwhile a lot of modified alkoxides are commercially available and it is therefore possible to choose the best mixture of these precursors to obtain materials with mechanical and functional properties tunable between those of polymers and glasses.

Also the sol-gel synthesis using alkoxy-silanes precursors needs catalyst for hydrolysis and condensation. The rate constant of acid-catalyzed hydrolysis increases when the number of organic substituents, which stabilize the positive charges on the metal, is low. The rate constant of hydrolysis of TEOS is three times lower than that of DMDES (dimethyl-diethoxy-silane). The contrary occurs in basic solutions.

Often, the inorganic condensation and the organic polymerization are antagonist because the first constitutes a steric hindrance for the second one and viceversa. Hence, the final material can possess some residual internal stresses, intrinsic defects or residual silanol

groups not condensed. Residual hydroxyls are dangerous if the material must be used in photonic or optical waveguides application, while the Si-OH contributes to the luminescence quenching of rare-earth-metal ions incorporated in hybrids.<sup>34-38</sup>

If the hybrid system is not built up from nanocrystalline components, the intricate mixture of inorganic and organic phases in most cases leads to amorphous materials. Therefore, X-ray or neutron scattering methods, which are of major importance to study the size and short-range order of the inorganic moieties present, are less applicable. Other techniques, like multinuclear NMR or FTIR spectroscopy and Raman scattering are important tools to investigate the chemical and structural background of sol-gel-based hybrid materials. This is also important to correlate the features of the microstructure to the synthetic parameters.

### 3.4 Two examples of network modifiers: 3-Glycidoxypropyl-trimethoxysilane (GPTMS) and 3-methacryloxypropyl-trimethoxysilane (MPTMS)

In this paragraph, we will focus on the properties of two hybrid precursors which have been largely exploited in many applications: the 3-Glycidoxypropyl-trimethoxysilane (GPTMS) and the 3-methacryloxypropyl-trimethoxysilane (MPTMS). Both of them are trifunctional precursors.

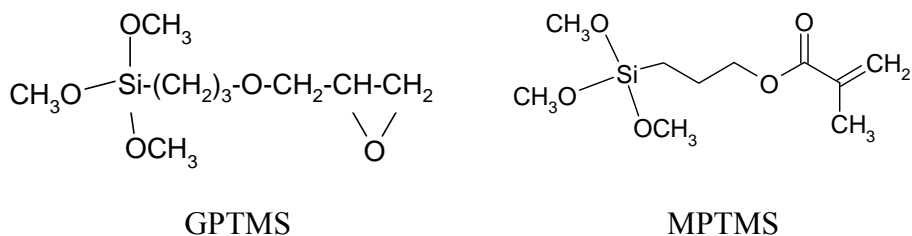


**Fig. 3.9:** Molecular structures of GPTMS (on the left) and MPTMS (on the right)

Organic group of GPTMS, containing an epoxide ring, can be crosslinked to form a poly(ethylene oxide) chain. The density of hybrid materials with the polymerizable epoxide group of the GPTMS is higher than that with the organically modified alkoxides whose organic groups are network modifiers.

The types of reactions that the epoxy group can undergo are represented in Fig. 3.10.

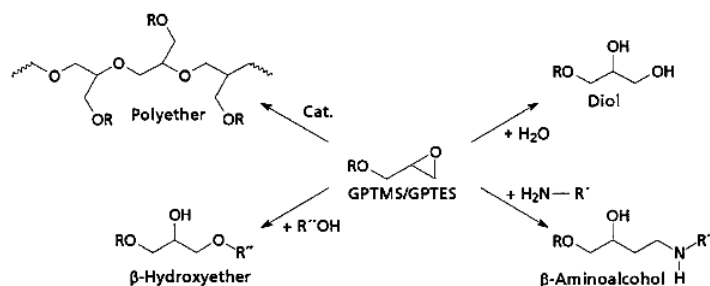


**Fig. 3.10:** Possible reaction pathways of Epoxy groups present in GPTMS (Ref. 31)

The epoxy group can undergo hydrolysis or alcoholysis to form the corresponding diol or  $\beta$ -hydroxy ethers or polyaddition reactions to form polyether linkages.

The polymerisation, that is the more useful mechanism, can be obtained by several routes, for instance by UV irradiation<sup>39</sup>, by adding a thermal initiator<sup>40</sup> or by using a proper catalyst in the synthesis. The most common of these catalysts are Lewis acids, such as zirconium, titanium and aluminium alkoxides. They catalyse the epoxy ring and, at the same time, are part of the inorganic network.<sup>41</sup>

Some references<sup>42,43</sup> in the literature compare the catalytic effect of the metal alkoxides on the ring cleavage efficiency, even if it is often difficult to operate with the same synthetic conditions in order to isolate only the effect of the catalysts. From the results of the <sup>13</sup>C-NMR experiments it is possible to evaluate the residual unopened epoxy ring, using different metal alkoxides and varying their concentrations. The authors<sup>42</sup> show that the maximum in ring-opening and condensation degree is found in hybrid sols and gels with 10% mole metal alkoxides. At this concentration, the activity of the metal alkoxides increases in the order:



Also the high catalytic efficiency of aluminum butoxyethoxide and boron trifluoride diethyl etherate ( $\text{BF}_3\text{OEt}_2$ ) is shown.<sup>43,44</sup> In particular, in Ref. 44 it is found that the  $\text{BF}_3\text{OEt}_2$  seems to have the highest catalytic efficiency in comparison with the other commonly used catalysts: 1-methylimidazole (MI),  $\text{Zr}(\text{O}^t\text{Bu})_4$ , and HCl. Longer reaction times or higher temperatures are generally required, especially for MI acting as base catalyst and polymerization initiator for the epoxide above 180 °C.<sup>45,46</sup>

The second hybrid precursor MPTMS has a methacrylic group which is available for the polymerization. The process can be activated by thermal decomposition of an initiator in

two radical species that attack the methacrylic double bond. Some examples of thermal initiators are the benzoyl peroxide (BPO) or the dicumyl peroxide (DCP).<sup>47</sup>

The polymerization of the methacrylic unit can be achieved also by UV or visible irradiation in the presence of a photoinitiator (photopolymerization). The photopolymerization is useful when organic dyes are present in the sample and they can not withstand the high temperatures necessary for the thermally activated process.

The photoinitiators that are commonly used are radical or cationic. The radical polymerization is the most used and involves as photoinitiators Irgacure 184<sup>48</sup>, Irgacure 2959<sup>49</sup> or Irgacure 369<sup>50</sup>. They belong to Norrish Type I class<sup>51</sup> of photoinitiators that form initiating radicals of the polymerization upon a direct photofragmentation induced by the light absorption. The radicals produced upon fragmentation can induce polymerization of the acrylate groups in MPTMS. Also the diaryliodonium and triarylsulfonium salts are employed as cationic photoinitiators for acrylate polymerization.<sup>52</sup>

Since an organic network is formed in the matrix of the primarily formed inorganic network, understanding the formation of the silicate backbone was of first importance to ensure the creation of crack free thick films through efficient polymerization. This was achieved by <sup>29</sup>Si NMR investigation of the inorganic network formation, as preliminary study for the further realization of optical waveguide devices using MPTMS as photopatternable material.<sup>53</sup>

### **3.5 Applications of hybrid organic-inorganic materials**

In the previous paragraphs we have presented only some highlights about the large number of features characterizing hybrid materials. It is clear that these properties can be widely employed for academic and industrial applications.

The main topics in which these materials are used are<sup>30,31,54-56</sup>:

- \* Optics and photonics
- \* Protective layers towards chemical and mechanical attacks
- \* Barrier systems
- \* Decorative coatings
- \* Bioactive sol-gel materials
- \* Microelectronics devices

- \* Photovoltaic cell applications
- \* Sensors
- \* Dental and cosmetics applications

Organics molecules, oligomers and biocomponents can be easily incorporated into hybrid siloxane-oxide matrices through physical or chemical links, thanks to the chemical similarity with the organic component of the host.

Concerning scratch and abrasion resistance applications, numerous ORMOCER are employed in commercial products. In general, these protective materials for metal surfaces are based on epoxy functionalized alkoxy-silanes polycondensed with Al, Ti or Zr compounds.<sup>57-60</sup> Also transparent plastics (CR39, polycarbonate, polymethyl methacrylate, etc.) have been coated with hybrid sols, exploiting their good mechanical properties, the high transparency and their processability at low temperatures.<sup>31,61</sup>

Decorative hybrid coatings also cover an industrial area of interest in packaging glass, glass sheets for furniture, glass in architecture<sup>62</sup> and glazing in automotive sector, thanks to their good adhesion properties on glass surfaces, the easy doping with organic dyes and their environmentally friendly properties.<sup>63,64</sup> Some hybrid coatings are also used for their antireflective properties.

Hybrid matrices as fiber-optic sensors<sup>65</sup> and sensor for oxygen, based on methyl-trimethoxy-silane and ethyl-triethoxy-silane doped with a Ru complex<sup>66</sup>, have been studied.

References [67,68,69,70,71,72] report on some studies about rare earth ions ( $\text{Eu}^{3+}$ ,  $\text{Tb}^{3+}$ ,  $\text{Nd}^{3+}$ ,  $\text{Er}^{3+}$ ) complexes embedded in matrices based on Zr-ormosil or Ti-ormosil for optical waveguide, up-conversion (color TV monitors, systems for switching and optical data storage), electrooptics applications.

These are only few of the applications for hybrid organic-inorganic composites. The most exciting feature of this new class of materials is the possibility to engineer the synthesis of structures from the molecular to the nanometric or micrometric scales, to satisfy the requirements for a variety of applications from biological and chemical sensing, catalysis, selective separation to optical communications and optical devices.



## REFERENCES

- <sup>1</sup> Stober, W., Fink, A., Bohn, E. *J. Colloid Interface Sci.*, 1968, 26, 62
- <sup>2</sup> Singh, R. and Chandra, S. IEEE Transactions on dielectrics and electrical insulation, 2004, 2, 264
- <sup>3</sup> Perez, J., Vilarinho, P.M., Kholkin, A. L. *Thin solid films*, 2004, 449, 20-24
- <sup>4</sup> Hu, S. H. et al. *J. of crystal growth* , 2004, 264, 307-311
- <sup>5</sup> Patra, A. et al. *Materials letters*, 2004, 58, 1059-1063
- <sup>6</sup> Nishio, P.; Tsuckiya, T. *Solar energy materials and solar cells*, 2001, 68, 279-293
- <sup>7</sup> Özkan, E.; Tepehan, F. Z. *Solar energy materials and solar cells*, 2001, 68, 265-277
- <sup>8</sup> Deepa, M. et al. *J. Mater. Sci.*, 2000, 35, 5313-5318
- <sup>9</sup> Z. Q. Yu et al. *J. of crystal growth*, 2003, 256, 210-218
- <sup>10</sup> Brinker, C.J.; Scherer, G.W. *Sol-gel science*, Academic Press 1989
- <sup>11</sup> Hench, L.L.; West, J.K. *Chem. Rev.* 1990, 90, 33-72
- <sup>12</sup> Livage, J., Babonneau, F., Sanchez, C. 'Sol-gel chemistry for optical materials', *Sol-gel optics: processing and applications*
- <sup>13</sup> Schmidt, H.; Scholze, H.; Kaiser, A. *J. Non-Cryst. Solids* , 1984, 63, 1-11
- <sup>14</sup> Kevin, M. and Reisfeld, R. *Opt. Mater.*, 1997, 8, 37-41
- <sup>15</sup> Sorek, Y. et al. *Chem. Mater.*, 9, 670-676
- <sup>16</sup> Zhan, Z. and Zeng, H.C. *J. of Non-Cryst. Solids*, 1999, 243, 26-38
- <sup>17</sup> Hench, L.L. and Noqués, J.L. 'Sol-gel processing of net shape silica optics', *Sol-gel optics: processing and applications*
- <sup>18</sup> Rao V. A. and Baghat S.D. *Solid State Sciences*, 2004, 6, 945-952
- <sup>19</sup> Parashar, V.K. et al. *J. of Non-Cryst. Solids*, 1996, 201, 150-152
- <sup>20</sup> Lenza R. et al. *J. of Non-Cryst. Solids*, 2003, 330, 216-225
- <sup>21</sup> Lenza R. et al. *J. of Mater. Science*, 2004, 39, 1363-1366
- <sup>22</sup> Niznansky, D. and Rehspringer J.L. *J. of Non-Cryst. Solids*, 1995, 180, 191-196
- <sup>23</sup> Rao A. P. and Rao A. V. *Materials Letters*, 2003, 57, 3741- 3747
- <sup>24</sup> Innocenzi, P. et al. *J. of Sol-Gel Science and Techn.* 2003, 26, 967-970
- <sup>25</sup> Pandey, P.C. et al. *Sensors and actuators B* , 2001, 75, 48-55
- <sup>26</sup> Pandey, P.C.; Upadhyay, S. *Sensors and actuators B* , 2001, 76, 193-198
- <sup>27</sup> Signorini, R. et al. *Carbon* 2000, 38, 1653-1662
- <sup>28</sup> Signorini, R. et al. *Multiphoton and light driven multielectron processes in organics: New phenomena, Materials and Applications*, 2000, 83-98
- <sup>29</sup> Signorini, R. et al. *J. Sol-gel Sci. Technol.* 2001, 22, 245-253
- <sup>30</sup> Sanchez, C. et al. *J. Mater. Chem.*, 2005, 15, 3559-3592
- <sup>31</sup> Schottner G. *Chem. Mater.* 2001, 13, 3422-3435
- <sup>32</sup> Schmidt, H. *J. of Non-Crystalline solids*, 1989, 112, 419-423
- <sup>33</sup> Schmidt, H. *J. of Non-Crystalline solids*, 1985, 73, 681-691
- <sup>34</sup> Innocenzi, P. et al. *J. of Non-Crystalline solids*, 1999, 259, 182-190
- <sup>35</sup> Brusatin, G.; Guglielmi, M.; Innocenzi P. *J. of Non-Crystalline solids*, 1997, 220, 202-209
- <sup>36</sup> Sorek, Y.; Reisfeld, R.; Weiss, A.M. *Chem. Phys. Letters*, 1995, 224, 371-378
- <sup>37</sup> Sorek, Y.; Zevin, M.; Reisfeld, R. *Chem. Mater.*, 1997, 9, 670-676
- <sup>38</sup> Wang, B. et al. *Macromolecules*, 1991, 24, 3449-3450
- <sup>39</sup> Brusatin, G. et al. *Progr. in Solid State Chem.*, 2006, 34, 223-229
- <sup>40</sup> Kasemann R, Bruck S, Schmidt H. *Proc. of SPIE* 1994; 2288:321
- <sup>41</sup> Bersani, D. et al. *Materials Letters*, 2001, 51, 208-212
- <sup>42</sup> Hoebbel, D., Nacken, M. and Schmidt, H. *J. of Sol-Gel Science and Techn.* 2001, 21, 177-187
- <sup>43</sup> Lee, T.H. et al. *J. of Sol-Gel Science and Techn.* 2002, 27, 23-29
- <sup>44</sup> Innocenzi, P. et al. *Chem. Mater.* 1999, 11, 1672-1679
- <sup>45</sup> Park, O.H. et al. *J. of Sol-gel Sci. Techn.* 1999, 16, 235-241
- <sup>46</sup> Epifani, M. et al. *J. of Sol-gel Sci. Techn.* 2003, 26, 441-446
- <sup>47</sup> Fanovich, M.A. *J. of Sol-Gel Sci. Techn.* 2002, 23, 45-52
- <sup>48</sup> Liu, J. et al. *J. of Non-Cryst. Solids* 2005, 351, 2440-2445
- <sup>49</sup> Innocenzi, P. and Brusatin, G. *J. of Non-Cryst. Solids* 2004, 333, 137-142
- <sup>50</sup> Houbertz, R. et al. *Appl. Phys. Lett.* 2004, 84, 1105-1107
- <sup>51</sup> Allen N.S. et al. *J. Photochem. Photobiol. A: Chem.* 1999, 126, 135-149
- <sup>52</sup> Li, S. et al. *J. of Photochemistry and Photobiology A: Chemistry* 2007, 191, 25-31
- <sup>53</sup> Feuillade M. et al. *Progr. in Solid State Chem.* 2006, 34, 87-94

- <sup>54</sup> Mackenzie, J.D. and Bescher, E.P. *J. of Sol-gel Sci. Techn.* 1998, 13, 371-377
- <sup>55</sup> Schottner, G. et al. *J. of Sol-gel Sci. Techn.* 1998, 13, 183-187
- <sup>56</sup> Sanchez, C. et al. *C. R. Chimie* 2003, 6, 1131-1151
- <sup>57</sup> Messaddeq, S.H. et al. *J. of Non-Crystalline solids*, 1999, 247, 164-170
- <sup>58</sup> Zheludkevich, M.L. et al. *J. of Mater. Chem.* 2005, 15, 5099
- <sup>59</sup> Que, W. et al. *Composites Science and Technology* 2003, 63, 347-351
- <sup>60</sup> Tanglumlert, W. et al. *Surface & Coatings Technology* 2006, 200, 2784-2790
- <sup>61</sup> Hwang, D. K. Et al. *J. of Sol-Gel Sci. and Techn.* 2003, 26, 783-787
- <sup>62</sup> Long, J.W. and Rolison, D.R. *Acc. Chem. Res.* 2007, 40, 854-862
- <sup>63</sup> Schottner, G.; Kron, J.; Deichmann, A. *J. sol-gel Sci. Technol.* , 1998, 13, 183-187
- <sup>64</sup> Smy, Ed *J. sol-gel Sci. Technol.* , 1998, 13, 233-236
- <sup>65</sup> Rose, K. et al. *J. sol-gel Sci. Technol.* , 1998, 13, 729-733
- <sup>66</sup> Mcdonagh, C. M. et al. *J. sol-gel Sci. Technol.* , 1998, 13, 207-211
- <sup>67</sup> Reisfeld, R. et al. *Optical Materials*, 2003, 24, 1-13
- <sup>68</sup> Reisfeld, R. et al. *J. of Luminescence*, 2003, 102-103, 243-247
- <sup>69</sup> Que, W.; Kam, C.H. *Optical Materials*, 2002, 19, 307-312
- <sup>70</sup> De Farias, R.F. et al. *Optical Materials*, 2003, 24, 453-456
- <sup>71</sup> Que, W. Et al. *J. of Applied Physics*, 2001, 89, 3058-3060
- <sup>72</sup> Giorgetti, E. et al. *J. of Non-Crystalline solids*, 1999, 255, 193-198

## CHAPTER 4

# Experimental techniques for the characterization of samples

In the first Chapter we have described some details about the theoretical determination of the two-photon absorption cross-sections of chromophores. In this Chapter, we will introduce the methods used for the measurement of the two-photon absorption spectra. For practical applications, it is important to determine the TPA spectra in order to define the spectral region where chromophores show the best efficiency.

Direct measurements, such as Z-scan, Non Linear Transmittance (NLT), pump and probe methods, are usually difficult because only a small fraction of photons is absorbed in the two-photon process. For these methods, high sample concentrations and high incident energies are necessary to generate a measurable signal.

Two-photon Induced Fluorescence measurement (TPIF) is an alternative approach to determining the TPA cross-sections providing higher sensitivity in respect of the previous methods. It is the best technique for fluorescent materials which fluorescence quantum yields are known. The use of low concentrations avoids some collateral phenomena, like non-linear scattering, self-focusing or thermal blooming. Moreover, the others methods are necessary for the characterization of non fluorescent materials.

In the first three paragraphs we will describe z-scan, NLT, pump&probe and TPIF techniques for the non-linear optical characterization of chromophores. Some theoretical principles of these methods will be emphasized and the characteristics of the experimental

set-ups will be further introduced. Major attention will be dedicated to the TPIF measurements, a technique established recently in our laboratory.

In the last Section, the principles of the confocal microscopy will be described. A confocal system has been installed in our laboratory and it has been used for the detection of the morphology images. The images obtained with this instrument will be exposed in the last chapter.

#### 4.1 Z-scan and Non Linear Transmittance (NLT) techniques

The z-scan technique permits the measurement of both the non-linear absorption and the non-linear refraction properties.<sup>1</sup> Using a single laser beam in a tight focus geometry, we measure the transmittance of a non-linear medium as a function of the sample position  $z$  measured relative to the focal plane.

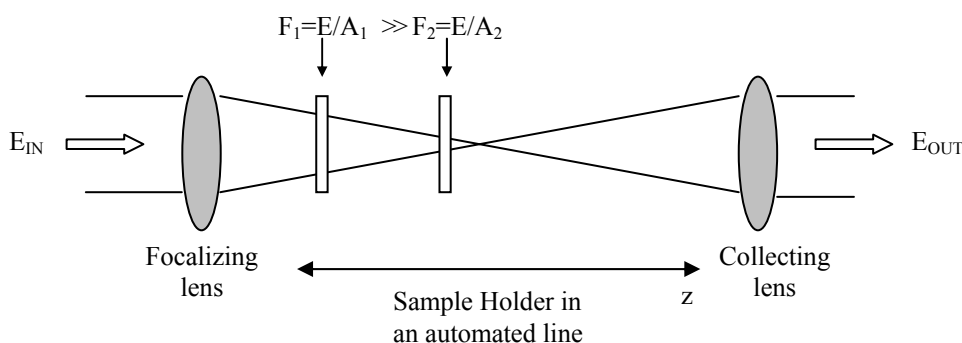


**Fig. 4.1:** Schematic representation of the geometry for z-scan measurements

As shown in Fig. 4.1, the irradiance (power per unit area) increases as the sample approaches the focal plane and the cross section area of the beam decreases. Away from the focus of the focusing lens, the beam irradiance is low and non-linear phenomena do not occur; hence, the transmittance remains constant. As the sample is brought closer to the focus, the non-linear processes are activated and the transmittance decreases. This configuration is called "open aperture" and allows the measurements of the non-linear absorption properties and the determination of the  $\beta$  parameter (see Eq. 4.2).

The "closed aperture" configuration consists on using an aperture in the far field before the collecting lens. The sign and the magnitude of the non-linear refraction coefficient are deduced from the "closed aperture" z-scan curve. By comparing the curves in the two configurations, it is possible to discriminate the contribution of the non-linear refraction effects from the non-linear absorption process.

In this work only measurements in open aperture configuration are performed, so in the following discussion only this method will be considered.

#### 4.1.1 Open aperture z-scan technique: theory

The theory of the z-scan method considers two assumptions: (i) the input beam possesses a Gaussian profile in time and space and (ii) the sample is "thin" compared to the focusing profile. The second condition is satisfied when the specimen thickness  $L$  is small enough that changes in the beam diameter within the sample are negligible. This implies that  $L \ll z_0$ , where  $z_0 = \pi \omega_0^2 / \lambda$  is the diffraction length of the beam or Rayleigh range,  $\omega_0$  and  $\lambda$  are the beam waist radius and the laser wavelength, respectively.

Under these assumptions, the normalized transmittance is given by:<sup>1</sup>

$$T(z) = \frac{1}{\sqrt{\pi} q_0(z)} \int_{-\infty}^{+\infty} \ln[1 + q_0(z) \exp(-\tau^2)] d\tau \quad 4.1$$

$$q_0(z) = \frac{\beta I_0 L_{eff}}{1 + z^2 / z_0^2} \quad L_{eff} = \frac{1 - e^{-\alpha L}}{\alpha} \quad 4.2$$

where  $\beta$  is the TPA coefficient and  $I_0$  is the peak irradiance at the focal plane.  $L_{eff}$  is the effective sample thickness which coincides with  $L$  for low absorbance values.

If  $|q_0| < 1$ , the logarithm function in Eq. 4.1 can be expanded in a Taylor series and the resulting formula is:

$$T(z) = \sum_{m=0}^{\infty} \frac{[-q_0(z)]^m}{(m+1)^{3/2}} \quad 4.3$$

Usually, the first six terms of the summation are sufficient to have accurate results. The open aperture z-scan curve is fitted by the six-terms expression of  $T$ , where  $q_0$  is one of the fitting parameters from which it is possible to obtain the value of  $\beta$ . From  $\beta$  we can calculate the value of the TPA cross-section, as expressed by the relation:

$$\sigma^{(2)} = \frac{\hbar \omega \beta}{N} \quad 4.4$$

where  $N$  is the number density of absorbing species. It is therefore important to know the concentration of the absorbing dye for the determination of the  $\sigma^{(2)}$ .

### 4.1.2 Open aperture z-scan technique: experimental set-up

The open aperture z-scan technique is used for the determination of  $\sigma_{\text{TPA}}$  of chromophores under ns pulses excitation. The optical set-up we have employed is displayed in Fig. 4.2.

The ns laser system consists of a dye laser (*Lambda Physik*-mod. FL 2002) pumped by an excimer laser (*Lambda Physik*-mod. EMG 101) at 308 nm. The repetition rate is 10 Hz and the pulse width is about 12 ns.

The dyes laser uses three different commercial dyes in order to cover the wavelength range from 670 to 860 nm. The dyes are provided by *Exciton* and their characteristics are reported in Table 4.I.

Dyes	Solvent	Emission range (nm)
<b>LDS 698</b>	Propylene carbonate	670 – 750
<b>LDS 759</b>	Methanol	720 – 790
<b>LDS 821</b>	Propylene carbonate	780 – 860

**Table 4.I:** Spectroscopic characteristics of the dyes for the dye laser

The incident energy is varied by using neutral filters (F1) and a polarization rotator (RP) in combination with a cube polarizer (P). The control of the beam collimation is achieved by a Kepler Telescope (KT). A beamsplitter (BS) is employed to divide the beam into two components: about 10% of the input beam is used for the measurements of the incident energy on the sample with the photodiode  $R_{\text{rif}}$ , and the remaining is sent to the focusing optical system.

The beam is focused by lens L1, with focal length of 60 mm. The sample is mounted on a micrometric translation stage (*Newport*-mod. M-UTMPP1HL) controlled by the computer. The transmitted beam is recollectored by a second lens (L2), with focal length of 50 mm, and detected by a photodiode.

A pyroelectric detector (*Molelectron*) is used for the measurement of the pulse energy. Since the most useful parameter is the fluence, defined as the pulse energy normalized over the area of the spot, we use a CCD camera (*Pulnix*, mod.-TM-7CN) to record the images of the laser beam profile.

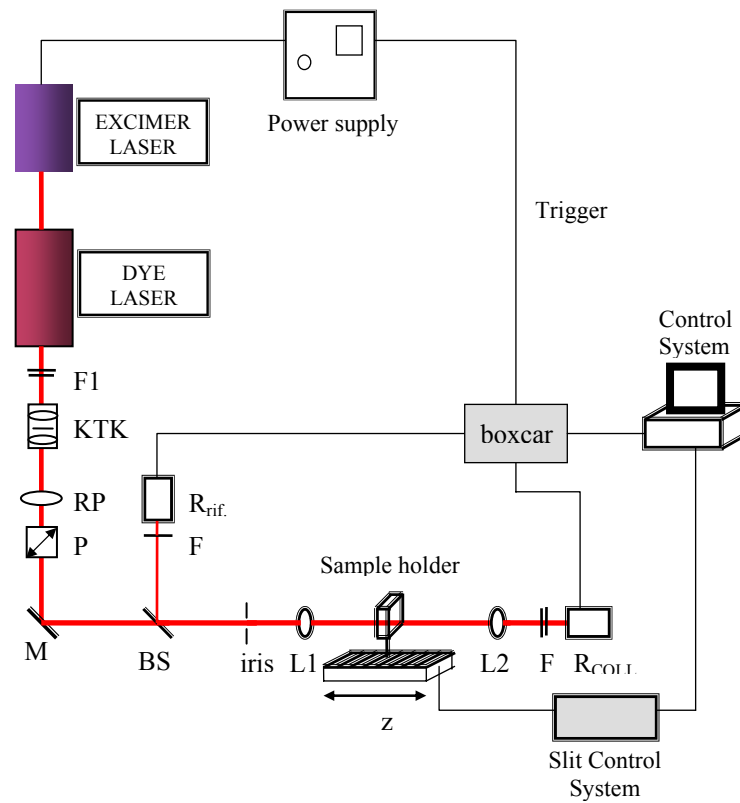


**Fig. 4.2:** Optical set-up for the z-scan measurements with ns pulses

Figure 3.3 depicts the CCD image and the 3D intensity profile of the laser beam in air. The final beam dimension at the beam waist is obtained with a fitting program considering a gaussian profile, well approximating the real beam shape.

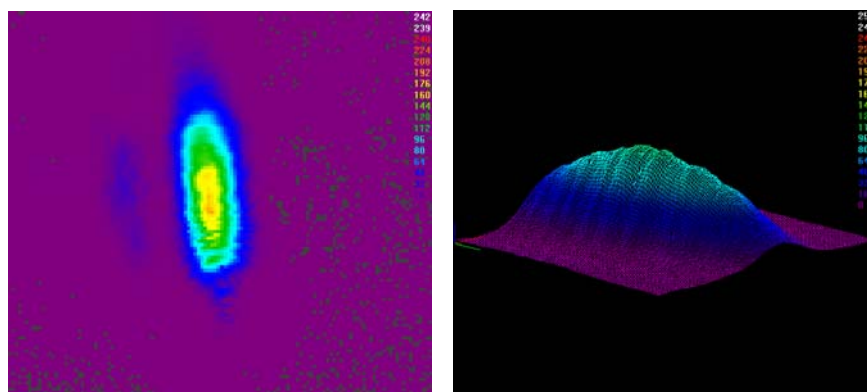


**Fig. 4.3:** CCD image and the 3D intensity profile (inset) of the laser beam in air

### 4.1.3 Non-linear transmission measurements

The set-up displayed in Fig. 4.2 is also used for the non-linear transmission (NLT) measurements.<sup>2,3</sup> This method consists on the detection of the transmitted signal as a function of the incident energy which is gradually incremented. The sample is placed at the beam waist of the focusing system. NLT permits the measurement of the optical limiting performances related to the decrease of the transmittance beyond the threshold incident intensity. From theoretical modeling of the quantitative dependence of the output intensity on the input intensity, it is possible to determine whether the process is due to two-photon or higher order absorption or Reverse Saturable absorption, and the corresponding non-linear absorption coefficient can be directly evaluated.

### 4.2 Pump&Probe method

Another technique employed for the determination of non-linear optical parameters is the Pump&Probe method. In this work, we have not used this method but we report here only some details about it. It consists on a two-beam time-resolved experiment where the absorption (or transmission) of a weak probe pulse is monitored in the presence of a strong pump pulse at different times. When the two beams are superimposed in time ( $\Delta t = 0$ ), a sudden change of the output intensity occurs, while for  $\Delta t > 0$  the registered signal will vary as function of  $\Delta t$ . By the fitting of the obtained curves, one can get direct information on whether the absorption is a sequential stepwise multiphoton process or a direct multiphoton process.

### 4.3 Two-photon Induced Fluorescence technique

#### 4.3.1 Analysis of the physical background of TPIF

Because the TPIF is a third-order process, its intensity depends quadratically on the intensity of the incident laser light. If the linear absorption is negligible, the attenuation of the incident beam in a material due to two-photon absorption process at a given time is described by:

$$\frac{dI}{dz} = -\beta I^2 \quad 4.5$$

where  $I$  is the intensity (defined as power per unit area) of the beam,  $z$  is the direction of propagation and  $\beta$  is the two-photon absorption coefficient.

The number of fluorescence photons collected per unit time is given by the relation:<sup>4</sup>

$$F(t) = 1/2 \phi \eta_S N_{abs} \quad 4.6$$

In this expression,  $\eta_S$  is the fluorescence quantum yield of the sample,  $N_{abs}$  is the number of photons absorbed per molecule and unit time and  $\phi$  is the fluorescence collection efficiency of the measurement system. The factor 1/2 is added in order to account for the two-photon process which involves the emission of one photon after the absorption of two photons. Equation 4.6 is valid in the assumption of no stimulated emission and self-quenching. If stimulated emission occurs,  $\eta_S$  increases and  $\phi$  should account for the preferential direction of the stimulated emission; if the fluorescence is partially quenched the effective  $\eta_S$  is reduced. The number of absorbed photons is proportional to the two-photon absorption cross-section  $\sigma$  and to the square of the incident intensity.  $N_{abs}$  is also a function of the dye local concentration  $C(\bar{r}, t)$  and the illuminated sample volume:

$$N_{abs}(t) = \int_V \sigma C(\bar{r}, t) I^2(\bar{r}, t) dV \quad 4.7$$

If saturation and photobleaching effects are not present, the concentration can be considered constant. When the time and space dependence of the intensity can be separated, Eq. 4.7 becomes:

$$N_{abs}(t) = \sigma C I_o^2(t) \int_V S^2(\bar{r}) dV \quad 4.8$$

$I_o(t)$  and  $S(\bar{r})$  are the temporal and spatial distribution of the incident beam, respectively. Experimentally, it is possible to measure only a time-average of the photon flux expressed in 4.9:

$$\langle F(t) \rangle = 1/2 \phi \eta_S C \sigma \langle I_o^2(t) \rangle \int_V S^2(\bar{r}) dV \quad 4.9$$

Because most detectors measure the average of  $I_o(t)$ , it is possible to rewrite the expression 4.9 as:

$$\langle F(t) \rangle = 1/2 g \phi \eta_S C \sigma \langle I_o(t) \rangle^2 \int_V S^2(\bar{r}) dV \quad 4.10$$

Where  $g$  is a measure of the second-order temporal coherence of the excitation source:

$$g = \langle I_o^2(t) \rangle / \langle I_o(t) \rangle^2 \quad 4.11$$

The relation 4.10 identifies the parameters necessary for the determination of the absolute value of the TPA cross-section:

- the spatial distribution of the laser beam  $\int_V S^2(\bar{r}) dV$ ,
- the degree of the second-order temporal coherence  $g$ ,
- the fluorescence collection efficiency  $\phi$ ,
- the fluorescence quantum yield  $\eta_S$ .

### 4.3.2 Second-order temporal dependence

For a quantitative measurement of  $\sigma_{\text{TPA}}$  it is important to consider not only the average but also the temporal fluctuations of the photon flux included in the factor  $g$ . For a generic pulsed excitation, the intensity is a periodic function over  $m$  cycles:

$$I_o(t) = I_0 \left( t + \frac{m}{f} \right) \quad m = 1, 2, 3, \dots \quad 4.12$$

where  $f$  is the repetition rate of the laser source.

Because of the periodicity of the excitation intensity, it is possible to consider only the factor  $g$  for one cycle. The second-order temporal coherence term can be expressed by:

$$g = \frac{g_p}{f \cdot \tau} = \frac{\int_{-1/(2f)}^{1/(2f)} I_o^2(t) dt}{f \left[ \int_{-1/(2f)}^{1/(2f)} I_o(t) dt \right]^2} \quad 4.13$$

where  $g_p$  is a dimensionless quantity depending only on the shape of the laser pulse,  $f \cdot \tau$  is the duty cycle and  $\tau$  is the excitation pulse width.

For Gaussian laser pulses,  $g_p$  is equal to 0.664, while for hyperbolic-secant square temporal profile  $g_p = 0.558$ . From Eq. 4.9, the average intensity becomes:

$$\langle F(t) \rangle = 1/2 \frac{g_p}{f\tau} \phi \eta_S C \sigma \langle I_o(t) \rangle^2 \int_V S^2(\bar{r}) dV \quad 4.14$$

For a mode-locked Ti:Sapphire laser with  $f \sim 100$  MHz and  $\tau \sim 100$  fs, the value of  $g$  is  $10^5$  approximately. This high value permits the excitation of chromophores at low average laser power.

### 4.3.3 Spatial dependence

The mathematical resolution of the spatial distribution of the incident beam depends on the shape of the beam. For this reason, in order to avoid big errors in the determination of this parameter, it is important to have a precise control on the laser beam shape.

In the case of diffraction-limited objective lens, the intensity distribution is expressed by the point-spread function. The dimensionless distance from the optical axis of the lens  $v$  and the distance from the in-focus plane  $u$  are expressed as:

$$v = \frac{2\pi(N.A.)\rho}{\lambda} \quad u = \frac{2\pi(N.A.)^2 z}{n\lambda} \quad 4.15$$

where  $N.A.$  is the numerical aperture of the optics ( $N.A. = n \cdot \sin\theta$ , with  $\theta$  the half-angle of collection for the lens),  $z$  and  $\rho$  are the distance along and away from the optical axis respectively,  $n$  is the refractive index of the medium and  $\lambda$  is the laser wavelength.

The paraxial form of the normalized intensity point-spread function ( $h^2[u, v]$ ), which is verified for  $\sin\theta < 0.7$  or  $N.A. < 1$  (oil-immersion objectives), is given by:

$$S(\bar{r}) = h^2(u, v) = \left| 2 \int_0^1 J_0(v\rho) \exp[-(1/2)iu\rho^2] \rho d\rho \right|^2 \quad 4.16$$

$S^2(\bar{r}) = h^4(u, v)$  cannot be integrated analytically. In the thick samples approximation, with thicknesses much greater than the focal length,  $S(\bar{r})$  can be numerically calculated from:

$$\int_{V \rightarrow \infty} S^2(\bar{r}) dV \approx \frac{8n\lambda^3}{\pi^3(N.A.)^4} \quad 4.17$$

Besides, the relation between the intensity  $I_0(t)$  and the instantaneous incident power  $P(t)$  is given by:

$$I_0(t) = \frac{\pi(N.A.)^2}{\lambda^2} P(t) \quad 4.18$$

Substituting Eqs. 4.16 and 4.17 into Eq. 4.9, we obtain:

$$\langle F(t) \rangle \approx 1/2 g \phi \eta_s C \sigma \frac{8n \langle P(t) \rangle^2}{\pi \lambda} \quad 4.19$$

Analogous results can be obtained for a Gaussian profile beam.

### 4.3.4 Fluorescence collection efficiency

Another important parameter to take into account is the efficiency of the fluorescence collection. This parameter can be expressed as:<sup>5</sup>

$$\phi = \phi_{dispers} \times \phi_n \quad 4.20a$$

$$\phi_{dispers} = \left[ \int f_{fluo}(\lambda) \times f_{PMT}(\lambda) \times \prod_i T_i(\lambda) d\lambda \right] / \int f_{fluo}(\lambda) d\lambda \quad 4.20b$$

Equation 4.20b shows the correction factor due to the wavelength dispersion of the response functions:  $f_{fluo}(\lambda)$  is the fluorescence spectrum of the emitting dye,  $f_{PMT}(\lambda)$  is the response function of the photomultiplier tube (PMT),  $T_i(\lambda)$  is the transmission spectrum of the i-th filter, generally used in front of the PMT. The integrals are calculated over the wavelength range of the fluorescence spectrum.

The second factor  $\phi_n$  takes into account the solid angle under which the emitting volume of the solution is seen from the detector. This correction factor is proportional to  $n^{-2}$ , in the assumption that the emitting volume is a point source with isotropic emission. The isotropic emission condition is generally satisfied if the incident intensity is not so intense to promote stimulated emission from the sample.

### 4.3.5 Fluorescence quantum yield (FQY) measurements

The determination of the fluorescence quantum yield of a chromophore plays a fundamental role for the correct calculation of  $\sigma_{TPA}$ . In the relations reported above, we have considered that the fluorescence quantum yield is the same if the chromophore is excited by one-photon absorption or by two-photon absorption. This is reasonable if we assumed that only the lowest vibrational state in the excited electronic level can relax through a radiative emission process and this is independent of the way employed for the excitation of the system. For this reason, the simplest way for determination of FQY consists on using a spectrofluorimeter as detector.

Because of the many problems associated with absolute quantum-yield measurements, several simple relative methods are employed. The most common method consists of comparing the emission spectra of dilute solutions of the sample and a standard compound, used as reference material with known quantum yield. The expression for the quantum yields is given by:<sup>6</sup>

$$Q_x = Q_r \left( \frac{K_r}{K_x} \right) \left( \frac{D_x}{D_r} \right) \left( \frac{n_x^2}{n_r^2} \right) \quad 4.21$$

$$K = \frac{\int S(\bar{\nu}) I(\bar{\nu}) d\bar{\nu}}{\int I(\bar{\nu}) d\bar{\nu}} \quad 4.21a$$

Where  $Q$  is the fluorescence quantum yield of the solution,  $K$  is the average detector output per photon over the emission spectrum (Eq. 4.21a),  $D$  is the detector response and  $n$  is the refractive index of the solution. The  $x$  and  $r$  subscripts refer to the sample and the reference respectively. In Eq. 4.21a,  $I(\bar{\nu})$  (quanta/sec  $\text{cm}^{-1}$ ) is the spectral distribution of the light on the phototube and  $S(\bar{\nu})$  is the relative sensitivity of the detector to light of wavenumber  $\bar{\nu}$  ( $\text{cm}^{-1}$ ).

For dilute solutions the Lambert-Beer's law is satisfied:

$$I_0 B = I_0 (1 - 10^{-AL}) \quad 4.22$$

$B$  is the fraction of light absorbed by the sample,  $I_0$  is the intensity light,  $A$  is the absorbance (A/cm) and  $L$  (cm) is the path length.

If the fluorescence intensity is proportional to  $I_0 B$ , the expression for the quantum yield becomes:

$$Q_x = Q_r \left( \frac{B_r}{B_x} \right) \left( \frac{I(\lambda_r)}{I(\lambda_x)} \right) \left( \frac{n_x^2}{n_r^2} \right) \left( \frac{D_x}{D_r} \right) \quad 4.23$$

Using the expansion in a power series of  $(AL)$  in Eq. 4.22, for low absorbance values, we obtain:

$$B = 1 - [1 - 2.303AL + (2.303AL)^2 / 2 + \dots] \approx 2.303AL \quad 4.24$$

Substituting this expression in Eq. 4.23, we derive the common formula for the determination of the FQY:

$$Q_x = Q_r \left( \frac{A_r(\lambda_r)}{A_x(\lambda_x)} \right) \left( \frac{I(\lambda_r)}{I(\lambda_x)} \right) \left( \frac{n_x^2}{n_r^2} \right) \left( \frac{D_x}{D_r} \right) \quad 4.25$$

In these equations,  $I(\lambda)$  is the relative intensity of the exciting light at wavelength  $\lambda$ ,  $n$  is the average refractive index of the solution,  $D$  is the integrated area under the corrected emission spectrum and  $A(\lambda)$  is the absorbance/cm of the solution at the exciting wavelength  $\lambda$ .

Equation 4.25 is valid if many assumptions are satisfied. For both compound the integrated luminescence intensity is assumed to be proportional to the fraction of absorbed light, all geometrical factors are identical, the excitation beams are

monochromatic, internal reflection effects are the same, reabsorption and reemission are negligible and the emission is isotropic. It is often difficult to take into account all of these effects, but it is possible to employ some cautions in order to minimize errors in the determination of FQY.

For our measurements of FQY, we used solutions with maximum absorbance of about 0.15, in order to minimize the reabsorption and the quenching effects. Both the standard and the unknown sample are made up to have similar absorbance at the excitation wavelength: by this way the attenuation of the excitation source is analogous in both cases and the number of the excited molecules can be considered similar. The absorbance is measured by a spectrophotometer (*Varian, Cary-5*) with resolution of 1 nm. The emission spectra are carried out using a *Jobin-Yvon-Fluomax* spectrofluorimeter.

We apply two correction factors due to reabsorption effects. To account for the reabsorption of the excitation beam, we consider that the number of absorbed photons is proportional to  $(1-10^{-AL/2})$  instead of  $AL$  ( $AL$  is obtained in the approximation of low absorbance - see Eq. 4.24).  $L$  is the optical path of the cuvette and  $L/2$  is the thickness across the excited sample.

Regarding the correction factor due to reabsorption of the fluorescence spectrum, we consider that the spectrometer measures an apparent corrected emission spectrum of the sample  $I_a(\bar{\nu})$  which is not the same as the molecular emission spectrum  $I(\bar{\nu})$ . From Beer's law  $I_a(\bar{\nu})$  and  $I(\bar{\nu})$  are related by:

$$I_a(\bar{\nu}) = I(\bar{\nu})10^{-AL/2} \quad 4.26$$

These two factors induce a correction of about 5-10% for absorbance lower than 0.2.

The choice of the standard compound for FQY measurements is also important to have the best overlapping of the two fluorescence spectra and, by this way, to reduce the experimental errors. We often used two or more standards to measure the FQY of the chromophores and the final result is the average between the values found. The fluorescence standards used are:

- Fluorescein in H<sub>2</sub>O at pH > 11, FQY = 0.93<sup>7,8</sup>;
- Coumarin 540A in EtOH, FQY = 0.56<sup>9</sup>, 0.4<sup>10</sup>, 0.26<sup>11</sup>, 0.38<sup>12</sup> (from our data, using Fluorescein as reference, we obtained FQY = 0.44)
- Rhodamine B in MeOH, FQY = 0.8<sup>13</sup>
- Rhodamine 6G in EtOH, FQY = 0.95<sup>8,14</sup>, 0.94<sup>15</sup>

### 4.3.6 Experimental TPIF method

It is clear from the last excursus that the calculation of all the factors involved in the Eq. 4.10 is generally difficult. In Ref. [5] an alternative method has been proposed. It consists of using the same set-up for the measurement of the fluorescence emission for the sample and for the compound whose TPA spectrum and fluorescence quantum yield are known in the literature.

We can write Eq. 4.10 for the sample and an analogous one for the reference. If we divide the two relations and reorganize them, we obtain:

$$\sigma_{TPA}^S = \sigma_{TPA}^R \frac{\langle F \rangle_S C_R \eta_R \phi_R}{\langle F \rangle_R C_S \eta_S \phi_S} \quad 4.27$$

In this relation,  $\sigma_{TPA}$  is the two-photon cross section,  $\langle F \rangle_S$  is the signal read by the detector, quadratically dependent on the excitation intensity,  $C$  is the concentration of the compound and  $\eta$  is the FQY. Finally,  $\phi$  is the correction factor for the collection efficiency, having the same general formula reported in Eq. 4.20. Its final definition depends on the geometry of the experimental apparatus employed, the wavelength dependence of the filters, the refractive index of the solutions, etc. The subscripts  $R$  and  $S$  refer to reference and sample, respectively.

It is important to note that other factors, such as the second-order temporal coherence, the square of the incident intensity, the spatial distribution of the laser beam, are cancelled because they are identical for the sample and for the standard.

The final expression is very simple and it is applicable for many classes of compounds.

### 4.3.7 Deviation from quadratic-intensity law

Recently, some researches have demonstrated a deviation from quadratic dependence in the two-photon emission experiments excited by high laser intensities.<sup>16</sup> We report here only few results of the proposed theory.

They consider a three-states model, as reported in Fig. 4.4.

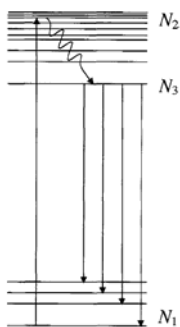


**Fig. 4.4:** Schematic representation of the three levels involved in the optical transitions

After two-photon excitation, state 2 relaxes rapidly by internal conversion to state 3 from which fluorescence is emitted. The corresponding molecular concentration in each states is given by  $C_i$  (where  $i=1,2,3$ ). Because the system is not at equilibrium, the concentrations  $C_i$  depend on time and space and the rate equation formalism is used for their calculation.

The rate equation for  $C_3$  is given by:

$$\frac{\partial C_3(t)}{\partial t} + B(t)C_3(t) = b(t)C_0 \quad b(t) = \left( \frac{\tau}{\tau_{23}} \right) \left[ \frac{\sigma_{TPA} I_0^2 \xi}{(h\nu)^2} \right] f(t)^2 \quad B(t) = b(t) + \tau_{31}^{-1}$$

$$C_1 + C_2 + C_3 = C_0 \quad 4.28$$

$\tau_{23}$  and  $\tau_{31}$  are the relaxation and the fluorescence times respectively.  $\xi$  is a dimensionless quantity arising from the spatial distribution of the laser beam and  $f(t)$  represents the temporal distribution of the laser pulses.

When the laser intensity increases, the population of state 3 is no more negligible and Eq. 4.28 can be integrated. This is simply obtained in the assumption of pulses with rectangular shape to yield:

$$N_3(t) = VC_3(t) = \left( \frac{b_0 N_0}{b_0 + \tau_{31}^{-1}} \right) \left\{ 1 - \exp[-(b_0 + \tau_{31}^{-1})t] \right\} \quad b_0 = \sigma_{TPA} I_0^2 \xi / (h\nu)^2 \quad 4.29$$

The average fluorescence photon flux emitted (over the pulse duration  $\Delta t$ ) is proportional to averaged  $N_3(t)$  that is:

$$F_2(I_0) = \langle F(t) \rangle = \frac{\phi\eta}{2\Delta t} \int_0^{\Delta t} N_3(t) dt \cong \frac{1}{2} N_0 \phi\eta \left\{ 1 + \frac{1}{(I_0^2 / I_S^{(2)})} [e^{-I_0^2 / I_S^{(2)}} - 1] \right\} \quad 4.30$$

$$I_S^{(2)} = \frac{(h\nu)^2}{\xi \sigma_{TPA} \Delta t}$$

The typical experimental curve of the photon flux  $F_2$  as a function of the incident intensity  $I_0$ , that they have measured, is reported below.

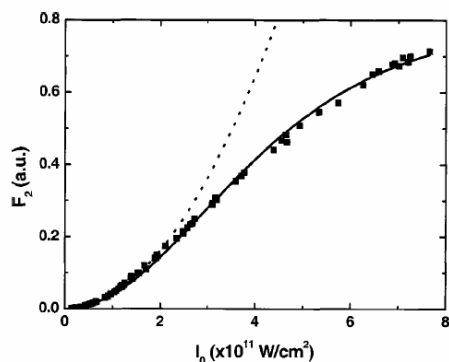


**Fig. 4.5:** Two-photon fluorescence intensity plotted vs the intensity of the incident laser. The quadratic intensity law (dotted curved) is obeyed only at the low excitation intensities. The solid curve is the fit to equation 4.30. (Ref. 16)

The fitting of the experimental data using Eq. 4.30 permits the determination of the parameter  $I_s^{(2)}$  that is called two-photon saturation intensity. By this way, it is possible to calculate the value of TPA cross-section using an absolute method but avoiding the calculation of all the auxiliary laser parameters required by Xu and Webb in Ref. [4]

#### 4.3.8 Experimental set-up and tests

In our laboratories we have realized and finely optimized the set-up to perform TPIF measurements. The optical set-up is schematically represented in Fig. 4.6.

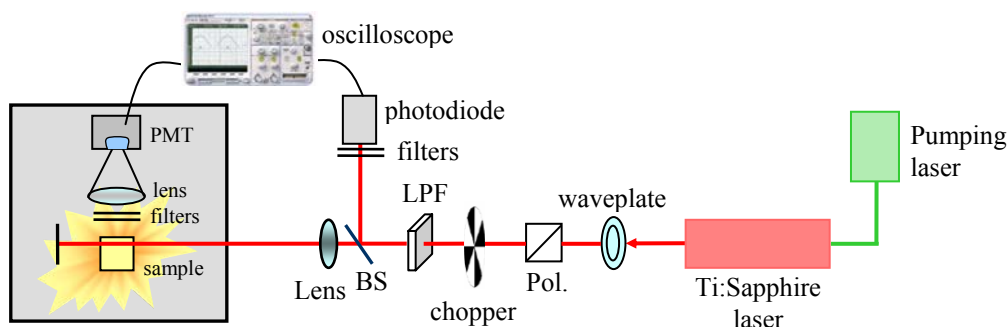


**Fig. 4.6:** Optical set-up for Two-photon Induced Fluorescence measurements

The excitation source is an ultrafast mode-locked Ti:Sapphire laser (*Coherent- Mira 900-F*), pumped by a compact diode-pumped Nd:YVO<sub>4</sub> laser emitting at 532 nm (*Verdi V-5*). The pulse duration is about 130 fs and the repetition rate is 76 MHz, which means that

there are approximately 13.2 ns between two pulses. The nominal wavelength range is from 710 to 1000 nm, even if the practical region is between 720 and 930 nm. The output wavelength can be simply modified by changing the birefringent filter position and moving the Brewster prism compensator.

The output intensity distribution is displayed in figure 4.7: the maximum is centred at 800 nm.

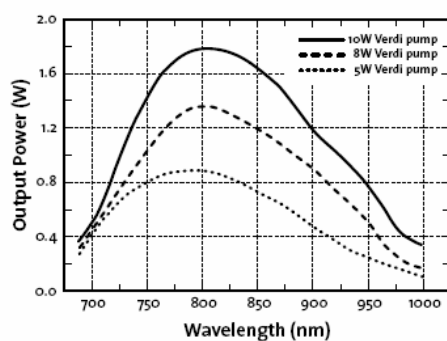


**Fig. 4.7:** Output power distribution of Ti:Sapphire Mira-900F laser

The intensity can be gradually varied by using a waveplate and a linear polarizer: when the optical axes are parallel the intensity is maximum and it diminishes to a minimum when the axes are orthogonal. The use of a chopper, at an arbitrary frequency of 215 Hz, is necessary for the detection of the signal by a photodiode or a phototube, which have time responses too slow to discriminate the pulses with 76 MHz of frequency.

The spurious laser components at low wavelength ( $< 550$  nm) are absorbed by the long-pass filter: this is important because these components can linearly excite the chromophore inducing interference for the two-photon excitation process. Besides, a beamsplitter divides the beam into two parts: about 10% of the overall intensity is sent to a photodiode that measures the incident energy and the remaining is used for the excitation of the sample.

The beam is focalized into the sample by a lens with a focal length of 40 cm. The sample is contained in a cuvette for fluorescence measurements with optical path of 10 mm. Because the Rayleigh range of the lens is about 10 mm, the beam can be approximately considered collimated along the entire sample cell. Besides, the beam passes near the wall of the cuvette (about 1mm) in order to reduce the reabsorption of the fluorescence signal before the detector.

Great attention has been devoted to the definition of the detection unit. Two are the main goals: the maximization of the fluorescence signal and the minimization of the spurious

pump laser signals. We have set the detection unit perpendicular to the excitation beam ( $90^\circ$  configuration): by this way only the components scattered by the solution or the cell could be measured by the detector. This component is very low but must be eliminated, especially with weak fluorescence signals. In fact, the scattering has a linear proportionality with the incident energy and can interfere with the square dependence of the TPIF signal. For this reason, we use a set of short pass filters before the phototube. We generally use three filters that are different depending on the spectral region of excitation. The transmittance spectra of these filters are reported below.

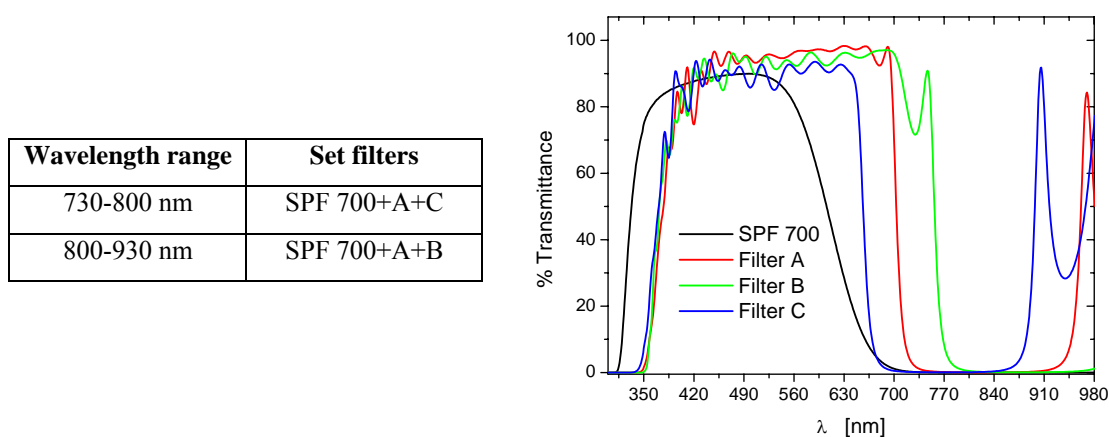


**Fig. 4.8:** Transmittance spectra of the short pass filters before the detector. The table on the left displays the combinations of the filters used at different wavelength regions.

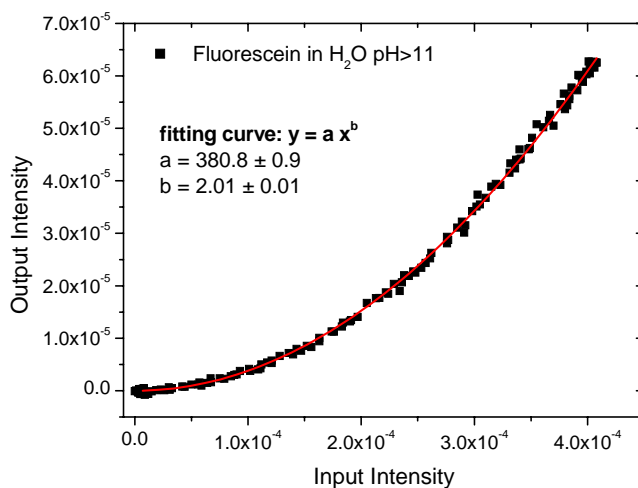
We have tried many combinations of lenses, in order to optimize the detection of the fluorescence signal. One possibility is the use of an appropriate lens and an optical fiber connected with a spectrometer (*Horiba Jobin Yvon - MicroHR*). In this way we would like to directly measure the fluorescence spectrum of the chromophore after the two-photon excitation. The main difficulty consists in the focusing of the fluorescence image (a cylinder of 10 mm height) into the 1 mm-core of the fiber, as well as the matching of the correct input angle that is defined by the numerical aperture of the fiber ( $28^\circ$  with respect to the normal axis). This configuration was not adopted because of the high optical losses, due to the use of many lenses, sometimes placed at great distance from the sample, and to the incorrect entrance on the optical fiber.

We have finally chosen a collection configuration that consists in the use of a lens with 40 mm focal length ( $F$ ). If it is set at distance  $2F$  from the sample, the fluorescence image is approximately recreated at  $4F$  distance and is focused onto the active area of the photomultiplier tube (*Hamamatsu- R636-10*).

The entire collection unit is set into a black box which guarantees the reduction of the internal reflexions of the pump beam.

The photodiode (measuring the input intensity) and the photomultiplier tube (measuring the output intensity) are connected to an oscilloscope interfaced with a personal computer. A *Labview*-application has been written for the data acquisition.

The method chosen is analogous to that described by Rumi et al. in Ref. [5]. At every excitation wavelength we collect the integrated intensity of the emission spectrum of the active dye as a function of the incident intensity, which is varied from 0 up to 100 MW/cm<sup>2</sup>. In order to eliminate the scattering contribution, we subtract the signal measured with a cell containing the pure solvent to the fluorescence signal emitted by the dye in solution. This is done both for the sample and the standard compound. The typical curve of TPIF signal is displayed in Fig. 4.9.



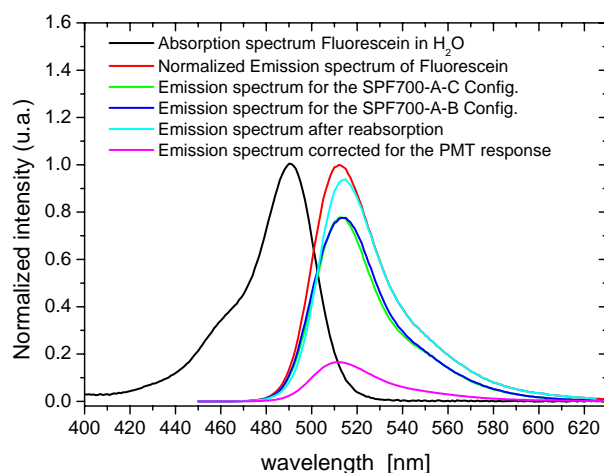
**Fig. 4.9:** TPIF curve as a function of the incident intensity for Fluorescein excited at 800 nm. The red line is the fit curve.

Figure 4.9 shows that the experimental data is well fitted by a quadratic curve, as predicted by the TPIF theory at low incident energies. For every fitting, we fix the exponential parameter to the value 2 in order to use the pre-exponential factor for the calculation of  $\sigma_{\text{TPA}}$  with the formula of Eq. 4.27.

As standards we used Fluorescein (in H<sub>2</sub>O pH>11, FQY=0.9) and Rhodamine B (in methanol, FQY=0.7), whose TPA spectra are reported in the literature. The typical concentrations are 2-5×10<sup>-5</sup> M, for chromophores with high fluorescence quantum yields, but they increase up to 5×10<sup>-4</sup> M if the FQY and  $\sigma_{\text{TPA}}$  value are low. In fact, if the emitted

signal is too low, it is more difficult to fit the data with a quadratic dependence and it is necessary to increase the dye concentration.

The correction factors, applied for the TPIF signal, take into account the absorption on the dye fluorescence spectrum – due to the SPF filters set in front of the detector – the reabsorption of the fluorescence inside the cell, and the spectral response of the PMT. The entity of these individual contributions depends on the spectral position of the emission spectrum of the studied chromophore and its concentration. We report here only the case of fluorescein as example.



**Fig. 4.10:** Absorption and Emission spectra of Fluorescein in H<sub>2</sub>O. The figure displays also the emission spectra corrected for the absorption of the filters, the reabsorption and the PMT quantum efficiency.

The main effect is determined by the PMT quantum efficiency but it is generally analogous for the sample and the standard. Besides, the reabsorption contribution is not negligible for Fluorescein (about 8%) because of the small Stokes shift.

In the first step, we have decided to reproduce some data reported in the literature in order to test our experimental set-up. The two papers we refer to are those reported by Xu-Webb (Ref. [4]) and by Xu (Ref. [17]). In these papers the absolute data of the TPA spectra are discussed.

The picture in Fig. 4.11 shows the fluorescence emission at room temperature of some chromophores under a low power UV irradiation at 254 nm. The first three cells contain semiconductor quantum dots solutions, the fourth one contains a Fluorescein solution and the last a Rhodamine B solution.

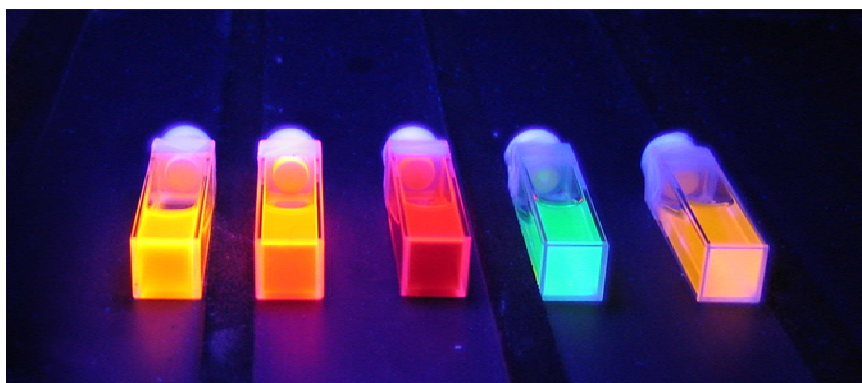


**Fig. 4.11:** Images of the emission from five different chromophores under irradiation at 254 nm

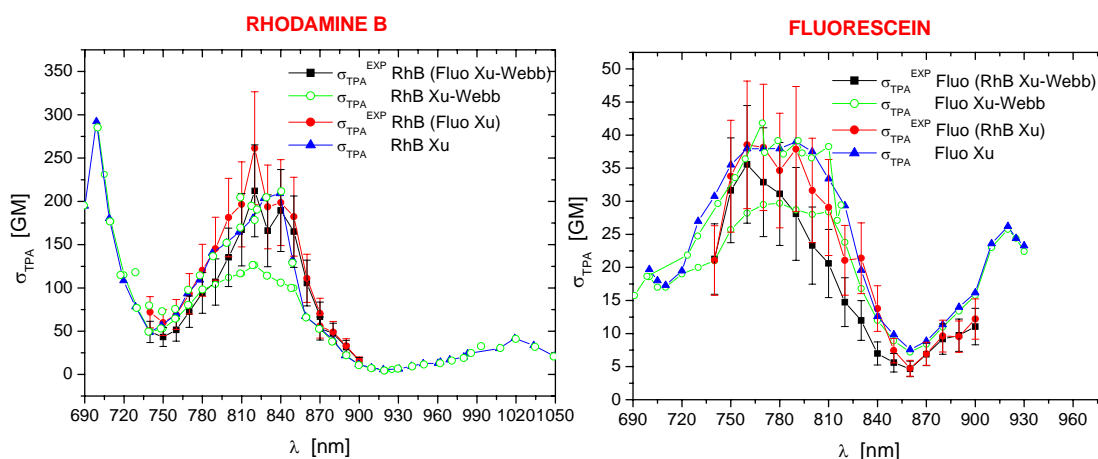


**Fig. 4.12:** TPA experimental spectra of Rhodamine B (on the left) and Fluorescein (on the right) and the TPA reference spectra.

In Fig. 4.12 our TPA spectra of Rhodamine B and Fluorescein are displayed together with the spectra reported in the literature. For Rhodamine B we have obtained the spectrum using the data of Fluorescein of Xu-Webb (black symbols) and those of Xu (red symbols) as references.

These two spectra can be compared with those of Rhodamine B in Xu-Webb (green symbols) and in Xu (blue symbols). The same thing is done for fluorescein in Fig. 4.12 in the right panel.

The error bars of the TPA data have been calculated using the error propagation formula and reflect the uncertainties of our experimental data, taking into account the reproducibility of the technique (two independent runs were performed), and the errors affecting the FQY and concentration. The error on the  $\sigma_{\text{TPA}}$  of the reference has not been explicitly considered. Xu and coworkers give an estimate of 30% for it.

Comparing our experimental data with those in the literature, we have concluded that our data is more similar to that published by Xu. For this reason, in next chapters, where the characterization of TPA systems will be described, we will display only the data obtained using Xu data as reference.

#### 4.3.9 Two-photon fluorescence spectra

One of the assumptions of the TPIF theory is that the excitation process does not influence the emission properties of the fluorophore. In order to confirm this hypothesis we have measured the fluorescence spectrum of the sample, using a two-photon excitation in a back-scattering geometry, and compared it to the one-photon excitation spectrum.

The laser beam and the TPA induced fluorescence are focused and collected by the same microscope objective (10X, NA=0.25). The fluorescence light is separated from the exciting laser beam by a dichroic filter, which reflects the low wavelengths, and then sent to a fiber coupled with a monochromator and a PMT tube. Short pass filters were used in front of the fiber to suppress the scattered laser light. Figure 4.13 shows the linear emission and the two-photon fluorescence spectra obtained for Fluorescein and Rhodamine B. The two-photon emission spectra are measured upon excitation at 800 and 850 nm for both chromophores.

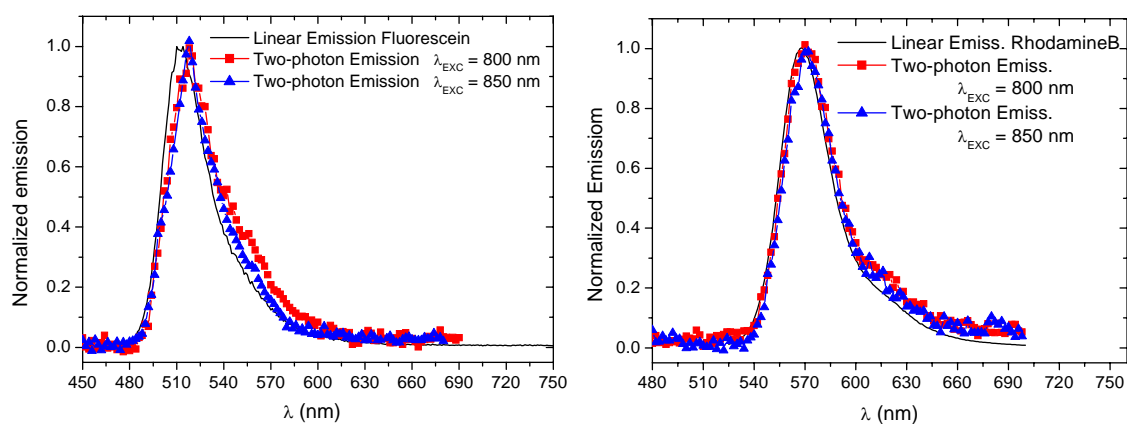


**Fig. 4.13:** Comparison between the fluorescence spectra excited by one-photon absorption (black line) and by two-photon absorption (red and blue symbols) for Fluorescein (left panel) and Rhodamine B (right panel)

It is evident that the two curves are very similar. The red shift of the emission maximum, especially for fluorescein, is due to reabsorption of the emission. The concentration of the solution is, in fact, higher than that used for TPIF measurements and the reabsorption is

more pronounced. Moreover, the TPA emission spectra are a little enlarged with respect to the linear fluorescence spectra; this is due to the resolution of the spectrometer which is defined by the aperture of the slits in front of the detector.

#### **4.4 Confocal microscopy: a powerful tool for the investigation on the morphology of micro- and nano-structures**

In this last paragraph, we will present some characteristics of the confocal microscopy recently mounted in our laboratories. This technique will be used for the morphological characterization of the structures created by the photopolymerization process.

The basic concept of the confocal microscopy was developed by a student in the mid 1950s for some studies on neural networks. Up to date the technique has become an important tool in many application fields, from biology to biomedical sciences, as well as in material science.

The working principles are quite simple. The confocal microscopy is generally based on revealing the fluorescence emitted by a sample. The schematic representation of this instrument is depicted in Fig. 4.14. Coherent light emitted by the laser system (excitation source) passes through a pinhole aperture, which is situated in a conjugate plane (confocal), with a scanning point on the specimen. A second pinhole is positioned in front of the detector which is a photomultiplier tube. As the laser is reflected by a dichromatic mirror and scanned across the specimen in a defined focal volume, secondary fluorescence emitted from points on the sample (in the same focal plane) pass back through the dichromatic mirror and are focused at the detector pinhole aperture. The fluorescence emission that occurs at points above and below the objective focal plane is not confocal with the pinhole and generates extended Airy disks in the aperture plane (out-of-focus fluorescence emission in Fig. 4.14).

Because only a small fraction of the out-of-focus fluorescence emission is delivered through the pinhole aperture, most of this extraneous light is not detected by the photomultiplier tube and does not contribute to the resulting image.

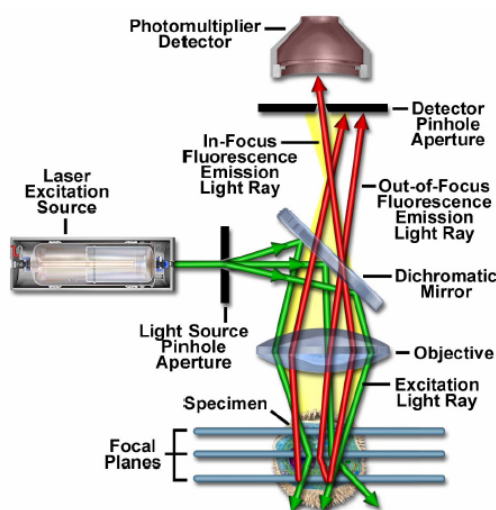


**Fig. 4.14:** Schematic diagram of the optical pathway and principal components in a laser scanning confocal microscope

The main difference between confocal and widefield microscopes is the character and the geometry of specimen illumination and of the emission detection, as depicted in Fig. 4.15. Traditional widefield epi-fluorescence microscope objectives focus a wide cone of illumination over a large volume of the specimen which is uniformly and simultaneously illuminated. Consequently, all the emission fluorescence is directed to the eyepieces or the detector. The final image is therefore obtained with a large amount of background light and autofluorescence originating from area out of the focal plane.

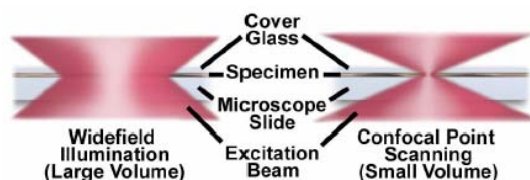


**Fig. 4.15:** Widefield versus confocal microscopy illumination volumes

In the confocal microscope the laser illumination source is firstly expanded to fill the objective rear aperture and then focused by the lens system to a very small spot (having dimensions from 0.25 to 0.8  $\mu\text{m}$ ) at the focal plane. The confocal spot size is determined by the microscope design, the wavelength of the incident laser light, the objective characteristics and the scanning unit settings. This illumination geometry as well as the use of small pinholes permits higher resolution and contrast than the traditional fluorescence microscopy. For confocal microscope the lateral and the axial resolutions are defined by:

$$r_{lat} = 0.4 \lambda / NA \qquad r_{axial} = 1.4 \lambda n / NA^2 \qquad 4.31$$

where  $\lambda$  is the wavelength of the excitation source,  $n$  is the refractive index of the specimen and  $NA$  is the numerical aperture of the microscope objective. The lateral resolution is about 30% higher than that of widefield microscope. The global improvement in the axial resolution of confocal system is also determined by the possibility of optical sectioning in thick sample. In fact, the final 3D images are obtained by the superposition of signal emitted from successive layers over the thickness of the sample.

The scan head is the heart of the confocal system and is responsible for rasterizing the excitation scans, as well as the photon signals from the specimen that are required to assemble the final image. A typical scan head contains inputs from the external laser sources, fluorescence filter sets and dichromatic mirrors, a galvanometer-based raster scanning mirror system, variable pinhole apertures for generating the confocal image, and photomultiplier tube detectors tuned for different wavelengths.

The confocal system we have staged in our laboratories is the FluoView FV300 by *Olympus*. It has an upright configuration and it is connected through optical fibers to an Ar and an Ar-Kr external laser sources. The scan unit of FV300 is reported in Fig. 4.16.

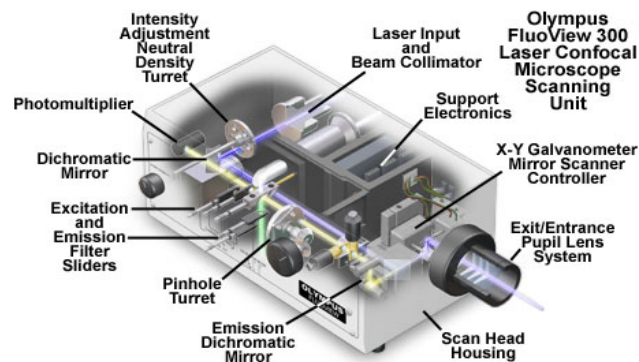


**Fig. 4.16:** Schematic representation of the scan unit of FluoView 300-Olympus confocal microscope

Our scan unit has two input slots, one is dedicated to the continuum laser sources and the other to the fs laser system (*Coherent- Mira 900-F*), which can be used for multiphoton excitation microscopy. In this case, the multiphoton excitation enables deep penetration into thick samples and eliminates the need of a pinhole aperture because fluorescence emission is restricted to a single focal plane.

Besides, the instrument is equipped with two photomultiplier detectors which permit the simultaneous collection of signals due to two different fluorophores emitting in diverse wavelength ranges.



## REFERENCES:

- <sup>1</sup> Sheik-Bahae, M. et al. *IEEE J. Quantum Electron.*, 1990, 26, 760-769
- <sup>2</sup> Menzel, R. *Photonics 2001*, Berlin, Ed. Springer
- <sup>3</sup> Karna S.,P. and Yeastes, A.T. *Non-linear optical materials: Theory and Modeling*, 1996, ACS Symposium Series N°628
- <sup>4</sup> Xu, C. and Webb, W.W. *J. Opt. Soc. Am. B*, 1996, 13, 481-491
- <sup>5</sup> Rumi, M. et al. *J. Am. Chem. Soc.* 2000, 122, 9500-9510
- <sup>6</sup> Demas, J.N. and Crosby, G.A. *J. of Phys. Chem.*, 1971, 75, 991-1024
- <sup>7</sup> Klonis, N. and Sawyer, W.H. *J. of Fluorescence*, 1996, 6, 147-157
- <sup>8</sup> Madge, D., Wong, R. and Seybold, P.G. *Photochem. and photobiol.*, 2002, 75, 327-334
- <sup>9</sup> Kubin, R.F. and Fletcher, A.N. *Chem. Phys. Lett.*, 1983, 99, 49-52
- <sup>10</sup> Drexhage, J. *Res NBS*, 1976, 80A, 421
- <sup>11</sup> Jones II, Jackson, Halpern, *Chem. Phys Lett.*, 1980, 72, 391
- <sup>12</sup> Jones II, Jackson, Choi, Bergmark *J. Phys. Chem.*, 1985, 89, 294
- <sup>13</sup> Bindhu, C.V. et al. *J. Phys. D: Appl. Phys.* 1996, 29, 1074-1079
- <sup>14</sup> Kubin, R.F. and Fletcher, A.N. *J. of Fluorescence*, 1982, 27, 455-462
- <sup>15</sup> Fisher, M. and Georges, J. *Chem. Phys Lett.*, 1996, 260, 115-118
- <sup>16</sup> Wang, C.H. et al. *J. of Chem. Phys.* 2005, 122, 084509-1-7
- <sup>17</sup> Xu, C. et al. *Bioimaging*, 1996, 4, 198-207



## CHAPTER 5

# Requirements for the realization of an Optical Power Limiter

High power laser systems are widely used at present in science, industry, communication systems, ecology and medicine. In many cases the human operator is directly located near such laser systems and there is the possibility of occasional hitting his eyes by the radiation. Therefore, the important problem is the development of optical devices, protecting eyes from laser radiation. The other important problem is the protection of sensitive photodetectors from the action of high power laser beams.

Nowadays, the commercially available protecting devices are optical filters, which do not transmit radiation at specific laser lines. They have two important disadvantages. Firstly, they are strongly colored in the visible range; besides, their large absorption avoids the correct detection of the signals at low energies when they are placed before a photodetector. Secondly, the filters may become transparent at high input intensity because of saturation of the absorption.

It is therefore important to search some other protection methods for the optimization of the attenuation factor. NLO materials, denoted as “*intelligent*” or “*smart*” materials, can potentially be simple and fast for controlling short optical pulses.

In the next section we define the behavior of an optical limiter and, in particular, the features required for its practical realization. We summarize the physical mechanisms that may lead the real material to approach such ideal behavior. In the successive paragraphs

we will describe the configuration for the optical limiter we have designed and the limits of the materials already used.

## 5.1 Requirements for the Optical limiter

This section deals with the basic concepts and requirements for an optical power limiter. In particular, the main attention will be dedicated to the figures of merit (FOM) required for the eye-protection.

The ideal behavior of an optical limiter<sup>1,2</sup> is schematically presented in Fig. 5.1-a.

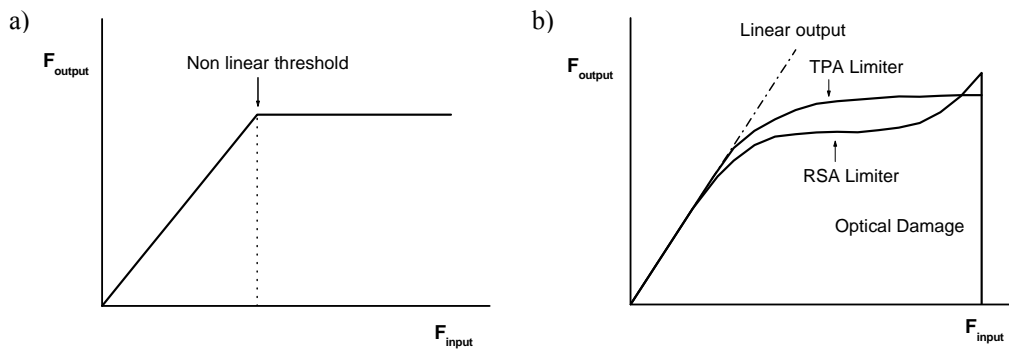


**Fig. 5.1:** Schematic representation of the ideal (a) and the real (b) behaviors of an optical power limiter

The output fluence has a linear dependence with the input one until the nonlinear threshold. At this point nonlinear absorption processes can be activated and the output fluence remains constant. The real behavior, shown in Fig. 5.1-b, is often different from this, because of the deviation of the output fluence from the ideal saturated value at high input intensity, until the optical damage of the material.

The requirements for the optical power limiter are<sup>3,4,5</sup>:

- high transparency (50-70%) for low energy radiation;
- good "photopic transmission", which is defined as the average of the transmission of the protection device in accordance with the eye sensitivity in the visible range<sup>6</sup>:

$$T_{ph.} = \frac{\int_{\Delta\lambda} V(\lambda)S(\lambda)T(\lambda)d\lambda}{\int_{\Delta\lambda} S(\lambda)V(\lambda)d\lambda} \quad 4.1$$

$V(\lambda)$  is the ocular relative spectral sensitivity for day vision,  $S(\lambda)$  is the spectral distribution of a normalized light source and  $T(\lambda)$  is the spectral transmission of the protection filter. For eye protection, the photopic transmission is recommended

to be greater than 15-20%: this value assures that the protection device does not drastically cut any wavelength in all the visible range.

- high attenuation of the transmittance in the nonlinear regime. Regarding the eye protection, retinal damage depends on many factors, like intra-ocular energy, laser wavelength, exposure duration, size and location of the retinal image.<sup>7</sup> Besides, the beam focusing on the retina increases the irradiance or fluence by a factor of  $10^5 - 10^6$ . Since the laser-induced damage threshold (LIDT) for visible radiation is currently considered to be at a fluence of  $1 \text{ J/cm}^2$ , an energy at the entrance of the pupil of a few  $\mu\text{J}$  would lead to irreversible damage. For the present day laser technologies, pulse energies in the 10 mJ range are quite common, meaning that the laser protection device should be capable of a  $10^4$ - $10^5$  attenuation factor (i.e. an optical density of 4-5 in the nonlinear regime).
- high "dynamic range", defined as the ratio between the optical damage threshold and the nonlinear optical threshold. This issue is satisfied if the nonlinear threshold is low and the material is resistant upon irradiation until high input energies.
- sensitive broadband response to long and short pulses, in order to guarantee the protection from tunable lasers;
- fast response times;
- high chemical, mechanical, thermal stabilities;
- low cost.

It is clear that the requirements for an optical power limiter are many and it is difficult to obtain a material matching all of them with high performances. The use of non linear optical properties can provide a useful way to overcome this problem.

### **5.1 Optical limiter based on nonlinear phenomena**

Some of the non linear optical mechanisms useful for optical limiting (OL), and already studied in the literature, are nonlinear absorption<sup>8,9</sup>, nonlinear refraction and scattering<sup>10-16</sup>, self-focusing and self-defocusing, photorefraction<sup>17-19</sup>, free-carrier absorption, intermolecular charge transfer absorption<sup>20-22</sup>, and photochromism.

Many of these NL mechanisms have been observed with fullerenes, carbon black suspensions, and metal porphyrins and phthalocyanines.

Thermal effects<sup>23-26</sup>, induced by the input laser on the solvent, cause a change of the refractive index of the solution. Through open aperture Z-scan measurements on C<sub>60</sub> solutions in toluene a peak-to-valley curve has been recorded, indicating the presence of a negative nonlinearity and, by this way, a self-defocusing effect. OL measurements of C<sub>60</sub> in 1-chloronaphthalene (1-CN) have shown a large thermal contribution to the OL.<sup>23</sup>

Nonlinear scattering<sup>27,28</sup> of C<sub>60</sub> solutions causes the spreading of a fraction of the input beam into a solid angle much wider than the acceptance angle of the detector. Nashold et al.<sup>29</sup> showed that liquid suspensions of carbon black act as optical limiters, as a result of an optical breakdown initiated by the absorption by the carbon particles.

The scattering in carbon black suspension has been compared with that in C<sub>60</sub> solution showing that with fullerenes the absorption, rather than the scattering, is the dominant process.

Finally, TPA<sup>30,31,32</sup> has been observed in the longer wavelength region, from 580 nm to 660 nm.

Some of these mechanisms, such as the nonlinear refraction and scattering or the self-defocusing, do not allow a safe protection from a laser beam especially if the device is used for eyes. In fact, these mechanisms do not involve the absorption of the incident energy and the laser beam can be further refocused in the eye damaging it. Therefore, we have concentrated the study on the materials that show non linear absorption. The more promising results in the visible range are obtained with materials showing Reverse Saturable Absorption (RSA). RSA is a sequential process due to linear absorption followed by absorption from the excited state.

### **5.3 Fullero pyrrolidine as RSA material: a convenient replacement for C<sub>60</sub>**

The RSA materials, largely studied in previous works, are fullerene (C<sub>60</sub>) and its derivatives. Their optical properties derive from the high degree of delocalization of the  $\pi$ -electrons. Owing to its high molecular symmetry, fullerene exhibits a weak ground-state absorption in most of the visible range, attributed to symmetry-forbidden transitions, weakly allowed by vibronic coupling. In the same region, both the singlet and the triplet excited-state absorptions are much stronger, showing the triplet-triplet absorption peak, centered at 750 nm. Fullerene is characterized by a very high value of the quantum yield for intersystem crossing: the triplet state is populated from the lowest singlet excited state in the nanosecond time scale. Unfortunately, fullerene is hardly processible into a solid

optical material, like doped polymers (PMMA<sup>2</sup>) and sol-gel glasses<sup>33</sup>, owing to its very low solubility in solvents commonly used for the preparation.

Much work has been done for the synthesis of fullerene derivatives with functionalizing units that increase the solubility in polar solvents.<sup>6</sup> Some derivatives of C<sub>60</sub> are reported in Fig. 5.2.

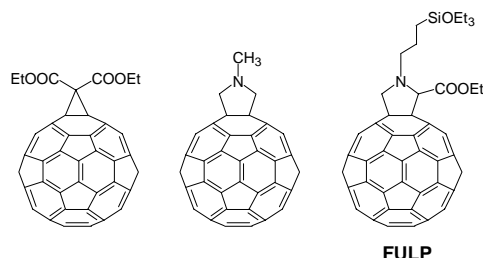


**Fig. 5.2:** Molecular structures of a methanofullerene (on the left), a fulleropyrrolidine (in the center) and an alkoxy-functionalized fulleropyrrolidine, called FULP (on the right)

The presence of the reactive alkoxy groups in FULP allows a good inclusion in sol-gel materials through covalent bonds between the NLO material and the host matrix. For this reason, we have chosen this derivative as RSA system. The FULP is synthesized by the group of proff. G. Scorrano and M. Maggini (University of Padova).

Moreover, since the high fullerene symmetry is here broken, a new transition around 690 nm becomes allowed and fullerene derivatives absorb at longer wavelengths where C<sub>60</sub> is practically transparent. The linear absorption spectra of C<sub>60</sub> (dashed line) and of FULP in toluene (solid line) are reported in Fig. 5.3.

Furthermore, the lowest triplet state absorption shifts to about 700 nm in the fullerene mono-adduct derivatives. The improved overlap between ground state and triplet state absorption, maintaining the absorption cross-section of the triplet higher than that of the ground state, is obviously beneficial for the RSA mechanism, extended to the near-IR range. One of the FOM for RSA materials is the ratio between the cross-sections of the excited and the ground state. For FULP at 690 nm this value is about 56, comparable with that of a Sn-phtalocyanine at 532 nm (FOM=31).<sup>5</sup>

FULP has been successfully included in sol-gel matrices, showing the maintenance of the optical properties from solution to bulk doped samples (see Fig. 5.3) and the possibility to increase its concentration up to the value of  $4 \times 10^{-2}$  M.<sup>6,33-37</sup>

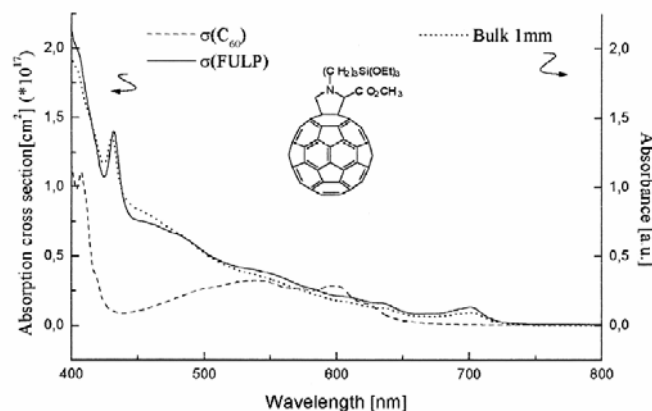


**Fig. 5.3:** UV-Visible absorption spectra of  $C_{60}$  (dash line), FULP in toluene (solid line) and FULP in a solid matrix (dot line). (Ref. 6)

From these considerations one can conclude that our pyrrolidino-fullerenes are good molecules for OL materials in the red region and can be used, incorporated in a sol-gel matrix, for protection devices.

#### 5.4 Optical limiter in a "Tandem" configuration

In our group a new configuration has been designed for the optimization of the performances of the optical limiter device. It is called "Tandem" configuration and considers the possibility of using two materials with different nonlinear optical properties, in order to increase the performances of the final device. In fact, a single material can not completely satisfy all the requirements for an optical limiter.

As anticipated in Chapter 1, the two systems are a Reverse Saturable Absorber and a Two Photon Absorber. The RSA mechanism is characterized by a low nonlinear absorption threshold. The TPA is activated at higher energies, when the RSA material does not work properly because the transmittance does not saturate to a plateau. Besides, if the TPA system is placed before the RSA one, it can protect the latter from the laser damage. These two issues can contribute to the increasing of the dynamic range and of the global attenuation factor.

Since RSA is a sequential absorption process dependent on the laser fluence, the nonlinear optical properties of the RSA materials are conveniently measured with ns or ps laser pulses. This requires that also the TPA material must be characterized in the same temporal regime. As explained in Section 1.7, in the case of multiphoton absorption the in long-pulses regime, the TPA cross-section becomes an effective value and it is denoted as

$\sigma_{\text{TPA}}^{\text{eff}}$ . The values of  $\sigma_{\text{TPA}}^{\text{eff}}$  are generally two orders of magnitude higher than the corresponding values of  $\sigma_{\text{TPA}}$ , measured with ultrashort pulses. Consequently, also the Tandem optical limiter will be tested with ns pulses.

In Chapter 6 we will present the results of both fs and ns characterization of TPA-dyes. It is important to notice that the first characterization is not essential for predicting the optical properties of the dyes for the OL application, in a Tandem configuration. The fs characterization is anyway important to have an idea of the TPA maximum wavelength and the efficiency of the two-photon absorption, also in view of possible applications different from OL. Moreover, the z-scan measurements performed with ns laser pulses permit one to estimate the  $\sigma_{\text{TPA}}^{\text{eff}}$ . These data are more useful for the definition of the performances of an optical limiter based on a TPA material.

### 5.5 Heterocyclic quadrupolar push-pull TPA dye

The two-photon absorber most studied in our laboratory for the OL application is an heteroaromatic quadrupolar A- $\pi$ -D- $\pi$ -A chromophore, which is properly functionalized with hydroxyl groups. This dye is called Bis-OH PEPEP and its molecular formula is depicted in Fig. 5.4. It is synthesized by the group of prof. G.A. Pagani and prof. A. Abboto (University of Milano-Bicocca).

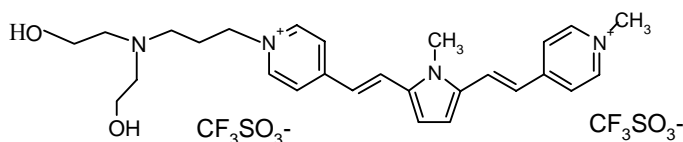


**Fig. 5.4:** Molecular structure of the TPA dye Bis-OH PEPEP

In Bis-OH PEPEP the donor group is a  $\pi$ -excessive pyrrolyl moiety and the acceptor one is a  $\pi$ -deficient heteroaromatic pyridine ring. The electronic properties of heteroaromatic rings have already been successfully employed for the design of efficient push-pull derivatives for second- and third-order nonlinear optical (NLO) activity.<sup>22</sup> Furthermore, the intrinsic tuneable nature of the functionalized rings makes these systems particularly appropriate to finely control electronic and optical properties.

Bis-OH PEPEP has been largely characterized by z-scan and NLT techniques using ns pulses and by TPIF, pump&probe and z-scan measurements in fs regime.<sup>22,38,39</sup>

Furthermore, we have noted that the FULP shows the best efficiency at 690 nm. Hence, also the TPA material should possess a high value of TPA cross-section at the same wavelength.

For completeness, we report in Fig. 5.5 the overall behavior of the spectra for PEPEP, measured with ns and fs pulses. They show an increase of the TPA cross section with decreasing wavelengths for both temporal regimes. This is well understood on the basis of the pre-resonance effect,<sup>40-41</sup> i.e. the influence of the one photon resonance when the pumping wavelengths approaches the one-photon allowed transition. With ns pulses the proximity of the one-photon resonance also implies an effective transfer of population to the first excited state and promotes further sequential absorption, according to the mechanism of Eq. 1.78 in Chapter 1. Moreover, as a consequence of having a multiphoton sequential absorption process, the TPA cross-section in ns regime shows a dependence on the incident intensity.

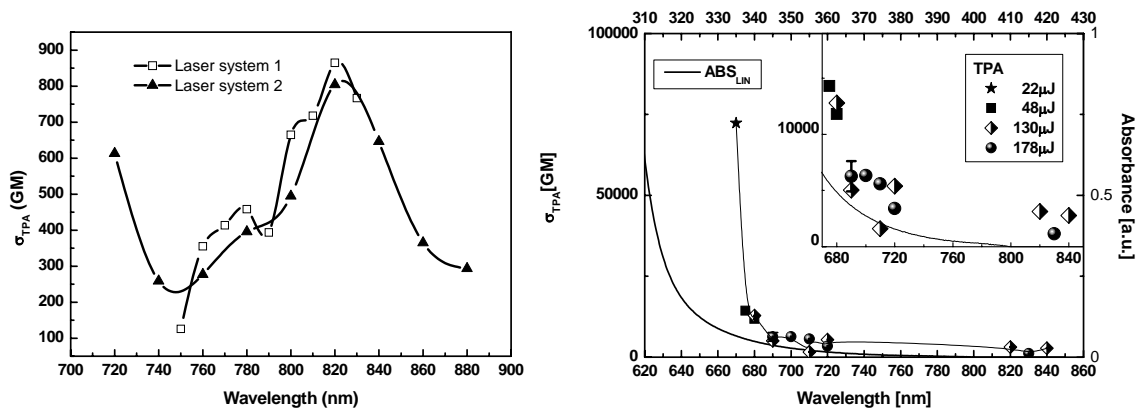


**Fig. 5.5:** TPA spectra of PEPEP in DMSO determined by TPIF method (on the left) and by z-scan technique in ns regime (on the right)

Focusing only on the non linear optical performance of PEPEP at 690 nm, we can observe that the  $\sigma_{TPA}^{eff}$  is about 6000-7000 GM.

In previous trials<sup>42</sup>, we have used both the FULP and the Bis-OH PEPEP as NLO-active materials embedded in a sol-gel matrix. The obtained samples were characterized singularly and in tandem configuration using NLT measurements. Figure 5.6 shows the NLT curves of a sol-gel sample doped with FULP, one doped with Bis-OH PEPEP and of the two materials composing the tandem configuration. The inset in Fig. 5.6a shows the sol-gel disks doped with FULP and Bis-OH PEPEP respectively.

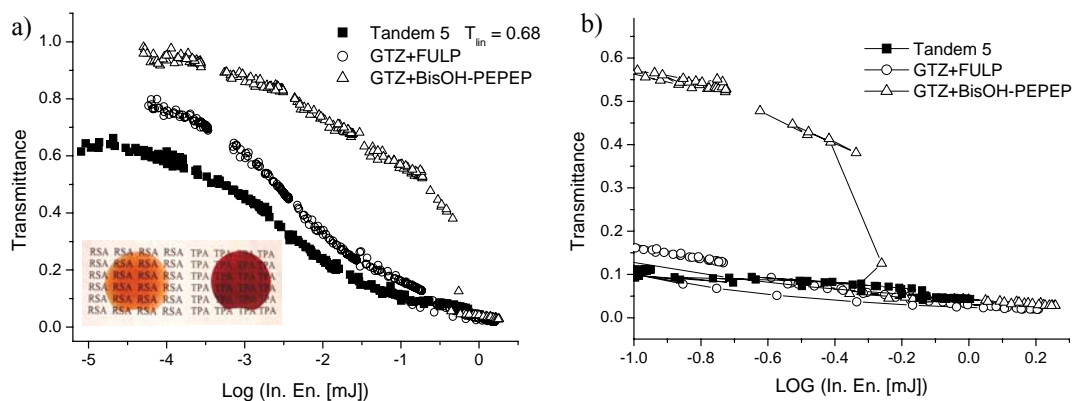


**Fig. 5.6:** NLT curves of a FULP-doped sol-gel sample (triangles), a Bis-OH PEPEP-doped material (circles) and of tandem limiter (full squares). The graph b) is the zoom of the region at high input energy.

It is possible to observe that the Bis-OH PEPEP system is not so efficient to increase the optical attenuation at high input energy, because of the  $\sigma_{\text{TPA}}^{\text{eff}}$  value which is too low for permitting the activation at sufficiently low energies and the increasing of the global attenuation factor.

The curves reported above evidence another important feature characterizing the real behavior of an optical limiter device: the damage threshold. In fact, the host material is damaged by the focalized laser beam at high energies (about 500  $\mu\text{J}$ ). The measurements show that the Bis-OH PEPEP has an activation threshold too close to the laser damage threshold of the matrix.

These results suggest two possible ways to overcome these negative effects. The first way consists on the testing of new TPA systems in order to find a compound with  $\sigma_{\text{TPA}}^{\text{eff}}$  higher than 7000 GM (reaching a theoretical estimate of 50000 GM for an efficient optical limiter based on TPA material). The second one consists in the study on new host matrices characterized by a higher laser damage resistance. The two aspects will be analyzed in Chapters 6 and 7.



## REFERENCES:

- <sup>1</sup> Swalen, J. D., Kajzar, F. *Nonlinear Optics*, 2001, 27, 13-32
- <sup>2</sup> Bozio, R. et al. *Photoactive Organic Materials*, 1996, 159-176, Kluwer Academic Publisher, Kajzar, F. ed.
- <sup>3</sup> Swalen, J. D., Kajzar, F. *Nonlinear Optics*, 2001, 27, 13-32
- <sup>4</sup> Hollins. R. C. *Current Opinion in Solid State and Materials Science*, 1994, 4, 189-196
- <sup>5</sup> Signorini, R., Bozio, R.; Prato, M. *Optical Limiting Applications in Fullerene: from synthesis to optoelectronic properties*, 2002, Kluwer Academic Publisher, D.M. Guldi and N. Martin eds.
- <sup>6</sup> Signorini, R. et al. *Carbon*, 2000, 38, 1653-1662
- <sup>7</sup> Hollins, R.C. Goals, Architectures and Materials for Broadband Eye Protection, *Nonlinear Optics*, 2001, 27(1-4), 1-11
- <sup>8</sup> Li, C. et al. *Chem. Phys. Lett.* 2004, 400, 569-572
- <sup>9</sup> Hongbing Z. et al. *Mater. Lett.* 2005, 59, 1395-1399
- <sup>10</sup> Fougeanet, F.; Fabre, J. C. *Mat. Res. Soc. Symp. Proc.*, 1997, 479, 293-298
- <sup>11</sup> Nashold, K. M. et al. *Nonlinear Optics*, 2001, 27, 101-120
- <sup>12</sup> Barbosa Neto, N.M. et al. *Applied Physics B-Lasers and Optics*, 2004, 78, 1-3
- <sup>13</sup> Sun, X. et al. *Applied Physics Letters*, 1998, 73, 3632-3634
- <sup>14</sup> Vivien, L. et al. *Optics Communications*, 2000, 174, 271-275
- <sup>15</sup> Mishra, S. R. *Chem. Phys. Lett.* 2000, 317, 510-514
- <sup>16</sup> Chin, K. C. et al. *Chem. Phys. Lett.* 2005, 409, 85-88
- <sup>17</sup> Wolfersberger, D. et al. *Nonlinear Optics*, 2001, 27, 405-412
- <sup>18</sup> West, R.; Wang, Y.; Goodson, T. J. *J. Phys. Chem. B*, 2003, 107, 3419-3426
- <sup>19</sup> Derkowska, B. et al. *Nonlinear Optics*, 2001, 27, 413-421
- <sup>20</sup> Reinhardt, B.A. et al. *Chem. Mater.*, 1998, 10, 1863-1874
- <sup>21</sup> Albota, M. et al. *Science*, 1998, 281, 1653-1656
- <sup>22</sup> Abbotto, A. et al. *Organic Letters*, 2002, 4, 1495-1498
- <sup>23</sup> Justus, B.L., et al. *Opt. Lett.*, 1997, 18, 1603-1605
- <sup>24</sup> Henary, F.Z. et al., *Adv. Mater.*, 1993, 5, 930-934
- <sup>25</sup> Harilal, S.S. et al. *J. of Appl. Phys.*, 1999, 86, 1388-1392
- <sup>26</sup> Wei, T.-H. et al. *Chem. Phys. Lett.*, 2000, 318, 53-57
- <sup>27</sup> Mishra, S.R. et al. *J. Phys. B: At. Mol. Opt. Phys.*, 1994, 27, L157-L163
- <sup>28</sup> Mishra, S.R. et al. *Appl. Phys. A.*, 1996, 63, 223-226
- <sup>29</sup> Nashold, K.M. and Walter, D.P. *J. Opt. Soc. Am.*, 1995, 12 (7), 1228-1237
- <sup>30</sup> Strohkendl, F.P. et al. *J. Phys. Chem. B*, 1997, 101, 8802-8808
- <sup>31</sup> Rao, S.V. et al. *Chem. Phys. Lett.*, 1998, 297, 491-498
- <sup>32</sup> Bezel, I.V. et al. *Chem. Phys. Lett.*, 1994, 218, 475-478
- <sup>33</sup> Brusatin, G.; Innocenzi, P. *J. of Sol-Gel Science and Technology*, 2001, 22, 189-204
- <sup>34</sup> Signorini, R. et al. *Multiphoton and Light Driven Multielectron Processes in Organics: New Phenomena, Materials and Applications*, 2000, 83-98, kluwer Academic Publishers, Kajzar, F. ed.
- <sup>35</sup> Innocenzi, P. et al. *J. of Sol-Gel Science and Technology*, 2000, 19, 263-266
- <sup>36</sup> Signorini, R. et al. *Nonlinear Optics*, 2001, 27, 193-208
- <sup>37</sup> Brusatin, G. et al. *Nonlinear Optics*, 2001, 27, 259-267
- <sup>38</sup> Signorini, R. et al. *Proceedings of the SPIE* 2003, 4797, 1-14
- <sup>39</sup> Signorini, R. et al. *submitted to J. Phys. Chem. A*
- <sup>40</sup> B. Dick, R.M. Hochstrasser, H.P. Trommsdorff, "Resonant Molecular Optics in Nonlinear Properties of Organic Molecules and Crystals", vol.2, p.159
- <sup>41</sup> Drobizhev, M. et al. *Chem. Phys. Lett.* 2003, 370, 690
- <sup>42</sup> Fortunati, I. *Tesi di laurea: "Materiali ibridi sol-gel per la limitazione ottica basata su assorbimenti multifotonici"*, Univ. of Padova, 2004



## CHAPTER 6

# **Characterization of new materials showing TPA properties**

One of the possible ways to optimize the performances of our optical limiter device is the employment of a TPA dye with higher TPA cross-section. By this way, the TPA threshold energy becomes lower, while maintaining analogous dye concentrations and avoiding the reduction of the photopic transmittance.

In this work we have concentrated the attention on the study and the characterization of new systems, obtained thanks to collaboration with different groups. These compounds have been characterized with ns and fs pulse experiments. In the next sections we will report results regarding the TPIF measurements with fs pulses and the z-scan analyses with ns pulses. The fs characterization permits us to determine the pure and the effective TPA spectra of the chromophores. By this way it becomes possible to sort out the more promising compounds and to perform a basic study on the structure-property relationships for the nonlinear optical interaction. The compounds showing best performances in the fs experiments have been successively characterized in the ns regime, to find the best materials for OL applications.

## 6.1 Non linear optical characterization of TPA dyes in solution

We have characterized several classes of compounds showing TPA properties. The list below can be useful to best follow the sequence in the exposed results:

- dipolar push-pull systems;
- dimers of PEP and MePEP;
- quadrupolar and Zn(II) octupolar systems;
- squaraines;
- semiconductor quantum dots;
- porphyrins;
- helicenes.

## 6.2 TPIF characterization of push-pull systems

The TPIF characterization is performed following the methodology already described in Chapter 4. For every compound analyzed, the experimental details will be reported. We generally have used Fluorescein and Rhodamine B as references and the final data are often the average of two data sets. The excitation wavelength range is between 730 and 920 nm.

For every sample we have also recorded the two-photon excitation fluorescence spectrum with the methodology presented in Subection 4.3.9. This spectrum nicely overlaps that obtained with a spectrofluorimeter, analogously to the graphs in Fig. 4.11 for Rhodamine B and Fluorescein. When the sample concentration is high, we can observe a red-shift in the two-photon excited spectrum caused by the reabsorption effect.

### - Dipolar molecules

We have studied three push-pull systems with dipolar structure synthesized by the group of Prof. G.A. Pagani and Prof. A. Abbotto (University of Milano-Bicocca). The molecular structures are reported in Fig. 6.1. These dipolar charge-transfer (CT) systems are the simplest TPA materials we can study.

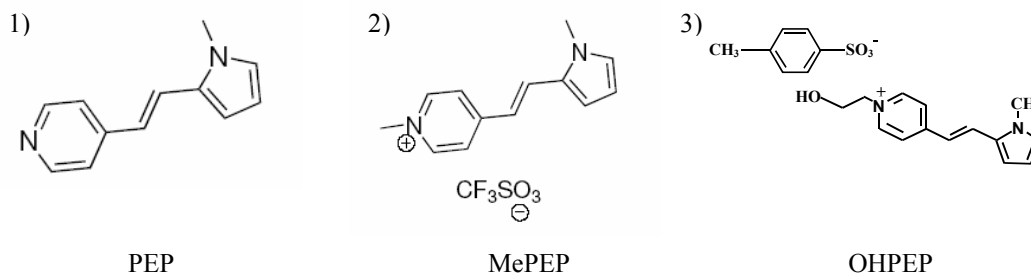


**Fig. 6.1:** Chemical structures of dipolar D- $\pi$ -A molecules called PEP (1), MePEP (2), OHPEP (3)

In these systems the donor group is a pyrrolyl moiety and the acceptor one is a pyridine (in PEP), a methyl-pyridinium (in MePEP), a hydroxyl-pyridinium group (in OHPEP).

The linear optical properties are summarized in Table 6.I.

SAMPLE	$\lambda_{\text{MAX}}$ (OPA) [nm]	$\lambda_{\text{MAX}}$ (Emiss) [nm]	FQY
PEP in DMSO	362	500	$(1.13 \pm 0.08) * 10^{-3}$
MePEP in DMSO	438	528	$0.005 \pm 0.001$
OHPEP in DMSO	439	508	$0.005 \pm 0.001$

**Table 6.I:** Linear optical properties of D- $\pi$ -A systems: maximum wavelengths of one photon absorption (OPA) and emission spectra and fluorescence quantum yield (FQY) data

As a consequence of the increasing substituent polarity on going from PEP to OHPEP, the absorption wavelength increases. In fact, a polar solvent stabilizes the separated charge excited state and the transition energy decreases.

The fluorescence quantum yields of these compounds are very low, this implies the use of solutions with high concentrations (up to  $6 \times 10^{-4}$  M). The TPA spectra are reported in Fig. 6.2, together with the OPA spectra for a comparison. The TPA wavelengths are halved for a direct comparison.

For the three compounds the TPA and the OPA spectra are centred at the same wavelength, which means that the same transition is allowed by one-photon and two-photon absorption, according to the theoretical prediction for non centrosymmetric molecules.

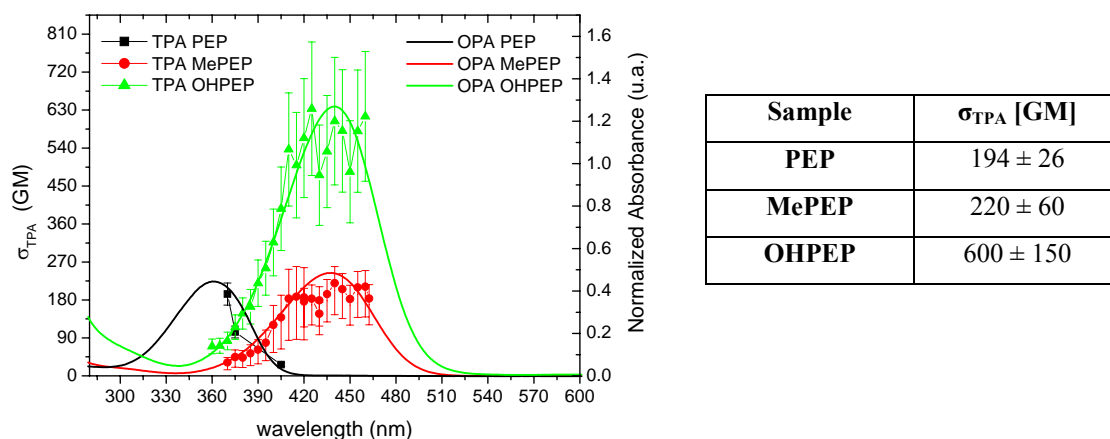


**Fig. 6.2:** OPA and TPA spectra of PEP (black symbols), MePEP (red symbols) and OHPEP (green symbols). The table on the right reports the TPA cross-section at the absorption maxima.

The low FQY values induce high uncertainties on the absolute value of the TPA cross-section. Nevertheless, we can observe an increased TPA response in OHPEP, suggesting an increased strength of the charge transfer dipole moment in comparison to MePEP.

We have also studied other dipolar organic molecules, namely, two terpyridine derivatives, called TD2 and TD3 (see Fig. 6.3), and their complexes with a Zn(II), in collaboration with the group of Prof. R. Ugo (University of Milano). The use of coordination metal complexes can be a useful way to modify the optical properties of the chromophores, as explained in paragraph 2.3. In this case we can explore the optical properties of two compounds mono-coordinated to a Zn(II) ion.

The ZnTD3Cl<sub>2</sub> complex is unstable.

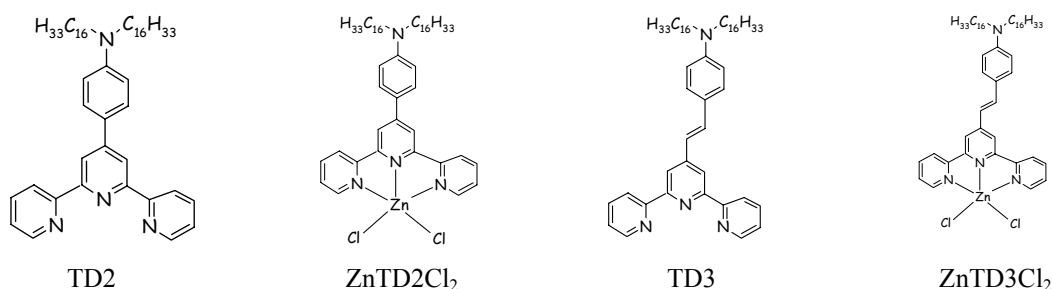


**Fig. 6.3:** Molecular structure of terpyridines (TD2 and TD3) and their complexes with Zn(II).

The linear and non linear optical properties of these systems are reported below.

Sample	$\lambda$ (OPA) [nm]	$\lambda$ (Em.) [nm]	FQY	$\sigma_{\text{TPA}}$ [GM]
TD2 in $\text{CH}_2\text{Cl}_2$	362	465	$0.42 \pm 0.01$	$62 \pm 8$
ZnTD2Cl <sub>2</sub> in $\text{CH}_2\text{Cl}_2$	427	535	$0.34 \pm 0.03$	$220 \pm 33$
TD3 in $\text{CH}_2\text{Cl}_2$	399	532	$0.40 \pm 0.04$	$370 \pm 55$

**Table 6.II:** Linear and nonlinear absorption and emission properties of TD2 and TD3. The FQY are calculated vs Coumarina 540A.

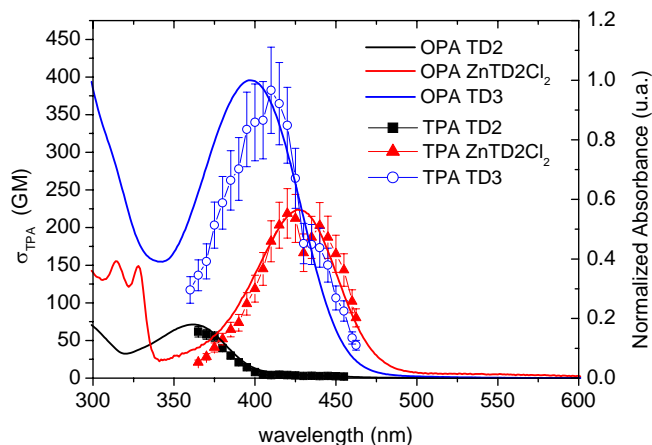


**Fig. 6.4:** TPA and OPA spectra of TD2, ZnTD2Cl<sub>2</sub> and TD3 in  $\text{CH}_2\text{Cl}_2$

The  $\sigma_{\text{TPA}}$  of the more  $\pi$ -delocalized terpyridine TD3 is higher (6-times) than that of TD2 and the TPA band of TD3 is red-shifted with respect to TD2. Analogous results are reported in Ref. [1]. One possible origin might be the increase of the dipole moment difference  $\Delta\mu_{eg}$  simply due to the lengthening of the  $\pi$  bridge.

The coordination of TD2 with a cationic Zn(II) center leads to an increase of the  $\sigma_{\text{TPA}}$  of 3.5 times. In this case, the red-shift is more pronounced if compared with the absorption of the ligand. This can be due to the increasing of the acceptor properties of the terpyridine ring, resulting in a bathochromic shift of the Intra Ligand Charge Transfer (ILCT).

If the terpyridine TD2 and TD3 can be simply modelled with the two-form two-state system introduced in Chapter 1 for D- $\pi$ -A molecules, the understanding of the enhancement effect for the Zn(II) complex can be more difficult. These experimental results are under theoretical investigation in collaboration with the group of Prof. A. Painelli (University of Parma).

Some other attempts are dedicated to the synthesis of the homoleptic complex  $\text{Zn}(\text{TD2})_2$  and the complex  $\text{Ru}(\text{TD2})\text{Cl}_3$ . Both of them can not be characterized because of the instability and the partial dissociation of the complexes. In particular, from the fluorescence spectra investigation it is possible to evidence the presence of the bis-

chelated, the mono-chelated and the free ligand components upon excitation at different wavelengths.

The complex with Ru(II) might be interesting because of the presence of the spin allowed  $d \rightarrow \pi$  Metal-to-Ligand-Charge Transfer band (MTLC) in the UV-Visible spectrum.<sup>2</sup> The MLCT band is red-shifted with respect to the ILCT. These systems are characterized by an efficient inter-system crossing process which promotes the transfer from  $^1\text{MTLC}$  to  $^3\text{MTLC}$  state. The  $^3\text{MTLC}$  state rapidly decays to the high spin d-d (metal centered, MC) states which are deactivated through non-radiative pathways. Unfortunately Ru-Terpyridine complexes are practically not luminescence at room temperature<sup>3</sup> and they cannot be characterized by TPIF technique.

### - Dimeric structures of PEP and MePEP

The PEP and MePEP are used as monomers for the synthesis of dimeric structures connected by an alkylic chain with different length. These systems have been provided by the group of Prof. A. Abboto (University of Milano-Bicocca).

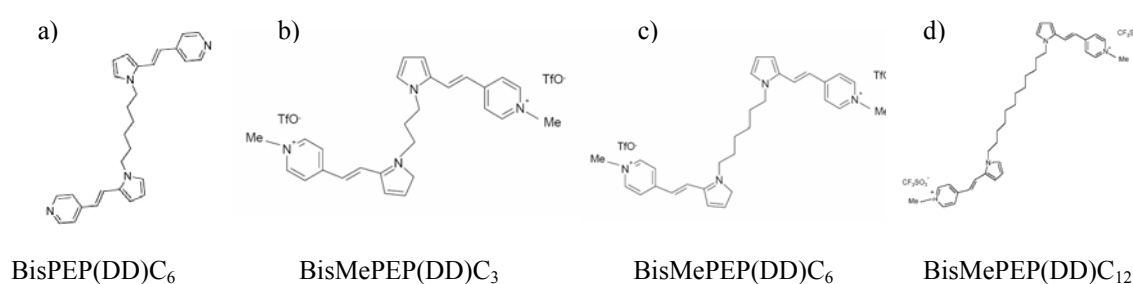


**Fig. 6.5:** Chemical structures of dimeric systems: BisPEP(DD)C<sub>6</sub> (a); BisMePEP(DD)C<sub>3</sub> (b); BisMePEP(DD)C<sub>6</sub> (c); BisMePEP(DD)C<sub>12</sub> (d)

The study of these dimeric structures is aimed to the investigation of the effect on the nonlinear optical response of the alkylic chain length, that acts as a spacer between the two monomer units. In such molecular aggregates there is the possibility to have a delocalization of electronic excitation among the monomer units. The presence of an exciton can influence the optical properties, especially the nonlinear optical response.

The optical properties are summarized in Table 6.III. If the linker moiety between the dipolar units permits an excitonic coupling between them, the investigation of the series of molecules in Fig. 6.5 allows us to experimentally investigate the effects of changing the inter-chromophoric distance on the linear optical properties and the TPA cross

section. From the linear absorption and emission spectral properties, it is evident that the alkyl chain is unable to permit the interaction between the monomers. In fact, MePEP and its dimers are charge separated systems and in solution they presumably tend to keep off, in order to stabilize their charges. This is more probable for the systems connected by long chains, as occurs in C<sub>6</sub> and in C<sub>12</sub> dimers.

Regarding the linear absorption and the emission properties, only the compound BisMePEP(DD)C<sub>3</sub> seems to show a small interaction between the dipolar units, as confirmed by the blue-shift of the absorption band (only 4 nm).

Analogous considerations can be made also for the TPA optical response. If there is an interaction, the  $\sigma_{\text{TPA}}$  should be enhanced by a cooperative effect, in respect to the simple summation of the monomers contributions.

Sample	$\lambda$ (OPA) [nm]	$\lambda$ (Em.) [nm]	FQY	$\sigma_{\text{TPA}}$ [GM]
PEP	362	438	$(1.13 \pm 0.08) * 10^{-3}$	$194 \pm 26$
BisPEP(DD)C <sub>6</sub>	362	440	$(1.65 \pm 0.07) * 10^{-3}$	$200 \pm 25$
MePEP	438	527	$0.005 \pm 0.001$	$220 \pm 60$
BisMePEP(DD)C <sub>3</sub>	434	527	$0.008 \pm 0.0003$	$335 \pm 40$
BisMePEP(DD)C <sub>6</sub>	438	527	$0.012 \pm 0.0004$	$330 \pm 65$
BisMePEP(DD)C <sub>12</sub>	440	527	$0.012 \pm 0.0007$	$335 \pm 40$

**Table 6.III:** Linear absorption, emission and TPA properties of PEP and MePEP and their dimers in DMSO solutions

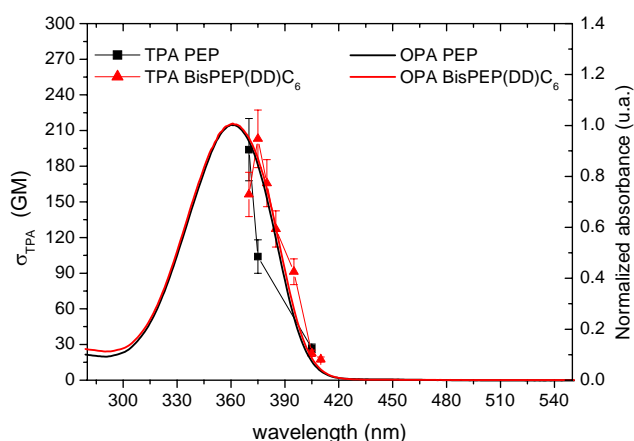


**Fig. 6.6:** One-photon and two-photon spectra of PEP and BisPEP(DD)C<sub>6</sub>

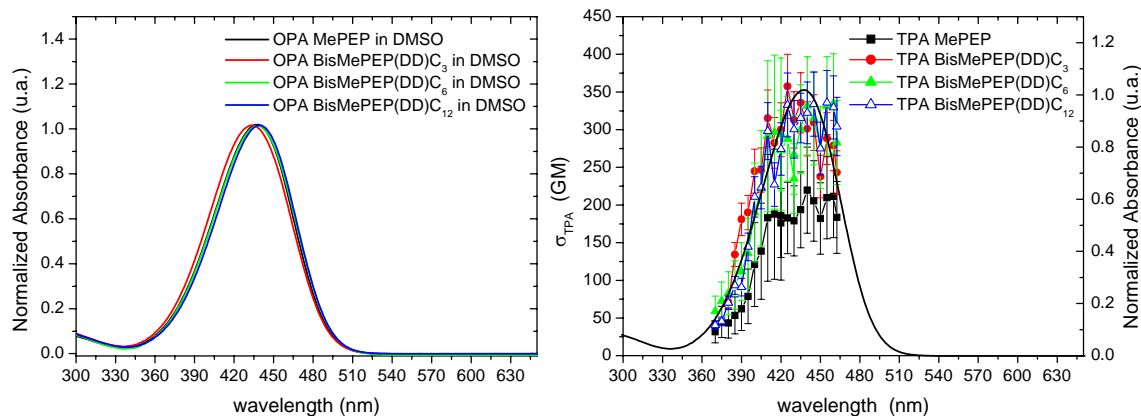


**Fig. 6.7:** One-photon absorption spectra (on the left) and two-photon absorption spectra (on the right) of MePEP and its dimers

The nonlinear optical responses of PEP and BisPEP(DD)C<sub>6</sub> are similar, even if we should expect a  $\sigma_{\text{TPA}}$  value for the dimer double with respect to the monomer unit. The dimers of MePEP possess similar TPA cross-sections which are 1.5-times the  $\sigma_{\text{TPA}}$  of the MePEP. Considering the large error bars, determined also by the low FQY data, we can assume that this factor is well approximated by the value 2.

### - Quadrupolar and octupolar structures

In collaboration with the groups of Prof. A. Abbotto and Prof. R. Ugo (Universities of Milano-Bicocca and Milano), two quadrupolar molecules are synthesised and their molecular structures are depicted below. As described in Chapter 2, one strategy to increase the nonlinear optical response for CT compounds consists in the enlargement of the  $\pi$ -delocalization. Following this strategy, we study the NLO properties of two quadrupolar systems.

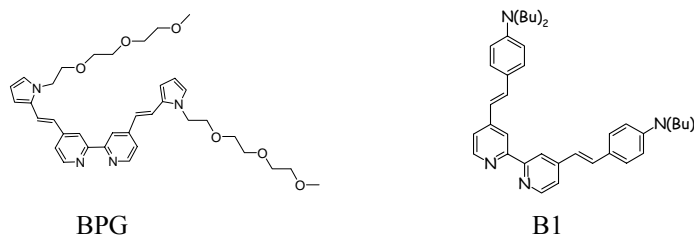


**Fig. 6.8:** Molecular structures of BPG and B1 compounds

In these chromophores, the acceptor unit is a bipyrindine and the donor is a  $\pi$ -excessive pyrrolyl ring in BPG and a dialkylanilino group in B1. The lateral tris(ethylene glycol)

mono-methyl ether chains are introduced in BPG in order to impart solubility in hydrophilic and polar solvents. BPG and B1 are further used as ligands for octupolar complexes with Zn(II).<sup>4</sup> B1 is also employed for the synthesis of a dipolar chromophore Zn(B1)Cl<sub>2</sub>, coordinated with one Zn(II).

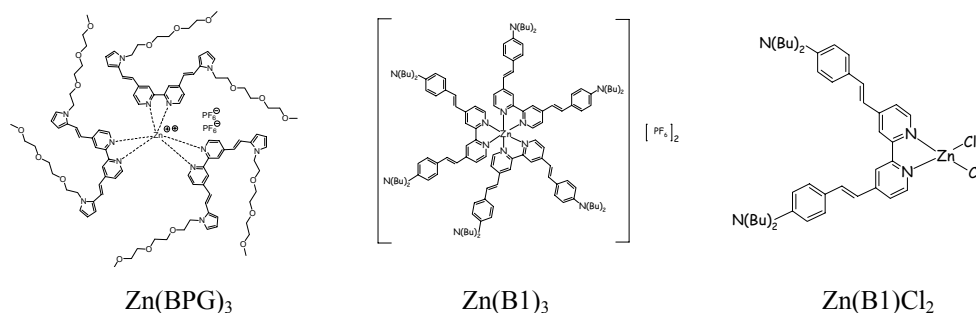


**Fig. 6.9:** The investigated octupolar molecules Zn(BPG)<sub>3</sub> and Zn(B1)<sub>3</sub> and the dipolar system Zn(B1)Cl<sub>2</sub>

The investigation on the TPA properties of octupolar complexes, compared to the free ligands, is aimed to detect any eventual enhancement effects, as theoretically predicted in Ref. [5]. Since there is no ligand field stabilization effect, Zn(II) has the ability to expand its coordination sphere and it is known to give tetrahedral complexes or octahedral complexes with diimine ligands. It is also possible to design either dipolar or octupolar D<sub>2d</sub> and D<sub>3</sub> molecules by simple controlled combination of one, two, or three bipyridyl ligands with Zn(II).<sup>6</sup>

The optical properties of our chromophores are shown in Table 6.IV.

Sample	$\lambda$ (OPA) [nm]	$\lambda$ (Em.) [nm]	FQY	$\lambda$ (TPA) [nm]	$\sigma_{\text{TPA}}$ [GM]
BPG in CH <sub>2</sub> Cl <sub>2</sub>	374	450	0.005 ± 0.003	730	190 ± 115
Zn(BPG) <sub>3</sub> in CH <sub>2</sub> Cl <sub>2</sub>	422	559	0.058 ± 0.005	820	530 ± 80
B1 in CH <sub>2</sub> Cl <sub>2</sub>	400	490	0.11 ± 0.01	760	275 ± 66
Zn(B1)Cl <sub>2</sub> in CH <sub>2</sub> Cl <sub>2</sub>	462	606	0.088 ± 0.009	920	1350 ± 205
Zn(B1) <sub>3</sub> in CH <sub>2</sub> Cl <sub>2</sub>	473	604	0.04 ± 0.01	895	1340 ± 280

**Table 6.IV:** Linear absorption, emission and TPA properties of BPG and B1 and their complexes with Zn(II)

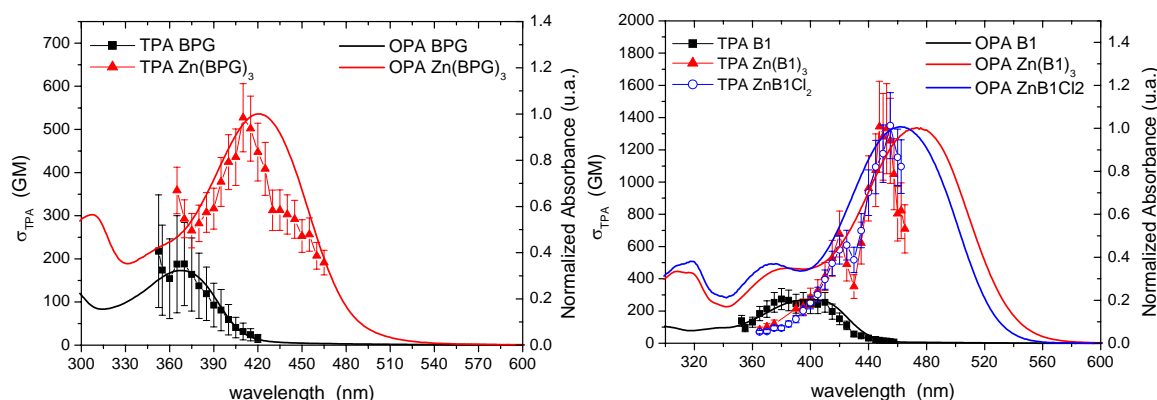


**Fig. 6.10:** OPA and TPA spectra of BPG and Zn(BPG)<sub>3</sub> (on the left) and of B1, Zn(B1)<sub>3</sub> and ZnB1Cl<sub>2</sub> (on the right) in CH<sub>2</sub>Cl<sub>2</sub>

Regarding the linear optical properties, it is possible to observe, in both cases, an intense red-shift of the absorption band for the complexes with respect to the free ligand. The bathochromic shift is of 48 nm for Zn(BPG)<sub>3</sub> and of 62 and 73 nm for ZnB1Cl<sub>2</sub> and Zn(B1)<sub>3</sub> respectively. The last data are in agreement with that reported in Ref. [6].

These compounds exhibit also high molecular extinction coefficients. The oscillator strengths<sup>7</sup> follow a 1:1.1:2.6 ratio for B1, ZnB1Cl<sub>2</sub> and Zn(B1)<sub>3</sub> respectively, as expected for noninteracting subchromophores (1:1:3). Similarly, for BPG and Zn(BPG)<sub>3</sub> the ratio between the oscillator strengths is equal to 1:3.1. These data are in agreement with the absence of an extended delocalization through Zn(II) between the bipyridyl subchromophoric, passing from the free ligand to the octupolar complex.

The large shift observed between the absorption and fluorescence maxima ( $\sim 4500 - 5500 \text{ cm}^{-1}$ ) is attributed to solvation effect. This effect is typical of molecules characterized by a strong dipole moment variation from the ground to the excited electronic state when dissolved in a polar solvent.<sup>8</sup> For the free ligands this is indeed the case. For the Zn(II) compounds, instead, a somewhat different process should be invoked for such an effect, since these systems do not possess a permanent dipole moment. If the ligands do not interact strongly with each other in the molecule, it is conceivable that the solvent will affect each of the three ligands in a separate way. Under this assumption, it is not possible to apply the simple dielectric continuum theory to take account of the solvation effect observed for the Zn(II) compounds.

Regarding the TPA spectra, it is possible to observe that the TPA spectra of the ligands follow the same trend as the OPA spectra. This behaviour is typical for non-centrosymmetric structures. Indeed, these molecular systems are free to rotate around

the 2,2'-bipyridine bond; therefore the present measurements suggest that the ligands are preferentially arranged in a non-centrosymmetric structure. Also for ZnB1Cl<sub>2</sub> the TPA and the OPA spectra peak at the same wavelength. In this case the presence of the Zn(II) avoids the rotation of the two arms and the structure is non-centrosymmetric.

Instead, the TPA spectra of the octupolar complexes are blue-shifted with respect to the OPA spectra, as predicted for centrosymmetric structures. In particular, we consider that, in the spectrum of Zn(B1)<sub>3</sub>, the second peak at about 840 (420 nm) will fall within the experimental error.

This blue shift can be promoted by the *D*<sub>3</sub> octupolar structure that the three ligands assume in the metal complex. Upon coordination the three excited states of the single ligands will give rise to three new states: two degenerate levels of symmetry *E* and one non-degenerate of symmetry *A*<sub>1</sub>. The energy difference between these two sets of states and their spectral position with respect to the ground state will depend on the magnitude and nature of the interactions existing between the three ligands connected by the central Zn(II). While the states *E* are both one- and two-photon allowed, state *A*<sub>1</sub> is just two-photon allowed. In the OPA spectrum only the transition towards the *E* symmetry levels should contribute, while in the TPA spectrum also the transition towards *A*<sub>1</sub> should appear. The blue-shift observed for the peak maxima going from the OPA to the TPA spectrum can be caused by the non-negligible contribution of the *A*<sub>1</sub> state to the TPA spectrum. Furthermore, it indicates that the *A*<sub>1</sub> state falls at higher energy with respect to the *E* degenerate states. On the other hand, the small spectral shift observed and the fact that there is just one single band in the TPA spectrum (pointing out that there is a small difference in the transitions energies towards the *E* and *A*<sub>1</sub> levels), indicate that the interactions between the ILCT transitions of the three ligands in the metal complex is presumably weak.

By comparing the TPA peak value, we can see that the presence of the Zn(II) in ZnB1Cl<sub>2</sub> promotes an increase of 4.9 times in the  $\sigma_{\text{TPA}}$  with respect to the ligand B1. This result is analogous to that found for ZnTD2Cl<sub>2</sub>.

Instead, if we see the  $\sigma_{\text{TPA}}$  of the octupolar complex Zn(BPG)<sub>3</sub>, we can observe that its TPA cross-section is equal to the sum of the individual contributions of the three bipyridyl ligands. The lack of enhancement of the TPA cross section observed in our measurements may be explained by the inability of the central Zn(II) to propagate the intramolecular charge transfer process between ligands and between ligands and the

central Zn(II) thus producing other types of cooperative CT transitions. The delocalized  $\pi$ -electrons are thus confined to the individual ligands.

This comment is not apparently true for the complex Zn(B1)<sub>3</sub> which has a TPA cross-section 4.8 times greater than the B1 ligand. In this case we must point out that, if the FQY of the complex is calculated using the Rhodamine B as reference, it becomes equal to 0.07 instead of 0.04. Using this value for normalizing the TPIF data, the peak  $\sigma_{\text{TPA}}$  of the complex reduces to 805 GM which is about 3 times of the cross-section of the ligand. This misalignment is the consequence of the great range of the standards fluorescence quantum yield values reported in the literature (as exposed in subsection 4.3.5). For the Zn(II) complex, it should be more correct to use the Rhodamine B as standard, whose emission spectrum is in the same region of the sample. Therefore, for the determination of the FQY of these compounds, we have chosen as standard the coumarin 540A, whose FQY is recalibrated through our measurements. By this way, it is possible to compare the TPA cross-section of different molecules and their complexes.

In any case, such conclusion is in partial agreement with the authors of the theoretical work<sup>5</sup> when they admit that the coupling among the ligands in the octahedral metal complex “is small”.

### 6.3 TPIF characterization of squaraines

Another class of molecules we have studied is that of the squaraine molecules synthesized by the L. Beverina (University of Milano-Bicocca).

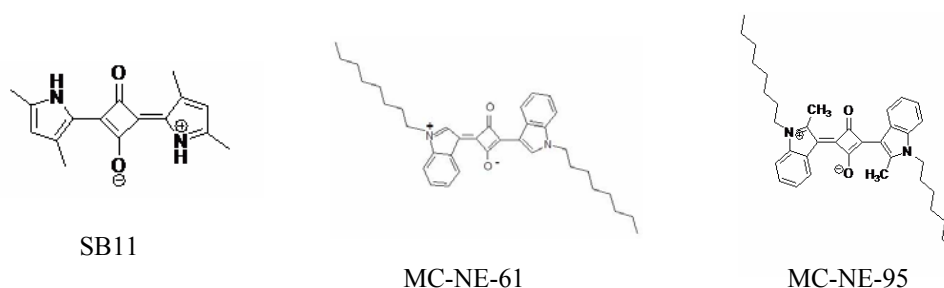


**Fig. 6.11:** Molecular structures of the squaraines SB11, MC-NE-61 and MC-NE-95

The squaraine dyes are attractive candidates for TPA studies owing to their very large ground-state transition dipole moments, near-parallel orientation of their ground and excited-state transition dipole moments, and the sharply rising low-energy side of their

linear absorption spectra allowing significant intermediate state resonance enhancement of the TPA response.<sup>9-11</sup>

Squaraine dyes consist of two electron donating endgroups (D) and a central electron withdrawing 1,3-disubstituted C<sub>4</sub>O<sub>2</sub>-unit (A) forming a D-A-D system. Squaraine SB11 has a more simple structure where the donor is a pyrrolyl ring. In MC-NE-61 and MC-NE-95 the donor groups are pyrrolyl-derivatives.

The absorption and emission spectra are shown in Fig. 6.12.

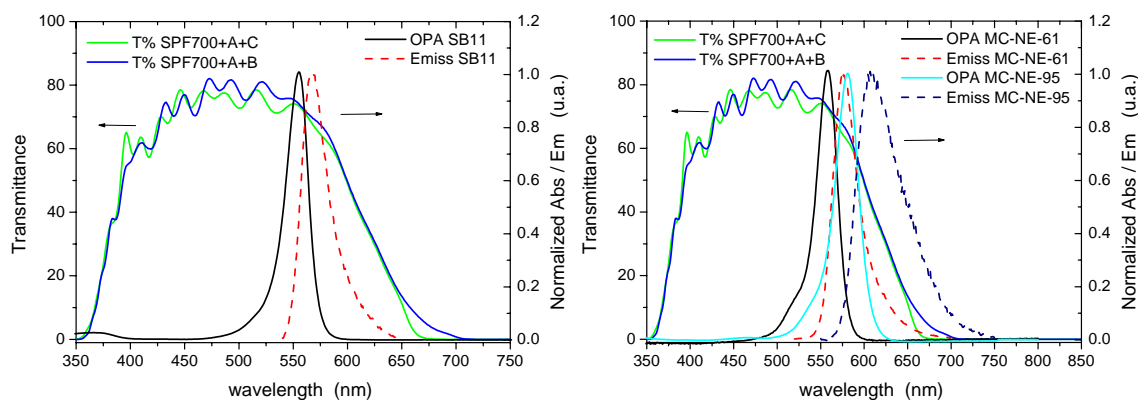


**Fig. 6.12:** OPA and emission spectra of SB11 (on the left) and of MC-NE-61 and MC-NE-95 (on the right). All compounds are dissolved in CH<sub>2</sub>Cl<sub>2</sub>.

Sample	$\lambda$ (OPA) [nm]	$\lambda$ (Em.) [nm]	FQY	$\lambda$ (TPA) [nm]	$\sigma_{\text{TPA}}$ [GM]
SB11 in CH <sub>2</sub> Cl <sub>2</sub>	555	568	$0.021 \pm 0.001$	NR	NR
MC-NE-61 in CH <sub>2</sub> Cl <sub>2</sub>	558	576	$0.53 \pm 0.01$	< 730	$450 \pm 50$
MC-NE-95 in CH <sub>2</sub> Cl <sub>2</sub>	580	610	$0.05 \pm 0.01$	< 740	$220 \pm 50$

**Table 6.V:** Linear absorption, emission and TPA properties of squaraines

In Fig. 6.12 we report also the transmittance spectra of the two configurations of filters that are used in front of the detector in TPIF set-up (see par. 4.3.8).

The one-photon absorption peak of the derivative MC-NE-61 is only few nm shifted in respect to SB11 squaraine. The derivative MC-NE-95 has instead an absorption peak more red-shifted. The only difference between this compound and the MC-NE-61 is the presence of the methyl groups on the pyrrolyl moiety. These lateral groups should break

the planarity of the squaraine structure. A consequence is the drastic reduction of the fluorescence quantum yield of MC-NE-95.

SB11 is characterized by a small Stokes shift causing an intense reabsorption of the fluorescence signal. This aspect, together with the probably small TPA cross-section, avoids the determination of any TPA data.

Thanks to the centro-symmetric structures, the lowest one-photon state is not allowed by two-photon absorption for both the other squaraines, as it is possible to observe in Fig. 6.13. With our excitation range, we cannot detect the TPA peaks.

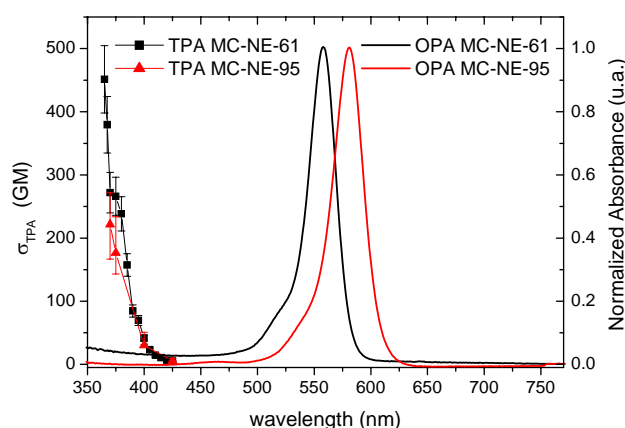


**Fig. 6.13:** OPA and TPA spectra of MC-NE-61 and MC-NE-95 in  $\text{CH}_2\text{Cl}_2$

Because of the high fluorescence quantum yield value, the TPIF measurements of MC-NE-61 can be performed using a solution with low dye concentration ( $C \sim 2 \cdot 10^{-5}$  M). For MC-NE-95 instead the concentration is increased up to  $3 \cdot 10^{-4}$  M. In this case the reabsorption of the fluorescence is very high (about 40%). Moreover, the emission spectrum is partially shifted from the transparency window of the filters used in front of the photomultiplier tube, as shown in Fig. 6.12. These two aspects induce a strong correction factor to the TPA data which are affected by great uncertainties. Therefore we cannot do any considerations about the effect of planarity breaking on the TPA response and on the  $\pi$ -delocalization length.

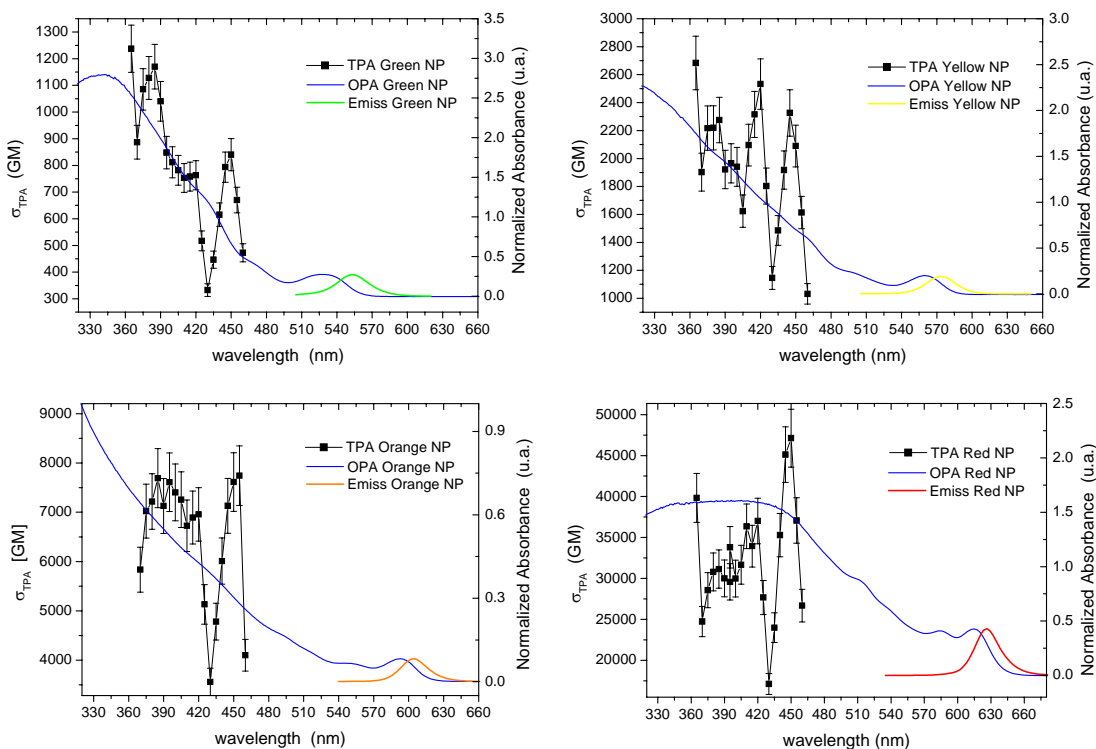
#### 6.4 TPIF characterization of semiconductor Quantum Dots

In this last section, we report the results on the TPIF characterization of semiconductor quantum dots provided from the collaboration with Prof. P. Mulvaney (University of Melbourne - Australia) and A. Martucci (University of Padova).

We have already seen that in the literature an enhancement of the third-order nonlinearity characterizing the QDs is reported, especially if compared to that of organic compounds. In this context, we have characterized different types of nanocrystals (NC) in way of evidence possible correlations between their physical and optical properties.

These systems are core-shell CdSe-CdS-ZnS nanocrystals (NC) of different sizes which determine the wavelength of the emission spectra.<sup>12</sup> The radii of four different colors emitters are 2 nm (green,  $\lambda_{PL}= 554$  nm), 2.6 nm (yellow,  $\lambda_{PL}= 573$  nm), 2.9 nm (orange,  $\lambda_{PL}= 604$  nm) and 3.2 nm (red,  $\lambda_{PL}= 626$  nm). The fluorescence quantum yields of these nanoparticles (NP) in chloroform solution are 1, 0.78, 0.49 and 0.46, respectively.

CdSe NCs are overcoated with a layer of a wide-gap inorganic semiconductor such as ZnS, which seems to be the best way for the surface passivation.<sup>13</sup> This allows one to greatly improve “electronic” passivation of NC surfaces, resulting, in particular, in a significant increase in the photoluminescence quantum yield. Moreover, the FQY values decrease when the dimensions of the nanoparticles increase, as a consequence of an increasing surface trapping and, consequently, nonradiative carrier losses that partially deactivate the fluorescence.<sup>14</sup>



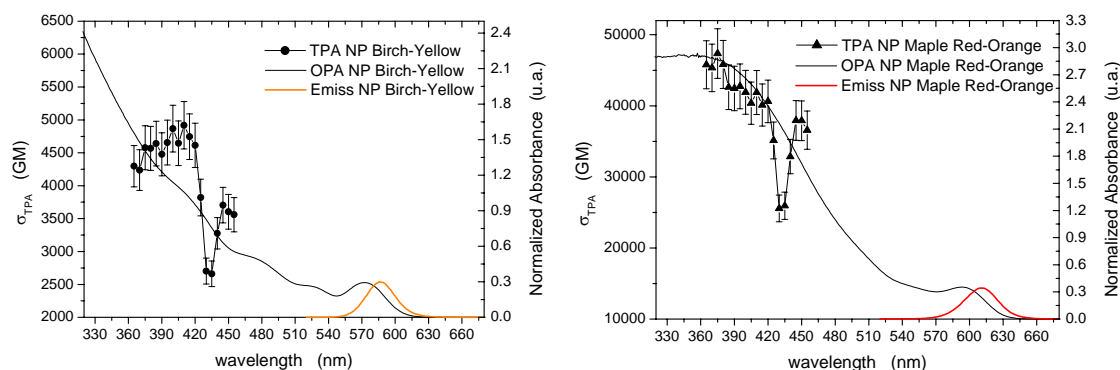
**Fig. 6.14:** OPA, emission and TPA spectra of Green, Yellow, Orange and Red nanocrystals in  $\text{CHCl}_3$

Figure 6.14 shows the linear and nonlinear optical properties of the nanocrystals. Regarding the TPA response, it is possible to observe that the value of  $\sigma_{\text{CdSe}}$  is proportional to the volume of the nanocrystal, as reported in [15]. The negative peak at about 430 nm (860 nm), present in all the TPA spectra, is an artefact due to the use of Rhodamine B as reference compound.

Finally, we have also analyzed the TPA properties of two semiconductor quantum dots samples purchased from *Evident Technology*. They have a core-shell structure where the core is of CdSe and the shell is of ZnS. As written in their specification sheet, the diameters of the nanocrystals is about 3.2 (sample Birch-Yellow) and 5.2 nm (sample Maple Red-Orange). These dimensions, and consequently their molar extinction coefficients, are determined by the first excitonic peak position using the formula for CdSe nanoparticles reported in Ref. [16].

It is important to note the difference between the nominal absorption peak wavelengths (572 and 610 nm for Birch-Yellow and Maple Red-Orange respectively) and the experimental ones (570 and 593 nm). We have used the nominal molar extinction coefficients to determine the concentrations of the solutions employed in TPIF measurements. The FQY of Birch-Yellow and Maple Red-Orange are 0.55 and 0.48 respectively using both Rhodamine B and Rhodamine 6G as standards.

We therefore have some doubts regarding the absolute values of the  $\sigma_{\text{TPA}}^{\text{eff}}$  reported in Fig. 6.15.



**Fig. 6.15:** OPA, emission and TPA spectra of NP Birch-Yellow (on the left) and of NP Maple Red-Orange (on the right)

From the experimental data, we can observe that the  $\sigma_{\text{TPA}}$  increase for NP with greater dimensions, analogously to the above results.

The values of TPA cross-section for semiconductor NCs are the highest ones if compared with the TPA cross-sections of organic systems. They are a very promising material for TPA applications.

### 6.5 Z-scan characterization using ns pulses

In this section, we report the results of the characterization of some chromophores upon excitation with ns pulses. The set-up for the z-scan method has been described in paragraph 4.1. The dye solution is held in a 1 mm-quartz cell.

For ns-regime characterization, we followed the same thread of the arguments of the fs-characterization results. We have firstly analyzed dipolar push-pull compounds and successively quadrupolar and octupolar systems. Afterwards, we have characterized both squaraines and porphyrins with high delocalization of the  $\pi$ -electrons. Finally also the semiconductor quantum dots are analyzed in ns temporal regime.

#### - Characterization of push-pull systems

The dipolar systems, such as PEP, MePEP and OHPEP, are also characterized in ns temporal regime, even if their  $\sigma_{\text{TPA}}^{\text{eff}}$  are too low to be measured with this technique. The required dye concentrations for performing Z-scan measurements are in generally high (up to  $3 \times 10^{-2}$  M). However, if the  $\sigma_{\text{TPA}}^{\text{eff}}$  is low, the detection of the variation in the transmitted signal becomes difficult because of the incipient damage of the cell.

Major attention has been dedicated to the study of the quadrupolar BPG and B1 systems and their complexes with Zn(II), reported in Figs. 6.16 and 6.17.

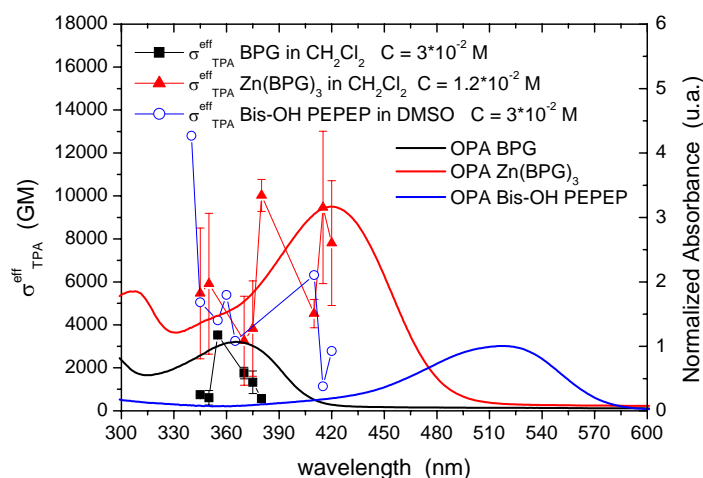


**Fig. 6.16:** OPA and TPA spectra of BPG (black line),  $\text{Zn}(\text{BPG})_3$  (red line) and Bis-OH PEPEP (blue line) from ns z-scan

Figure 6.16 shows the TPA spectra of BPG and  $\text{Zn}(\text{BPG})_3$  in  $\text{CH}_2\text{Cl}_2$  and their OPA spectra, where the TPA wavelengths are halved. For comparison we report also the TPA spectra of the Bis-OH PEPEP, the TPA molecule used in previous tests of our optical limiter. All these data are collected using analogous incident energy in order to directly compare the optical responses of the different chromophores, which are energy-dependent in ns regime.

We can observe that the  $\sigma_{\text{TPA}}^{\text{eff}}$  values differ by more than one order of magnitude from that measured with fs pulses. This is due to a multiphoton sequential absorption taking place with long pulses. From the data in Fig. 6.16 it is difficult to highlight a defined and well shaped peak in the TPA spectra, especially for the octupolar complex. This is probable due to the large amount of energetic levels contributing in different ways in the sum-over-states expression for TPA cross-section. By this way it is possible to determine only an average value for the  $\sigma_{\text{TPA}}^{\text{eff}}$ .

The ns-TPA Bis-OH PEPEP, shows an increase of the TPA cross section with decreasing wavelengths. This behaviour is analogous to that reported in Fig. 5.5.

The octupolar complex  $\text{Zn}(\text{BPG})_3$  has a maximum  $\sigma_{\text{TPA}}^{\text{eff}}$  value of about 10000 GM. This value is a little higher than that of Bis-OH PEPEP.

The results about the ligand B1 and its complex  $\text{Zn}(\text{B1})_3$  are difficult to compare because of the diverse intensity required for the activation of nonlinear absorption at every excitation wavelength. In Fig. 6.17 the TPA and OPA spectra of B1 and  $\text{Zn}(\text{B1})_3$  are shown where the employed energies are explicitly pointed out.

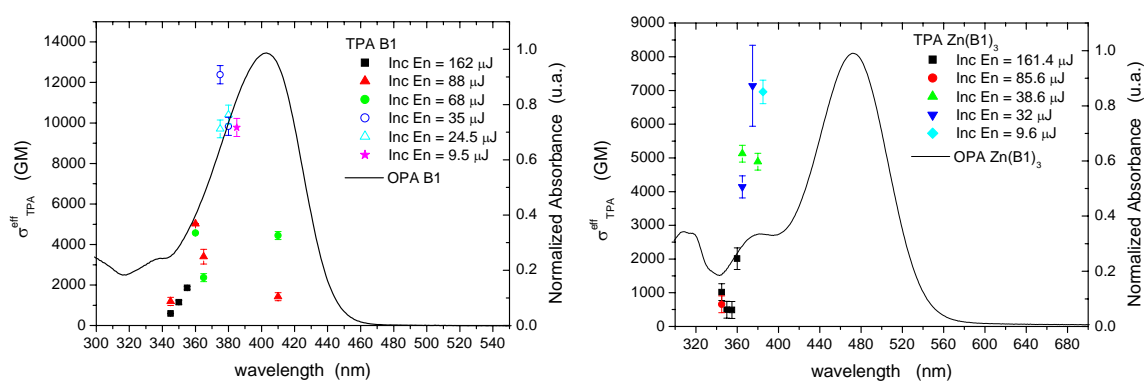


Fig. 6.17: OPA and TPA spectra of B1 and  $\text{Zn}(\text{B1})_3$  in  $\text{CH}_2\text{Cl}_2$

We can note that the nonlinear absorption of B1 is activated at lower energies in correspondence with the absorption maximum at about 400 nm. For the  $\text{Zn}(\text{II})$  complex the threshold energy diminishes and  $\sigma_{\text{TPA}}^{\text{eff}}$  increases at higher wavelengths, until 770 nm

(385 nm). In this case the increasing of  $\sigma_{\text{TPA}}^{\text{eff}}$  can be due to the transition towards the  $A_1$  symmetry level which is two-photon allowed, as described above.

### - Characterization of squaraines and porphyrins

Within the three squaraine systems characterized using fs pulses, we have chosen to characterize the MC-NE-61 system, showing the best fs performance, also with ns pulses. The obtained TPA spectrum is shown in Fig. 6.18.

The  $\sigma_{\text{TPA}}^{\text{eff}}$  value of MC-NE-61 is about 10000 GM in the range 690-730 nm. The value is almost constant in this region, even if the squaraine showed an increase of the instantaneous  $\sigma_{\text{TPA}}$  in TPIF measurements.

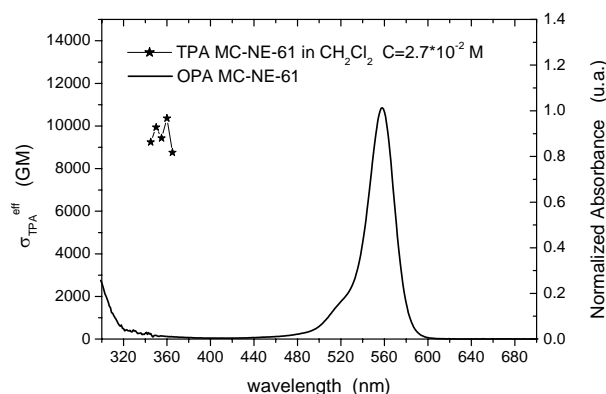


**Fig. 6.18:** OPA and TPA spectra of squaraine MC-NE-61 in  $\text{CH}_2\text{Cl}_2$

Another class of molecules, studied using z-scan technique with ns laser pulses, is that of porphyrins. We have characterized an asymmetric porphyrin system synthesised by the group of Prof. M. Pizzotti (University of Milano).

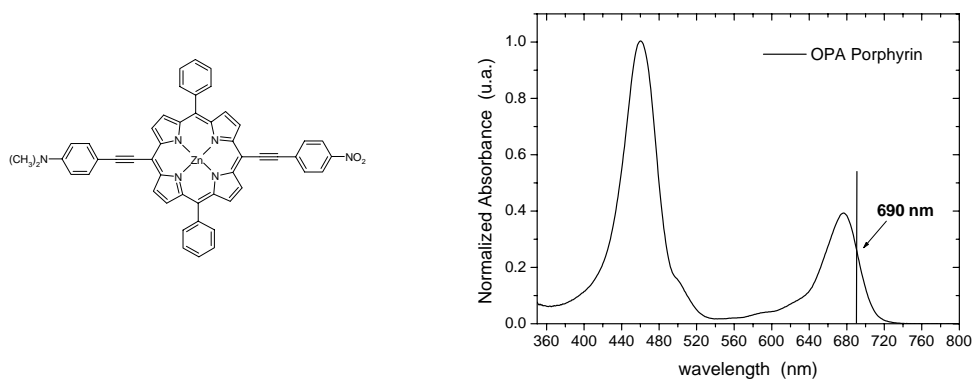


**Fig. 6.19:** Chemical structure of asymmetric porphyrin and the OPA spectrum

The high absorbance of the Q band centered at about 680 nm does not permit us to measure the TPA cross-section.

The other four systems we have analysed are synthesized by the group of Prof. M. Prato (University of Trieste). Their chemical structures are reported in Fig. 6.20.

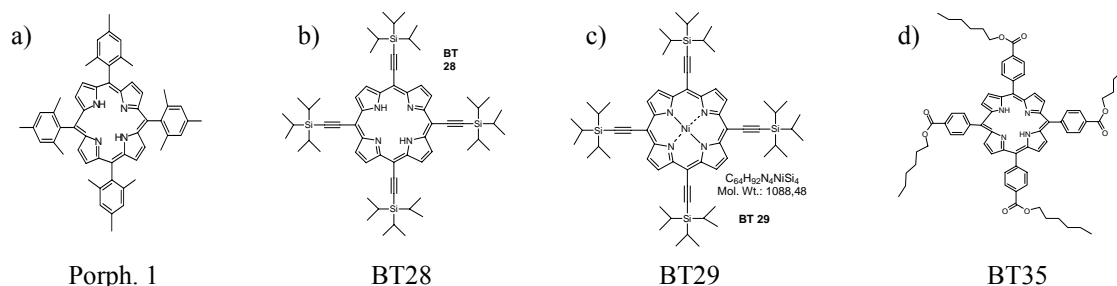


**Fig. 6.20:** Chemical structures of Porph.1 (a), BT28 (b), BT29 (c) and BT35 (d)

The simplest system is the porphyrin 1, while in the BT35 the phenyl units are functionalized by a carbonyl derivative group. In BT28 the phenyl units are substituted by four lateral groups linked to the central ring by ethynic bridge and BT29 is analogous to BT28 coordinating a Ni atom in the center.

For these systems we have performed the z-scan characterization only at 690 nm, which is the working wavelength of our Tandem Optical limiter. The linear absorption spectra of the porphyrins are shown below. The right panel represents the zoom around 690 nm of the absorption spectra of the solutions used for the measurements.

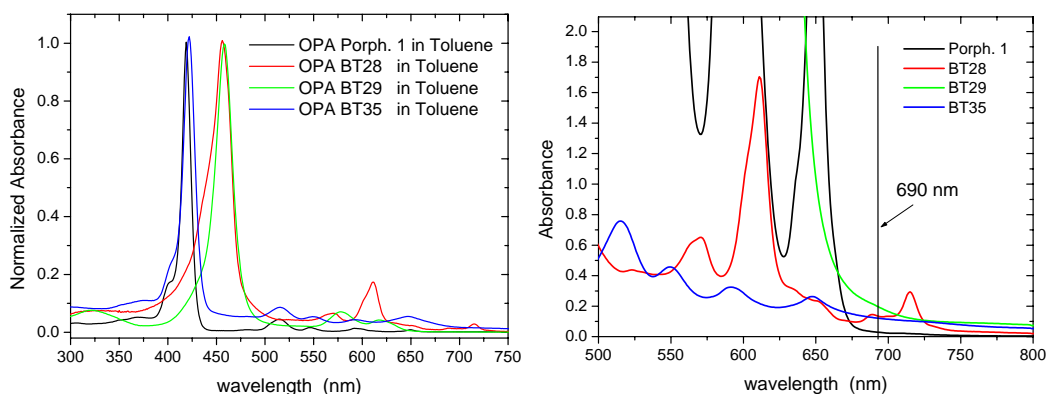


**Fig. 6.21:** Normalized OPA spectra of the studied porphyrins; on the right: the zoom of the absorption spectra of the solutions for z-scan measurements in the region between 500 and 800 nm

The main problem using these systems is the presence of Q bands at low energies which reduces the photopic transmittance, especially if high concentrations are employed. This fact is more noticeable for BT28 and BT35, and we need to reduce their concentrations down to  $4 \times 10^{-4}$  M to perform the z-scan measurements. Because of the low concentration, the BT35 does not show any TPA properties.

For the other porphyrins, the trend of the  $\sigma_{\text{TPA}}^{\text{eff}}$  versus the incident energy is shown in graph 6.22. The inset is the zoom of the lower values range of the  $\sigma_{\text{TPA}}^{\text{eff}}$ .

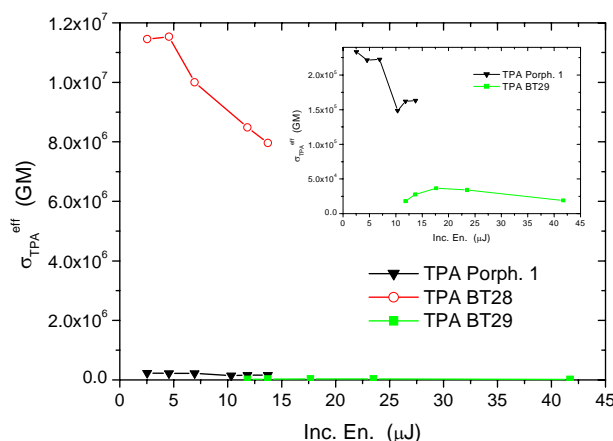


**Fig. 6.22:**  $\sigma_{\text{TPA}}^{\text{eff}}$  data versus the incident energies

The nonlinear threshold energies are lower than that used for the activation of the previously studied push-pull systems. The porphyrin BT28 possesses the highest value of  $\sigma_{\text{TPA}}^{\text{eff}}$  ( $1.1 \times 10^7$  GM) which is 50-times higher than the porphyrin 1. We note that, after the coordination with the Ni(II) in BT29, the  $\sigma_{\text{TPA}}^{\text{eff}}$  is reduces of 400 times with respect to BT28.

For these systems we have performed also the NLT measurements at 690 nm and the obtained curves, corrected for the linear scattering, are shown in Fig. 6.23.

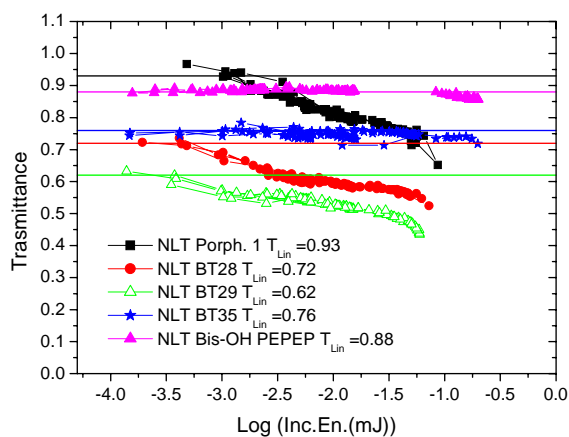


**Fig. 6.23:** NLT curves at 690 nm relative to the porphyrins and Bis-OH PEPEP

The NLT curve of BT35 is substantially constant with the incident energies. The porphyrin 1 seems to have a NLT curve that is similar to an RSA one. The transmittances of BT28 and BT29 decrease at low incident energies (until 4  $\mu\text{J}$ ). After this value, they become nearly constant and decrease again at high energies, when the multiphoton absorption can take place.

### - Characterization of helicenes

We have also characterized a helicene system and its derivative containing an acceptor group, provided by the group of Prof. S. Maiorana (University of Milano). These molecules have been already studied for their second-order NLO properties caused by the motion of the polarizable electrons along the helix path.<sup>17</sup>

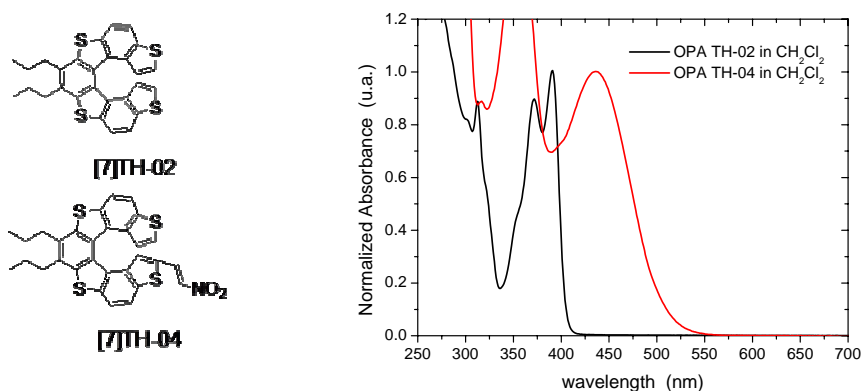


Fig. 6.24: Helicenes TH-02 and TH-04 molecular structure (on the left) and their OPA spectra (on the right)

The z-scan measurements are performed only at 690 nm. At this wavelength, the TH-02 does not show any detectable TPA response while the TH-04 has a  $\sigma_{\text{TPA}}^{\text{eff}}$  value of about 4000 GM, even if the system is substituted with a strong acceptor moiety.

### - Characterization of semiconductor quantum dots

Finally, we have analyzed the multiphoton absorption properties of the two semiconductor quantum dots purchased by *Evident Technology*. For the determination of the concentration of the QDs solutions we refer again to the extinction coefficients provided by the manufacturer. Therefore we have some doubts regarding also the absolute values of the  $\sigma_{\text{TPA}}^{\text{eff}}$ .

Sample	1 <sup>st</sup> excitonic peak (nm-exper.)	Nomin. Conc. [M]	$\sigma_{\text{TPA}}^{\text{eff}}$ @ 690 nm [GM]
QDs Birch-Yellow	572	$1.44 \times 10^{-4}$	$\sim 2 \times 10^5$
QDs Maple Red-Orange	593	$8 \times 10^{-5}$	$\sim 6 \times 10^5$

**Table 6.VI:** Absorption data, nominal concentration and TPA cross-section at 690 nm of QDs sample in Toluene solution

Analogously to the considerations done for TPIF characterization of QDs, we can observe that also the  $\sigma_{\text{TPA}}^{\text{eff}}$  is proportional to the volume of the nanocrystals. The TPA cross-sections of Maple Red-Orange and of Birch-Yellow QDs are respectively about 100 and 60 times higher than the value of Bis-OH PEPEP.

With the same solutions we have collected the NLT curves. In order to exclude the eventual fluorescence signal from the detection, we have used a short pass filter (onset at 645 nm) before the photodiode. The obtained curves are depicted in Fig. 6.25.

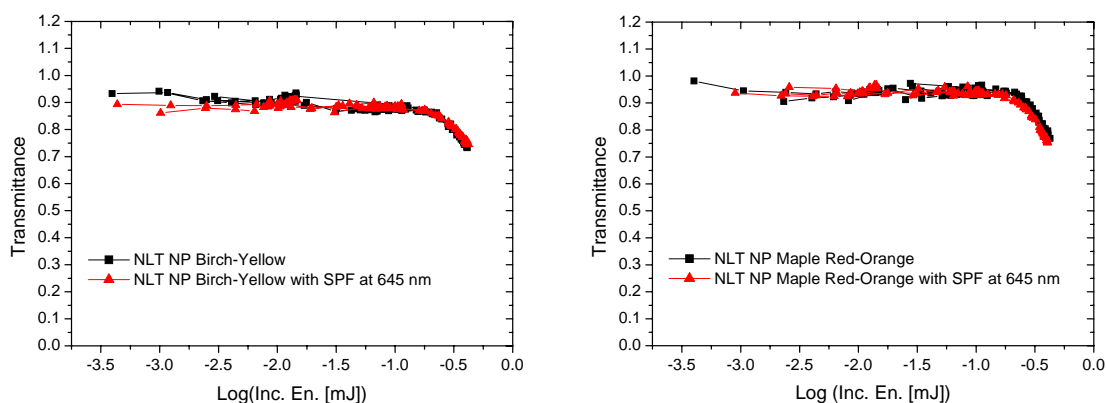


**Fig. 6.25:** NLT curves of NP Birch-Yellow (on the left) and of NP Maple Red-Orange (on the right). The red curve is collected with a SPF before the detector.

We can note that the NLT curves collected with and without the filter are substantially identical, showing that the fluorescence signal is not detected by the photodiode. The ratio between the linear and nonlinear transmittance is about 1.2 for both samples. At higher energies the cell is damaged.

## 6.7 Conclusions of the nonlinear optical characterization of TPA absorbers in solution

In this chapter we have presented the results of the characterization of TPA dyes in solution, using both fs and ns pulses. Looking at the results obtained from TPIF measurements, the dipolar complex with Zn(II), inducing a strong increase in the acceptor strength, seems to be a promising molecule. Another class of interesting systems is that of semiconductor quantum dots. The nanocrystals with greater dimensions exhibit a TPA cross-section of 40000 GM which is the highest value measured in fs temporal regime.

When we employ ns laser pulses, the  $\sigma_{\text{TPA}}^{\text{eff}}$  accounts for the optical response due to the multiphoton absorption process. By this way, the measured  $\sigma_{\text{TPA}}^{\text{eff}}$  values are more than one order of magnitude greater than those measured with fs pulses. If we concentrate on the TPA response at 690 nm, the target for our optical limiter, we can observe that the push-pull systems do not exhibit much higher TPA cross-sections with respect to the quadrupolar Bis-OH PEPEP. Instead, the porphyrin 1 can be a promising material for optical limiting and its hydroxyl-functionalized derivative is under preparation.

Finally, also the semiconductor QDs have high  $\sigma_{\text{TPA}}^{\text{eff}}$  values. In the next Chapter we will show some attempts at their inclusion in a sol-gel matrix.

## REFERENCES:

- <sup>1</sup> Righetto, S. *J. of Mater. Chem.* 2006, 16, 1439-1444
- <sup>2</sup> Maury, O. and Le Bozec H. *Acc. of Chem Res.* 2005, 38, 691-704
- <sup>3</sup> Sauvage, J.-P. et al. *Chem. Rev.* 1994, 94, 993-1019
- <sup>4</sup> Mazzucato, S., Fortunati, I. et al. *Phys. Chem. Chem. Phys.* 2007, 9, 2999-3005
- <sup>5</sup> Liu, X. J. et al. *J. Chem. Phys.* 2004, 120, 11493-11499
- <sup>6</sup> Senechal, K. et al. *J. Am. Chem. Soc.* 2002, 124, 4560-4561
- <sup>7</sup> The oscillator strength  $f$  is estimated by the following relationship:  $f=4.319 \cdot 10^{-9} \cdot \epsilon \cdot \nu_{1/2}$  where  $\epsilon$  is the molar absorptivity and  $\nu_{1/2}$  represents the half-height bandwidth ( $\text{cm}^{-1}$ )
- <sup>8</sup> J.R. Lackowicz, *Principles of Fluorescence Spectroscopy*, Kluwer Academic/Plenum, New York, 1999
- <sup>9</sup> Fu, J. et al. *J. Opt. Soc. Am. B* 2007, 24, 67-76
- <sup>10</sup> Scherer, D. et al. *Chem. Phys.* 2002, 279, 179-207
- <sup>11</sup> Chung, S. J. et al. *J. Am. Chem. Soc.* 2006, 128, 14444-14445
- <sup>12</sup> Jasieniak, J. *J. Adv. Mater. In press*
- <sup>13</sup> Klimov, V. I. et al. *Science*, 2000, 287, 1011-1013
- <sup>14</sup> Klimov, V. I. et al. *Science*, 2000, 290, 314-317
- <sup>15</sup> Klimov, V. I. *J. Phys. Chem. B* 2000, 104, 6112-6123
- <sup>16</sup> Yu, W. W. et al. *Chem. Mater.* 2003, 15 (14), 2854-2860, corrected in volume 15, 2003
- <sup>17</sup> Clays, K. et al. *Chem. Phys. Lett.* 2003, 372, 438-442



## CHAPTER 7

# Synthesis and characterization of new sol-gel matrices for Optical Limiting

The second part of the study for the realization of an optical power limiting device consists in the synthesis and characterization of the materials that can be used as host for the NLO active dyes. In this context we employ organic-inorganic hybrid materials, composed of inorganic oxide structures and interpenetrated cross-linked organic polymers. The hybrid network can combine the most important glasslike with the polymerlike properties.<sup>1-3</sup> This aspect can be particularly useful when large laser power density is used, because of the possible higher laser damage resistance, especially if compared with that of polymeric systems.<sup>2</sup>

An in-depth study of the laser damage effect and its mechanisms has never been done for hybrid materials. The mechanisms of optical damage depend on a multiplicity of factors including the laser parameters, such as pulse duration<sup>4</sup>, beam size and wavelength<sup>5</sup>, and the microstructural characteristics and defects of the material. For use with single shots of short-pulse lasers, the main mechanisms involved are avalanche ionization, multiphoton ionization or impurity breakdown.<sup>6,7</sup> For multi-shot radiation, the mechanism is more complicated because of accumulation of irreversible changes in the matrix during the sequence of pulses. Generally, Laser-Induced Damage Threshold (LIDT) in a single-shot test is higher than that measured in a multi-shot one.<sup>6</sup>

In addition, the morphology of the damaged region is influenced by the used laser parameters, as it is reported in the literature for fused silica and CaF<sub>2</sub>. Short pulses,  $\tau < 10$  ps, and small spot sizes can generate sharp cracks located at the peak of Gaussian beam, where the fluence (pulse energy per unit area) is high enough to produce multiphoton ionization. For longer pulses ( $\tau > 20$  ps), the damage fluence have a  $\tau^{1/2}$  dependence, because of the transfer of kinetic energy to the lattice and diffusion during the laser pulse. In this regime, the damage is thermal and characterized by melting and boiling of the whole irradiated area.<sup>8</sup>

In Section 7.1 the synthesis of the hybrid sol-gel matrices will be presented. Successively, the non linear optical characterization of all the matrices will be presented and between them four matrices are chosen for a further characterization because of their higher laser damage resistance. These samples are mechanically, thermally, microstructurally and optically analysed in order to correlate the microstructural properties to the optical damage resistance. Finally we will report some results regarding the embedding of few materials in sol-gel matrices.

### **7.1 Synthesis of the hybrid matrices**

In the Chapter 3 we have introduced some details about the sol-gel method and the precursors that are commonly used for many applications. In this work we have prepared different matrices in collaboration with Dr. Giovanna Brusatin (University of Padova).

They are based especially on the hybrid precursor 3-Glycidoxypropyl-trimethoxysilane (GPTMS). Some transition metal alkoxides have been employed as catalysts for the cleavage of the epoxy ring of GPTMS. In some cases, we also used the tetraethoxysilane (TEOS) as inorganic network former.

Moreover, in some matrices the hybrid precursor was the Dimethyldiethoxysilane (DMDES), where two functionalities on the Si atom are methyl groups and the others are hydrolyzable ethoxy units.

Here we briefly report the protocols for the sol-gel synthesis of the different matrices. The schemes of the synthesis will help understanding further comments regarding the results of the last four matrices (called GTZ, GZH, GBZ and GZB). In fact, among all the sol-gel materials, we have dedicated more attention to the microscopic, thermal and mechanical

characterization of the last four ones, in order to correlate the optical damage resistance against ns pulses at 690 nm to the microscopic properties.

- **DMDES-TEOS-TiO<sub>2</sub>**: DMDES is added to the TEOS, prehydrolyzed with acidified water, and the solution is kept in magnetic stirring for few minutes. The Ti-isopropoxide is mixed with the solvent methoxyethanol and rapidly added to the solution with DMDES and TEOS. The final solution is refluxed at 80°C for 1.5 hours. The molar ratio between the precursors DMDES:TEOS:Ti is equal to 4:5:1 or 6:3:1
- **G-TEOS-Al 7-2-1**: GPTMS and tetraethoxysilane (TEOS) are co-hydrolyzed for 3 hours under reflux at 80°C with acidified water and ethanol as solvent. Al-secbutoxide is mixed with the solvent methoxyethanol and rapidly added to the solution with DMDES and TEOS. The solution is refluxed at 80°C for 1 hour. The molar ratio used is: GPTMS:TEOS:Al(OBu)<sub>4</sub> = 7:2:1
- **G-TEOS-Ti 7-2-1**: the synthesis is identical to the previous one, but Ti-isopropoxide is used here.
- **G7Zr3; G7Ge3; G7Ti3; G7Hf3**: for these matrices, the GPTMS is prehydrolyzed with water containing NaOH (NaOH:H<sub>2</sub>O=0.003) for one night in magnetic stirring. The second precursor (Zr-butoxide, Ge-tetraetoxide, Ti-isopropoxide and Hf-butoxide), previously diluted in methoxyethanol, is mixed to the GPTMS solution. This solution is kept under reflux at 80°C for 2 hours. The molar ratio between the GPTMS and the second precursors is equal to 7:3 in all cases.
- **GTZ**: GPTMS and tetraethoxysilane (TEOS) are co-hydrolyzed for 3 hours under reflux at 80°C with acidified water and ethanol as solvent. The solution with Zr(OBu)<sup>t</sup><sub>4</sub>, acetylacetone and the residual solvent is rapidly added to the GPTMS and TEOS solution and refluxed at the same temperature for 1.5 hours. The molar ratios used are: GPTMS:TEOS:Zr(OBu)<sup>t</sup><sub>4</sub> = 9:3:1; GPTMS+TEOS:H<sub>2</sub>O = 1:3.3; GPTMS:HCl = 1:0.004; Zr(OBu)<sup>t</sup><sub>4</sub>:AcAc = 1:1.1.
- **GZH**: the synthesis is analogous to GTZ, but without using TEOS. In this case, the molar ratios are GPTMS:Zr(OBu)<sup>t</sup><sub>4</sub> = 12:1 and GPTMS:H<sub>2</sub>O:HCl = 1:3:0.004
- **GBZ**: GPTMS is pre-hydrolyzed in basic conditions, using NaOH, under reflux at 80°C for one hour. The sequence of the procedure is the same as described for the synthesis of GTZ. The molar ratios used are: GPTMS:Zr(OBu)<sup>t</sup><sub>4</sub> = 12:1; GPTMS:H<sub>2</sub>O:NaOH = 1:3:0.002.

- **GZB**: the molar ratios are the same as for GBZ, but the two steps of the synthesis are inverted. At first, GPTMS is added to the solution of  $Zr(OBu^t)_4$ , AcAc and methanol and refluxed for 1.5 hours. Then, water and NaOH are added to the solution drop by drop and refluxed for one hour.

Because of its high reactivity, the  $Zr(OBu^t)_4$  must be chelated with acetylacetonate (AcAc). The solutions are filtered with 0.2  $\mu\text{m}$ -filters and they are further cast in specific Teflon boxes designed to obtain bulk disks. The solutions are kept in an oven at 60°C for few days until their complete gelification. The samples have the desired thickness (about 0,5 mm) and are used for further analyses without any other treatment, like grinding and polish.

Some of the sol-gel samples are shown in Fig. 7.1. We can note the high transparency of the specimens.



**Fig. 7.1:** Images of some sol-gel samples

## 7.2 Non linear optical characterization: a measurement of the optical damage threshold

The measurements of the optical damage at 690 nm have been carried out by NLT experiments, performed with the same set-up already discussed for the characterization of the dyes in solution. The thickness of the sol-gel samples must be smaller than the Rayleigh Range defined by the focusing optical system used: in this way the laser fluence is kept constant along the beam path inside the sample.

The CCD camera is used for the determination of the beam waist dimensions which are necessary for the calculation of the fluence on the sample.

The characteristic curve of NLT measurements of a sol-gel sample is shown in Fig. 7.2 where the transmittance is plotted versus the input energy. Increasing the input energy,

when optical damage occurs, the transmittance rapidly drops, the corresponding input energy is defined as damage threshold energy. At this point, local bright cracklings are visible.

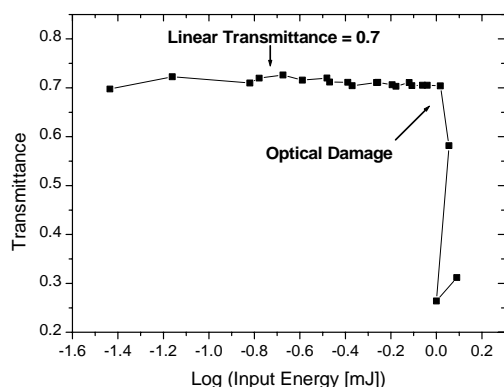


**Fig. 7.2:** Example of Non Linear Transmittance curve for GZB sample

In the next table, we present the fluence data at optical damage point for every sample. The values reported are obtained from the average of 5-10 measurements in different positions on the specimens in order to minimize the effect of local defects or discontinuities on the threshold data. In some measurements, the maximum fluence of the laser can not damage the samples, even if the same samples are damaged at lower fluences irradiated in different spots.

Sol-gel matrices	$F_{\text{damage}}$ (after synthesis) [J/cm <sup>2</sup> ]	$F_{\text{damage}}$ (one year after) [J/cm <sup>2</sup> ]
1) DMDES-TEOS-TiO <sub>2</sub> , 4-5-1	20,6	35.5
2) DMDES-TEOS-TiO <sub>2</sub> , 6-3-1	34.9	21.9
3) G-TEOS-Al 7-2-1	40; > 68	90; > 106
4) G-TEOS-Ti 7/2/1	26	58
5) G7Zr3	7.8	23
6) G7Ge3	27.6	> 42.5
7) G7Ti3	16.3	36.3; > 42.5
8) G7Hf3	25.6	26.5
9) GTZ	18; > 29	100
10) GZH	16.6	200
11) GBZ	32,3; > 35,3	85
12) GZB	24; > 34	150

**Table 7.I:** Fluences at damage threshold measured after the synthesis and one year later

From the data reported, it is interesting to note that the fluences at damage generally increase when the measurements are performed one year after their preparation. A possible explanation of this behavior can be correlated to the aging of the sol-gel samples. In fact, even if the samples are densified in an oven for few days, the reactions are not

probably completed. After one year, samples become more stable, also towards the laser irradiation.

As anticipated above, the last four samples possess the highest resistance to the optical damage. For this reason they have been thoroughly characterized by Infrared and UV-Visible spectroscopies, Differential Thermal and Thermogravimetric Analyses (DTA-TGA). Their Elastic Modulus values are also measured. In the next section we will report the results of the characterization.<sup>9,10</sup>

### 7.3 Experimental analyses

The techniques used for the characterization of the sol-gel samples are listed below:

- Infrared spectra are recorded in the range 400-6000  $\text{cm}^{-1}$  by a Fourier Transform Infrared Interferometer (*Perkin-Elmer 2000*) on pellets of powders in KBr. The IR spectra are normalized with respect to the peak at 2935  $\text{cm}^{-1}$  relative to vibrations of  $-\text{CH}_2$  groups, used as an internal standard.
- UV-Visible spectra of the disks are collected with the spectrometer *Varian-Cary5* from 300 to 800 nm, with a resolution of 1 nm.
- The characterization of the thermal behavior of hybrid materials is performed on powder samples by a Differential Thermal and Thermogravimetric Analyser (STA 409/429-*Netzsch*). The samples are placed in an alumina crucible and heated in air with heating rate of 10°C/min up to 1000°C.
- The elastic modulus of the samples is determined using the mechanical resonance frequency in the flexural mode of vibration produced by an elastic strike with an impulse tool, as described in ASTM-C1259-96.<sup>11</sup> This method permits one to calculate the elastic modulus of the test specimens with known mass, geometry (rectangular cross-section bars) and resonance frequency, from the formula:

$$E = 0.95 \frac{mf_f^2 L^3}{b t^3} T_1$$

$$T_1 = 1 + 6.58(1 + 0.07\mu + 0.81\mu^2) \left(\frac{t}{L}\right)^2 - 0.87 \left(\frac{t}{L}\right)^4 - \left[ \frac{8.34(1 + 0.20\mu + 2.17\mu^2) \left(\frac{t}{L}\right)^4}{1.00 + 6.34(1 + 0.14\mu + 1.54\mu^2) \left(\frac{t}{L}\right)^2} \right]$$

where,  $E$  is the Young modulus [Pa];  $m$  is the mass of the bar [g];  $b$ ,  $L$  and  $t$  are the width, the length and the thickness of specimen respectively [mm];  $f_f$  is the fundamental flexural resonant frequency of the bar [Hz];  $T_1$  is a correction factor for  $f_f$  and  $\mu$  is Poisson's ratio.

The strains used are small, so that the elastic moduli measured are near the origin of the stress-strain curves. The samples should be isotropic and homogeneous without evident discontinuities, such as large cracks or voids that can interfere with the measurements. Besides, the modulus value is inversely proportional to the cube of the thickness and variations in dimension can have a significant effect in the calculation. The instrumentation used is *Grindosonic MK5 J.W.Lemmens*.

The four different synthesis procedures have strong influence and consequences on the final hybrid matrix structures, which in turn might affect the laser damage resistance. One of the main synthesis parameter is the organic and inorganic polymerization degree: the organic and the inorganic networks growth is generally competitive and can be conducted separately. Besides, the use of basic or acid catalysts influences the rate of hydrolysis and condensation reactions and consequently the structure of final gels. When the synthesis is performed in acidic conditions, the condensation rate is lower and the structure is generally characterized by a linear growth of chains. On the contrary, the gels synthesized in basic conditions are characterized by a higher condensation degree.

#### *IR analyses*

The two basic catalyzed systems, GBZ and GZB, are obtained by inducing firstly the inorganic or organic condensation, respectively. The basic medium of GBZ sol-gel synthesis is shown to produce a very large degree of inorganic condensation.<sup>12</sup> Moreover, the basic environment inhibits the activity of the Zr alkoxide, which is well known to produce the epoxy polymerization at a reaction temperature of 80°C, behaving as Lewis acid.<sup>13</sup> The IR spectra in Fig. 7.3b show the following features: the unopened epoxy ring vibrations<sup>14</sup> of GBZ are still visible at 910, 1250 and 3060 cm<sup>-1</sup>. The vibrations due to Si-OH or SiO<sup>-</sup> groups at 970 cm<sup>-1</sup> (Fig. 7.4) are almost absent in this system and the -OH absorption around 3400 cm<sup>-1</sup> is lower than in the other systems shown in Fig. 7.3, confirming the large inorganic condensation degree of this system (Fig. 7.3b).

The IR signal in the region 1000-1200 cm<sup>-1</sup> is related to the asymmetric stretching of Si-O-Si bonds. With GPTMS based hybrid films synthesized in basic conditions without Zr(OBu<sup>†</sup>)<sub>4</sub> the final matrices are formed in large part by condensed species that provide very dense structures in which the organic epoxy groups are not polymerized. This is revealed by the quite different shape of the spectrum around 1000-1200 cm<sup>-1</sup> with respect to the others: a main absorption of silica species at larger frequencies is visible only in

GBZ (around  $1140\text{ cm}^{-1}$ ) and is due to condensed cage species<sup>15</sup>, while the absorption of linear species around  $1030\text{-}1060\text{ cm}^{-1}$  is present in all systems (Fig. 7.4).

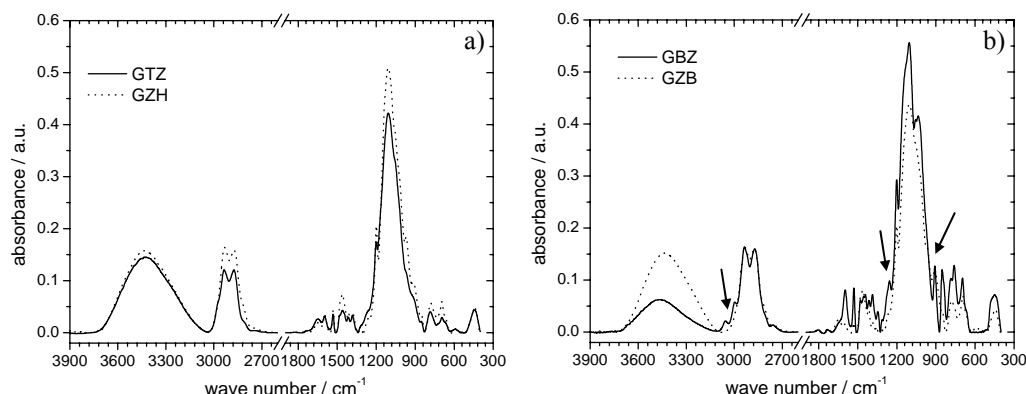


**Fig. 7.3:** FT-IR spectra of a) matrices obtained in acidic conditions (GTZ and GZH) and b) matrices in basic conditions (GBZ and GZB). The arrows point out the residual signals coming from the epoxy ring in sample GBZ.

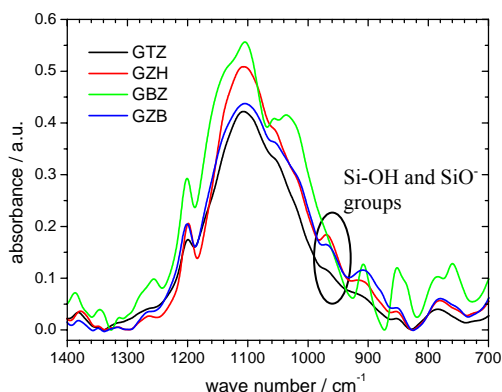


**Fig. 7.4:** FT-IR spectra of GTZ, GZH, GBZ and GZB matrices in the region  $1400\text{-}700\text{ cm}^{-1}$ . The signals at about  $970\text{ cm}^{-1}$  are related to hydroxyl groups.

By inverting the order of addition of NaOH and  $\text{Zr}(\text{OBU})_4$ , in GZB a very different structure is achieved. Here the epoxy polymerization is almost completed (see the residual vibrational absorption at  $910\text{ cm}^{-1}$  in Fig. 7.4) and the basic reaction of the sol that follows the organic condensation cannot produce a large inorganic condensation degree as in GBZ, because of the presence of the organic network. The absorption around  $1100\text{ cm}^{-1}$  is similar to that of the systems obtained in acidic conditions, with a larger absorption around  $1030\text{-}1060\text{ cm}^{-1}$ , revealing that, notwithstanding the basic catalysis of the sol performed after organic polymerization, the structure is mainly linear and less condensed with respect to GBZ. This is evidenced by the large Si-OH absorption<sup>16</sup> at  $3400$  and  $970\text{ cm}^{-1}$ . At about  $965\text{ cm}^{-1}$  it is also visible the signal of deprotonated silanols

(SiO<sup>-</sup>) that is almost absent in the GBZ and GTZ matrices spectra, which are the most condensed ones.<sup>17</sup>

The acidic catalysis generally gives inorganic network with linear structures less condensed than those produced in basic catalysis. The acidic catalysis of the sol for GTZ and the presence of Zr alkoxide promote the inorganic hydrolysis and condensation of the quadrifunctional silica precursor Tetraethoxysilane. Moreover, the acidic medium supports the activity of Zr(OBu<sup>t</sup>)<sub>4</sub> toward the epoxy ring as shown in Fig. 7.3a for samples GTZ and GZH. The larger absorption at 3400 cm<sup>-1</sup> of GTZ can be due to adsorbed water, whose presence is revealed at 1630 cm<sup>-1</sup>.

Therefore, GTZ and GBZ are the matrices with a lower residual Si-OH groups content (Fig. 7.4): in GTZ, Zr(OBu<sup>t</sup>)<sub>4</sub> is probably responsible for a promotion of the inorganic condensation of TEOS and in GBZ the basic catalysis as the first step favors the inorganic condensation.

### Thermal analyses

DTA and TGA thermal analyses (Fig. 7.5) show in all cases an endothermic effect around 100-200 °C, due to residual solvent and water evaporation: this effect is more pronounced for samples GZH and GZB. From 200 to 350 °C the weight loss is attributed to thermal degradation and carbonization of the organic groups. Between 350 and 600 °C, the weight loss is due to combustion of organic compounds and further inorganic condensation. Afterwards, all the organic moieties are burnt off but the inorganic condensation continues up to 1000 °C. Also the presence of AcAc, used to chelate Zr(OBu<sup>t</sup>)<sub>4</sub> and entrapped in the materials, can influence the combustion curves at elevated temperatures.

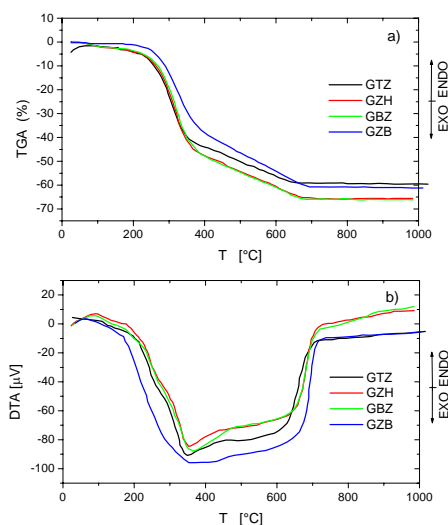


**Fig. 7.5:** TGA (a) and DTA (b) curves of GTZ, GZH, GBZ and GZB samples

From these data we can conclude that GZH and GZB matrices are the less crosslinked ones while GBZ and GTZ matrices have a larger condensation degree.

### UV-Visible spectra

All samples are transparent and weakly yellow colored. Figure 7.6 reports the UV-Visible spectra of GBZ, GZB, GZH and GTZ sol-gel materials normalized with respect to their thickness, in order to make possible a semi quantitative comparison between them. All matrices possess high transparency in the whole visible region, until 800 nm. Besides, it is possible to observe that aging does not alter the optical transparency in the visible region even if the spectra are slightly different toward UV wavelengths. The  $\lambda_{\text{cut-off}}$  positions are related, for the first few months, to the aging time indicating the presence of small microstructural modifications, which should be further investigated. After this initial period, they maintain unchanged the  $\lambda_{\text{cut-off}}$  positions indicative of sample with high optical stability.

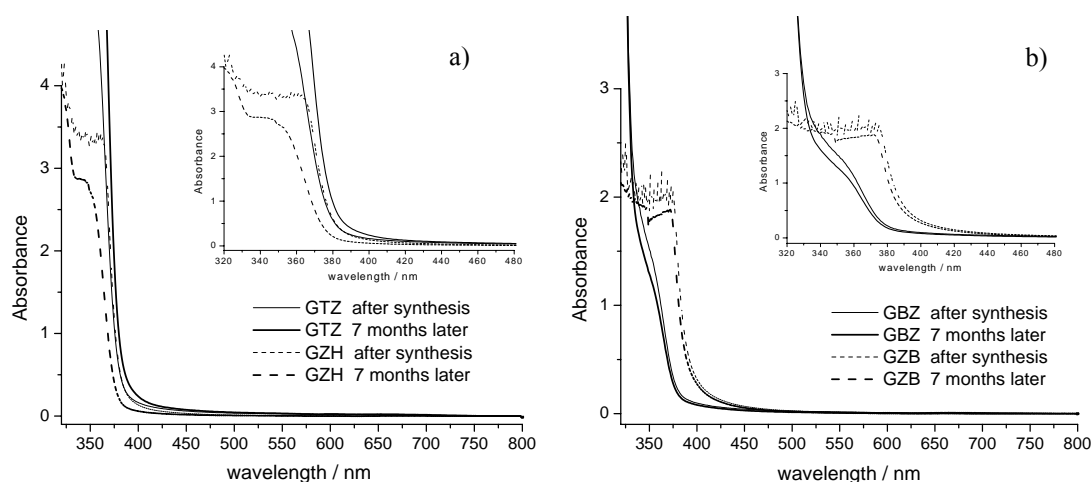


**Fig. 7.6:** UV-Visible spectra of GTZ and GZH (a) and of GBZ and GZB (b) after synthesis and seven months later. The insets are the enlargements of the region 320-480 nm.

### Mechanical characterization

Table 7.II shows the elastic Young's modulus of specimens after thermal treatment at about 60 °C. The values are the average of numerous measurements on different specimens (examples are shown in Fig. 7.7) and the errors reported are the standard deviations.

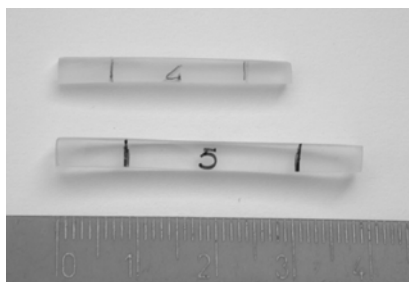


**Fig. 7.7:** Examples of specimens of GTZ, used for the elastic modulus measurements

The elastic moduli are much lower than the common values for inorganic glasses (50-90 GPa)<sup>18</sup> and are, instead, typical of thermoplastic polymers.<sup>19</sup> This is due both to the presence of organic components and the incomplete condensation of the inorganic network. In the samples GZH and GZB, where the  $Zr(OBu^t)_4$  catalyst favors the organic polymerization, that inhibits the formation of the inorganic network, the elastic modulus values are in fact lower.

The presence of TEOS in GTZ increases the elastic modulus of this sample. Indeed, TEOS is a tetrafunctional precursor that promotes the formation of tetrahedral silica units in the hybrid network and this process increases the stiffness of the material. Besides, in GBZ the increase of the Young's modulus is due to the high degree of inorganic condensation promoted by the basic synthesis.

#### *Laser damage measurements*

NLT measurements, at 690 nm, have been performed in regions of the sample having good optical quality. This has been checked by observing the transmitted beam shape with the CCD camera: when the beam passes through a good position its intensity profile remains similar to that measured in air. As an example, the CCD images, with the 3D intensity profiles, of the laser beam in air and transmitted from GBZ sample are depicted in Fig. 7.8a and 7.8b. These data are reported again in the third column of Table 7.II.

In order to investigate the effect of surface defects on the optical damage, a macroscopic artificial scratch has been produced on the surface of samples. The scratched sample has been irradiated by the laser beam at 690 nm, showing a linear light scattering over a larger area, as is shown in Fig. 7.8c.

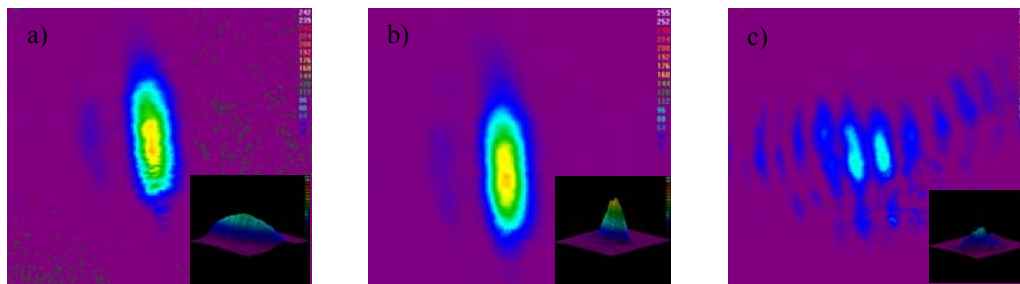


**Fig. 7.8:** CCD image of the laser beam in air (a), after passing through a GZB sample in a good optical region (b) and through a scratched region of the same sample (c). The insets display 3D intensity profiles.

The spot after the damaged region becomes distorted because of linear scattering and diffraction process and the intensity is spread out over the enlarged area, giving larger beam sizes and lower damage threshold fluences. The experimental values are reported in the last column of Table 7.II: they are drastically reduced even if the pulse energy at the damaging threshold is not very different from the first measurements.

Samples	Elastic Modulus [MPa]	$F_{dam} \lambda=690 \text{ nm}$ [ $\text{J}/\text{cm}^2$ ]	$F_{dam} \lambda=690 \text{ nm scratch}$ [ $\text{J}/\text{cm}^2$ ]
<b>GZB</b>	$29 \pm 3$	150	2.5
<b>GZH</b>	$81 \pm 7$	200	2.2
<b>GTZ</b>	$168 \pm 13$	100	2
<b>GBZ</b>	$195 \pm 77$	85	3
<b>SiO<sub>2</sub><sup>18</sup></b>	$\sim 70000$		
<b>PEO<sup>19</sup></b>	$500 @ 300 \text{ K}$		

**Table 7.II:** Elastic modulus values and fluence at damage threshold in a good optical region and in a scratched region.

*Optical analyses*

The optical quality of the films, observed by an optical microscope at different magnifications and by an Enviromental Scanning Electron Microscopy (ESEM), was high in all samples. The damaged areas have also been analyzed and some pictures of them are presented in Fig. 7.9 and 7.10. The damaged region on the scratch (Fig. 7.9-c) seems to be larger than that obtained in the analogous measurements performed in a good optical quality zone. This can be a further proof of the spreading of the damaged area when a scratched region is involved.

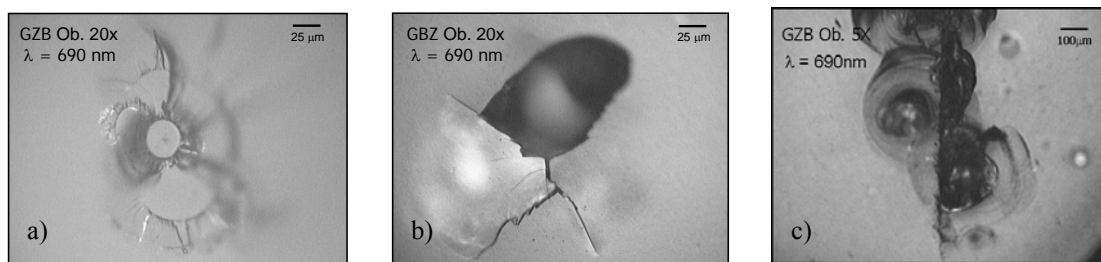


**Fig. 7.9:** Images by Optical Microscopy of damaged regions after irradiation at 690 nm for different samples. The picture c) is relative to the optical damage on scratched region.

Figure 7.10 reports, as an example, the ESEM image of a different sample of GTZ matrix doped with the FULP molecule. The well defined crack of this doped sample, occurring around  $80 \text{ J/cm}^2$  incident fluence, is similar to the others showing that the crack mechanism is related to the host matrix, rather than the NLO system embedded in it.

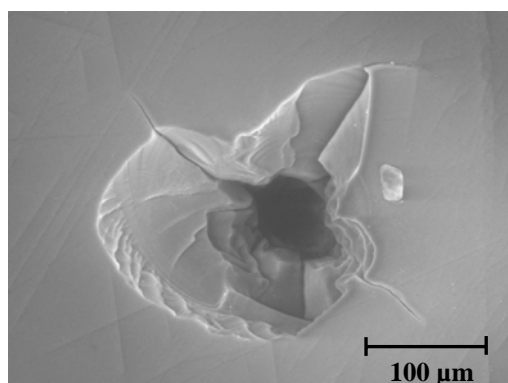


**Fig. 7.10:** ESEM image of the optical damaged region on a GTZ sample doped with FULP

The laser damage measurements seem to demonstrate that the degree of condensation and the mechanical properties have important roles in optical damage. The damage fluences at 690 and the Elastic Modulus values have an opposite trend, except for the GZB sample, i.e. materials with lower elastic modulus are more resistant and are damaged at higher laser fluences. Indeed, stiffer materials develop larger thermal stresses around the area illuminated by the laser beam. Furthermore, the larger is the degree of inorganic condensation, the longer is the stress relaxation time and stress can increase in the material. Besides, as the data reported in the last column of Table 7.II demonstrate, a superficial scratch or an inhomogeneity can remarkably decrease the performances of the material, behaving as a crack initiator.

Also the observation of the optical damaged regions may be useful. Looking at all the images reported in Figs. 7.9 and 7.10, it is possible to observe that the shapes of the damages can be very different and may be related to internal stresses or defects of the irradiated area of the sample. On the edges of these regions some cracks can develop in order to relax the accumulated elastic energy. In fact, the avalanche-breakdown mechanism<sup>7,20</sup> seems to be the main mechanism for damaging by pulsed lasers. For this process, free electrons of the material are accelerated by interaction with the incident electric field. They can ionize other atoms creating new free electrons accelerated themselves by the incident pulses. Some of this energy imparted to the electrons can locally heat the sample and damage through crack formation or melting. Free initial electrons present in the materials can be created by thermal excitation, multiphoton excitation or from crystal defects.

By this way, the artificial scratches created in our samples can act both as a source of these electrons, accelerating the damage process, and critical flaws for crack propagation.

It is also important to remember that in bulk samples there are many precursors with nanometric sizes which can have an important role as damage initiators at high incident intensity. Moreover, particles of polishing material, used for the surface finishing of oxide optics, can be trapped in microcracks in the subsurface layer which can be mechanically damaged after polishing. Formation of cracks is associated to the generation of free surfaces. Oxygen can escape forming oxygen deficient clusters which can absorb UV light.

When the surface temperature of the nanostructures, wherever they are generated, reaches some critical values, a thermal explosion produces a plasma effect leading to the damage of the material.<sup>21</sup> In fact, the shapes of our damaged regions remember a local explosion. It is anyway difficult to eliminate these nanoprecursors from the material.

Finally, in the literature some attention has been devoted to the study of the effect of ns laser pulses on polymer host materials.<sup>22</sup> In that article the authors show that a high molecular flexibility of a polymer elastomer matrix is fundamental for dissipation of the laser energy and absorption of the thermo-mechanical stress near to the laser spot. Therefore, a highly crosslinked material contains molecules with little flexibility and its laser damage threshold is lower. These remarks can bring to a further explanation of our laser damage results. GZH matrix, showing the highest resistance to the laser damage, is characterized by long ethylenoxide chains and low inorganic condensation degree. The organic chains are therefore more flexible and can better support the thermal stress

induced by the laser. In GZB the inorganic densification can slightly prevent the motion of the organic moieties.

#### 7.4 Embedding of core-shell nanoparticles in a sol-gel matrix

We have chosen the matrix G7Hf3 as host for the core-shell nanoparticles of *Evident Technology* described in Section 6.4. The NPs, dispersed in toluene solution, have been concentrated in order to reduce the solvent quantity. They are further mixed to the G7Hf3 sol in a quantity to have a ratio of  $2 \times 10^{-5}$  and  $8.5 \times 10^{-6}$  for Birch-yellow and Maple Red-Orange sample, respectively, between the moles of NP and the moles of  $(\text{SiO}_2 + \text{HfO}_2)$ . The two sols are kept in an oven at  $60^\circ\text{C}$  for two days. The final bulk materials are luminescent when irradiated with a UV-lamp, but they show a slightly different UV-Visible spectra if compared with the spectra of the NPs in solution.

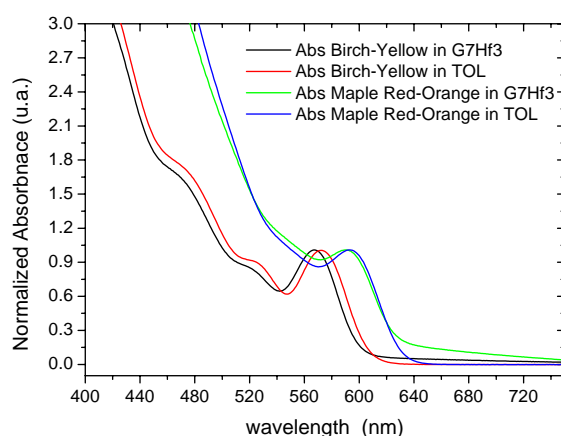


**Fig. 7.11:** UV-Visible spectra of the Birch-Yellow and Maple Red-Orange nanoparticles in toluene solution and in G7Hf3 matrix

The excitonic peaks remain well-shaped even after the inclusion of the NPs in the matrix, but they are enlarged and blue-shifted with respect to the peak in solution. Moreover, the scattering background is increased. These evidences can be related to a surface modification of the nanoparticles when they are mixed with the sol-gel solution. These quantum dots have a capping agent that contains long alkylic chains. These chains are insoluble in the sol-gel solution and they can be removed from the NP surface, making it more instable.

These samples are also characterized by NLT measurements at 690 nm with ns pulses. The NLT curves remain constant until the laser damaging and the non linear absorption of the nanoparticles is not activated. This is probably due to the low concentrations

employed or to changes in the photophysics when the quantum dots aggregate inside the sol-gel matrix.

### **7.5 Concluding remarks**

We have synthesized different hybrid matrices using the sol-gel method. The use of hybrid precursors is very useful for the preparation of host materials for optics application. Among all the systems we have synthesized, we have chosen four matrices (GTZ, GZH, GBZ and GZB) to be fully characterized. It is interesting to note how apparently little modifications in the synthesis protocols can generate materials with different microscopic properties. In fact, in these samples,  $Zr(OBu^t)_4$  has been chosen as catalyst for the development of the organic structure. Besides, the sol-gel precursors, the synthetic route and the reaction medium have been varied and it has been possible to find a correlation between their final structure and the damage threshold fluence. One of the main results is the direct correlation between the elastic properties of the materials and their resistance to the laser irradiation.

The sol-gel hybrid materials are anyway good candidates for the realization of an optical device.

In the last section, we have shown some attempts at embedding QDs in a sol-gel matrix. These results show the difficulty to use NPs as NLO-active materials for optical limiting applications in ns temporal regime because of the high concentrations required and the high cost of the nanoparticles commercially available. Moreover, the use of the correct capping agent for these materials can be useful for reaching good dispersion, elevated concentrations and high stability which are properties required for the realization of the device.

## REFERENCES:

- <sup>1</sup> P. Innocenzi, G. Brusatin, *J. of Sol-gel Science and Techn.* 2003, 26, 967-970
- <sup>2</sup> D.L. Ou, A.B. Seddon, *J. of Sol-gel Science and Techn.* 1997, 8, 139-145
- <sup>3</sup> A. Jitianu et al., *Mater. Science and Engin. C* 2003, 23, 301-306
- <sup>4</sup> B.C. Stuart et al., *Phys. Rev. B* 1996, 53, 1749-1761
- <sup>5</sup> C.W. Carr et al. *Phys. Rev. Lett.* 2003, 91, 127402.
- <sup>6</sup> Y. Zhao, W. Gao, J. Shao, Z. Fan, *Appl. Surf. Sci.* 2004, 227, 275-281
- <sup>7</sup> R.W. Boyd, *Nonlinear Optics* Academic Press 2003
- <sup>8</sup> B.C. Stuart et al., *Phys. Rev. Lett.* 1995, 74-12, 2248-2251
- <sup>9</sup> I. Fortunati et al. *Proc. of SPIE*, 2007, 6653, 665314-1-9
- <sup>10</sup> I. Fortunati et al. *Accepted by J. of Non-Cryst. Solids*
- <sup>11</sup> ASTM C 1259-94: Standard test method for dynamic Young's modulus, shear modulus, and Poisson's ratio for advanced ceramics by impulse excitation of vibration. ASTM Designation C1259-94, 1994 ASTM Annual Book of Standards. American Society for Testing and Materials, Philadelphia, PA.
- <sup>12</sup> C. Brinker, *J. Sol-gel Science* Academic Press 1989
- <sup>13</sup> D. Hoebbel et al., *J. of Sol-gel Science and Techn.* 2001, 21, 177-187
- <sup>14</sup> P. Innocenzi et al., *J. of Non-Cryst. Solids* 1999, 259, 182-190
- <sup>15</sup> L. Matejka, et al. *J. of Non-Cryst. Solids* 2000, 270, 34-47; J. Choi et al. *Macromolecules* 2003, 36, 5666-5682
- <sup>16</sup> P. Innocenzi, *J. of Non-Cryst. Solids* 2003, 316, 309-319
- <sup>17</sup> A. Fidalgo and L.M. Ilharco, *J. of Non-Cryst. Solids* 2001, 283, 144
- <sup>18</sup> T. Iwamoto and J.D. Mackenzie, *J. of Sol-gel Science and Techn.* 1995, 4, 141-150
- <sup>19</sup> A. Bartolotta et al., *Phys. Rev. B* 1993, 48, 10137-10142
- <sup>20</sup> Efimov, O. M. *Proc. of SPIE*, 2003, 5273, 61-72
- <sup>21</sup> Feit, D. M. et al. *Proc. of SPIE*, 2003, 5273, 74-81
- <sup>22</sup> Jiang, H. et al. *Proc. of SPIE*, 1998, 3472, 157-162



## CHAPTER 8

# Up-converted lasing

In recent years, a considerable amount of effort has been devoted to frequency up-conversion laser materials and devices which produce a shorter wavelength (in the visible or UV range) lasing output when pumped at longer wavelength (IR). Two major approaches can be used to reach this goal. One is based on sequential stepwise multiphoton in rare-earth doped materials<sup>1,2</sup>; the other is based on direct two-photon absorption induced population inversion in dye solutions<sup>3-6</sup> and dye doped-solid matrices<sup>7,8</sup>. The development of dye-doped thin films or channel waveguide lasers looks more promising because of the benefits of low cost, high compactness and compatibility with other micro-optic elements or integrated optical circuits.

In this chapter we show the up-converted lasing properties in dimethyl sulfoxide solution of two push-pull chromophores, OH-PEP and PEPEP already characterized in the previous chapter. Some attempts at embedding these organic dyes in sol-gel materials have been made and the lasing properties have been tested.

Further, we will show the results of lasing of new semiconductor quantum dots embedded in a zirconia matrix. Our experiments reveal the lasing properties after one-photon (at 400 nm) and two-photon pumping (at 800 nm).<sup>9</sup> The two-photon optical pumping of semiconductor nanoparticles is the first case reported in literature.

## 8.1 Two-photon pumping of organic push-pull dyes in solution

The use of sources at longer wavelengths is more convenient for pumping the organic dyes as compared to conventional single photon pumping, because of their higher photostability and reduced Rayleigh scattering at these wavelengths. Also, since the absorption of the pump beam is low, it is possible to extract gain from the doped-bulk rather than a thin film layer of the medium. Moreover, upconverted lasing does not require phase matching, and can easily provide a broad tuning range. Using semiconductor diode lasers as pumping sources, the cost of up-conversion laser can be very low. However, the efficiencies of two-photon pumped (TPP) lasing so far reported are rather low,<sup>4,6,10</sup> and the relationship between molecular structure and efficiencies of TPP lasing is still unclear, making it difficult to design such materials.

The organic molecules that are studied for up-conversion lasing are based on push-pull structures containing pyrrole and pyridinium rings differently substituted. Some of these molecules are depicted below:<sup>4,6,10</sup>

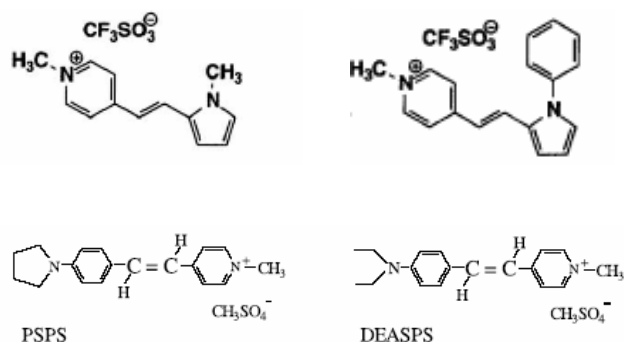


**Fig. 8.1:** Molecular structures of push-pull molecules studied for up-conversion

When a system is excited by a light source, spontaneous emission can occur and it is in general incoherent and randomly emitted in all directions. However, if the pump pulse is polarized, the emission will have a preferred direction perpendicular to the pump's polarization. Thus, spontaneous emission will create coherent stimulated emission along its direction of propagation, which is the Amplified Spontaneous Emission (ASE). When the TPP mechanism is involved, the NLO system is excited through the simultaneous absorption of two photons in the near-IR range. Consequently, the system must possess a non-negligible TPA-cross section at the pumping wavelength.

Moreover, the ASE band is centered at a wavelength shorter than the pump one, as depicted in Fig. 8.2.

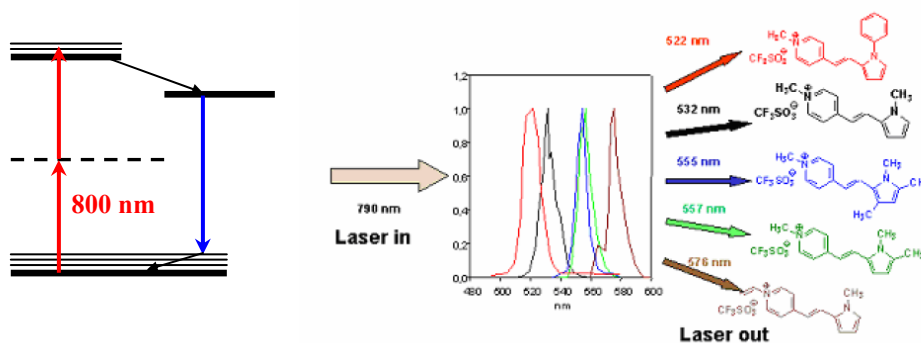


**Fig. 8.2:** TPP mechanism for push-pull molecules

The great advantage of using push-pull molecules consists in the possibility of changing the lateral substituents on the heteroaromatic rings in order to tune the emission wavelength. The ASE appears as a narrow band on the fluorescence spectrum.

When the concentration of the dye contained in a quartz-cell is very high (about  $1-3 \times 10^{-2}$  M), the single-path TPP gain is so high that even the Fresnel reflection feedback from the two parallel optical windows is enough to generate a cavity lasing. This is possible only if the beam is perpendicular to the windows surfaces. If the incident angle is larger than  $4-5^\circ$ , the cavity lasing is no longer observed due to a big deviation of the cavity axis from the pump beam.

## 8.2 Measurements of ASE emission under two-photon pumping of a dipolar and a quadrupolar push-pull molecule in solution

We have characterized the ASE emission properties of the molecules OHPEP and the PEPEP, already described in previous chapters, having molecular structures:

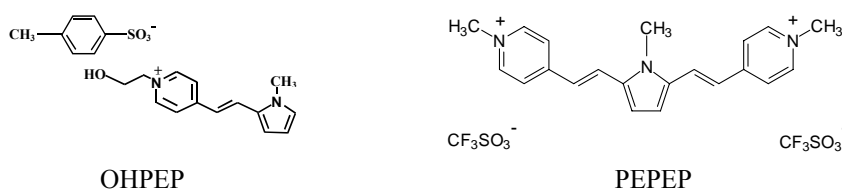


**Fig. 8.3:** Molecular structures of OHPEP and PEPEP

The optical pump system is the amplified Ti-Sapphire laser system (*Spectra Physics*) delivering  $\sim 130$  fs pulses, with 0.7 mJ pulse energy, at  $\sim 800$  nm. By controlling the Pockels cells in the regenerative amplifier, the repetition rate was reduced to 10 Hz, in

order to reduce the thermal blooming in the solution. The output energy is attenuated by means of neutral filters and it is finely varied by a half waveplate followed by a polarizer. The beam is then focalized through a 10 cm-focal length lens onto a 10-mm path quartz-cell. The transmitted beam is refocusing into an optical fiber connected to a spectrometer (*Ocean Optics*) by using a lens with a focal length of 5 cm placed at about 10 cm from the cell. Moreover a cut-off filter is employed before the fiber to eliminate the pump beam. The OHPEP and PEPEP molecules are diluted in DMSO at concentrations of  $10^{-2}$  M and  $3 \times 10^{-3}$  M, respectively. We collect the emission spectra as the incident pump energy increases. Beyond a threshold value, the ASE is activated and the ASE peak appears in the spectrum. Unfortunately, for the OHPEP it is not possible to distinguish visually the spontaneous emission contribution from the ASE peak, also at low intensities. Anyway, it is possible to compare the ASE signal with the emission spectrum measured with a spectrofluorimeter.

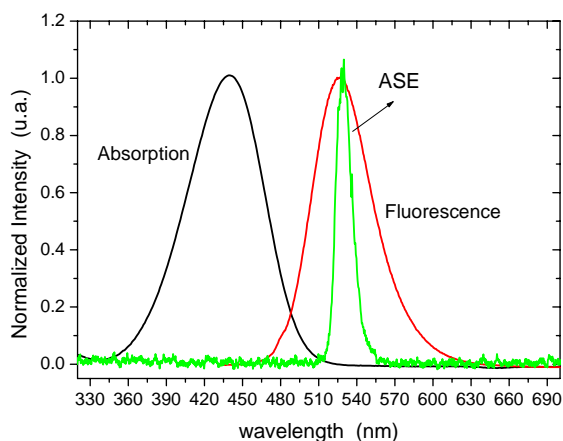


**Fig. 8.4:** Normalized absorption (black line), one-photon induced fluorescence (red line) and two-photon pumping lasing (green line) spectra of OHPEP in DMSO solution

Looking at the spectra reported in Fig. 8.4, two main features can be observed: a red-shift and a narrowing of the ASE signal with respect to the one-photon induced fluorescence. The first aspect can be explained by the reabsorption effect in a high concentration and thick solution sample: only the wavelengths beyond the red-edge of the absorption band can be amplified. The second feature is due to combination of the reabsorption and the gain effects: the blue part of the emission spectrum can not lase due to reabsorption losses and the gain of the red-tail part of the fluorescence band does not reach the threshold for amplification.

For PEPEP molecule, it is possible to measure the threshold energy for the ASE through the collection of the emission spectra at different incident energies. The emission spectra are depicted in Fig. 8.5.

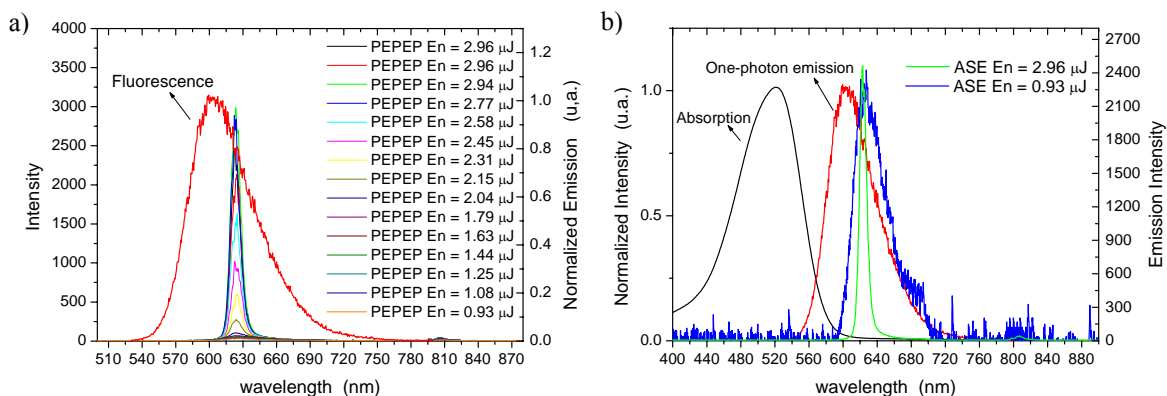


**Fig. 8.5:** a) Normalized one-photon induced fluorescence (red line) and two-photon pumping lasing spectra at different energies; b) normalized absorption (black line); one-photon induced fluorescence (red line) and two-photon pumping lasing at 2.96  $\mu\text{J}$  (green line) and 0.93  $\mu\text{J}$  (blue line) spectra of PEPEP in DMSO solution.

Also PEPEP shows the same characteristics as OHPEP after TPP. When the input energy is low, the two-photon induced emission spectrum is similar to that induced by one-photon absorption, even if it is red-shifted due to the reabsorption effect. At the ASE threshold energy, the ASE peak occurs and is characterized by a strong spectral narrowing.

The negative aspect of these organic fluorophores is the low stability upon laser irradiation. In fact, we have done some attempts at embedding these molecules in sol-gel matrix and, in particular, in GTZ matrix (in Section 7.1 are reported details about this material). The dye concentrations employed are very high (about  $3 \times 10^{-2}$  M). The doped-sol-gel solution is used for the preparation of films by spin-coating on a quartz substrate. The film is then irradiated with the laser beam at 800 nm focused with a cylindrical lens ( $f = 20$  cm). Because of the relatively small thickness of the film, the ASE threshold energy is high and the photobleaching of the dye occurs before any detection of the ASE signal.

### 8.3 Using CdSe-CdS-ZnS Quantum Dots as highly efficient material for amplified spontaneous emission

The semiconductor materials have obtained great attention as optical gain media useful in laser technology.

The electronic spectrum of QDs consists of well-separated atomic-like states with an energy spacing that increases as the dot size is reduced. In very small QDs, the spacing of the electronic states is much greater than the available thermal energy, inhibiting thermal depopulation of the lowest electronic states, which should result in a lasing threshold that is temperature-insensitive. Moreover, the emission wavelength is size-dependent and can be continuously varied over a wide energy range. This versatility makes the QDs very promising materials for the realization of devices based on their optical and electrical properties.<sup>11-15</sup>

The semiconductors quantum dots we have use for testing the ASE properties are described in Sections 6.4 and 6.5. They are based on a core of CdSe and a multiple shell composed of CdS and ZnS, synthesised through chemical protocols. The wide-gap semiconductor used for overcoating the core allows one to significantly improve emission quantum yields by reducing surface-related non radiative carrier losses.<sup>12,16,17</sup> It is demonstrated that the use of capping agents like the tri-*n*-octylphosphine oxide (TOPO) diminishes the degree of surface passivation in comparison with the epitaxial ZnS layer.<sup>18</sup> The traps can be either on the surface of the QD,<sup>19</sup> at the core-shell interface,<sup>20</sup> or in the surrounding matrix itself.<sup>21</sup> The latter factor therefore implies that a careful selection of a suitable host matrix is necessary to achieve stable QD composites. Moreover, also the multiparticle Auger relaxation is in competition with the radiative process.

The matrix used as host for the nanocrystal is zirconia. This matrix acts as a type-I host for all CdSe QD sizes, as illustrated in Fig. 8.6. In a Type I structure, the conduction and valence electrons in the dopant cannot in principle access the matrix because it is energetically unfeasible.<sup>22</sup>

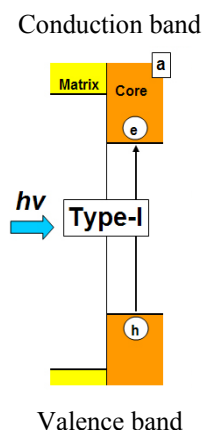


**Fig. 8.6:** The localization of the electron and hole carriers across a heterostructure interface in a type-I configuration

The films we have characterized are doped with three different size quantum dots. The samples are prepared by the group of Prof. P. Mulvaney (University of Melbourne-Australia) in collaboration with A. Martucci (University of Padova). The TEM images of the three QDs are reported below.

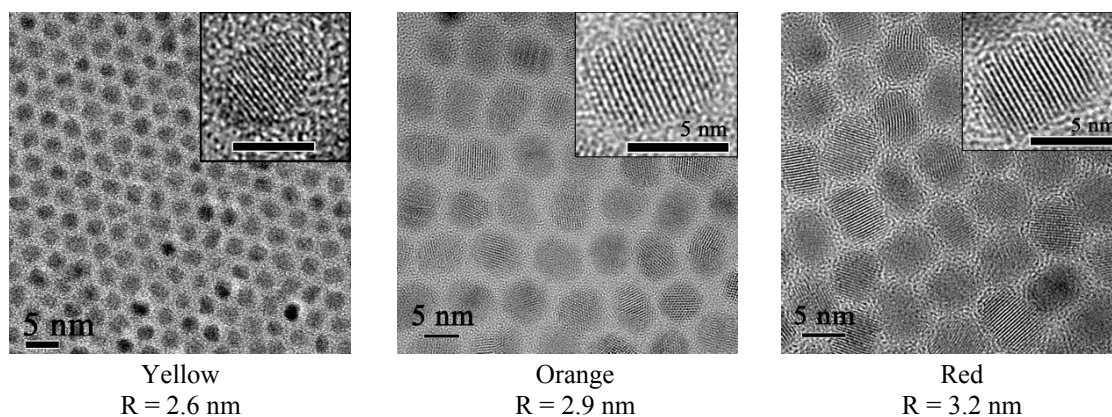


**Fig. 8.7:** TEM images of the nanocrystals: Yellow (on the left); Orange (in the centre); Red (on the right)

#### 8.4 Measurements of the gain of zirconia doped films

In our laboratories we have measured the ASE threshold energy and the gain of the three different samples, upon irradiation with a fs laser at 400 nm (one-photon pumping) and 800 nm (two-photon pumping).

ASE measurements are performed on a Ti:Sapphire laser system (*Spectra Physics*) with pulses of 150 fs and 1KHz repetition rate at 800 nm. With a BBO doubling crystal and a cut-off filter a 400 nm wavelength beam is obtained. The intensity of the input beam is varied with neutral filters and, for a fine tuning, with a half waveplate followed by a polarizer.

The beam is focused with a 20 cm focal length cylindrical lens onto the sample. The sample edge emitted beam, in a lateral configuration, was detected by an optical fiber connected to a micro-spectrometer (*Ocean Optics*), with a typical collection setup shown in Fig. 8.8.

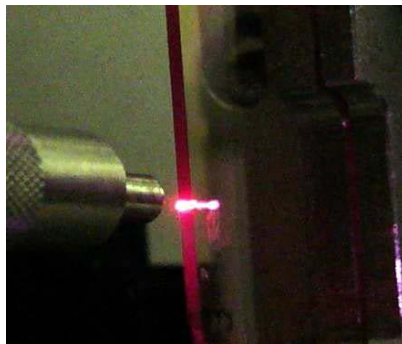


**Fig. 8.8:** Light collection set-up in lateral configuration

Figure 8.9 shows the ASE signals generated within the  $\text{ZrO}_2$ -QD composites under one-photon optical excitation at 400 nm at room-temperature. An overlay of the spontaneous PL signals at low power in the composites is also included. A similar figure can be reported for two-photon excitation. Notably, the ASE peak always appears on the red-side of the PL maximum with a calculated energy difference of  $\sim 25\text{--}35$  meV.

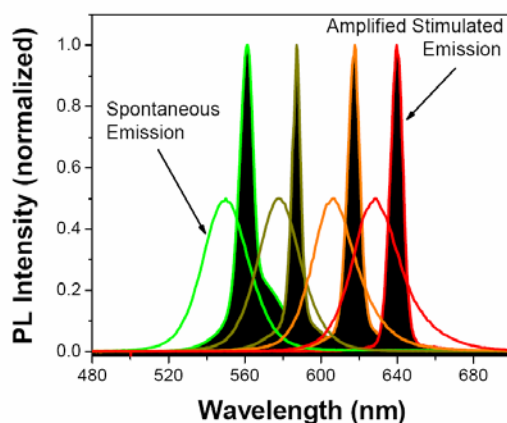


**Fig. 8.9:** ASE peaks and steady state emission of  $\text{ZrO}_2$ -QD composites under 400 nm irradiation

The ASE threshold energies are determined by recording the emission spectra at varying incident energies. For the one-photon pumping at 400 nm, it is also possible to detect the ASE band in a zirconia sample doped with green QDs (radius of 2.1 nm). The ASE is not activated upon two-photon excitation. The threshold data, upon 400 and 800 nm irradiation, are reported in Tables 8.I and 8.II.

Sample	Radius (nm)	Solution PL <sub>max</sub> (nm)	Threshold f <sub>1</sub> (mJ/cm <sup>2</sup> )*	σ <sub>1</sub> (cm <sup>2</sup> )	<N <sub>1</sub> >	g(cm <sup>-1</sup> )
Green	2.1	547	1.4	5.2E-16	1.4	124
Yellow	2.6	573	0.55	9.4E-16	1.0	100
Orange	2.9	604	0.38	2.0E-15	1.5	151
Red	3.2	625	0.15	5.4E-15	1.6	88

**Table 8.I:** Parameters describing the CdSe-CdS-ZnS quantum dots and obtained data for one-photon excitation at 400 nm

Sample	Threshold f <sub>2</sub> (mJ/cm <sup>2</sup> )*	σ <sub>2</sub> (GM)	<N <sub>2</sub> >	g(cm <sup>-1</sup> )
Green	-	985	-	-
Yellow	19.8	2450	1.0	106
Orange	10.8	7400	0.9	116
Red	7.0	26000	1.4	144

**Table 8.II:** Obtained data for two-photon excitation at 800 nm

The single photon optical pumping mechanism makes use of the high one photon absorption cross-sections ( $\sigma_{\text{CdSe}}$ ) of semiconductor nanocrystals, with  $\sigma_{\text{CdSe,1photon}} \sim 10^{-15} \text{ cm}^2$ . Neglecting saturation at the pump energy and assuming a temporal pulse pump width less than the recombination time, the average number of electron-hole pairs,  $\langle N_1 \rangle$ , generated by a single laser pulse is calculated for a given pump fluence,  $f$  (photons/cm<sup>2</sup>), simply as  $\langle N_1 \rangle = f\sigma_1$ . A high absorption cross-section is therefore advantageous for low threshold lasing. The value of  $\sigma_{\text{CdSe}}$  is proportional to the volume of the nanocrystal.<sup>23</sup>

For two-photon excitation the average number of e-h pairs created for every photon pair is given as  $\langle N_2 \rangle = f^2\sigma_2/\tau_p$ , where  $\sigma_2$  is the two-photon absorption cross-section and  $\tau_p$  is the pulse duration (s). It differs from  $\langle N_1 \rangle$  as it is dependent on the square of the incoming fluence and the temporal pulse width. A high local fluence and short pulses are therefore particularly advantageous for exciton generation with this pumping mechanism.

Under degenerate two-photon optical excitation above the exciton resonance at 800 nm (1.55 eV), two photons are simultaneously absorbed whereas normally the excitation would be from a single photon of double the energy (400 nm = 3.1 eV). The schematic representation of the optical pumping mechanisms is depicted in Fig. 8.10.

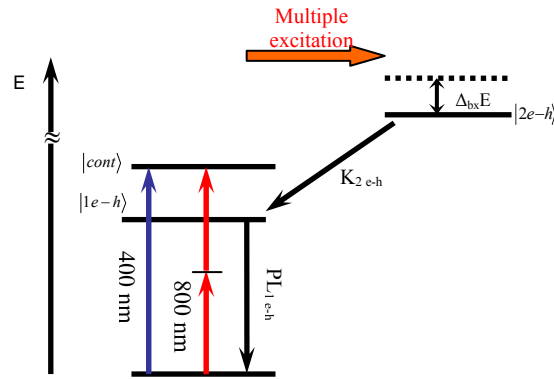


**Fig. 8.10:** Schematic representation of the absorption processes in a quantum dot specie, under both one- and two-photon excitation.

Excitation above the lowest absorption resonance restricts the saturation onset of 1-photon absorption thereby allowing for multi-exciton generation within a single nanocrystal.<sup>16</sup> Any excitons formed in the semi-continuum region decay within a picosecond to the lowest available state; that is one dictated by a Poisson state-filling model.<sup>23</sup> In the case of two excitons in a single nanocrystal, both will decay to the doubly degenerate  $1S(e)-1S_{3/2}(h)$  state.<sup>24</sup>

For cases where two electron-hole pairs have been created (biexciton), the lowest excited state is shown to experience an interaction energy  $\Delta_{bx}$  which can be either positive (carrier repulsion) or negative (exciton attraction). The red shift of the ASE peaks shown in Fig. 8.9 is indicative of a biexciton state. A negative interaction energy ( $\Delta_{bx}$ ) causes a red-shift of the biexciton resonance to a lower-energy from that of single electron-hole pair PL, i.e.  $\Delta_{bx,CdSe} \sim -30 \text{ meV}$ .<sup>25</sup>

For moderately well passivated dots, nonradiative Auger relaxation of doubly excited particles, dominates over surface trapping and imposes an intrinsic limit on the lifetimes of the optical gain. When QDs are pumped into high-energy excited states, population inversion and the buildup of optical gain are only possible if the relaxation down to the ground state is faster than the Auger process time.

Regarding the threshold data reported in Tables 8.I and 8.II, we can observe that the threshold fluence values in the 2-photon regime at 800 nm are in general  $\sim 20-30$  times larger than that measured for 1-photon regime. Using the threshold fluence data it is possible to calculate the average number of electron-hole pairs for both pumping mechanisms ( $\langle N_1 \rangle$  and  $\langle N_2 \rangle$  in Tables 8.I and 8.II). The lower limit for generating optically inverted states in CdSe type-I structures is  $\langle N \rangle \sim 1.4$ . This value is well

approached in both regimes. Such results highlight that the generation of optical gain states in these systems is very important.

In Fig. 8.11 we show the temporal stability of the ASE emission of the red-QDs under one- and two-photon excitation. Extremely high stability is observed with excitation at 400 nm with no appreciable loss in ASE observed in over 1 h of illumination ( $\sim 3.6 \times 10^6$  pulses). For excitation at 800 nm we observe a comparably high stability factor with up to 70% of the original ASE intensity retained following a similar time period.

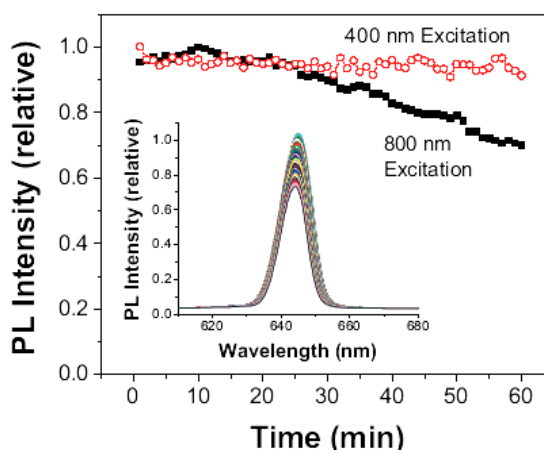


**Fig. 8.11:** A comparison of temporal stability of the ASE signal for red-QDs under one- and two-photon excitation. In the inset: ASE spectra obtained during the stability measurements at 800 nm excitation.

This high stability is the largest one measured, especially if compared with the organic dyes.

One significant advantage of type-I heterostructures for optical gain applications is the high gain coefficient ( $g$ ) that these nanocrystals possess ( $g \sim 40\text{-}140 \text{ cm}^{-1}$ ).<sup>26,27</sup> In order to determine if the nanocrystals utilized in this study are also viable options for optical gain media, variable stripe measurements (VSL) were performed at room temperature. The effective modal gain was extracted by numerically fitting experimental data to an Auger limited 1-D amplifier model similar to the analytic model proposed by Chan *et al.*<sup>27</sup>

$$\frac{dI_{bx}(z)}{dz} = g(z) \exp\left(-\frac{z-z_0}{l_a}\right) I_{bx}(z), \text{ where } \begin{cases} z < z_0, g(z) = 0 \text{ and } I_{bx}(z) = 0 \\ z \geq z_0, g(z) = g \end{cases}$$

$$\frac{dI_{sx}(z)}{dz} = J_{sp}$$

$$I(z) = I_{bx}(z) + I_{sx}(z)$$

Here  $I_{bx}$  and  $I_{sx}$  are the bi- and single- exciton emission intensities, respectively,  $J_{sp}$  is the spontaneous emission factor accounting for the magnitude of incoherent spontaneous emission,  $z_0$  is an offset fitting parameter allowing for pump beam inhomogeneity at the

sample edge and consequently the ASE onset, and  $l_a$  is defined as the bi-exciton lifetime multiplied by the speed of light. This simple model only applies if  $z_0$  is small because waveguide losses and re-absorption in that case are minimized. One example of typical VSL measurement is depicted in Fig. 8.12, which features a red composite optically pumped at 800 nm. This data is fitted to the Auger limited model to give an overall modal gain  $g \sim 144 \text{ cm}^{-1}$ .

The extracted gain coefficients are summarized in Tables 8.I and 8.II for both the one- and two- photon optical pumping mechanisms. In both cases the overall modal gain coefficients have values which range between  $\sim 100$  and  $160 \text{ cm}^{-1}$ . These depend strongly on the sample studied, the overall volume fraction of quantum dot inclusion and the observed losses in the waveguides.

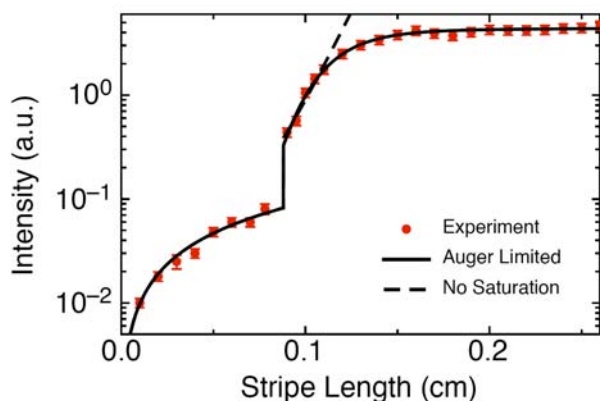


**Fig. 8.12:** A typical stripe measurement performed on a red quantum dot composite film. The experimental data ( $\bullet$ ) is fitted to i) an Auger limited 1-D amplifier model (—) and ii) a classical 1-D amplifier model with no saturation (- -). Error bars are included to indicate the uncertainty in the measurement.

## 8.5 Conclusions

In this chapter we have analysed the ASE properties of both organic compounds and semiconductor core-shell quantum dots. In the first case it is possible to detect the ASE emission of the dyes in solution pumped by two-photon excitation. Instead, the inclusion of the dyes in a sol-gel matrix inhibits the measurement of the ASE signal due to the low stability of the organic compounds under intense laser irradiation. On the contrary, the ASE measurement of CdSe-CdS-ZnS nanocrystals in solution is practically impossible because of the high number of nonradiative pathway at the interface QDs-solvent. The inclusion of these QDs of different sizes in a zirconia matrix is an excellent way to

increase the lasing properties and to improve the temporal stability under both one- and two-photon excitation.

Based on these results, one can envisage that, through the use of low two-photon lasing threshold materials, such as that based on CdSe-CdS-ZnS, there exists a real possibility for the development of infra-red optically pumped micron-sized lasers.



## REFERENCES:

- <sup>1</sup> Chen, X. B. et al. *Opt. Comm.*, 1999, 160, 364-375
- <sup>2</sup> Qin, X. et al. *Appl. Phys. Lett.* 2007, 90, 073104
- <sup>3</sup> He, G. S. et al. *Opt. Comm.*, 1997, 140, 49-52
- <sup>4</sup> Wang, X. et al. *Opt. Mater.*, 2002, 20, 217-223
- <sup>5</sup> Zhou, Y. F. et al. *J. of Molec. Struct.* 2002, 613, 91-94
- <sup>6</sup> Abbotto, A. et al. *Synth. Metals*, 2001, 121, 1755-1756
- <sup>7</sup> He, G. H. et al. *Opt. Comm.*, 1994, 111, 82-85
- <sup>8</sup> Shirota, K. et al. *Appl. Phys. Lett.* 2004, 84, 1632-1634
- <sup>9</sup> Jasieniak, J.J., Fortunati, I., Gardin, S., Signorini, R., Bozio, R., Martucci, A. and Mulvaney, P. *Adv. Mater.* 2008, 20, 69-73
- <sup>10</sup> Ren, Y. et al. *J. of Mater. Chem.* 2000, 10, 2025-2030
- <sup>11</sup> Klimov, V. I. *Semiconductor and Metal Nanocrystals*, 2004, Marcel Dekker, Inc.
- <sup>12</sup> Piryatinski, A. et al. *Nanoletters*, 2007, 7, 108-115
- <sup>13</sup> Achermann, M. et al. *Nanoletters*, 2007, 6, 1396-1400
- <sup>14</sup> Schaller, R. D. et al. *Nature Phys.* 2005, 1, 189-194
- <sup>15</sup> Chan, Y. et al. *Appl. Phys. Lett.* 2004, 85, 2460-2462
- <sup>16</sup> Klimov, V. I. et al. *Science* 2000, 290, 314-317
- <sup>17</sup> Xie, R. et al. *J. Am. Chem. Soc.* 2005, 127, 7480
- <sup>18</sup> Klimov, V. I. et al. *Science* 2000, 287, 1011-1013
- <sup>19</sup> Gomez, D. E. et al. *Small* 2006, 2, 204
- <sup>20</sup> Manna, L. et al. *J. Am. Chem. Soc.* 2002, 124, 7136
- <sup>21</sup> Blackburn, J. L. et al. *J. Phys. Chem. B* 2003, 107, 14154
- <sup>22</sup> J. Jasieniak, et al. *Adv. Funct. Mater.* 2007, 17, 1654-1662
- <sup>23</sup> Klimov, V. I. *J. Phys. Chem. B* 2000, 104, 6112-6123
- <sup>24</sup> Van Embden, J. and Mulvaney, P. *Langmuir* 2005, 21, 10226
- <sup>25</sup> Klimov, V. et al. *Phys. Rev. B* 1994, 50, 8110-8113
- <sup>26</sup> Malko, A. V. et al. *Applied Physics Letters* 2002, 81, 1303-1305
- <sup>27</sup> Chan, Y. et al. *Appl. Phys. Lett.* 2005, 86, 073102



## CHAPTER 9

# One- and Two-photon induced Photopolymerization

In the last years, photopolymerization has attracted great attention from researches in the industrial and scientific sectors. It is an important technique for the fabrication of devices in the fields of optoelectronics, microelectronics, stereolithography or microfluidics. Photo-induced polymerization offers multiple advantages, including spatial and temporal controls, fast curing speed at room temperature, large efficiency and great versatility on the initial prepolymer blend. Particularly in the field of photonics, a set of different and conflicting properties is required, needing a tailoring of the architectures and morphologies in going from the molecular to the micrometric scale.

In this chapter we report on the study of the photopolymerization process in all polymeric matrices based on acrylate units. An accurate study is devoted to the photopolymerization of hybrid organic-inorganic films containing silica and zirconia precursors, as inorganic components, and photopolymerizable acrylic and methacrylic groups. Films are doped with a proper photo-initiator for radical polymerization of (meth)acrylic units.

The photopolymerization has been performed with different laser sources, a CW Ar<sup>+</sup> laser and a femto-second laser, using many excitation energies, for different times, in air and in inert atmosphere. After the development of the unexposed regions with a suitable solvent, the photopolymerized structures are observed with confocal optical microscopy, environmental scanning electron microscopy (ESEM) and atomic force microscopy

(AFM). The effects of the photopolymerizable mixture composition, the irradiation parameters (like laser power and exposure time) and the external atmosphere in which the photopolymerization is performed are investigated.

Accordingly, in this chapter we will show the possibility to exploit the multiphoton absorption of a properly synthesized photo-initiator to create microstructures. The photo-initiator must have high TPA-cross section at the photopolymerization wavelength, together with high efficiency in generating radicals after the irradiation.<sup>1</sup> The fabrication of 3D microstructures using multiphoton absorption processes is a promising technique involving low amount of incident exposure dose with potentially high spatial resolution.

### **9.1 State of the art of photopolymerization technique**

The most studied systems for photopolymerization are based on (meth)acrylates which undergo free-radical polymerization after photoinitiator activation with adequate wavelength sources.

Conventional one-photon photopolymerization generally employs UV lamps or UV light.<sup>2</sup> This technique is largely used in the coating industry for the surface protection of various materials (plastics, metals, papers) by fast drying varnishes, based on acrylate resins.<sup>3,4</sup> Optical gratings of holographic polymer, dispersed in liquid crystal medium, are also studied.<sup>5</sup> Moreover, the fields of microelectronics and stereolithography are involved with the photocurable chemicals. However, the conventional lithography based on one-photon UV polymerization is unable to reduce the dimensions of the created structures below the diffraction limit (hundreds of nm). Many of the architectures for micro- and nano-devices demand the ability to create 3D structures, which is not possible with conventional methods.

One of the new techniques is based on Two-Photon Induced Photopolymerization (TPIP) in which the photoresist simultaneously absorbs two photons during the laser irradiation within a small spatial region, determined by the dimension at the beam-waist of the focused excitation laser beam.<sup>6,7</sup> By scanning the position of the laser focus in 3D dimensions, it is possible to arbitrarily create three-dimensional shapes with sub-100 nm features sizes. Several groups have utilized this process to write 3D lithographic and photonic band gap structures or 3D optical storage memories.<sup>8-11</sup>

However, materials commonly used for these purposes are organic polymers: a great variety of prepolymer resists have been studied.<sup>12,13</sup> In this context, we report on the

investigation of innovative sol-gel hybrid organic-inorganic materials, containing acrylated functionalities and a novel photoinitiator characterized by a high two-photon absorption cross section in the wavelength range used. As described in chapter 3 the sol-gel chemistry, based particularly on the use of hybrid organic/inorganic materials, is largely exploited as an efficient way to design a large variety of novel materials reaching the control of the structure at a nanometric scale and often superior properties with respect to polymers, such as high optical quality (for example low optical losses), good mechanical and chemical resistance (such as superior resistance against dry etching processes and scratch), high flexibility in the final material properties design (for example refractive index tunability) and the possibility of embedding large amounts of active compounds. All of these properties can be used for the realization of a functional optical material exploiting the photopolymerization.

The overall polymerization in hybrid materials is, however, a quite complex process because several synthesis parameters can affect the final structure. The extent of the inorganic condensation is a crucial aspect because the organic polymerization is always in competition with the formation of the inorganic network.

The mechanism of photopolymerization for acrylic groups is severely inhibited by atmospheric molecular oxygen causing numerous effects, including slow process rates, low conversion and short polymer chain length.<sup>14</sup> To overcome this undesirable effect, large efforts are employed, such as the use of an inert atmosphere, higher concentration of photoinitiator or higher incident source energies to produce a larger amount of radicals. Some groups also report the design of new photocurable monomers with properly studied functionalities which can avoid the oxygen inhibition process.<sup>15,16</sup>

Besides, finding methods that are capable of revealing the polymerization process in a real time and in convenient ways is one of the major tasks for the study of the process. Up to now, FT-IR<sup>14,2,17</sup> and real time Raman<sup>18</sup> spectroscopies are the main techniques useful to investigate the rate and the efficiency of the photopolymerization. Unfortunately, these techniques become inadequate for the characterization of sub-micrometric structures because their dimensions are smaller than the spatial resolution of these spectroscopies. In the literature only morphological analyses are reported for structures created by TPIP.

## 9.2 Non linear optical characterization of photoinitiators

An essential step before performing a photopolymerization process consists in the optical characterization of the available photoinitiators. For one-photon photopolymerization, it is sufficient to measure the one-photon absorption spectrum of the photoinitiator for defining the best wavelength range for excitation. Moreover, for the TPIP process it is necessary to know the TPA spectrum of the photoinitiator.

For the photopolymerization of acrylic systems, we have considered two initiators. The first is the commercial Ethyl - 2,4,6 - Trimethylbenzoylphenylphosphinate (*Basf*-Lucirin LR8893X) whose molecular structure is shown below.

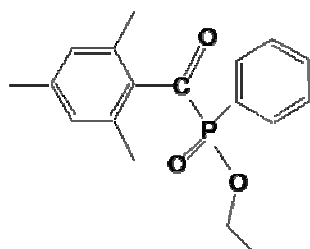


**Fig. 9.1:** Molecular structure of Lucirin LR8893X

Unfortunately, this initiator absorbs in the UV region with a peak at 370 nm and it is not possible to detect the TPA spectrum using the TPIF method, in the 720-930 nm wavelength range. In fact, this compound is used for UV photopolymerization of polyester-acrylic resins.<sup>19</sup>

The second photoinitiator ((E,E,E,E,E)-1,13-bis-[4-(diethylamino)phenyl]-tri-deca-1,3,5,6,8,10,12-hexaen-7-one), labelled "TPP") was synthesized by the group of Prof. C. Andraud (ENS of Lyon-France). It has been produced through the cetolization-crotonization reaction from (E,E)-5-[4-(diethylamino)phenyl]penta-2,4-dienal and acetone in basic conditions.<sup>20</sup>

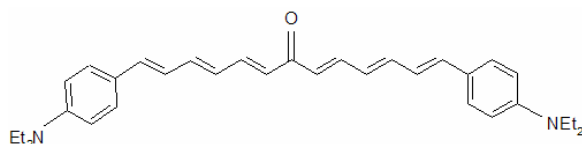


**Fig. 9.2:** Molecular structure of TPP

In order to know the best wavelength for the irradiation of the samples which will contain the TPP, it is first necessary to characterize its non linear optical properties in solution.

We use the TPIF method in the fs regime to determine its TPA spectrum which is reported in Fig. 9.3 together with the one-photon absorption. The TPA spectrum measured with ns regime is reported elsewhere.<sup>21</sup>

The wavelength abscissa scale of the TPA spectrum is halved to have a direct comparison with the linear absorption. The maximum of TPA does not coincide with the peak of OPA because of the symmetric structure of TPP.

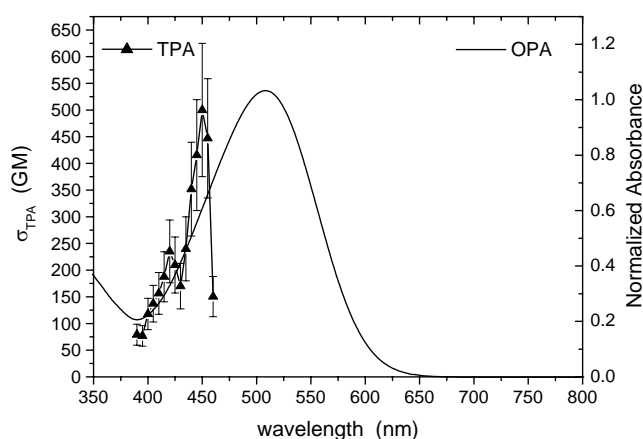


**Fig. 9.3:** Linear (OPA) and Nonlinear (TPA) absorption of the photoinitiator in  $\text{CHCl}_3$

### 9.3 Materials used as prepolymer blend for further photopolymerization process

In this work we have deeply studied three different matrices: one is completely organic polymeric, the others, based on hybrid organic-inorganic materials, are obtained by the sol-gel method. The matrices are synthesized in collaboration with G. Brusatin and Prof. M. Guglielmi (University of Padova).

Firstly, we have decided to use the same polymeric matrix, already employed by the group of Prof. C. Andraud, for photopolymerization at 1064 nm.<sup>21</sup> As described below, we have used different excitation wavelengths for our experiments, but this attempt is important for testing the reliability of the two excitation set-up which have been mounted and tested for the first time in our laboratories.

This polymeric resin, hereafter denoted with "SAN-Mon", consists of 0.5% photoinitiator, 70% monomer (tris(2-hydroxyethyl) isocyanurate triacrylate with a radical inhibitor level of 100 ppm) and 29.5% polymer binder (poly(styrene-co-acrylonitrile) (75/25)-SAN). The molecular structures of the monomer SR368 (*Sartomer*) and the SAN polymer (*Aldrich*) are depicted below.

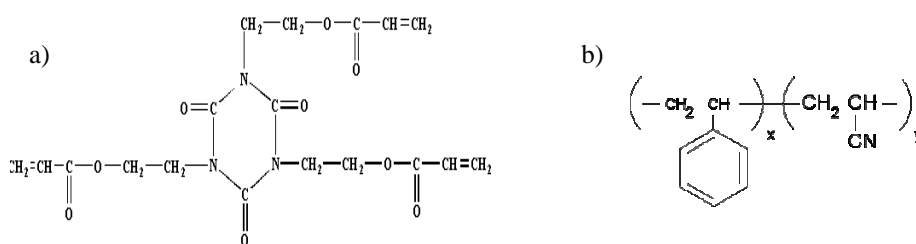


**Fig. 9.4:** Molecular structures of SR368 (a) and SAN (b)

The other two matrices are obtained from sol-gel hybrid precursors mixed with inorganic ones, providing mechanical strength to the material. All the organic parts contain acrylic or methacrylic polymerizable units.

For the preparation of the first one (called "MZrMA"), 3-(Methacryloxy)propyl]trimethoxysilane (MPTMS) is stirred in the presence of acidified water for one hour to promote the hydrolysis of the methoxy groups. Zr-butoxide ( $\text{Zr}(\text{OBU}^t)_4$ ) and Metacrylic acid (MAA) are separately allowed to react by stirring for five minutes. The two solutions are mixed together, neutralized with NaOH and put under stirring for one hour, before the addition of the photoinitiator, previously solubilized in chloroform. Methoxyethanol is the solvent used for the synthesis. The molar ratios are:  $\text{MPTMS}:\text{Zr}(\text{OBU}^t)_4:\text{MAA}=5.5:1.5:3$ ;  $\text{MPTMS}:\text{H}_2\text{O}:\text{HCl}=1:3:0.01$ .

For the preparation of the second matrix (called "MZrMAMon"), the first part of the synthetic route is analogous to the previous one. After the addition of the Zr-Butoxide, the monomer SR368, dissolved in methoxyethanol, is added and the solution is kept under magnetic stirring for one hour. The molar ratios used with this matrix are:  $\text{MPTMS}:\text{Zr}(\text{OBU}^t)_4:\text{SR368}:\text{MAA}=3:1:5:2$ ;  $\text{MPTMS}:\text{H}_2\text{O}:\text{HCl}=1:3:0.01$ .

Both for MZrMA and MZrMAMon matrices the amount of photoinitiator, added to the sol-gel solution, is equal to 0.2 % with respect to the numbers of acrylic groups.

The sol-gel solutions, containing an oxide-concentration of 150 gr/l, and the polymeric one are kept in ultrasonic bath for 15 min to allow a good dispersion of the TPP. These solutions are used to prepare films by spin-coating technique at 2000 rpm for 30 sec. Samples with different thicknesses, ranging from approximately 1.3-1.5  $\mu\text{m}$  to few microns, are prepared.

The optical quality of the films is good, even if the samples obtained from solutions containing the monomer SR368 tend to form crystalline microstructures four days after the deposition. Some of these structures are shown in Fig. 9.5.

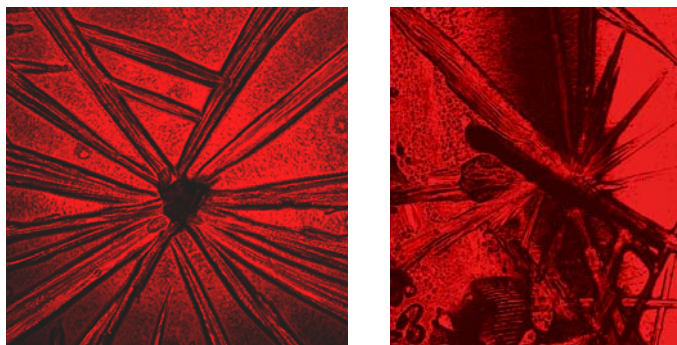


**Fig. 9.5:** Confocal images of crystallites on samples containing SR368

Table 9.I summarizes the main characteristics of the composition of the three materials here studied.

Samples	Molar ratios	wt %
SAN-MON		SAN:SR368=29.5:70
MZrMA	MPTMS:Zr(OBu <sup>t</sup> ) <sub>4</sub> :Metacrylic acid=5.5:1.5:3	
MZrMAMon	MPTMS:Zr(OBu <sup>t</sup> ) <sub>4</sub> :SR368: Metacrylic acid =3:1:5:2	

**Table 9.I:** Composition data of SAN-Mon, MZrMA and MZrMAMon materials

#### 9.4 Thermal polymerization: a preliminary study before the photopolymerization

The polymerization can be achieved also through a thermal process where an appropriate thermal initiator generates free radicals when treated at temperatures higher than its decomposition temperature. Some examples of the thermal initiators are the 2,2'-azobisisobutyronitrile (AIBN), the potassium persulfate (KPS) and the benzoyl peroxide (BPO).<sup>22-24</sup>

We have used the BPO as thermal initiator to polymerise our systems. This compound decomposes at 80-90 °C generating two benzoyl radicals,<sup>25,26</sup> as depicted in Fig. 7.6.

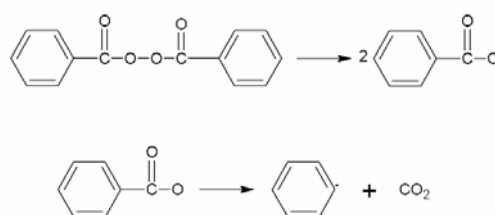


**Fig. 9.6:** Decomposition mechanism of benzoyl peroxide

The BPO is added, in quantity equal to 0.5 wt. %, to the SAN-Mon solution, while for the other sol-gel matrices, BPO is equal to the 2% with respect to the number of acrylic groups.

After the deposition of the films obtained from these solutions, samples are treated at 90°C every 5 min for 45 min. This treatment is carried out by a heating plate directly connected to the spectrometer. A simple way to monitor the degree of polymerization consists in the collection of the IR spectra before and after the thermal treatment. The degree of polymerization can be derived from the variation of the IR peaks assigned to the stretching vibrational mode of the (meth)acrylic groups and of the carbonyl units C=O.<sup>14,17,2</sup> The FTIR spectra are performed with a *Jasco 620* Spectrometer in the 400 - 4500 cm<sup>-1</sup> range, with 2 cm<sup>-1</sup> resolution. Here we concentrate the attention only in the 1850-1500 cm<sup>-1</sup> spectral region, where it is possible to observe the main peaks correlated to the polymerization process.

Figure 9.7 shows FTIR spectra in the region between 1850 and 1500 cm<sup>-1</sup>, of the SAN-Mon film after the deposition and after the thermal curing at 90°C for 45 min. The red line is the spectrum collected after a further treatment in an oven at 110°C for 30 min.

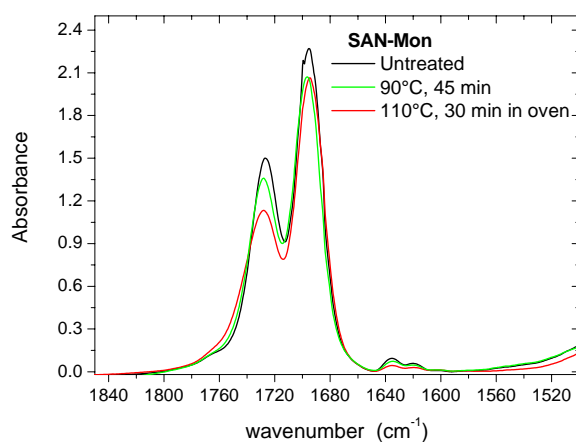


**Fig. 9.7:** FTIR spectra of SAN-Mon film after deposition (blue-line), after the thermal curing at 90°C (green line) and after the treatment at 110 °C.

The two peaks at  $\sim 1726$  and  $\sim 1695$  cm<sup>-1</sup> are associated with the stretching of the carbonyl groups. Generally, the splitting into two peaks related to the carbonyl are due to the presence of acrylate units in the monomer SR368. In fact, a cheto-enol tautomerization<sup>27</sup> takes place in the acrylate group, generating two different chemical environments for the carbonyl. It is possible to observe a decrease in intensity of these peaks, a small shift to higher wavenumbers and a small enlargement, due to the reduction of the change in the mobility of C=O groups,<sup>28</sup> when the temperature increases.

Besides, the band at  $\sim 1410 \text{ cm}^{-1}$  is associated with the stretching of the acrylic groups.<sup>29</sup> Also the intensity of these peaks decreases after the thermal treatments. These evidences are correlated to the gradual opening of the C=C bonds.

The curing in an oven at  $110^\circ\text{C}$  seems to be more efficient in opening the double bonds with respect to the heating at  $90^\circ\text{C}$ . A higher temperature can increase the rate of formation of radicals. Moreover, the oven treatment probably permits a more uniform heating of the sample. These two aspects can explain the better efficiency of the curing at  $110^\circ\text{C}$ .

Analogously, we report the IR spectra for the MZrMAMon and MZrMA samples in the region  $1500\text{-}1850 \text{ cm}^{-1}$ , before and after the thermal treatment at  $90^\circ\text{C}$ .

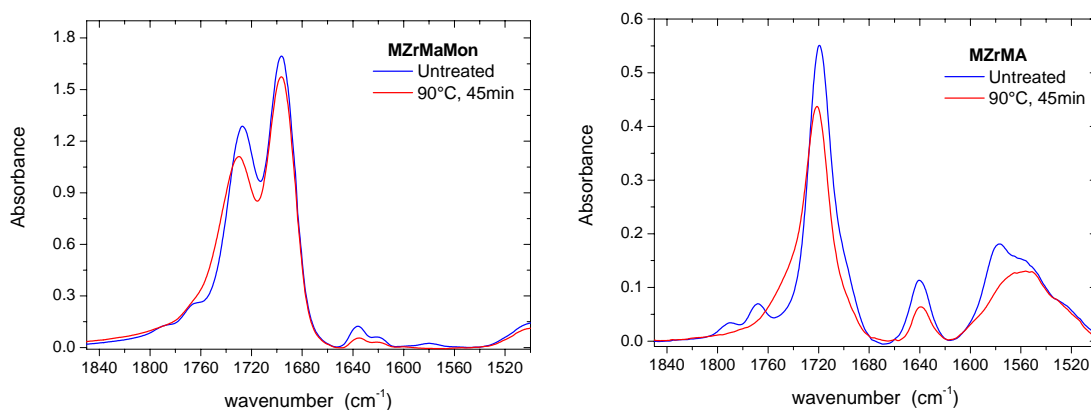


**Fig. 9.8:** FTIR spectra of MZrMAMon (on the left) and MZrMA (on the right) films after deposition (blue-line) and after the thermal curing at  $90^\circ\text{C}$

We can firstly note that the double peaks related to the carbonyl groups are also present in the IR spectra of MZrMAMon. On the contrary, in MZrMa there is only one band centered at  $\sim 1720 \text{ cm}^{-1}$ . In fact, the second matrix does not contain the monomer which is the unique precursor where the C=C bonds are acrylates. Methacrylic functionalities, contained in MPTMS and in methacrylic acid precursors, prevent the cheto-enol tautomerization. Analogously, in MZrMA the stretching of the C=C groups is centered at  $\sim 1640 \text{ cm}^{-1}$  which can be assigned to the methacrylic stretching.<sup>2,17</sup> This band, present also in MZrMAMon, confirms its assignment to methacrylic groups.

After the thermal curing the intensity of the bands related to the C=C and C=O decreases and the band associated with the C=O bonds is enlarged. These data confirm the polymerization of the organic groups even if it is only a partial process. In fact, the organic polymerization can be in part inhibited by the inorganic polycondensation promoted by the thermal heating.

## 9.5 One-photon polymerization

In one-photon polymerization experiments, we use, as excitation wavelength, the 488 nm line of an Argon ion laser (*Spectra Physics 165*), providing a maximum optical power of about 300 mW. The beam is focused on the front surface of the sample using a cylindrical lens (with a focal length of about 20 cm) to form an excitation stripe having a width of about 30  $\mu\text{m}$  and a length of some millimetres. The choice of this wavelength is due to the proximity with the absorption maximum of the photoinitiator (see Fig. 7.3). By this way, we are sure to best excite the TPP.

The inclusion of the photoinitiator into the solid matrices does not affect their optical properties. As an example, Fig. 7.9 reports the UV-Vis spectra of the photoinitiator in a chloroform solution and in MZrMAMon matrix. It also shows the UV-Vis spectrum of the same matrix after irradiation with laser systems.

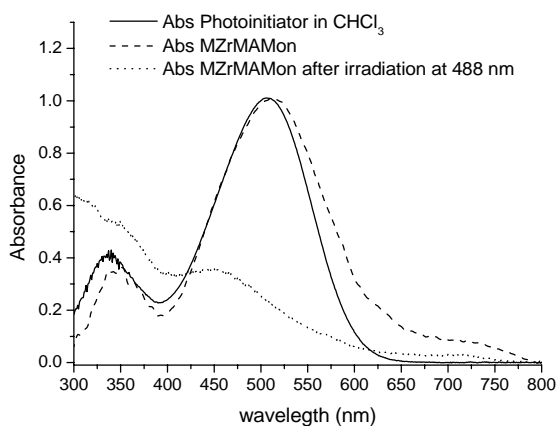


**Fig. 9.9:** UV-Vis spectra of the photoinitiator in the  $\text{CHCl}_3$  solution (continuum line), in the MZrMAMon film before (dash line) and after (dot line) irradiation, at 488 nm.

The irradiation causes a local bleaching of the films, visible even by eye, which is probably a sign of the break of the electron conjugation along the photoinitiator chain (see Fig. 9.10). A possible mechanism for the formation of initiating radicals consists in the formation of a radical on the carbonyl group following the breaking of the chain. By this way the basic unit is shorter than the original structure of the TPP and the absorption shifts to the UV region.

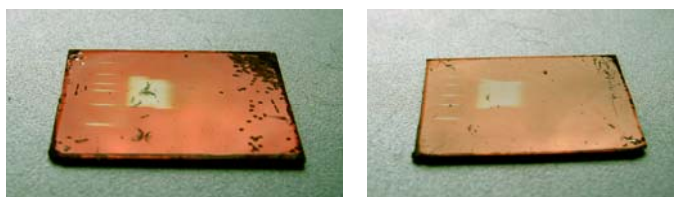


**Fig. 9.10:** Images of the photobleaching on SAN-Mon samples after irradiation at 488 nm

For SAN-Mon films, we have performed some irradiations changing the exposure times from 1 sec to 30 sec, while the incident power is kept constant at 30 mW. The films after irradiation are developed with acetone. The polymerized structures are analyzed by confocal microscope.

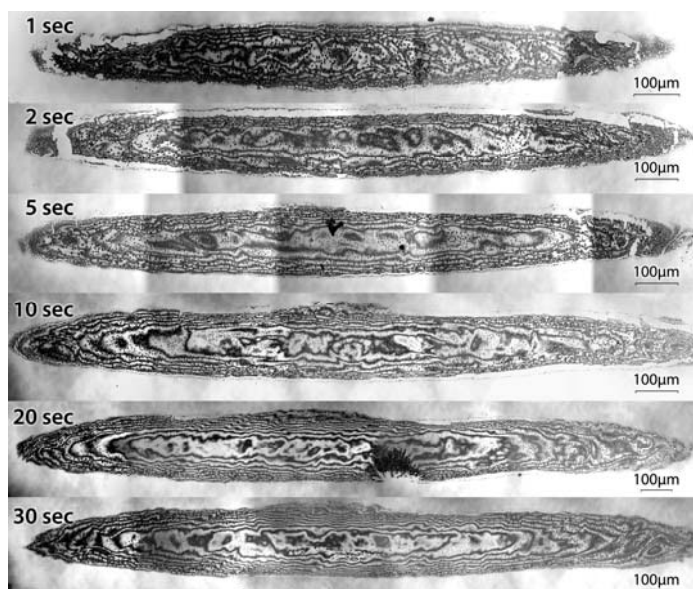


**Fig. 9.11:** Confocal images for the photopolymerized structures of SAN-Mon sample at different exposure times at 488 nm.

The line obtained with 30 sec exposure time has a lateral dimension which is about double that obtained with an irradiation of 1 sec ( $\sim 200$  vs  $\sim 100$   $\mu\text{m}$ ). In fact longer exposure permits a greater growth of the polymerized regions.

For the other sol-gel matrices we have done a more specific study of the photopolymerization process. In fact, we have chosen to investigate also the effect of the external atmosphere, as well as the effects of the different incident energies and exposure

times. In the following section we will show the results of the photopolymerization at 488 nm on hybrid films.

All the polymerized structures are efficiently developed using a mixture of Methoxyethanol and Acetone (50:50). The first solvent promotes the dissolution of sol-gel components that do not undergo the inorganic condensation while the second can dissolve the unreacted monomer units.

Two films from MZrMA and two from MZrMAMon sols are deposited by spinning. One of each is polymerized, at 488 nm, in air, while the others are irradiated in a box with a continuum flux of inert gas ( $N_2$ ), in order to investigate the effect of atmospheric oxygen on the acrylate photopolymerization. All the films are kept in nitrogen flux for five minutes prior to exposure in order to promote the replacement of the air diffused in the pores of the sol-gel film with inert gas.

All these samples are irradiated for a time varying from 1 second to 1 minute, at energy varying from 25 mW to 300 mW.

Samples MZrMA polymerize at 300 mW energy for few minutes of irradiation. In this case the photopolymerization both in air and in nitrogen flux is not so efficient to allow the formation of structures resistant to the developer attack. By confocal microscopy it is possible to observe that the structures are not well resolved.

Matrices containing also the triacrylated monomer, MZrMAMon, show a more efficient photopolymerization process, thanks to the larger number of double bonds available. Indeed, the photopolymerization carried out both in air and in nitrogen atmosphere produces lines resistant to the development. Thin samples, irradiated in air, need higher incident energies: only the lines obtained at 300 mW, with high exposure times (few minutes), remain on the substrate. For the same sample, treated in  $N_2$ , all lines resist to the development (down to 50 mW) indicating that the photopolymerization in inert atmosphere is more efficient.

By performing the same experiment in MZrMAMon thick films it is possible to observe that the photopolymerization takes place both in air and in nitrogen, for energies varying from 25 to 300 mW (reaching a lower limit of 10 mW for treatment in  $N_2$ ). The obtained structures differ in the dimensions: in air, using low energies, the final stripes are more defined and thinner. Figure 9.12 shows samples photopolymerized at 10 mW, in air (panel a) and in nitrogen (panel b) atmosphere: the thickness of the first stripe is around 20  $\mu\text{m}$ , while with the second one it is 100  $\mu\text{m}$ .

Comparing the sizes of the obtained structures with the dimensions of the focused beam, it is possible to confirm that in air the photopolymerization is spatially more confined than in N<sub>2</sub>.

MZrMA matrices, without the presence of the monomer, can mainly produce linear oligomeric organic chains. Indeed, the presence of the triacrylated monomer probably allows the formation of branched oligomeric chains due to its molecular ring-structure with three acrylic side groups. This monomer, on one side, promotes the photopolymerization at lower energies; on the other side it makes it more difficult to reach the confinement of the photopolymerization at higher energies in N<sub>2</sub> atmosphere. In order to obtain well defined and low dimensional structures, performing the photopolymerization in air using low energies appears to be more convenient.

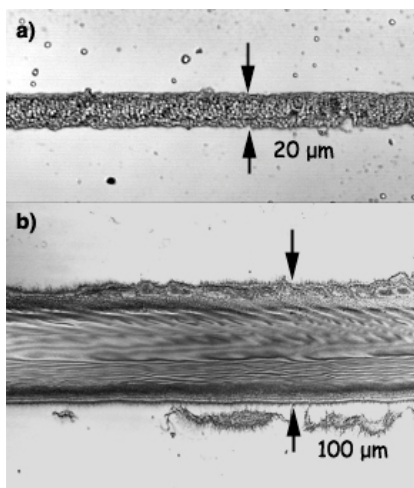


**Fig. 9.12:** Confocal images of the lines after the development stage of MZrMAMon sample irradiated at 488 nm at 10 mW, in air (a) and N<sub>2</sub> (b)

Also in these cases, it is possible to use the FT-IR analysis for evaluating the degree of organic photopolymerization.

Figure 9.13 reports the IR spectra of the MZrMAMon film before and after the photopolymerization and the development. The photopolymerization of large areas is obtained by moving the sample with respect to the laser spot. By this way, it is not possible to have a precise control of the energy doses and the exposure times and it is difficult to estimate from the IR spectra the polymerization degree after each energy value or irradiation time. Anyway, it is possible to observe a decrease of peaks at 1410 cm<sup>-1</sup> and 1635 cm<sup>-1</sup> as a consequence of the photopolymerization.

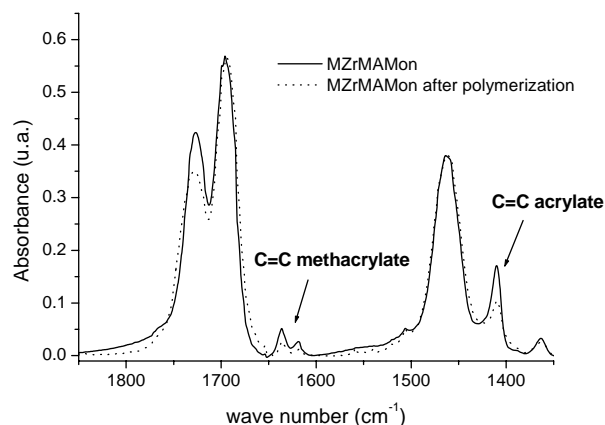


**Fig. 9.13:** FT-IR spectra of film MZrMAMon before (continuum line) and after photopolymerization (dash line) normalized with respect to the peak of carbonyl group at 1700 cm<sup>-1</sup>.

## 9.6 Two-photon polymerization

The two-photon polymerization experiments are performed with the fs laser system already used for the TPIF measurements. The wavelength of excitation is fixed at 850 nm, near to the maximum of the TPA spectrum of the photoinitiator and to the maximum emission of the laser system: by this way we guarantee high values of TPA cross-section and high incident energies.

The laser beam crosses an iris diaphragm, a couple of linear polarizers and absorbing filters. The relative position of the optical axes of the two polarizers allows the control of the final optical power. Afterward, the beam is reflected by a mirror, crosses a second iris diaphragm before being focused with two commercial microscope objectives. In this case the intensity is focused on a single spot.

For the photopolymerization of the SAN-Mon films, we have used a microscope objective 10X and a numerical aperture of 0.25. The diameter dimension of the laser beam at the focal position is estimated to be about 10  $\mu\text{m}$ , considering a propagation of a Gaussian beam in the microscopic objective.

For the TPIP experiments on MZrMAMon and MZrMA samples, we have employed a microscope objective 50X (*Olympus UMPlanFL*) with a numerical aperture of 0.8 and a working distance of 0.66 mm. The position of the focal volume is controlled perpendicularly and along the beam propagation with micrometric screws. The diameter of the laser beam at the focal position is estimated to be 5  $\mu\text{m}$ .

### 9.6.1 TPIP on SAN-Mon films

We have firstly tested the photopolymerization process on SAN-Mon samples. Two different energies (350 and 450 mW) are employed and the exposure times are varied from 1 sec to 20 sec. Figure 7.14 shows the confocal images of the developed structures after irradiation with 350 mW (on the left) and 450 mW (on the right) at different exposure times.

From the images reported in Fig. 7.14 it is possible to observe that the spots have approximately a circular shape. The spots obtained with 450 mW and higher exposure times have a less defined shape. This can be a consequence of the difficulty to confine the incident energy only in the focal volume.

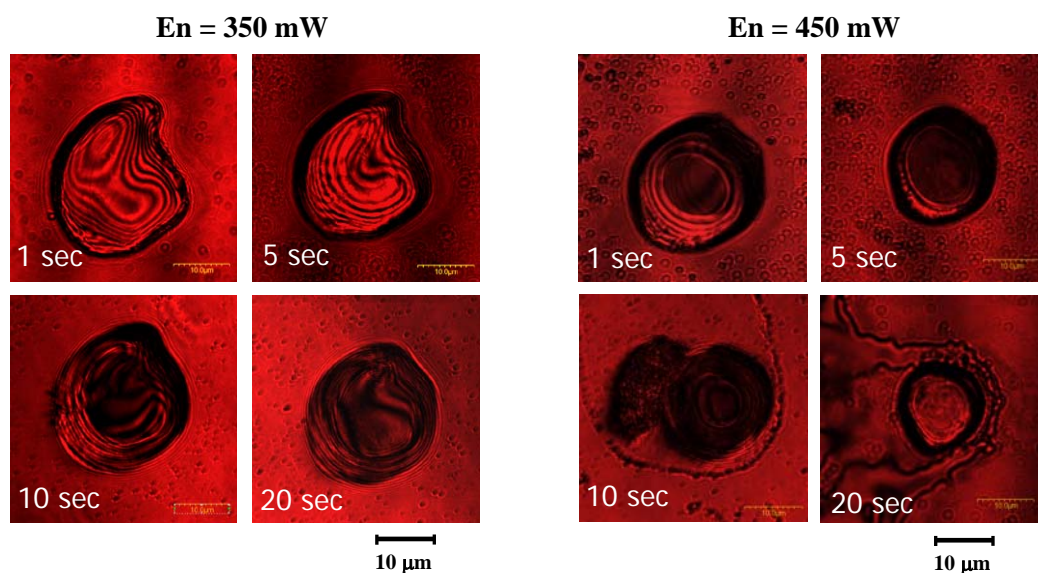


**Fig. 9.14:** Confocal images of the spots after development stage of SAN-Mon sample, irradiated at 850 nm, at different exposure times. The spots are obtained with incident energies equals to 350 mW (on the left) and 450 mW (on the right).

The dimensions of the spots (about 15  $\mu\text{m}$ ) are not influenced by the different energies or irradiation times. Considering the diameter of the laser beam at the focal position (about 10  $\mu\text{m}$ ), the intensities on the samples are equals to  $4.5 \times 10^{10}$  (for 350 mW) and  $5.7 \times 10^{10}$   $\text{W}/\text{cm}^2$  (for 450 mW). These data are comparable with that reported in reference [21] for an excitation source at 1064 nm, pulses with duration of 0.64 ns and repetition rate of 13.6 KHz. The major difference is in the incident exposure dose, expressed in  $\text{J}/\text{cm}^2$ . In fact, in Ref. [21] Martineau et al. show that the estimated threshold exposure dose is

about  $2 \text{ kJ/cm}^2$ . This value is related to the minimum exposure duration that would lead to an infinitely thin polymerized point.

If we consider that our minimum exposure time is 1 sec and the repetition rate of the laser is 76 MHz, the exposure dose becomes  $5 \times 10^2 \text{ kJ/cm}^2$ . Our value is about 250 times larger than that reported in Ref. [21]. Unfortunately, for the moment we can not control the exposure time under 1 second.

### 9.6.2 TPIP on MZrMAMon and MZrMA films

For the TPIP experiments on MZrMAMon and MZrMA samples, the incident energies are varied from 10 to 450 mW, and the exposure times are varied from 1 to 60 sec, using air and nitrogen atmosphere.

We note that in this case it is less important to control the experimental atmosphere in order to increase the efficiency of the process. The reason can be probably attributed to the fact that TPIP promotes the photopolymerization only in the focal volume. If the beam is focused into the sample, closer to the film-substrate interface, the volume interested in the TPA process is not in direct contact with the external atmosphere. By this way, the inhibition effect due to the molecular oxygen is less important.

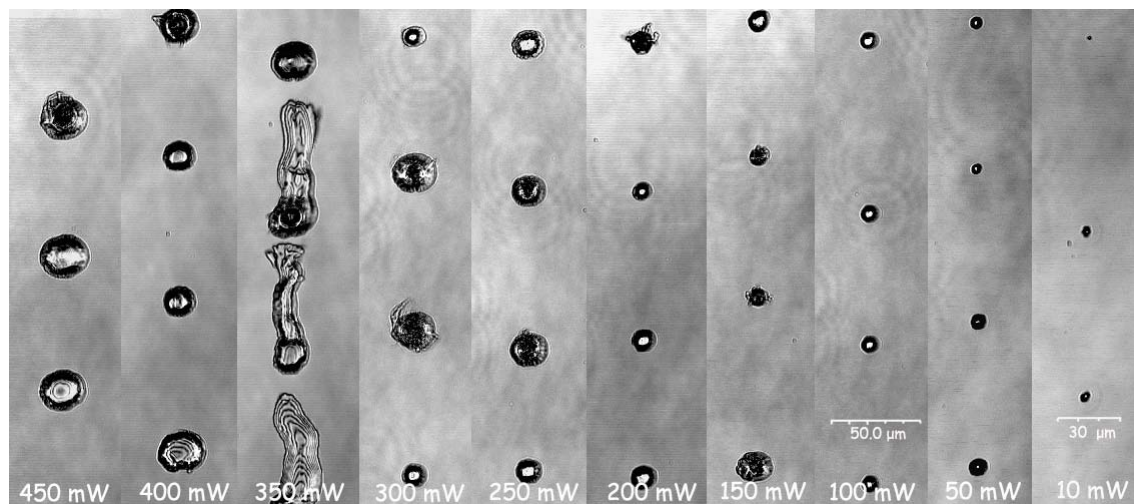


**Fig. 9.15:** Confocal images of the spots after development stage of MZrMA sample, irradiated at 850 nm, at different incident energies.

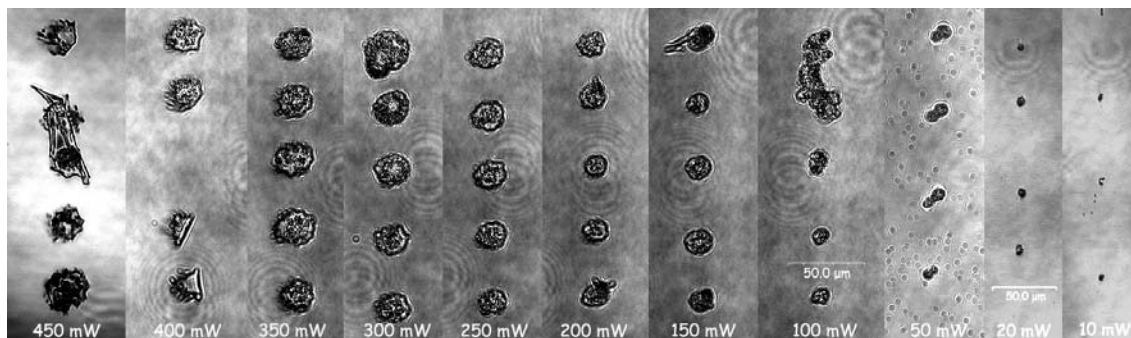


**Fig. 9.16:** Confocal images of the spots after development stage of MZrMAMon sample, irradiated at 850 nm, at different incident energies.

With MZrMA and MZrMAMon samples the effect of the input energies and the exposure times on the final features has been investigated, performing all the irradiations in air atmosphere. Figures 9.15 and 9.16 show respectively the confocal images of the patterns of MZrMA and MZrMAMon remained on the substrate after the development stage. Each slide represents the polymerized dots obtained with with a given energy, whose value is indicated at the bottom, and 1 sec irradiation time. From the micrographs, it is possible to observe that the resolution on the final structure becomes more defined when the input energy decreases. In fact, it is possible to control the polymerization reactions when the energy dose is low enough to prevent diffusion of the radicals over an area larger than the laser spot. This control is more efficient in MZrMA sample while in the presence of the monomer, at high energy, the photopolymerized regions are less confined. The variation of the irradiation time does not affect the spot dimensions. Table 9.II reports, as examples, the estimated diameter values of the dots for both matrices, at different energies. By comparing these values with the estimated dimension of the laser beam used, it is possible to confirm that only low energies allow obtaining structures with sizes comparable to the dimensions of the laser beam used.

Incident Energies [mW]	Spot diameter MZrMA [ $\mu\text{m}$ ]	Spot diameter MZrMAMon [ $\mu\text{m}$ ]
450	25	27
400	17	21
350	20	18
300	20	20
250	15	19
200	12	17
150	10	15
100	9	13
50	8	10
10	5	5

**Table 9.II:** Estimated diameter values of developed dots on MZrMA and MZrMAMon films, irradiated at 850 nm.

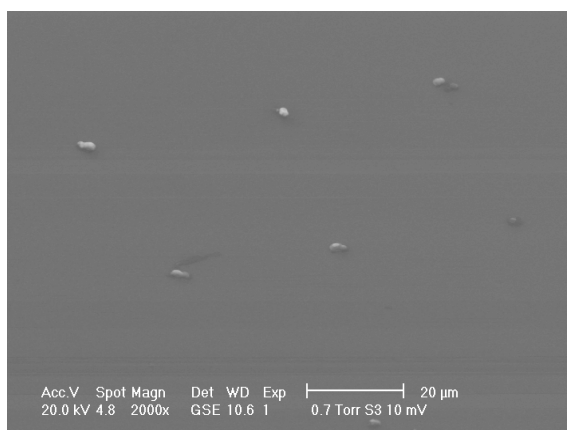


**Fig. 9.17:** ESEM image of a pattern of circular spots created by TPIP on MZrMAMon film with 10 mW input energy.

The ESEM (*Philips Mod. XL30*) micrograph of a developed pattern, created on MZrMAMon films, with an input energy of 10 mW, is reported in Fig. 9.17. All the features resist to the development stage and have approximately uniform dimensions.

When the laser energy increases the photopolymerization regions are less confined and irregular as shown in Fig. 9.18 and 9.19.

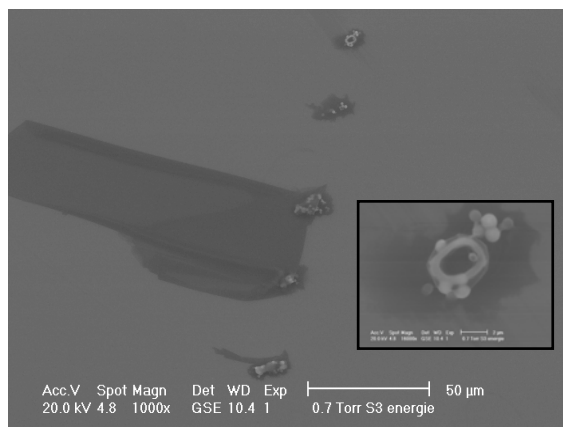


**Fig. 9.18:** ESEM image of spots created by TPIP on MZrMAMon film with input energy of 100 mW. The inset reports a zoom of one dot.

Figure 9.18 reports the ESEM image of a line of dots obtained by irradiating the MZrMAMon sample, with 100 mW, and the magnification of one of them in the inset. Figure 9.19a is the 3D-AFM (*Ntegra Mod. NT-NTD*) micrograph of one structure of the same sample. All images show inhomogeneous and irregular structures clearly related to the photopolymerization performed at high energies. The 3D-AFM image of a MZrMAMon sample, irradiated at 10 mW, is depicted in Fig. 9.19b. At this energy the obtained structure is well defined and more homogeneous.

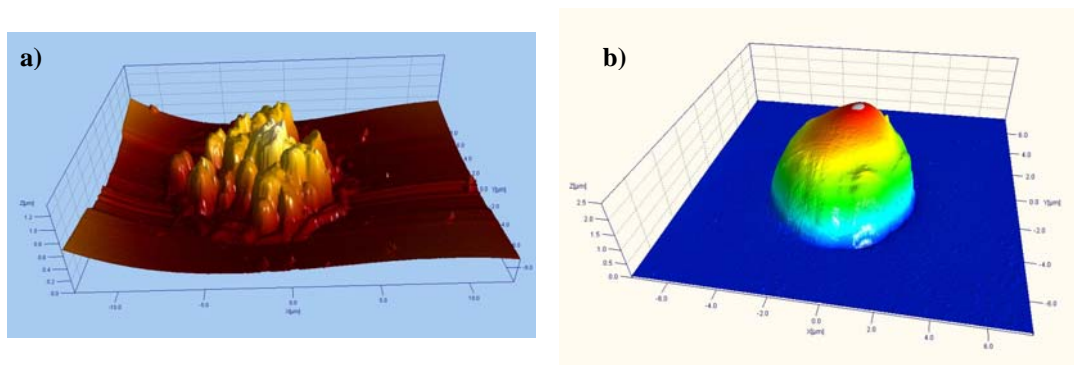


**Fig. 9.19:** 3D-AFM profile of one MZrMAMon dot obtained by TPIP at 850 nm employing 100 mW (a) and 10 mW (b) pulse energy.

The chemical characterization of the structures created through TPIP is very difficult because of the small dimensions. We have been using the IR spectroscopy both in ATR and in a focalized configuration, but the resulting spectra have too low intensities to precisely reveal any chemical modifications after the photopolymerization.

## 9.7 Conclusions

In this chapter we have reported the results on the photopolymerization of different materials. One of these is obtained by all polymeric compounds. The others, obtained by sol-gel synthesis, consist in a blend of organic-inorganic hybrid precursors with acrylic and methacrylic functionalities. The photopolymerization has been induced by one- or two-photon absorption processes, activated by using a novel photoinitiator.

We have tested the efficiency of photopolymerization by varying different parameters, like the incident energies, the exposure times and the external atmosphere. One of the main factors influencing the efficiency in one-photon polymerization is the presence of molecular oxygen. Instead, this issue becomes less important when two-photon excitation is employed.

For hybrid samples, the excitation energies are one of the first parameter to be controlled, especially when two-photon polymerization is performed, for the realization of structures with small dimensions. This is an important result useful for the fabrication of micro- and nano-patterns on sol-gel materials for 3D-photonic applications.

## REFERENCES:

- <sup>1</sup> Fortunati, I. et al. *Proc. of SPIE*, 2007, 6645, 664520-1-11
- <sup>2</sup> Houbertz, R. et al. *Appl. Phys. Lett.*, 2004, 84(7), 1105-1107
- <sup>3</sup> Pola, J. et al. *Surf. and Coat. Techn.* 2002, 149, 129-134
- <sup>4</sup> McLean, L.R. et al. *Thin Solid Films* 1983, 99, 127-131
- <sup>5</sup> Wang, F. et al. *Appl. Phys. B* 2007, 86, 117-122
- <sup>6</sup> Nakahama, T. et al. *Thin Solid Films*, 2006, 499, 406-409
- <sup>7</sup> Sun, H. B. et al. *Appl. Phys. Lett.*, 2003, 83(6), 1104-1107
- <sup>8</sup> Cumpston, B. et al. *Lett. to Nature*, 1999, 398, 51-54
- <sup>9</sup> Miwa, M. et al. *Appl. Phys. A*, 2001, 73, 561-566
- <sup>10</sup> Klein, S. et al. *Appl. Phys. Lett.*, 2005, 86, 211118
- <sup>11</sup> Teh, W.H. et al. *J. of Appl. Phys.*, 2005, 97, 054907
- <sup>12</sup> Houbertz, R. *Applied Surface Science*, 2005, 247, 504-512
- <sup>13</sup> Houbertz, R. *Adv. Eng. Mater.* 2003, 5(8), 551
- <sup>14</sup> Studer, K. et al. *Progress in Organic Coatings*, 2003, 48, 92-100; 101-111
- <sup>15</sup> Lee, T.Y. et al. *Polymer*, 2004, 45, 6155-6162
- <sup>16</sup> Kilambi, H. et al. *Polymer*, 2007, 48, 2014-2021
- <sup>17</sup> Innocenzi, P. and Brusatin, G. *J. of Non-Cryst. Solids*, 2004, 333, 137-142
- <sup>18</sup> Cai, Y. et al. *Polymer*, 2006, 47, 6560-6566
- <sup>19</sup> Engardio, T. J. and Dalsin, P. D. *Production of photopolymerized polyester high index ophthalmic lenses, Pat. N° 6099123*
- <sup>20</sup> Lemerrier, C. et al. *New J. Chem.* 2006, 30, 1606-1613
- <sup>21</sup> Martineau, C. *Synth. Metals*, 2003, 138, 353-356
- <sup>22</sup> Zhang, Z. et al. *Polymer* 2006, 47, 6970-6977
- <sup>23</sup> Whan Gun Kim, W. G. and Lee, J. Y. *Polymer* 2003, 44, 6303-6309
- <sup>24</sup> Lizotte, J. R. et al. *J. of Polymer Science: Part A: Polymer Chemistry*, 2002, 40, 583-590
- <sup>25</sup> Duann, Y.F. et al. *Polymer*, 2004, 45, 6839-6843
- <sup>26</sup> Scoriah, M.J. et al. *Polymer Bulletin*, 2006, 57, 157-167
- <sup>27</sup> Brown, W. H. and Foote, C. S. *Chimica Organica*, 2° ed. 1998, EdiSES
- <sup>28</sup> Innocenzi, P. and Brusatin, G. *Chemistry of Materials*, 2003, 15, 4790
- <sup>29</sup> Studer, K. et al. *Progress in Organic Coating*, 2003, 48, 92, 101



## FINAL REMARKS

In this work we have investigated the two-photon and multi-photon absorption properties of different classes of materials. These non linear absorptions play an important role in many applications in photonics and in biological and medical fields.

The high efficiency of the two-photon absorption process is an essential parameter for the practical use of the TPA chromophores. It is therefore necessary to characterize the non linear optical properties of the available TPA systems, in order to select the materials with the highest TPA cross-section in the spectral region required by the application. A large part of this project has been devoted to the realization and the optimization of the set-up for the two-photon induced fluorescence (TPIF) method, a technique newly introduced in our laboratory for the measurement of the TPA cross section in a wide range.

The TPIF measurements have been performed using a Ti:Sapphire laser as excitation source, characterized by pulses of 130 fs in the wavelength region between 720 and 930 nm. The absolute TPA cross-section at every wavelength is determined by the normalization of the TPA spectrum of the studied dye with the spectrum of the reference chromophore (generally Fluorescein or Rhodamine B). TPA spectra of the materials used as reference are known in literature, even if sometimes the values reported in different papers do not coincide.

In order to test the quality of the new experimental set-up, we have firstly measured the TPA spectra of some dyes already reported in the literature. We have shown that our results are in perfect agreement with the data reported by Xu, C. et al. [*Bioimaging*, 1996, 4, 198-207]. We have therefore used these values to normalize the experimental data of our compounds. The TPIF measurement is a very sensitive method even if the resulting absolute TPA cross section values can be affected by large errors. The main uncertainty arises from the choice of a suitable reference for standardization.

We have employed this method to characterize many classes of fluorescent systems: dipolar push-pull; dimers of PEP and MePEP; quadrupolar and Zn(II)-coordinated octupolar systems; squaraines and semiconductor quantum dots. For all of these compounds we have determined the TPA spectrum. The characterization of some compounds, such as the dipolar and the dimers, is useful for carrying on a basic study on the interactions involved in the TPA process. These experimental results are under theoretical investigation, in order to correlate the TPA response with the molecular and photophysical parameters of the examined systems.

Moreover, we have demonstrated that the studied Zn(II) octupolar complexes possess a maximum TPA cross-section which is merely the sum of the three ligands. This is an important result to show that the Zn metal is not an efficient template to extend the delocalization of the  $\pi$ -electrons over the three branches nor is there any effective through-space excitonic coupling. Probably, a different metal or a modified steric configuration can favor the enhancement in the TPA response going from the ligand to the complex. Instead, the monocoordination of ligand TD2 with a cationic Zn(II) centre leads to an enhancement of  $\sigma_{\text{TPA}}$  with respect to free ligand. In this case the coordinating Zn ion strongly modifies the acceptor properties of the terpyridine group.

Finally, the semiconductor core-shell CdSe-ZnS quantum dots, with different sizes, possess the highest values of the TPA cross-section. In these systems the reduction of their sizes below the exciton Bohr radius (about 5 nm in CdSe) causes strong effects on their optical properties. The main consequences are the blue-shift in the bandgap of quantum dots, if compared with the bulk semiconductor, and the appearance of discrete sub-bands corresponding to quantization along the direction of confinement. The increase of the density of states both for valence and conduction bands produces a large enhancement of oscillator strength upon quantum confinement, leading to an increase of the optical response of these systems.

In this work we have studied the possibility to use the TPA properties of such materials for three different applications: optical limiting, up-conversion lasing and two-photon induced photopolymerization.

For the optical limiting application, we are interested in the non linear absorption response of the TPA system. Instead, the TPA property alone is not sufficient for the other applications. In fact, for the up-conversion lasing, after the two photon absorption, the system must be able to yield amplified emission in suitable conditions. Regarding the last application, the TPA absorber must initiate the photopolymerization process through the formation of free reactive radicals.

The realization of practical all-solid state devices requires both the use of an efficient active material and a suitable solid medium, where the non linear optical properties of the dopant remain unchanged. We have used the sol-gel method for the preparation of the host matrices, using inorganic and hybrid organic-inorganic precursors. The use of hybrid precursors is very useful for the preparation of host materials in optics application.

#### **- Optical limiting application**

The optical limiter device proposed in our group is based on the use of two disks doped respectively with a TPA absorber and a system showing RSA properties. Because the tested RSA material shows the best efficiency at 690 nm, using ns pulses, it is necessary to test the device in the same conditions. Previous trials on a tandem prototype have shown two main limits: the low efficiency of the quadrupolar TPA dye (called Bis-OH PEPEP) and the low laser damage resistance of the matrix. We have therefore tested the TPA response of new systems and synthesized new sol-gel materials in order to improve the performances.

The characterization of the TPA absorber in the ns regime is performed with z-scan technique. It allows measuring effective TPA cross sections ( $\sigma_{\text{TPA}}^{\text{eff}}$ ) characterized by values more than one order of magnitude greater than those measured with fs pulses. In this case we have characterized many classes of compounds, like dipolar, quadrupolar and octupolar systems, squaraines, porphyrins and semiconductor quantum dots, in solutions. The more promising material is a porphyrin molecule and its hydroxyl-functionalized derivative: it is under preparation for the successive embedding in a solid matrix. Moreover, also in ns regime the semiconductor quantum dots show high TPA cross-sections. We have here reported the results of their inclusion in a sol-gel matrix. The data

are promising, even though some issues, like reaching a high concentrations and avoiding the possible precipitation of the nanoparticles, remain to be addressed.

Regarding the second aspect, we have synthesized different hybrid matrices. In particular, four of them (GTZ, GZH, GBZ and GZB) have been mechanically, thermally, micro-structurally and optically characterized. It is interesting to note how apparently little modifications in the synthesis protocols can generate materials with different microscopic properties. One of the main results is the direct correlation between the elastic properties of the materials and their resistance to the laser irradiation. The GZH matrix shows the highest fluence at damage and the lowest elastic modulus. This is an important result and can be explained with the thermo-mechanical principles. In fact, stiffer materials develop larger thermal stresses around the area illuminated by the laser beam and the optical damage occurs at lower fluences. Another important consideration concerns the worsening of the optical damage resistance in the presence of superficial or structural defects on the material. It is therefore important to treat samples in such a way to reduce the defects.

#### **- Up-conversion application**

Part of this work has been devoted to the analysis of the lasing properties of both organic push-pull molecules and semiconductor core-shell quantum dots using a fs laser. It has been possible to detect the amplified spontaneous emission (ASE) peak of the organic compounds only in solution using high concentrations. In fact, if they are embedded in a sol-gel film the activation of the ASE process is too high and a photobleaching occurs.

On the contrary, for the nanoparticles the matrix, together with the presence of the CdS-ZnS shell, plays an essential role in the reduction of the nonradiative pathways. By these ways the fluorescence quantum yield is maintained high and the optical amplification can take place before the ultrafast non-radiative Auger recombination.

The inclusion of these QDs of different size in a zirconia matrix is an excellent way to increase the lasing properties and to improve the temporal stability under both one- (at 400 nm) and two-photon excitation (at 800 nm). This is the first work reported in literature where some hetero-structures are used as lasing material upon two-photon excitation.

Based on these results, the use of low threshold two-photon lasing materials, such as that based on CdSe-CdS-ZnS, is a promising way for the development of infra-red optically pumped micron-sized lasers.

### **- Two-photon induced photopolymerization application**

The two-photon induced photopolymerization is an important tool for the fabrication of micro- and nano-structured material. In this case, the quadratic dependence on the intensity of the TPA process is exploited for inducing a local modification on the material below the diffraction limit. In the literature only polymeric blend based on acrylic or methacrylic units are used as photoresist material. We have studied the possibility to employ also hybrid organic-inorganic sol-gel materials with acrylic and methacrylic functionalities.

A suitable photoinitiator is used to activate the photopolymerization process, induced by one- or two-photon absorption processes. In the first case, the process is activated by an Ar<sup>+</sup> laser at 488 nm and in the second case by a fs Ti:Sapphire laser at 850 nm. After the excitation, the chain of the photoinitiator is probably broken and two radicals are available for the activation of the polymerization.

We have tested the efficiency of the photopolymerization by varying different parameters, like the incident energies, the exposure times and the external atmosphere. One of the main factors influencing the efficiency in one-photon polymerization is the presence of molecular oxygen. Instead, this issue becomes less important when two-photon excitation is employed.

For hybrid samples, the excitation energies are one of the first parameter to be controlled, especially when two-photon polymerization is performed, for the realization of structures with small dimensions. This is an important result useful for the fabrication of micro- and nano-patterns on sol-gel materials for 3D-phonic applications.



## *Ringraziamenti*

Eccoci alla pagina dei ringraziamenti! Innanzitutto, un sentito ringraziamento al prof. Renato Bozio per l'attenta cura che dedica alla sua attività scientifica e per il suo guizzo geniale di fronte ad ogni problema. Sono profondamente grata di aver lavorato con Raffaella, Camilla e Giovanna: tre donne di grandissima tenacia, disponibilità e umanità che sanno districarsi con grinta tra la loro attività scientifica e la vita personale. Credo di dovere un ringraziamento particolare a Raffaella che ha saputo essermi amica e confidente in moltissime occasioni, sempre pronta a dare consigli e suggerimenti nella più totale semplicità e discrezione. Mi ha dato la possibilità di imparare molte cose sia dal lato umano sia scientifico... grazie davvero!

Un pensiero particolare lo dedico a Sara, compagna d'avventure strabilianti nel mondo della fluorescenza e dei "due fotoni"! Ricordo le giornate trascorse in laboratorio al buio, bloccando ogni raggio di luce che potesse dare fastidio alla misura e cambiando tutte le lenti che siamo riuscite a scovare nei vari armadi. A tenerci compagnia, le belle chiacchiere a fiumi sui nostri vissuti e i nostri futuri... Di quel periodo ricordo con molto affetto, e a volte con nostalgia, le pause pranzo

(più o meno lunghe!) mangiando un panino al volo e subito pronti per le mitiche partite all'Amico del Giaguaro... Evviva la compagnia del Giaguaro! Grazie ad Alessandro, fornitore ufficiale di carte pronte all'uso in ogni momento, a Sara che assieme ad Elena erano le migliori mentitrici, ad Andrea che a causa della sua assoluta tranquillità nel mangiare partecipava solo a metà delle partite, a Mirko, Mirco, Matteo e Roberto per le grasse risate! Grazie ancora a Mirko per le pause caffè, richieste a qualunque ora della giornata, per gli scambi di libri e opinioni e per aver introdotto l'evento ufficiale dello Scambialibro, per le "Scommesse del giorno" davanti alla macchinetta del caffè, per le sue vicissitudini e avventure di tutti i tipi e infine per la sua semplicità!

Un pensiero ai vari dottorandi e borsisti...

A Michele per la sua pazienza nel rispondere alle mie domande anche nei momenti meno adatti; a Elisabetta (o meglio Lisabetta!!) che ha sempre saputo esprimere con molta semplicità e spontaneità il suo modo d'essere; a Eleonora e Ida, compagne di confidenze e promotrici della pausa tè ("Evviva le tre sindacaliste moschettiere!" O meglio... Le tre grazie, a nostro modesto parere!); a Samu che è da poco tornato a rallegrare le giornate; a Enzo che ha saputo essermi amico e sostenitore in molte circostanze. E ancora, a Simone che, nonostante tutte le sue malefatte, ha scritto il programma per l'acquisizione dei dati, facendoci risparmiare moltissimo tempo; a Roberto per la calma di fronte agli eventi e per lo spritz alla sera; a Giorgio per le vicissitudini con le sue due donne... e per l'euro ancora incastonato nella macchinetta del caffè; a Simone e Gabriele per l'aiuto in laboratorio; a Tiziano che mi ha fatto capire che non sempre è possibile andare d'accordo con tutti...

E infine un ringraziamento ai colleghi di Ingegneria... a Gioia e Alessandro per il grosso impegno nel tentare di gestire e di capire il difficile mondo delle nanoparticelle! A Marco per il sarcastico umorismo che lo contraddistingue e per la sua disponibilità nel dare aiuto e brillanti idee. Infine a Jlenia che, nonostante il suo frequente sconforto rispetto ai risultati ottenuti, si è dimostrata sempre molto capace e disponibile.

Venendo poi alle persone a me più vicine e care, devo un ringraziamento speciale a Michele che ha saputo conquistarmi con la sua profonda sensibilità, con il suo calore e la sua fidata presenza. Un ringraziamento anche alla mia famiglia, in particolare a Moira e Sabrina, che sento fortemente legate a me e su cui sono certa potrò contare ogni volta ne avrò bisogno, e ai miei splendidi nipotini Marco e Daniele.

Un ultimo pensiero lo dedico a tutte quelle persone che direttamente o indirettamente mi hanno affiancato in questi tre anni, donandomi momenti di vera felicità.